

Engineering models in wind energy aerodynamics

Development, implementation and analysis
using dedicated aerodynamic measurements

PROEFSCHRIFT

ter verkrijging van de graad van doctor
aan de Technische Universiteit Delft,
op gezag van de Rector Magnificus Prof. ir. K.C.A.M. Luyben
voorzitter van het College voor Promoties,
in het openbaar te verdedigen
op dinsdag 27 november 2012 om 15 uur
door

Jan Gerhard SCHEPERS

Ingenieur Luchtvaart en Ruimtevaarttechniek
geboren te Winterswijk.


Dit proefschrift is goedgekeurd door de promotors:

Prof. dr. G.J.W van Bussel
Prof. dr. Ir. G.A.M. van Kuik

Samenstelling promotiecommissie:

Rector Magnificus	Voorzitter
Prof. dr. G.J.W van Bussel	Technische Universiteit Delft, promotor
Prof. dr. ir. G.A.M. van Kuik	Technische Universiteit Delft, promotor
Prof. dr. ir. T. van Holten	Technische Universiteit Delft
Dr. ir. L.M.M Veldhuis	Technische Universiteit Delft
Prof. dr. J.N. Sørensen	Technical University of Denmark
Dr. S. Schreck	National Renewable Energy Laboratory NREL
Ir. H. Snel	Energie Onderzoek Centrum Nederland, ECN
Prof. dr. ir. drs H. Bijl	Technische Universiteit Delft, reserve

Printed by Ipskamp, The Netherlands;

Printing was made possible by  **ECN**

ISBN:978-94-6191-507-8

All rights reserved. No part of the material protected by this copyright notice may be reproduced or utilized in any form or by any means, electronic or mechanical, including photocopying, recording or by any information storage and retrieval system, without the prior permission of the author.

Author email:schepers.gerard@gmail.com

*To the generation of Erik and Sander: That this work may be a modest
contribution to a more clean and prosperous world*

Acknowledgements

Writing this thesis was a very pleasant task. It sometimes felt a bit like a journey through time because some of the described results go back to the 1980's and 1990's when wind energy research projects were carried out with different people in a very different setting.

Most of the described work comes from cooperation projects. That means that this work wouldn't have been possible without the help, inspiration, ideas and results of very many colleagues in, but also outside ECN.

I very much would like to thank all my colleagues at ECN-Wind. Although this thesis has largely been written in own time the findings come from projects which are carried out within the ECN organization to which many colleagues contributed. It is impossible to list all colleagues but Herman Snel needs to be mentioned. He initiated and contributed to so much of the described research and he has been a tremendous source of inspiration for me. Edwin Bot helped me with the cumbersome task of fine tuning various figures. More important, he also worked on the fine tuning of the Farmflow modelling and the understanding of wind farm measurements, the results of which are described in this thesis. I also would like to acknowledge my former group leader Peter Eecen who always supported and stimulated the writing of this thesis and did whatever he could to make this possible.

Making this thesis in Latex was a wise decision and I am still amazed by the fact that it only took a split second to include large portions of text and figures as produced in the 1980's into the present report. And if something went wrong due to my clumsiness there was always the help from a Latex wizard like Bernard Bulder.

Another wizard is Koen Boorsma with whom I had the pleasure to work together in the Mexnext project. Several findings from that project as described in this report are the result of very intense discussions behind a computer screen when we processed the data and tried to understand them.

Of course I also would like to thank Gijs van Kuik and Gerard van Bussel for their support and their critical reviews. They gave me the opportunity to spend some time at TUDelft to write this thesis. This gave me a better look in their "kitchen" by which I am even more impressed by the activities there. Equally important was the support from Sylvia Willems who managed to help me with really every practical problem which I had to face in doing this PhD. I hope, also from the perspective of NHL, for a continuation of the cooperation with Delft.

And then there is an almost infinite number of colleagues outside ECN with whom I cooperated. It is impossible to mention them all but I always experienced this cooperation as very pleasant in particular during the various project meetings at sometimes very exotic places. Through these cooperations I got access to a wealth of unique results, e.g. measurements from the world's largest wind tunnel: NASA-Ames or from the largest off-shore wind farms. Without these (and other) contributions this PhD wouldn't have been possible at all.

Also, I donot want to forget the funding agencies. For example, the former Senter NOVEM agency which sponsored many of the projects described in this thesis. The same holds for the EU. Several results come from IEA projects which were carried out under the auspices of the IEA Executive Committee, the members of which where always very helpful in establishing mondial research cooperations. These IEA projects formed and still form great opportunities for cooperation not only within Europe but with parties all over the world, including the US, Canada, Korea, Japan and China.

Last but definitely not least. I realize that there isn't a worse cliché than writing that this thesis was only possible through the unconditional support from my home front (Henrike, Erik, Sander). Still it needs to be written because it is so very true! As a matter of fact this thesis has been my excuse for doing completely nothing at home for more than a year. I am really looking forward to return to normal life again. Thank you!

Summary

The subject of aerodynamics is of major importance for the successful deployment of wind energy. As a matter of fact there are two aerodynamic areas in the wind energy technology: Rotor aerodynamics and wind farm aerodynamics. The first subject considers the flow around the rotor and the second subject considers the (wake) flow within a wind farm. For both areas calculational models have been developed which are implemented in rotor design and wind farm design codes respectively. Accurate rotor design codes enable a reliable design of wind turbines and an optimization towards a higher energy production and lower loads, i.e. towards a lower cost of energy. They are also required to avoid design errors and hence to reduce investment risks of wind turbine manufacturers. Accurate wind farm design codes are needed to predict the production losses and the load increase on turbines in a farm due to wake effects. They also support the optimization of wind farms (e.g. through farm control) by which the energy losses and the load increase from wake effects (and consequently the costs/kWh) are minimized.

For both areas the complexity of models range from engineering methods to very advanced Computational Fluid Dynamics (CFD) methods. The term engineering method is meant to indicate a model which casts a complicated flow phenomenon into a transparent form. This generally goes together with an economic computer usage. In this respect it is very important to realize that wind energy design calculations are inherently very time consuming by which advanced CFD models are still beyond the routine possibilities of industry. As such engineering methods form the only alternative for that purpose.

The main aim of the present thesis is then to describe several developments of the last 25 years which have led to the present generation of aerodynamic engineering models. It will be shown that much progress has been made

both on the field of rotor aerodynamics as well as on the field of wind farm aerodynamics and that this progress was highly supported by the fact that dedicated aerodynamic measurement data have become available. The progress is illustrated by the engineering models which are developed and validated by ECN in several large (inter)national cooperation projects in which these measurements played an important role. The author of this thesis was heavily involved in these projects and often acted as coordinator. Since these projects were performed in close cooperation with other institutes (which used different types of models), the activities of the author can be placed in a wider context.

The first part of the thesis is devoted to rotor aerodynamics. Basically the subject of rotor aerodynamics can be subdivided in two parts: The first part deals with the global flow field around a wind turbine. This type of modelling is called induction aerodynamics, since its main goal is to determine the induced velocities at the blade. The second part deals with the loads on a wind turbine blade as a response to this flow situation and is called blade aerodynamics. Current engineering models for rotor aerodynamics topic are built around the Blade Element Momentum (BEM) theory. The Blade Element Momentum theory in itself is very basic, e.g. it is derived for 2-dimensional, stationary, homogenous and non-yawed conditions. For this reason several engineering models have been developed which overcome these simplifications and which act as add-on's to the basic BEM theory. These engineering add-on's have been developed for the field of blade aerodynamics and for the field of induction aerodynamics.

In this thesis a comparison is made between current engineering models and the engineering models from 25 years ago. The engineering methods from 25 years ago were not much more than the very basic BEM theory with a Prandtl tip loss correction and a turbulent wake correction. Moreover a tower shadow model based on a dipole model and a 'geometric' correction for cone and tilt angle were included, while yaw was modelled with the advancing and retreating blade effect only. Since then the models for airfoil aerodynamics have been improved by adding unsteady and three-dimensional effects. These unsteady effects can be divided in viscous dynamic stall effects and non-viscous effects at low angles of attack. The three-dimensional effects occur at the inner part of the blade where stall is delayed and at the outer part where the tip decreases the loads. In terms of induction aerodynamics, models have been added for dynamic inflow, the azimuthal variation of the induced velocity at yaw and a model for root losses.

The progress in the rotor aerodynamic engineering models from ECN is mainly described along results of four subsequent IEA Tasks: IEA Task 14 and 18, IEA Task 20 and IEA Task 29(Mexnext). An IEA Task (sometimes called an IEA Annex) is a cooperative project carried out under auspices of the International Energy Agency IEA. The goal of IEA Tasks 14 and 18 was to create a database of detailed aerodynamic measurements which all have been taken on turbines under atmospheric conditions. The goal of IEA Task 20 was to analyze the measurements which have been taken by the National Renewable Energy Laboratory NREL on a 10 meter diameter wind turbine which was placed in the very large NASA-Ames wind tunnel. Finally IEA Task 29(Mexnext) analyzed the measurements which have been taken in the EU Project Mexico on a wind turbine rotor with a diameter of 4.5 meters placed in the Large Low Speed Facility (LLF) of the German Dutch Wind Tunnel (DNW). In all of these experimental programs pressure distributions were measured at different locations along the rotor blades. Moreover the Mexico experiment mapped the flow field upstream, in and downstream of the rotor plane.

The detailed aerodynamic measurements from the IEA Tasks were found to be very useful in the development, improvement and validation of these engineering models because they made it possible to extract aerodynamic phenomena which are hidden in the very global information from conventional measurement programs. It is concluded that only detailed aerodynamic measurements may be used for validation of aerodynamic design models: A validation on basis of global turbine(blade) loads does not give a decisive answer on the accuracy of aerodynamic models due to the fact that 'compensating errors' may occur. Moreover it will be shown that the measurements revealed several shortcomings in aerodynamic engineering methods which partly could be 'repaired', sometimes with the help of more refined models.

Several recommendations are made on rotor aerodynamics. This includes some specific further improvements which are still possible to the current state of engineering models. Amongst other things, models for the annulus averaged induction at yaw, tip loss effects and time constants at dynamic inflow can be improved further. These improvements can be established by calibrating engineering methods to results from more advanced aerodynamic models (e.g. CFD or free vortex wake methods). The background for this recommendation lies in the fact that the validation of these advanced aerodynamic models with the detailed aerodynamic measurements from the IEA Tasks showed a clear added value from such methods on these fields.

Moreover it is concluded that three-dimensional and unsteady effects on the drag deserve more attention.

However the most important recommendation is related to the observation of an unbalance in the aerodynamic wind energy society: Much effort is spent on the development of aerodynamic models (often of little mutual differences) but the amount of experimental validation material is (too) limited. Therefore it is recommended to intensify the activities on rotor aerodynamic measurements in both the wind tunnel and the field. Special attention should be paid to the measurement of those phenomena which, until now, are still largely concealed (e.g. boundary layer phenomena) or unclear (e.g. the relation between blade loads and underlying flow field which is found puzzling in the Mexico experiment).

The present thesis also describes the progress which has been made on the field of wind farm aerodynamics. Opposite to the situation for rotor aerodynamics, where the BEM model can be appointed as the main model, the variety of models for wind farm aerodynamics is much larger. This is partly due to the fact that a wind farm aerodynamic model should cover much more aspects: It should model both the aerodynamic behavior of the rotor (which generates the wake) as well as the turbulent wake downstream of this rotor. The fact that calculational time is such an extreme constraint adds to the diversity: As a consequence CFD modelling of wind farm aerodynamics often only refers to the modelling of the wake and not to the modelling of the rotor. It also makes that wind farm and rotor aerodynamics are sometimes considered to be fully separate subjects. This is seen as an undesired development since the aerodynamics of the wake is largely determined by the aerodynamics of the rotor standing in front of the wake.

In this thesis the main characteristics of the wake flow behind a wind turbine are described together with a survey of wind farm aerodynamic models. Most of the attention is focussed on an intermediate between the very basic models and the CFD codes, i.e. the parabolized wake models. These models are relatively economic in computer usage (by which they are still considered to be engineering models) where they model the so-called far wake in a physically accurate way. The disadvantage lies in the fact that they generally need an empirical treatment of the near wake. This again goes together with a very simple modelling of the rotor. The progress in wind farm aerodynamic models is then illustrated with ECN's wind farm design code Farmflow (based on the former Wakefarm wake model) which combines a parabolized $k-\epsilon$ turbulence

model for the far wake with results from a physical free vortex wake method for the near wake.

The measurements on wind farm aerodynamics used in this thesis mainly come from the ECN Wind Turbine Test Site Wieringermeer, EWTW. This research farm consists of five wind turbines in a line set-up with a rated power of 2.5 MW and a rotor diameter and hub height of 80 meter. The turbines are extensively instrumented, where a meteorological mast is available to measure the free stream or the wake conditions. A major advantage of these measurements lies in the research environment by which data have been recorded over a very long period of high quality. The EWTW measurements revealed various new wake aerodynamic phenomena and they offered validation material for the improvement and validation of the Farmflow code. The observations on the EWTW farm are compared with those on large off-shore wind farms, the measurements of which were supplied within the EU project Upwind. In the EWTW line set-up the largest power loss due to wake effects (and hence the lowest overall power) appears at the second turbine in the farm. The turbines deeper in the farm have a slightly higher power. This is opposite to the situation in large off-shore wind farms where the power keeps decreasing for turbines deeper into the farm. This can be explained by lateral wake effects and the size of those large (array) wind farms. The power behavior in both the EWTW as well as in the large array wind farms was predicted well with Farmflow.

Several conclusions on wind farm aerodynamics are drawn. The most important conclusion is that as for the situation on rotor aerodynamics, much progress has been achieved over the past decades. This is illustrated with the developments from Wakefarm to Farmflow. In the beginning of the 1990's only single wakes were considered. These were modelled with a very simple approach: The wind turbine was represented by an actuator disc with a near wake model based on momentum theory (and later empiricism). The far wake was modelled with a turbulence model tuned for non wind energy applications. Since then the near wake models has been refined and multiple wake effects are taken into account in both axial and lateral direction. Furthermore the turbulence model has been calibrated for wind turbine wake situations. For the development of wind farm engineering models in general it is very important that some CFD models entered the (research) scene in which the rotor is modelled with more advanced methods than the actuator disc approach (e.g. with actuator lines). Such advanced models can now be used for calibration of more simple models.

Several subjects for wind farm aerodynamics have been identified which still need more attention. As such it is recommended to intensify research on these fields. This holds amongst other things for the validation and improvement of multiple wake models and near wake models in multiple wake situations. Also the interaction of wind farms with the outer atmosphere deserves more attention. Moreover there is a need to refine the turbulence models for wind farm aerodynamics. Another main question to be answered is the importance of rotor aerodynamics for wake aerodynamics. More specifically it should be determined whether it is justified to model the rotor as an actuator disc. The answer to this question can be found by comparing results from CFD codes, which models both the rotor and the wake in a detailed way, with results from a similar code in which the rotor is replaced by an actuator disc.

As for the situation on rotor aerodynamics it is again concluded that progress on the field of wind farm aerodynamics is hampered by a shortage of high quality validation material. For this reason it is recommended to intensify the measurement activities for wind farm aerodynamics. In this thesis minimum requirements for such measurement programs are given. Measurements anyhow need to be done on full scale wind farms, preferably in combination with wind tunnel measurements. The first type of measurements yield representative information but generally lack a sufficient degree of detail for a complete interpretation of the wind farm aerodynamic problem. Furthermore field measurements are difficult to interpret due to the stochastic turbulent environment in the free atmosphere. The second type of measurements can yield very detailed and easy interpretable information but the scale of the model turbines is far too small. An interesting intermediate is then the so-called ECN scaled wind farm. This farm consists of 10 wind turbines with a rotor diameter of 7.6 m and a rated power of 10 kW. The farm is heavily instrumented where the size is sufficiently large to make the results at least to some extent, representative for full scale situations. The combination of full scale measurements, scaled farm measurements and wind tunnel measurements then forms the most complete experimental base for wind farm aerodynamics even though each type of measurements has its own drawbacks.

Samenvatting

Aërodynamica is van groot belang voor een succesvolle toepassing van wind energie. In feite kan men in de windenergie technologie twee gebieden onderscheiden waarin de aërodynamica een rol speelt: Rotor- en windpark aërodynamica. Rotor aërodynamica behelst de stroming rondom de rotor terwijl wind park aërodynamica de (zog) stroming binnen een windpark beschouwt. Voor beide gebieden zijn rekenmodellen ontwikkeld die zijn geïmplementeerd in rotor- en windpark ontwerp codes. Nauwkeurige rotor ontwerp codes leiden tot een betrouwbaar ontwerp van windturbines en een optimalisatie naar een hoge energieproductie en lage belastingen. Daarmee verlagen ze de kosten per kWh. Ook zijn ze nodig om ontwerpfouten te voorkomen waarmee ze de investeringsrisico's voor windturbine fabrikanten verminderen. Nauwkeurige windpark ontwerp codes zijn nodig om productie verliezen en de verhoging van de belastingen op turbines in een park te kunnen voorspellen. Daarmee is het mogelijk parken te optimaliseren (bijvoorbeeld door middel van parkregelingen), waarbij het energieverlies en de belasting toename (en daarmee de kosten per kWh) worden geminimaliseerd.

Voor beide gebieden zijn modellen ontwikkeld variërend van zogenaamde engineering methoden tot zeer geavanceerde Computational Fluid Dynamics (CFD) methoden. Engineering modellen, zijn modellen die een ingewikkeld fysisch proces terugbrengen tot een meer eenvoudige transparante beschrijving. Dit gaat veelal gepaard met een relatief korte rekentijd. In dit opzicht is het zeer belangrijk om te beseffen dat windenergie ontwerp-berekeningen inherent zeer rekenintensief zijn, waardoor geavanceerde CFD modellen nog niet routine matig door de industrie zijn in te zetten. Om de rekentijd nog enigszins binnen te perken te houden zijn derhalve efficiënte engineering modellen onontbeerlijk.

Het belangrijkste doel van dit proefschrift is dan het beschrijven van een aantal ontwikkelingen uit de afgelopen 25 jaar die hebben geleid tot de huidige generatie aërodynamische engineering modellen. Aangevoerd wordt dat er veel vooruitgang is geboekt, zowel op het gebied van de rotor aërodynamica als op het gebied van windpark aërodynamica. Veel van deze vooruitgang is te danken aan het feit dat gedetailleerde aërodynamische metingen beschikbaar zijn gekomen. De voortgang wordt geïllustreerd door de engineering modellen die zijn ontwikkeld en gevalideerd door ECN in diverse grote (inter)nationale samenwerking projecten waarin dergelijke metingen een grote rol speelden. De auteur van het proefschrift was nauw betrokken bij deze projecten en trad veelal op als coördinator. Het feit dat deze activiteiten plaatsvonden in samenwerking met andere partners maakt dat de ECN activiteiten en modellen kunnen worden geplaatst in een bredere context.

Het eerste deel van dit proefschrift beschrijft de rotor aërodynamica. Dit onderwerp kan worden verdeeld in inductie en blad aërodynamica. Inductie aërodynamica behelst de stroming rondom de rotor. Het wordt zo genoemd omdat het de z.g. geïnduceerde snelheden bij het blad bepaalt. Blad aërodynamica behelst dan de bepaling van de belastingen op het blad als responsie op de stroming bij het blad.

Engineering methoden voor rotor aërodynamica zijn gebaseerd op de z.g. Blad Element Impuls (BEM) theorie. De oorspronkelijke BEM theorie is erg simpel en afgeleid voor 2-dimensionale, stationaire, homogene stroming zonder scheefstand. Daarom worden z.g. engineering add-on's toegevoegd aan BEM ter correctie van deze simplificaties. Deze engineering add-on's zijn ontwikkeld voor het gebied van blad aërodynamica en voor het gebied van de inductie aërodynamica.

In dit proefschrift wordt een vergelijking gemaakt tussen de huidige engineering modellen en die van 25 jaar geleden. 25 Jaar geleden bestonden de aërodynamische modellen in ontwerpcodes uit niet veel meer dan een standaard BEM model waaraan een Prandtl tip correctie en een correctie voor de z.g. turbulent wake state waren toegevoegd. Verder werd de toren gemodelleerd met een dipool, en er waren geometrische correcties voor de kegel- en tilthoek. Tenslotte werd scheefstand gemodelleerd met alleen het z.g. advancing and retreating blade effect. Sindsdien zijn verschillende modellen toegevoegd. Op het gebied van de profielaërodynamica gaat het dan om de modellering van instationaire effecten (o.a. dynamic stall) en 3-dimensionale

verschijnselen. Deze instationaire verschijnselen zijn te verdelen in (visceuze) dynamic stall effecten en (niet-visceuze) effecten bij kleine invalshoek. De modellering van drie-dimensionale effecten is toegevoegd die plaatsvindt aan de binnenkant van het blad waar overtrek wordt uitgesteld en aan de buitenkant van het blad waar de tip zorgt voor een verlaging van de belastingen. Wat betreft inductie aerodynamica zijn dynamic inflow effecten toegevoegd alsmede de azimuthale variatie van de inductie bij scheefstand. Tenslotte zijn wortelverliezen (het equivalent van de Prandtl tip loss factor aan de wortel) toegevoegd.

De voortgang in de ECN engineering modellen op het gebied van rotor aërodynamica wordt vooral beschreven aan de hand van resultaten uit vier opeenvolgende 'IEA Tasks': IEA Task 14 en 18, IEA Task 20 en IEA Task 29 (Mexnext). Een IEA Task (soms IEA Annex genoemd) is een samenwerkingsproject uitgevoerd onder auspiciën van de Internationaal Energie Agentschap IEA. Het doel van de IEA Tasks 14 en 18 was om een database van gedetailleerde aërodynamische metingen op te stellen die allemaal zijn genomen aan turbines in de vrije atmosfeer. Het doel van IEA Task 20 was om de metingen van NREL (het National Renewable Energy Laboratory uit de VS) te analyseren die zijn gedaan aan een 10 meter diameter windturbine die is geplaatst in de zeer grote NASA-Ames windtunnel. IEA Task 29 (Mexnext) analyseerde de metingen die zijn genomen in het EU-project Mexico aan een windturbine rotor met een diameter van 4,5 meter die is geplaatst in de Grote Lage Snelheid Faciliteit (LLF) van de Duits-Nederlandse Windtunnel (DNW). In al deze experimenten werden drukverdelingen gemeten op verschillende locaties langs de rotorbladen. Bovendien werd bij het Mexico experiment de stroming rondom en in het rotorvlak gemeten.

De gedetailleerde aërodynamische metingen van deze IEA Tasks bleken buitengewoon nuttig en maakten aërodynamische verschijnselen zichtbaar die voorheen verborgen bleven bij conventionele meetprogramma's waarin alleen globale rotor(blad) belastingen werden gemeten. Een van de conclusies bestaat dan ook uit de constatering dat alleen gedetailleerde aërodynamische metingen kunnen worden gebruikt voor de validatie van aërodynamische ontwerp modellen: een validatie op basis van globale rotor (blad) belasting geeft geen doorslaggevend antwoord omtrent de nauwkeurigheid van aërodynamische modellen vanwege het feit dat 'compenserende fouten' kunnen optreden. Ook wordt er een onbalans in de windenergie aërodynamica wereld geconstateerd: Veel activiteiten zijn gericht op de ontwikkeling van aërodynamische modellen (vaak met weinig onderlinge verschillen), maar de

hoeveelheid experimenteel validatie materiaal is (te) beperkt.

Verder leverden de metingen verschillende tekortkomingen in de modellering op die deels konden worden 'gerepareerd', soms met behulp van meer geavanceerde modellen.

Een aantal aanbevelingen worden gedaan voor het gebied van rotor aerodynamica. Dit betreft in de eerste plaats enkele specifieke verbeteringen die nog aan de huidige engineering modellen kunnen worden toegevoegd. Het betreft dan onder andere de verbetering van engineering modellen voor de modellering van de annulus gemiddelde geïnduceerde snelheid bij scheefstand, de modellering van tipverliezen en de modellering van de tijdconstante in dynamic inflow. Deze modellen kunnen worden verfijnd op basis van een calibratie met resultaten uit meer verfijnde aerodynamische modellen (CFD of vrije wervel modellen). De validatie van deze geavanceerde aerodynamische modellen met metingen uit de IEA Tasks leverde namelijk een duidelijke meerwaarde van deze modellen op deze gebieden. Daarnaast wordt het modelleren van drie-dimensionale en instationaire effecten op de weerstand als een ondergeschoven kind gezien dat meer aandacht verdient.

De belangrijkste aanbeveling hangt echter samen met de constatering dat het aerodynamisch validatie materiaal in de wind energie wereld veel te beperkt is. Als zodanig wordt aanbevolen de activiteiten op het gebied van de experimentele rotor aerodynamica te intensiveren. Dit dient zowel in de wind tunnel als in het veld te gebeuren. Speciale aandacht moet worden besteed aan de meting van fenomenen die tot nu toe nog grotendeels verborgen zijn gebleven (bijv. grenslaag verschijnselen).

Dit proefschrift beschrijft vervolgens de ontwikkelingen op het gebied van windpark aerodynamica. De verscheidenheid van modellen in de wind park aerodynamica blijkt veel groter te zijn dan die in de rotor aerodynamica (waar BEM het belangrijkste model is). Dit is deels te wijten aan het feit dat een windpark model meer aspecten dient te beschouwen: Het moet namelijk zowel het aerodynamische gedrag van de (zog-genererende) rotor beschrijven als wel het turbulente zog stroomafwaarts van deze rotor. Daarnaast is de eis van rekefficiëntie voor een windpark nog strenger. Daarom verwijst CFD modellering van windpark aerodynamica vaak alleen naar de modellering van het zog en niet naar de modellering van de rotor, Hierdoor worden zog en rotor aerodynamica veelal volledig afzonderlijk worden beschouwd. Dit wordt gezien als een ongewenste ontwikkeling, aangezien de aerodynamica van

het zog grotendeels wordt bepaald door de aërodynamica van de rotor die voor het zog staat.

In dit proefschrift worden de belangrijkste karakteristieken van een windturbine zog beschreven alsmede een overzicht van windpark aërodynamische modellen. Veel aandacht gaat uit naar een compromis tussen zeer elementaire zogmodellen en de zeer gedetailleerde CFD modellen. Dit compromis bestaat uit de zogenaamde geparaboliseerde zog modellen. Deze modellen hebben als voordeel dat ze relatief efficiënt zijn wat betreft rekentijd (waarvoor ze nog steeds worden beschouwd als engineering modellen) terwijl ze toch een goede fysische beschrijving leveren van het zogenaamde verre zog. Nadeel is dat ze normaal gesproken een empirische behandeling van het nabije zog vereisen. Dit gaat veelal gepaard met een zeer eenvoudige modellering van de rotor. De vooruitgang in wind park aërodynamica wordt dan geïllustreerd met de ECN Farmflow code (gebaseerd op het vroegere Wakefarm zogmodel). In dit model is een geparaboliseerd $k-\epsilon$ turbulentie model voor het verre zog gecombineerd met een fysisch vrij wervel zog model voor het nabije zog.

De metingen op het gebied van de wind turbine aërodynamica die in dit proefschrift worden gebruikt zijn vooral afkomstig van het EWTW (ECN Windturbine Test Site Wieringermeer). Dit onderzoekspark bestaat uit vijf wind turbines in een lijn-opstelling met een nominaal vermogen van 2,5 MW en een rotor diameter en ashoogte van 80 meter. De turbines zijn uitgebreid geïnstrumenteerd. Ook is er een meteorologische mast waarmee de zogkarakteristieken zijn gemeten. Een groot voordeel van deze metingen ligt in het feit dat het een onderzoeks park betreft waarbij onderzoeksvragen centraal zijn gesteld. Zo zijn data gemeten over een zeer lange periode van hoge kwaliteit. De EWTW metingen toonden diverse nieuwe zog fenomenen en vormen materiaal voor de validatie en verbetering van de Farmflow code. De bevindingen uit het EWTW zijn vergeleken met die van grote off-shore windparken uit het EU-project Upwind. Het blijkt dat in de EWTW lijn-opstelling het grootste vermogensverlies als gevolg van zogeffecten (en dus de laagste totale vermogen) optreedt bij de tweede turbine in het park. De turbines dieper in het park presteren iets beter. Dit in tegenstelling tot de situatie in grote offshore-windparken waar het vermogen blijft afnemen voor turbines dieper in het park. Dit kan worden verklaard door zijdelingse zog effecten en de enorme afmetingen van de grote off-shore windparken. Deze trends in vermogens blijken goed te worden voorspeld door Farmflow.

Een aantal conclusies worden getrokken. De belangrijkste conclusie is dat, gelijk aan de situatie voor rotor aerodynamica, veel vooruitgang is geboekt in de afgelopen decennia. Dit wordt geïllustreerd aan de hand van de ontwikkeling van Wakefarm tot Farmflow. In het begin van de jaren 1990 werden alleen enkelvoudige zogen gemodelleerd. Deze werden op zeer eenvoudige manier beschouwd: De windturbine werd gerepresenteerd als een actuator disc, waarachter het nabije zog op zeer eenvoudige wijze werd gemodelleerd. Het verre zog werd gemodelleerd met een turbulentie model dat voor niet-windenergie toepassingen was ontwikkeld. Sindsdien is het nabij-zog modellen verfijnd en zijn meervoudige zogen (in axiale en zijdelingse richting) in rekening gebracht. Verder is het turbulentiemodel gecalibreerd voor windturbine situaties. Zeer belangrijk voor de ontwikkeling van engineering modellen in het algemeen is dat er ondertussen in de research wereld een aantal CFD-modellen zijn ontwikkeld waarin de rotor op een meer geavanceerde wijze wordt gemodelleerd dan met een actuator disc (bijvoorbeeld door middel van actuator lines). Dergelijke geavanceerde modellen kunnen nu worden gebruikt voor het calibreren van meer simpele modellen.

Verschillende onderwerpen voor windpark aerodynamica zijn geïdentificeerd die nog te weinig aandacht hebben gekregen. Derhalve wordt aanbevolen het onderzoek op deze gebieden te intensifieren. Dit betreft o.a de validatie van meervoudige zog modellen en de modellering van het nabije zog in een meervoudig zog. Ook de interactie van windparken met de buitenatmosfeer verdient meer aandacht. Belangrijk is ook de noodzaak om turbulentie modellen voor windpark aerodynamica te verfijnen. De belangrijkste vraag die moet worden beantwoord is het belang van de rotor aërodynamica voor zog aërodynamica. Meer in het bijzonder dient de betrouwbaarheid van een actuator disc modellering te worden bepaald. Het antwoord op deze vraag kan worden gevonden door vergelijking van resultaten uit een CFD codes, die de rotor op een gedetailleerde wijze kunnen modelleren maar ook als een actuator disc.

Net als voor de situatie op rotoraërodynamica kan opnieuw geconcludeerd worden dat de vooruitgang op het gebied van windpark aërodynamica ernstig wordt belemmerd door een tekort aan kwalitatief hoogwaardig validatie materiaal. Om deze reden wordt aanbevolen om de meetactiviteiten voor windpark aërodynamica te intensiveren. In dit proefschrift wordt een minimum meetprogramma vastgesteld. In ieder geval dienen full scale metingen gedaan te worden bij voorkeur aangevuld met windtunnelmetingen. Full scale metingen leveren representatieve informatie, maar het nadeel ligt in de geringe mate van detail en de moeilijkheid metingen uit de stochastische vrije atmosfeer te

interpreteren. Wind tunnel metingen geven zeer gedetailleerde, eenvoudig te interpreteren informatie maar de schaal van de benodigde model turbines in de windtunnel is veel te klein. Een interessante tussenvorm is dan het zogenaamde ECN schaal windpark. Dit park bestaat uit 10 windturbines met een diameter van 7,6 m en een nominaal vermogen van 10 kW. Het park is zwaar geïstrumenteerd, terwijl de afmetingen groot genoeg zijn om de resultaten, althans tot op zekere hoogte, representatief te kunnen beschouwen voor een full scale situatie. Een combinatie van full scale metingen, schaalpark metingen en wind tunnel metingen levert dan een compleet experimenteel beeld van de windpark aërodynamica, ook al dient onderkend te worden dat elk type metingen zijn eigen nadelen heeft.

Notations

Symbol	Description	Unit
A or A_r	Rotor area	m^2
A_1 and A_2	Amplitudes in model for induced velocity at yaw, see eqn. 3.19	[deg]
a	Axial induction factor in rotor plane (u_i/V_w)	-
a.o.a.	Angle of attack	deg
a'	Tangential induction factor in rotor plane equation 2.34	-
B	Number of blades	-
C_P	Power coefficient, equation 2.14	-
$C_{D,ax}$	Axial force coefficient, equation 2.11	-
$dC_{D,ax}$	Axial force coefficient, applied on a blade element	-
C_μ	Constant in k- ϵ turbulence model	-
c	chord	m
c_d	Profile drag coefficient	-
c_l	Profile lift coefficient	-
$c_{l,0}$	Lift coefficient at zero angle of attack	-
$c_{l,inviscid}$	Lift coefficient from thin airfoil theory: $c_{l,0} + 2\pi\alpha$	-
c_n	Normal (perpendicular to chord) force coefficient	-
c_{res}	(In Mexico experiment): Resultant force coefficient see section 5.5	-
c_t	Tangential (along the chord) force coefficient	-
c_{torque}	Torque coefficient, based on rotor tip speed see equation 5.4	-
D	Rotor diameter	m
D_{exp}	Expanded rotor diameter, equation 2.8	m
D	Drag per unit length	N/m
F	Prandtl tip loss factor, equation 3.1	-
F	Force	N
F_{ax}	Axial force	N
dF_{ax}	Axial force on blade element	N
$F_{inplane}$	Inplane force	N
$dF_{inplane}$	Inplane force on blade element	N
f	Non-dimensional streamwise coordinate x/R in equation 2.15	-
f	Frequency	Hz
f	Time scale in Dynamic Inflow process, see section 7.3.2	s
f_a	Factor in Dynamic inflow process, equation 7.4	-
f_{cl}	Factor in 3D correction for lift coefficient, equation 3.12	-
f_{cd}	Factor in 3D correction for drag coefficient, equation 3.16	-

Symbol	Description	Unit
h	Height	m
h_{hub} or h_t	hub height	m
$I(h)$	Turbulence intensity in x direction at height h	%
$k(h)$	Turbulent kinetic energy at height h	m^2/s^2
$k_{\text{um}}, k_{\text{Rw}}$	Constants in mixing length eddy viscosity model	-
L	Monin-Obukhov length scale or turbulence length scale	m
L	Lift per unit length	N/m
l	Mixing length	m
M_{flat}	Flatwise moment	Nm
M_{yaw}	Yawing moment, defined such that a negative moment is 'restoring', see figure 3.6	Nm
dM_{yaw}	Contribution of yawing moment from an instrumented blade section, equation 8.7	Nm/m
\dot{m}	Mass flow	kg/s
n	Normal force (normal to the chord) per unit length	N/m
P	Power	kW
P_0	Power at zero yaw angle	kW
p	Pressure	N/m^2
Q	Torque	Nm
dQ	Torque from blade element	Nm
q	Dynamic pressure	N/m^2
R	Rotor radius	m
R_w	Wake radius	m
R_{tower}	Tower radius	m
r	Radial coordinate w.r.t. rotor or wake center	m
rpm	Rotor speed	rpm
S	Spectrum value of velocity	m^2/s
s	Coordinate along the airfoil surface	m
t	Tangential force (along the chord) per unit length	N/m
t	Time	s
t	Temperature	K
$t.s.r.$	Tip speed ratio ($\Omega R/V_w$)	-
$U_{\infty}(h)$	Free stream wind speed at height h	m/s
U_{hub}	Free stream wind speed at hub height	m/s
u, v, w	(General): Total velocities in x(or s), y and z direction	m/s
$u, v, w,$	(In Wakefarm): perturbation velocities in x, y and z (direction	m/s
u_i	Axial induced velocity	m/s
$u_{i,0}$	Rotor (or annulus) averaged axial induced velocity	m/s
u_t	Tangential (in-plane) induced velocity	m/s
u^*	Friction velocity	m/s

Symbol	Description	Unit
u_{def}	Velocity defect (relative to free stream)	m/s
u_{max}	Maximum velocity deficit	m/s
U_1, U_2, U_3, U_4	Velocities in streamtube see figure 2.1	m/s
U_d	Velocity at rotor disc see figure 2.1	m/s
V_{eff}	Wind speed at blade element, see figure 2.6	m/s
V_{ax}	Total velocity axial to rotor plane	m/s
V_{tan}	Velocity component in inplane direction ($V_w \sin(\phi_y)$), figure 3.5	m/s
V_{tun}	Tunnel speed	m/s
V_{tr}	Transport velocity of vorticity	m/s
V_w or V_{wind}	Wind speed	m/s
x, y, z	(In atmospheric or wind tunnel flows): Coordinate system such that x is horizontal coordinate in streamwise direction, and z the vertical coordinate	m
x, y, z	(In blade aerodynamics): Coordinate system such that x is along the chord and y along the blade radius	m
x_0	Initial wake length, see section 9.3	m
z_0	Roughness height	m

Greek symbols	Description	Unit
α	(In rotor aerodynamics): angle of attack	deg
α	(In wake aerodynamics): Mixing length constant	-
Δc_l	Difference between $c_{l,\text{inviscid}}$ and 2D viscous value of c_l	-
Δa	At dynamic inflow events: Difference in equilibrium values of axial induction factor	-
ΔF	At dynamic inflow events: Difference in load values	[N] or [Nm]
Γ	Vortex strength (often: bound vortex strength)	m^2/s
Γ_{root}	Root vortex strength	m^2/s
γ	Vorticity density	m/s
γ	In Mexico experiment: 'Resultant force angle', see section 5.5	deg
γ_{ax}	Axial vorticity density component in wake	m/s
γ_t	Tangential vorticity density component in wake	m/s

Greek symbols	Description	Unit
ϵ	Dissipation rate of turbulent kinetic energy	m^2/s^3
ϵ	Twist angle at a blade element	deg
η	Relative radial coordinate in wake: r/R_w	-
λ	Tip speed ratio ($\Omega R/V_w$)	-
Λ	Modified tip speed ratio, equation 5.3	-
λ_r	Local tip speed ratio ($\Omega r/V_w$)	-
χ	Wake skew angle, equation 3.18	deg or rad
ϕ	Inflow angle at blade element	deg
ϕ_r	Azimuth angle (blade angle), unless otherwise stated positive according to figure 3.5, with zero azimuth at '6 o' clock'	deg
$\phi_{\max,x}$	Azimuth angle at which the quantity x is maximum	deg
$\phi_{\min,x}$	azimuth angle at which the quantity x is minimum	deg
ϕ_y	Yaw angle positive according to figure 3.6	deg
ρ	air density	kg/m^3
Ω	Rotor speed	rad/s
ω	Induced rotational speed	rad/s
Ψ	Stream function	$[\text{m}^2/\text{s}]$
Ψ_1 and Ψ_2	Phase angles in model for induced velocity at yaw, see eqn. 3.19	[deg] [deg]
Ψ_m	Function in free stream wind profile equation 9.13	-
θ	Pitch angle	deg
σ	Local solidity ($B_c/2\pi r$)	-
σ	Standard deviation of the wind speed	m/s
$\sigma_x, \sigma_y, \sigma_z$	Standard deviation of the wind speeds in x,y,z direction	m/s
τ	Time constant	s
τ_s or τ_r	Shear stress in s and r direction	N/m^2
ξ	Height above ground non-dimensionalized with Monin-Obukhov length h/L	-

Subscripts	
1,2	(In wind farm aerodynamics): first or second turbine in a row
1,2,3,4	(In rotor aerodynamics): locations in stream tube, see figure 2.1
1,2	(In Dynamic Inflow events): before and after the dynamic inflow event
2D,3D	Two dimensional or three dimensional value
add	Added (perturbation value, relative to undisturbed value)
absolute	Absolute value
ax	Axial
d	Disc value
def	Deficit
down	Downward pitching step
e.m.	Engineering model
ibl	Blade number
max	Maximum value
meas.	Measured value
min	Minimum value
nw	Near wake
pitot	From pitot tube
pressure	At pressure side of airfoil
ref	Reference value
relative	Relative value
suction	At suction side of airfoil
t	Tangential
tap	Value at pressure tap
tr	Transport
tun	Tunnel value
up	Upward pitching step
w	Wake value
∞	free stream

Abbreviations and Acronyms	
AWSM	Aerodynamic Wind Turbine Simulation Module (free wake lifting line method), see section 2.3.2
Az	Azimuth angle
CFD	Computational Fluid Dynamics
BEM	Blade Element Momentum
CRES	Center for Renewable Energy Sources
DTU	Technical University of Denmark
DNW	German Dutch Windtunnel
ECN	Energy Research Center of the Netherlands
EWTW	ECN Wind Turbine Test Site Wieringermeer
EU	European Union
Farmflow	ECN's Wind Farm Design code (based on Wakefarm wake model)
IEA	International Energy Agency
KARI	Korean Aerospace Laboratory
LLF	Large Low Speed Facility (of DNW)
Meas	Measurement
Mexico	Measurements and Experiments in Controlled Conditions (EU project)
LES	Large Eddy Simulation
MM	Meteorological mast
NREL	National Renewable Energy Laboratory
NTUA	National Technical University of Athens
n.r.	Not reliable
PHATAS	ECN Program for Horizontal Axis Analysis and Simulation, (aero-elastic code based on BEM), see section 2.3.1
OJF	TU Delft Open Jet Facility
PIV	Particle Image Velocimetry
RANS	Reynolds Averaged Navier Stokes
r.v.	Root vortex
TU Delft	Technical University of Delft
T_x	Turbine number x in EWTW
Wakefarm	Parabolized wake model from ECN

Contents

Acknowledgements	i
Summary	iii
Samenvatting	ix
Notations	xvii
I Introduction, Goal and Outline	1
1 Introduction, goal and outline	3
II Rotor Aerodynamics	13
2 Rotor aerodynamic models	15
2.1 Blade element momentum (BEM) theory	15
2.1.1 Axial momentum theory	15
2.1.2 Blade element theory	19
2.1.3 Axial blade element momentum theory	22
2.1.4 Tangential Blade Element Momentum Theory	23
2.2 Advanced rotor aerodynamic models	25
2.3 ECN's aerodynamic models	26
2.3.1 PHATAS	26
2.3.2 AWSM	28
2.4 Concluding remarks on rotor aerodynamic models	28

3	Uncertainties and assumptions in Blade Element Momentum theory and engineering add-on's	31
3.1	Assumption of incompressible flow	32
3.2	Assumption of inviscid flow	33
3.3	Assumption of annular independency, axi-symmetry	33
3.4	Assumption of actuator disc concept	34
3.5	Turbulent wake	36
3.6	Assumption of stationary conditions	38
3.6.1	Unsteady airfoil aerodynamics	39
3.6.2	Dynamic Inflow	41
3.7	Assumption of 2D airfoil aerodynamics	43
3.8	Yawed flow	47
3.9	Cone angle, tilt angle, unconventional blade shapes	53
3.10	Tower effects	54
3.11	Benchmarks, impact of uncertainties on design loads	55
4	Field and wind tunnel measurements on rotor aerodynamics as performed in IEA Tasks	57
4.1	Introduction on rotor aerodynamic measurements from IEA Tasks	57
4.2	Measurement uncertainties	59
4.3	IEA Task 14 and 18: Field Rotor Aerodynamics: Description of projects, experimental set-up and measurements	61
4.4	IEA Task 20: NREL's Phase VI (NASA-Ames) measurements: Description of project, experimental set-up and measurements	65
4.5	IEA Task 29 (Mexico) measurements: Description of project and experimental set-up	68
4.5.1	Mexico: Tunnel effects	73
5	Progress in blade aerodynamics using the aerodynamic field and wind tunnel measurements from IEA tasks	79
5.1	Introduction on blade aerodynamics	79
5.2	Angle of attack in wind turbine experiments	81
5.3	Dynamic pressure and non-dimensionalization of aerodynamic coefficients in wind turbine experiments	84
5.4	Relation between local aerodynamic loads and global rotor loads	86
5.5	Influence of rotational speed and scale on aerodynamic coefficients	91
5.6	Inventory of analyzes on IEA Task 14/18 data	94

5.7	Comparison between calculated and measured local aerodynamic loads	98
5.7.1	IEA Task 14/18: Comparison between calculations and field measurements	98
5.7.2	IEA Task 20: Comparison between between calculations and NREL Phase VI (NASA-Ames) measurements	104
5.7.3	IEA Task 29 (Mexnext): Comparison between calculations and Mexico measurements	106
5.7.4	Improved model for 3D effects at airfoil aerodynamics, using measurements from IEA Task 14/18/20	111
5.7.5	Comparison between calculations from modified model and measurements	119
5.8	Conclusions and recommendation on blade aerodynamics	121
6	Progress on induction aerodynamics, based on flow field measurements from IEA Task 29	125
6.1	Introduction on induction aerodynamics	125
6.2	Cylindrical vortex sheet method	127
6.3	IEA Task 29(Mexnext): PIV measurements at non-yawed conditions	129
6.3.1	Tip vortex strength in relation to blade circulation	129
6.3.2	Axial velocity traverses	131
6.3.3	Radial velocity traverses	136
6.3.4	Flow non-uniformities in the rotor plane	138
6.4	Summary, conclusions and recommendations on the field of induction aerodynamics	149
7	Progress on Dynamic Inflow based on measurements from the EU Dynamic Inflow projects and IEA Tasks 20 and 29	155
7.1	Introduction on Dynamic Inflow	155
7.2	EU projects 'Dynamic Inflow'	156
7.2.1	Engineering model for dynamic inflow	156
7.2.2	Measurements on Tjæreborg turbine	158
7.3	IEA Task 20: Dynamic Inflow effects in NREL's Phase VI(NASA-Ames) experiment	161
7.3.1	Comparison between calculations and measurements	164
7.3.2	Time constant (time scale) analysis	168
7.4	IEA Task 29(Mexnext): Rotor speed steps from Mexico experiment	172
7.5	Summary, conclusions and recommendations on Dynamic Inflow	173

8	Progress on yaw aerodynamics based on measurements from national, EU and IEA projects	179
8.1	Introduction on yaw aerodynamics	179
8.2	Yaw angle dependency of power	181
8.3	Azimuthal load variation at yaw	183
8.3.1	Azimuthal variation of induced velocity at yaw (skewed wake effect)	184
8.3.2	Global description of load variation at yaw	191
8.4	IEA Task 20: NREL's Phase VI(NASA-Ames) measurements in yaw	195
8.4.1	Results at a tunnel speed of 5 m/s	197
8.4.2	Results at a tunnel speed of 15 m/s	199
8.5	IEA Task 29(Mexnext): Mexico measurements in yaw	204
8.5.1	Flow field and tip vortices at yaw	204
8.5.2	Comparison between calculated and measured results	206
8.6	Summary, conclusions and recommendations on yaw aerodynamics	216
III	Wind Farm Aerodynamics	219
9	Wind farm aerodynamic models	221
9.1	Introduction on wind farm aerodynamics models	221
9.2	Near wake versus far wake; Parabolization	222
9.3	Global wake behavior	224
9.4	Classification of wake aerodynamic models	227
9.5	Description of Farmflow/Wakefarm model	229
9.5.1	Free stream modelling	230
9.5.2	Parabolization	233
9.5.3	Wake modelling	234
9.5.4	Multiple wake modelling	236
9.5.5	Wind direction fluctuations	237
9.5.6	Grid size and boundary conditions	237
9.6	Summary on wind farm models	238
10	Assumptions and uncertainties in wind farm aerodynamic models	241

11 Progress on wind farm aerodynamic models at ECN using measurements from EU and national projects	247
11.1 Introduction on wind farm aerodynamic measurements and the ECN models used	247
11.2 Wind farm measurements from the ECN Wind Turbine Test Site Wieringermeer, EWTW	250
11.2.1 Description of EWTW farm, turbines and instrumentation	250
11.2.2 Comparison between calculated and measured power losses	253
11.2.3 Comparison between calculated and measured wake velocity and wake turbulence profiles	256
11.2.4 Some further analysis of EWTW measurements	258
11.3 Wind farm effects in large off-shore wind farms	263
11.3.1 Description of Horns Rev Wind farm	263
11.3.2 Comparison between calculated and measured power losses	263
 IV Conclusions and recommendations	 267
12 Conclusions and recommendations for further research	269
12.1 Conclusions on rotor aerodynamics	270
12.2 Recommendations for further research on rotor aerodynamics	272
12.3 Conclusions on wind farm aerodynamics	276
12.4 Recommendations for further research on wind farm aerodynamics	279
 Bibliography	 283
 V Appendices	 297
A IEA Task 14/18: Description of experimental facilities	299
A.1 Aerodynamic test facility of Delft University of Technology, TUDelft	299
A.2 Aerodynamic test facility of the Energy Research Center of the Netherlands, ECN	301
A.3 Aerodynamic test facility of Imperial College, IC and Rutherford Appleton Laboratory, RAL	301
A.4 Aerodynamic test facilities of National Renewable Energy Laboratory, NREL	302

A.5 Aerodynamic test facility of Mie University	303
A.6 Aerodynamic test facility of RISØ	304
B Model for induced velocities at yaw	309
C Contribution of author to thesis	313
Curriculum-vitae	319

Part I

Introduction, Goal and Outline

Chapter 1

Introduction, goal and outline

It is well acknowledged that aerodynamics plays a very important role in the successful deployment of wind energy. Thereto it should be realized that a wind turbine is an aerodynamic machine since it extracts kinetic energy from the wind and transforms it into mechanical energy. This transformation of energy is an aerodynamic process.

The relevance of aerodynamics for wind energy applications is mainly found in two areas:

1. Rotor aerodynamics. This area focusses on the aerodynamic behavior of the rotor. It is of importance for the optimization and design of individual wind turbines since it determines the energy production, the loads and stability of a wind turbine.

The modelling of rotor aerodynamics is known to be subject of large uncertainties, see e.g. [Schepers et al. \(2002c\)](#) and [Simms et al. \(2001\)](#). Several phenomena, like 3D geometric and rotational effects, instationary effects, yaw effects, stall, tower effects etc, contribute to unknown responses in particular at off-design conditions. These unknown responses make it very difficult to design cost-effective and reliable wind turbines. Turbines behave unexpectedly, experiencing instabilities, or higher loads than expected. These higher loads should be covered with costly safety factors. Alternatively the loads may be lower than expected

which implies an over dimensioned (and costly) design.

Basically the subject of rotor aerodynamics can be subdivided in two parts: The first part deals with the global flow field around a wind turbine. This type of modelling is called induction aerodynamics, since its main goal is to determine the induced velocities at the blade. The second part deals with the loads on a wind turbine blade as a response to this flow situation and is called blade aerodynamics.

2. Wind farm aerodynamics. This area focusses on wake effects and the (generally negative) consequences on performance and loads of turbines within a wind farm. The importance of wind farm aerodynamics has become very prominent in recent years, now the majority of wind turbines, both on-shore and off-shore, got clustered in (very) large farms. As such the turbines are almost continuously located in the wake of one or more turbines. This has made the subject of wind farm aerodynamic(modelling) very essential for a reliable optimization of wind farms.

The main wake effect is often considered to be the lower wind speed behind the turbine(s) since this decreases the energy production of the next turbines and as such the economical performance of a wind farm. The resulting energy loss of a wind farm is very much dependent on the conditions and the lay-out of the farm. Calculations in [Schepers \(2012\)](#) show that it can even be 20% for a farm of 140 turbines which are located at a spacing of 5 rotor diameters. Apart from the loss in energy production an additional wake effect is formed by increased velocity fluctuations of a different character than the free stream turbulence. This leads to higher fatigue loads.

The main aim of this thesis is to describe the knowledge which has been generated over the last 25 year on the field of aerodynamic engineering models. The progress is illustrated by the assessment, validation and improvement of (mainly) ECN models using dedicated measurements which have become available in various large international cooperation projects. The author of this thesis was heavily involved in these projects and often acted as coordinator, see Appendix C. Since these projects were performed in close cooperation with other institutes (which used different types of models), the activities of the author can be placed in a wider context.

As such the thesis offers insight into the strengths and weaknesses of aerodynamic engineering models which is essential information to assess the value

of such models. Eventually the analysis lead to directions for future research along which, according to the author's opinion, engineering methods can be improved further.

The term engineering method often indicates a simplified and generalized representation of a complex physical phenomenon which is difficult to comprehend with a more complex aerodynamic model. At the same time it indicates that the calculational time remains within acceptable limits for design calculations. In this respect it is very important to realize the role of calculational time which, for wind energy calculations, is much more crucial than it is for most other areas of technology. This is in particular true for the calculation of a design load spectrum: A large number of 10 minute time series have to be calculated and combined into an overall load spectrum in order to reflect the statistics of the wind over the entire 20 years lifetime of a wind turbine. This can make the number of time steps for such calculations more than 1 million.¹ Bearing in mind that every time step requires an aerodynamic calculation this puts severe constraints on the computational efficiency of the aerodynamic model.

Wind farm calculations are even more demanding due to the large size of wind farms where the wake flow felt by a turbine in a farm is wind direction dependant and different from turbine to turbine. This implies that all wind turbines in the farm need to be considered at very many different wind directions

As such the performance of wind energy aerodynamic models is inextricably connected to their computational effort. This has made the so-called Blade Element Momentum (BEM) theory the most popular model for rotor aerodynamics. Although this theory is a computational efficient model indeed, it is also a very simplified model which in principal is valid for stationary, 2D and non-yawed conditions only. These simplifications are (partly) overcome by 'engineering add-on's' which cover these deficiencies. Such engineering add-on's are often destillated from more advanced aerodynamic models and/or measurements with several tuning factors. They are still of a simplified character and when added to the BEM theory they donot significantly increase the calculational effort.

For wind farm aerodynamics the variety of models is much larger by which

¹Even 7.2 Million based on 120 time series (i.e. 6 realizations at 20 wind speeds) of 10 minutes and a time step of 0.01 seconds

it is less straightforward to appoint a dominant model. For large wind farms the complexity of the flow problem is very extreme and several aspects play a role which, in principle should be included in a wind farm model. One can think of unsteady effects (including wake meandering), effects of atmospheric stability, merging of wakes and the interaction of the wind farm with the outer atmospheric boundary layer. In principle all of these aspects could be included in advanced CFD codes but this would yield calculational times which are longer than the lifetime of the wind farm itself! Therefore most wind farm codes are based on time averaged models, often of an empirical, computational efficient nature. One step further in physical accuracy are the parabolized wake models where parabolization can be seen as a technique to reduce the calculational effort while at the same time the modelling of the physical processes in the far wake remain at a reasonable high level. The main problem with a parabolized method lies in the near wake region which, in principle, cannot be modelled in a physical sound way. For this reason the near wake is often represented with an empirical velocity profile which serves as an initialization for the far wake. The drawback of this approach lies in the fact that a generally valid initial velocity profile is not easy to determine.

The basic structure of this PhD-thesis is illustrated in figure 1.1. The thesis is (apart from the introductory and concluding parts) divided in two main parts: Part II contains the chapters 2 to 8 and is focussed on rotor aerodynamics where Part III contains chapters 9 to 11 and is devoted to wind farm aerodynamics. Each part starts with a global description of the relevant (engineering) models, and their uncertainties and remedies to overcome these uncertainties. Thereafter several analysis are described which are all directed towards a better understanding of the ECN models and which use measurement results from (cooperation) projects in which the author has been involved.

More specifically the thesis is structured as follows:

In chapter 2 the basic principles of the BEM model are described. More advanced rotor aerodynamic model are also briefly touched upon but these methods donot form the core of this thesis. As a matter of fact results from advanced methods are mainly used as reference and inspiration material for engineering models. Therefore the interested reader on advanced aerodynamic models is referred to other literature on this field e.g. the review of aerodynamic models from [Sørensen \(2011\)](#).

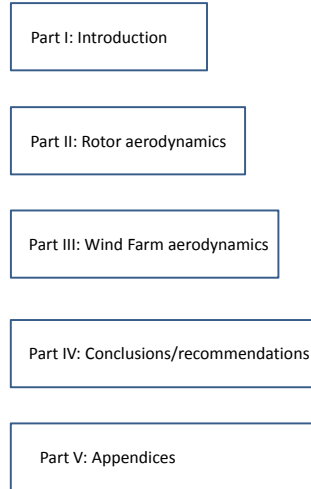


Figure 1.1: Global roadmap of the thesis

Then the assumptions and simplifications in the BEM model and a description of the engineering add-ons to overcome these simplifications, are given in chapter 3.

Further progress on the field of rotor aerodynamics, in terms of validation and development of (mainly) ECN engineering methods, is then largely described along the results of four subsequent IEA Tasks (IEA Task 14, 18, 20 and 29, see chapter 4). An IEA task (sometimes called an IEA Annex) is a joined research project, organized under the auspices of the International Energy Agency IEA (www.ieawind.org).

The IEA Tasks 14, 18, 20 and 29 were all built around databases of dedicated aerodynamic experiments in which the aerodynamic loads were measured at different positions along the rotor blade. In the IEA Tasks 14 and 18 ([Schepers et al. \(2002a\)](#)) a database was created of aerodynamic measurements on field facilities, where IEA Task 20 ([Schreck \(2008\)](#)) used measurements taken by the USA National Renewable Energy Laboratory (NREL) on a tur-

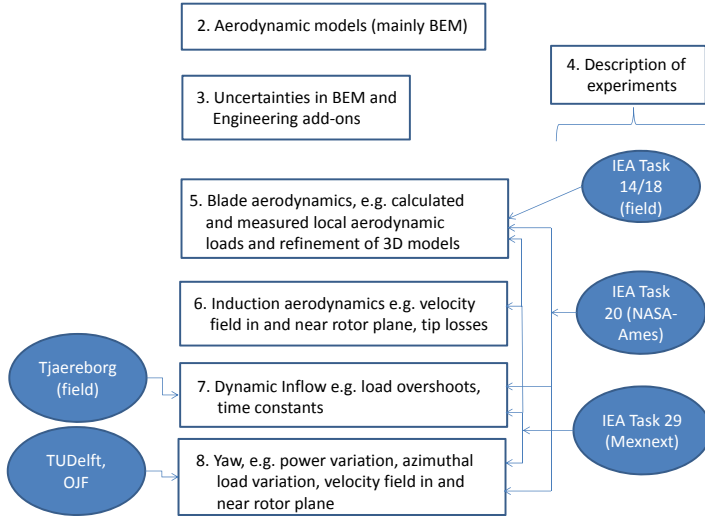


Figure 1.2: Roadmap of Part II: Rotor aerodynamics (The experiments used in the various analyzes are indicated in blue)

bine which was placed in the very large NASA-Ames wind tunnel. Furthermore IEA Task 29 Mexnext ([Schepers, Boorsma et al. \(2011\)](#)) applied rotor and flow field measurements taken within the EU project Mexico on a turbine which was placed the Large Low Speed Facility (LLF) of the German Dutch Wind Tunnel DNW. It is emphasized that, although these IEA tasks formed major projects on the field of rotor aerodynamic measurements and analysis, they were definitely not the only projects. Examples from other experimental programs are the detailed flow field measurements as performed in the Open Jet Facility (OJF) of the University of Delft. These measurements have been analyzed in e.g. [Haans \(2011\)](#) or [Sant \(2007\)](#). Another example are the flow field measurements from Mie University in [Kamada and Maedo \(2011\)](#). Results from these measurements are used occasionally within the present thesis.² Global measurements of e.g. blade root bending moments, power or

²It is worthwhile to mention that Mexnext-II, which is the recently started follow-up project of IEA Task 29 forms a cooperation project in which all useable (and publicly available) aerodynamic

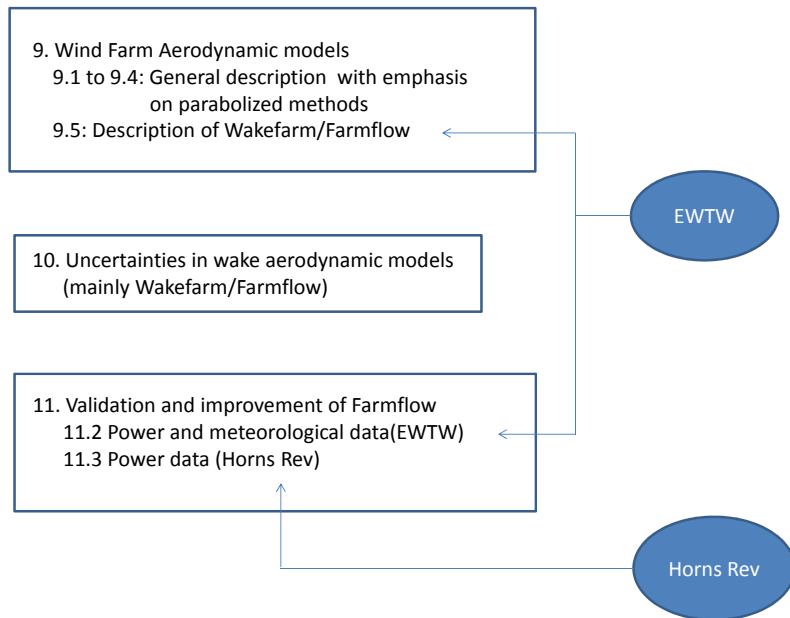


Figure 1.3: Roadmap of Part III: Wind Farm aerodynamics (The experiments used in the various analyzes are indicated in blue)

rotor shaft torque are also used occasionally. An example are the measurements taken by DTU on the Danish Tjæreborg turbine as described by Øye (1991) and used in e.g. Snel and Schepers (1994).

Then chapter 5 describes progress on the field of blade aerodynamics. Several aspects are treated but most important is a comparison between calculated and measured local aerodynamic loads. On basis of these comparisons a refined model for the correction of airfoil data to BEM is developed. Chapter

measurements will be analyzed. This includes measurements from the OJF, Mie University and many more.

6 describes a validation of the generally accepted ideas on the induction behavior around wind turbines. Thereto the flow field in and near the rotor plane is studied using the Mexico PIV measurements. Suggestions are given for a refinement of so-called tip loss models which cover the flow non-uniformity in the rotor plane. Chapter 7 describes progress on the so-called dynamic inflow phenomenon. Dynamic Inflow occurs at e.g. pitch angle steps and leads to an overshoot in loads after which the load decays gradually towards an equilibrium value. The measurements from the present research allowed to assess the radial dependency of overshoots as well as the time constants. Chapter 8 describes progress which has been made on the field of yaw aerodynamics. The main attention is focussed on the behavior of the power with yaw angle where furthermore the azimuthal load variations due to yaw at different radial positions is studied in combination with flow field measurements.

It must be noted however that the distinction between the various subjects is not always very strict and that e.g. dynamic inflow and yaw are largely driven by the induction at the rotor blades.

In summary the 'roadmap' of Part II on rotor aerodynamics is sketched in figure 1.2 which also indicates the main sources of measurements used in the various analyzes.

The final chapters of this thesis consider the subject of wind farm aerodynamics. This order reflects the idea that the aerodynamics of the rotor (partly) determines the behavior of its downstream wake. As such the chapters on wind farm aerodynamics should build upon the chapters on rotor aerodynamics. In this respect it is surprising to note that this is not always realized in the wind energy society, where wind farm aerodynamics is often considered to be fully independent from rotor aerodynamics.

The progress on the field of wind farm aerodynamics starts with an overview of aerodynamic wake models in chapter 9. It will be shown that a large variety of models exists of very different computational efficiency and physical degree of detail. The further developments on the field of wind farm aerodynamics are then described using ECN's Wakefarm model, see section 9.5, which at a later stage was implemented in the wind farm design code Farmflow (Bot (2011)). The Farmflow/Wakefarm model is a parabolized wake method and can, to some extent, be considered as being representative for engineering types of wind farm models. The model originates from the UPMWAKE model as developed by the Universidad Polytechnica de Madrid, see Crespo

et al. (1985). It has been improved within several national and European projects, e.g. the EU Joule projects Dynamic Loads in Wind Farms, see [Tindal \(1993\)](#) and [Adams \(1995\)](#), the European project 'ENDOW', see [Barthelmie et al. \(2003\)](#) and the Work Package Flow of the EU project 'Upwind', see [Barthelmie et al. \(2011\)](#).

Then chapter 11 describes results from measurements which have been used to validate and improve the most recent version of Farmflow. It must be realized however that the complexity and the scale of the wind farm aerodynamic flow problem is of another order than it is for the rotor aerodynamic problem by which the supporting measurements inevitably remain of a rather global character. As a matter of fact, a thorough understanding of the wind farm aerodynamic problem requires a detailed flow field mapping in the entire farm in combination with detailed measurements of the aerodynamic behavior of all rotors. However, usually only a very limited amount of data (e.g. turbine powers) are supplied which are taken on commercial wind farms, the owners of which lay their first priority on the commercial exploitation of the farm.

The ECN Wind Turbine Test Site Wieringermeer, EWTW is then one of the few research farms in the world where priority is given to understand the wind farm aerodynamic problem by means of high quality measurements. An extensive analysis of the measurements of these EWTW measurements took place in [Schepers, Obdam and Prospathopoulos \(2012\)](#). In section 11.2 it is described how the EWTW measurements were used to improve and validate the most recent version of Farmflow from section 9.5. The validation and calibration of model parameters was not only based on power data but also on meteorological data in the wake. In addition section 11.3 describes how measurements on the large commercial off-shore wind farm Horns Rev were used in the validation of Farmflow.

In summary the 'roadmap' of Part III on wind farm aerodynamics is sketched in figure 1.3 which also indicates the main sources of measurements used in the various analyzes.

The last chapter (chapter 12) summarizes the conclusions from the described activities leading to recommendations for further research.

Finally it is noted that the precise contribution of the author to the present research is described in Appendix C.

Part II

Rotor Aerodynamics

Chapter 2

Rotor aerodynamic models

2.1 Blade element momentum (BEM) theory

Most of the present wind turbine design codes are based on the so-called Blade Element Momentum (BEM) theory. The BEM theory can be considered as a combination of the Blade Element Theory, which models the blade aerodynamics, and the Momentum Theory which models the induction aerodynamics. It was first described by [Glauert \(1935\)](#). Since then it has been reported in many textbooks on wind turbine technology which is the reason why this thesis only gives a concise description of the basic BEM theory. In the sections 2.1.1 to 2.1.3 the axial BEM equations are discussed where the energy extraction process is based on axial forces and velocities only. In section 2.1.4 an equation is added for the forces and velocities in inplane (rotational) direction.

2.1.1 Axial momentum theory

The axial momentum theory applies the conservation laws on a 1D stream tube (see figure 2.1) in axial direction. The rotor is modeled as an actuator disc, which can be seen as a hypothetical semi-transparent disc which exerts an axial force (F_{ax}) on the flow. The flow within the disc plane is assumed to be uniform which is the reason why an actuator disc is often described as a rotor with an infinite number of blade, since a finite number of blades would make the flow within the rotor plane non-uniform.

The positions 1, 2, 3 and 4 refer to the locations far upstream, just upstream of the rotor plane, just downstream of the rotor plane and infinitely far downstream of the rotor. The velocity at position 1 (U_1) is the free stream wind speed V_w . The locations 2 and 3 are both at an infinitely small distance upstream and downstream from the disc by which $U_2 = U_3 = U_d$ with U_d the disc velocity. This disc velocity is written as the free stream wind speed minus the so called axial induced velocity, where the axial induced velocity is the velocity reduction in the rotor plane due to the energy extraction of the actuator disc, denoted as u_i . Hence $U_d = V_w - u_i$. The axial force on the rotor implies a pressure jump ($p_2 - p_3$) over the disc.

The main aim of the axial momentum theory can then be seen as finding a relation between the axial induced velocity and the axial force on the disc. Thereto the following conservation laws are applied:

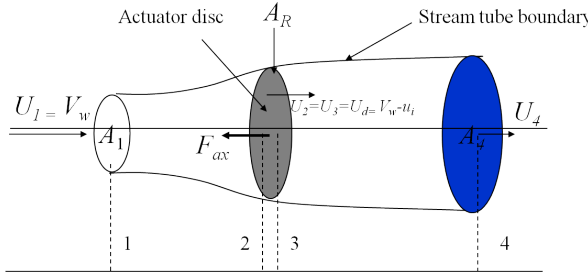


Figure 2.1: Streamtube, also indicated are the axial velocities as used in the axial momentum theory

- Conservation of mass (flux):

$$\dot{m} = \rho U_1 A_1 = \rho U_d A_R = \rho U_4 A_4 \quad (2.1)$$

- Conservation of axial momentum (flux):

$$\dot{m}(U_4 - U_1) = F_{ax} \quad (2.2)$$

Note that the net axial force from the pressure forces on the stream tube can be shown to be zero (see e.g. [Hansen \(2008\)](#)) by which the total force on the stream tube in axial direction i.e. the right hand side of equation 2.2, is formed by the axial force which the actuator disc exerts on the flow (F_{ax})

- Conservation of energy (flux, ie power):

$$\dot{m}(0.5U_1^2 - 0.5U_4^2) = P_{\text{disc}} = F_{\text{ax}}U_d \quad (2.3)$$

This shows that the kinetic energy which is extracted from the stream tube equals the energy absorbed by the actuator disc (P_{disc}).

By combining equations 2.1, 2.2 and 2.3 it is found that:

$$U_d = 0.5(U_1 + U_4) \quad (2.4)$$

Now U_1 is written as the wind speed V_w and all relevant properties are expressed in terms of the unknown axial induction factor $a = u_i/V_w$.

Hence:

$$U_d = V_w(1 - a) \quad (2.5)$$

and the mass flow in the stream tube (equation 2.1) can be written as:

$$\dot{m} = \rho V_w(1 - a)A_r \quad (2.6)$$

and equation 2.4 yields:

$$U_4 = V_w(1 - 2a) \quad (2.7)$$

Conservation of mass yields the following relation for the 'expanded diameter' at location 4:

$$D_{\text{exp}} = D\sqrt{\frac{1 - a}{1 - 2a}} \quad (2.8)$$

Then equation 2.2 gives the following relation between the axial force and axial induced induction factor:

$$F_{\text{ax}} = \rho V_w^2 2a(1 - a)A_r \quad (2.9)$$

which more conveniently is written in the following form:

$$C_{D_{\text{ax}}} = 4a(1 - a) \quad (2.10)$$

with $C_{D_{\text{ax}}}$ the axial force coefficient

$$C_{D_{\text{ax}}} = \frac{F_{\text{ax}}}{0.5\rho V_w^2 A_r} \quad (2.11)$$

The power which the actuator extracts from the flow in the stream tube is found from equations 2.3, 2.5 and 2.9 and yields:

$$P = \rho V_w^3 2a(1 - a)^2 A_r \quad (2.12)$$

The most convenient way of writing this equation is in the form of:

$$C_P = 4a(1 - a)^2 \quad (2.13)$$

In which C_P is the power coefficient which is defined as

$$C_P = \frac{P}{0.5\rho V_w^3 A_r} \quad (2.14)$$

The power coefficient can be seen as a measure for the efficiency of a wind turbine, since it defines the fraction of power which is extracted by the rotor from the available power in an amount of air passing through an area A_r with the free stream velocity V_w (This available power can be shown to be $0.5\rho V_w^3 A_r$). The maximum C_P according to equation 2.13 is 16/27 which is found at $a = 1/3$. It is noted that the actual power coefficient of a wind turbine will be lower due to losses from the finite number of blades, the airfoil drag and wake rotation (although there is some recent discussion on the effect from rotation where the radial pressure gradient due to the centrifugal force might lead to a gain in C_P , see e.g. [Sørensen and van Kuik \(2011\)](#)).

Many references explain the momentum theory with Bernoulli's equation instead of equation 2.3 (the conservation of energy). Such approach obviously results in the same outcome since Bernoulli's equation is derived from the conservation of energy but it provides direct information on the pressures within the streamtube.

Some more insight on the behavior of the pressures and the velocities in the streamtube can be obtained from figure 2.2. This figure shows the velocity decay and the pressures in streamwise direction, obtained from a simplified vortex wake method, see e.g. [Wilson \(1986\)](#) or [Snel and Schepers \(1994\)](#). It yields the following relation for the induced velocity as function of the downstream distance to the rotor (Note that the downstream distance (f) is made non-dimensional with the rotor radius, i.e $f = x/R$):

$$\frac{u_i(x)}{u_i(x = \infty)} = 0.5 + \frac{0.5f}{(f^2 + 1)^{0.5}} \quad (2.15)$$

It can easily be derived that the results from this vortex wake method are fully compatible to the momentum theory. However the vortex wake method provides the velocities in the entire region between location 1 and location 4 where the momentum theory only considers the velocity at position 1 (i.e. the

free stream velocity V_w), the velocity in the rotor plane (i.e. $U_d = V_w(1 - a)$) and the velocity at position 4 (i.e. $U_4 = V_w(1 - 2a)$)).

Equation 2.15 can be used to investigate the rate with which the velocity decays from U_d to U_4 , which is important information for wind farm aerodynamic models, see section 9.2. It is found that at 2 rotor diameters behind the wind turbine the wake is almost completely expanded since

$u_i(x = 4R) = 0.985u_i(x = \infty)$. Even at $1.5D$ a large part of the wake expansion has already taken place since $u_i(x = 3R) = 0.97u_i(x = \infty)$). Figure 2.2 also presents the pressures which are related to the velocities through Bernoulli's equation:

$$0.5\rho V^2 + p = \text{constant} \quad (2.16)$$

This equation shows that the decrease in velocity towards the rotor goes together with an increase in pressure. This pressure increase is followed by a pressure drop across the rotor plane which is related to the axial force $(p_2 - p_3)A_r = F_{ax}$. Further downstream in the wake, the decrease in velocities leads to an increase in pressure towards the free stream pressure.

It is noted that the pressure drop across the rotor plane is asymmetric, since the overpressure at position 2 (i.e. $p_2 - p_1$) is larger than the underpressure at position 3 ($|p_3 - p_1|$, recall that $p_4 = p_1$). This can qualitatively be understood from equation 2.16 in differential form:

$$\rho V dV + dp = 0 \quad (2.17)$$

Now the velocity decrease between locations 1 and 2 is similar to the velocity decrease between locations 3 and 4 (i.e. it is the induced velocity) by which dV upstream of the rotor can be considered similar to dV downstream of the rotor. The higher mean velocity level in the region between 1 and 2 then yields a higher value of dp in this region. This makes the pressure difference between locations 2 and 1 larger than the pressure difference between locations 4 and 3.

2.1.2 Blade element theory

The equations from the momentum theory, as described in the previous section, model the global flow field around the wind turbine rotor in terms of the induced velocities as function of the axial force on the rotor (equation 2.9 (or 2.10)). In wind turbine design codes, equation 2.9 (or 2.10) is applied on concentric rings (annuli) with radial extent dr , see figure 2.3. It must be noted that

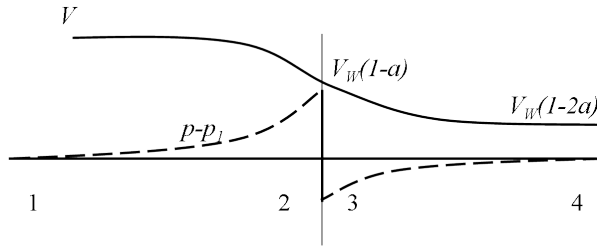


Figure 2.2: Velocity and pressure decay in streamwise direction

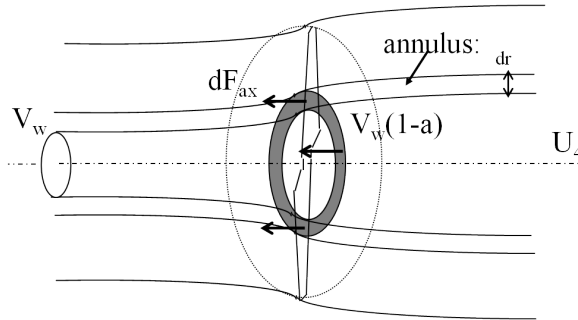


Figure 2.3: Division of streamtube into annuli

by dividing the actuator disc in annuli the pressures acting on the boundaries of these annuli should in principal be added to the momentum balance. However [Sørensen and Mikkelsen \(2001\)](#) find on basis of CFD calculations the contribution from these pressure forces to be small.

The axial force at the left hand side of this equation is then calculated with the blade element theory as the sum of the forces in axial direction on all blade elements located in this ring. Thereto the lift and drag forces on the blade elements are decomposed in axial direction, where the lift and drag forces are calculated from the airfoil coefficients, i.e. the lift (c_l) and drag (c_d) coefficients. These airfoil coefficients are a characteristic of the airfoil shape and they are a function of Mach number, Reynolds number and angle of attack (i.e. the angle between the incoming velocity and the chord line). For wind turbine applications the Mach number dependency can generally be neglected where the dependency on the Reynolds number is relatively weak

by which many codes prescribe the airfoil characteristics in tabular form as function of angle of attack only. The tables of airfoil characteristics are usually known from wind tunnel measurements.

More specifically the lift force (per unit length) is given by:

$$L = c_l(\alpha)0.5\rho V_{\text{eff}}^2 c \quad (2.18)$$

and the drag force is given by:

$$D = c_d(\alpha)0.5\rho V_{\text{eff}}^2 c \quad (2.19)$$

The angle of attack and effective velocity in these equations are found from the so-called velocity triangle, see figure 2.4, using the induced velocity or axial induction factor: Figure 2.4 shows the inplane velocity to be Ωr (at a later stage a tangential induced velocity will be added) and the axial velocity equals $V_w(1 - a)$.

Hence:

$$V_{\text{eff}}^2 = V_w^2(1 - a)^2 + \Omega^2 r^2 \quad (2.20)$$

where

$$\alpha = \phi - \epsilon \quad (2.21)$$

with ϕ the inflow angle:

$$\phi = \text{atan}[V_w(1 - a)/\Omega r] \quad (2.22)$$

and ϵ the twist angle (in case of non-zero pitch angles, the pitch angle should also be subtracted from the inflow angle in equation 2.21). Furthermore figure 2.4 shows the inflow angle ϕ to be the angle between the axial and lift direction with which the lift and drag forces can be decomposed in axial direction:

$$dF_{\text{ax}} = [L\cos(\phi) + D\sin(\phi)]dr \quad (2.23)$$

However it is very important to note that, although the actual axial force on the annulus obviously contains a (small) component from the drag, this component is generally not included in the axial force balance from equation 2.9. The main reasoning behind this approach lies in the idea that the drag force leads to a velocity change in the viscous wake behind the blade element which is not considered to be part of the induced velocity hence the axial force on the annulus is written as:

$$dF_{\text{ax}} = L\cos(\phi)dr \quad (2.24)$$

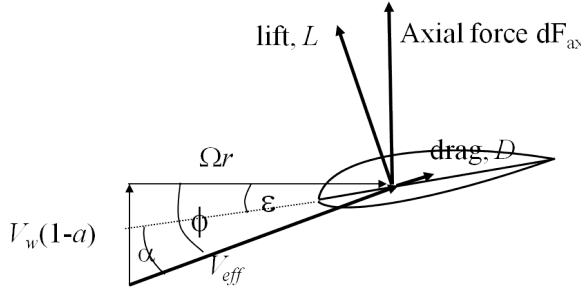


Figure 2.4: Blade element with lift, drag and velocity diagram

2.1.3 Axial blade element momentum theory

In the previous sections the axial momentum theory (equation 2.9) and the axial blade element theory (a combination of the equations 2.24, 2.18, 2.20, 2.21 2.22) are described.

Both theories form a relation between the axial induction factor and the axial force which are combined into the Blade Element Momentum (BEM) Theory:

$$2a(1-a)\rho V_w^2 dA_r = Bc \frac{1}{2} \rho V_{eff}^2 c_l \cos(\phi) dr \quad (2.25)$$

which reduces to:

$$4a(1-a)V_w^2 = \sigma V_{eff}^2 c_l(\alpha) \cos(\phi) \quad (2.26)$$

using dA_r (the area of the ring) = $2\pi r dr$ and σ (the local solidity) = $Bc/(2\pi r)$.

The effective velocity, angle of attack and inflow angle in the right hand side of equation 2.26 are found from the equations 2.20, 2.21 2.22 and expressed in terms of the axial induction factor using the (known) tip speed ratio, which is defined as:

$$\lambda = \frac{\Omega R}{V_w} \quad (2.27)$$

and the local tip speed ratio, defined as

$$\lambda_r = \frac{\Omega r}{V_w} = \frac{r}{R} \lambda \quad (2.28)$$

This yields:

$$V_{eff}^2 = V_w^2 (\lambda_r^2 + (1-a)^2) \quad (2.29)$$

$$\phi = \arctan \frac{1 - a}{\lambda_r} \quad (2.30)$$

$$\alpha = \phi - \epsilon - \theta \quad (2.31)$$

with which the axial induction factor in equation 2.26 can be solved iteratively.

2.1.4 Tangential Blade Element Momentum Theory

The sections 2.1.1 to 2.1.3 describe the BEM equations in axial direction. The main result is equation 2.26. It is a relation between the induced velocity in axial direction (or axial induction factor) and the axial force on a blade element. In a similar way a second momentum equation can be derived for the relation between the force on a blade element in inplane direction (dF_{inplane} , where $dF_{\text{inplane}}r$ represents the contribution of the blade element to the torque dQ) and the induced velocity in this direction. This tangential (inplane) induced velocity is denoted as u_t or ωr with ω the induced rotational speed. The system is closed with a second blade element relation for dF_{inplane} using a velocity diagram to which the tangential induced velocity is added. Thereto

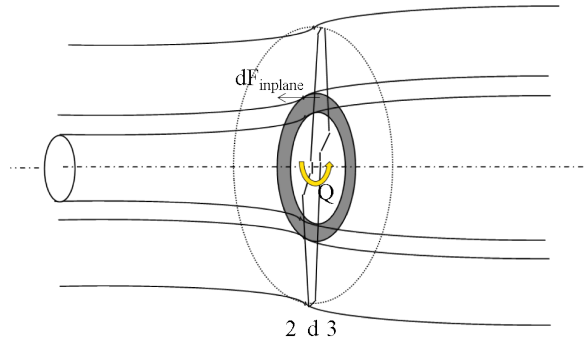


Figure 2.5: Stream tube concept for BEM equation in inplane direction

the positions 2, d and 3 are defined. Position 2 is located just upstream of the rotor plane, d represents the disc value and position 3 is just downstream of the rotor plane respectively, see figure 2.5. The tangential induced velocity just downstream of the rotor plane (denoted as $u_{t,3} = \omega_3 r$ with ω_3 the wake rotation) is calculated with the conservation of angular momentum from the torque dQ :

$$dQ = \rho V_w (1 - a) \omega_3 r^2 dA_r \quad (2.32)$$

The torque (or inplane force) is found from the blade element theory by decomposing the lift force in inplane direction with the inflow angle ϕ (Note that the drag forces are again not included in the calculation of the induced velocities).

$$dF_{\text{inplane}} = \frac{dQ}{r} = L \sin(\phi) \quad (2.33)$$

see figure 2.6.

The determination of the lift (from the effective velocity and angle of attack) and the inflow angle is then almost similar to the procedure described in section 2.1.3, the only difference is the addition of the tangential induced velocity in the velocity triangle. This velocity triangle however does require the tangential induced in the rotor plane (i.e. at position d) where equation 2.32 only includes the rotation at position 3, just downstream of the rotor. According to [de Vries \(1979\)](#) the tangential induced velocity in the rotor plane is half the tangential induced velocity at point 3, hence

$$\omega_d = \omega_3/2 = a' \Omega \quad (2.34)$$

in which a' the tangential induction factor. As such a' relates the tangential induced velocity in the rotor plane to the rotational speed of the rotor.

Then, by combining equation 2.32, 2.33, 2.34 and equation 2.18 it is found that:

$$4a'(1-a)V_w \Omega r = \sigma V_{\text{eff}}^2 c_l(\alpha) \sin(\phi) \quad (2.35)$$

Hence, in summary a complete BEM model is formed by the equations 2.26, 2.35, the velocity diagram relations from figure 2.6:

$$V_{\text{eff}}^2 = V_w^2 [\lambda_r^2 (1+a')^2 + (1-a)^2] \quad (2.36)$$

$$\phi = \arctan \frac{1-a}{\lambda_r (1+a')} \quad (2.37)$$

$$\alpha = \phi - \epsilon - \theta \quad (2.38)$$

and the airfoil coefficients as function of angle of attack.

From these equations, the axial and tangential induction factors are solved iteratively. With the resulting lift and drag force on the blade element, the forces can be decomposed in each direction and the overall forces and moments along the entire rotor blade are known by summing over the relevant elements.

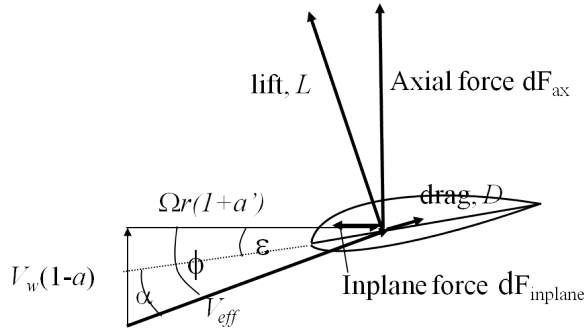


Figure 2.6: Blade element with axial and inplane force

2.2 Advanced rotor aerodynamic models

In the previous sections the BEM model has been described. The short calculational time of this model makes it especially suited for the routine calculation of a design load spectrum of a wind turbine, but it should also be acknowledged that the model is based on a large number of simplifications. These will be explained in more detail in section 3. Some of these uncertainties can be covered with so-called engineering add-ons, but they too generally require several simplifications.

For this reason much effort is spent within the wind energy society on the development and validation of Computational Fluid Dynamics (CFD) codes (e.g. Reynolds Averaged Navier Stokes (RANS) models or even more advanced LES models). The most famous example is the in-house made CFD code Ellipsys-3D from RISØ-DTU although in recent years also more and more commercial CFD codes (e.g. Ansys-CFX or Fluent) entered the scene.

Results from CFD codes have proven to be extremely useful in providing detailed insights into the aerodynamic behaviour of a wind turbine, but the calculational time remains orders of magnitude higher than the calculational time from BEM. This is the reason why much effort is also spent on intermediate methods between BEM and CFD e.g. free vortex wake methods.

An example of a free vortex wake method is the AWSM code as developed by ECN see section 2.3.2. The calculational time of AWSM is sufficiently short

to use it for some special load cases, for which the basic BEM model, as explained in the sequel of this thesis, is known to be inaccurate (e.g. yawed cases, fast pitching actions etc). AWSM is also used for the more accurate aerodynamic modelling of unconventional blade shapes, e.g. winglets and swept blades, see [Maggio and Grasso \(2011\)](#)

The benefit from free vortex wake methods (and CFD) however mainly lies on the field of research purposes and they often served as food for inspiration for the development of several engineering methods for BEM.

Although ASWM calculates the induction in a much more physical way than the momentum theory its calculation of blade loads still relies on the blade element theory, which implies that tables of airfoil data should be prescribed. The Rotorflow code as developed at ECN overcomes this limitation. This model calculates the viscous effects along a blade with an integral boundary layer method. This viscous model is then coupled to an inviscid panel method by which both the blade element part and the momentum part are calculated in a more physical manner than BEM where nevertheless the calculational time is much shorter than the calculation time needed for CFD.

In summary the different types of rotor aerodynamic models can then be classified according to figure 2.7: Simple but fast engineering types of models, and thorough but time consuming CFD methods. The free wake lifting line code AWSM and the coupled viscous-inviscid code Rotorflow form a group of models which fall in between these two extremes.

2.3 ECN's aerodynamic models

Many of the calculational results which are presented in the present thesis are produced by two ECN codes: The aero-elastic code PHATAS and the free wake lifting line code AWSM. Results from the latter code are mainly used to support the analysis from engineering methods.

2.3.1 PHATAS

PHATAS, the 'Program for Horizontal Axis wind Turbine Analysis and Simulation', is an aero-elastic code developed by ECN. The aerodynamic model from this program is based on the Blade Element Momentum Theory as de-

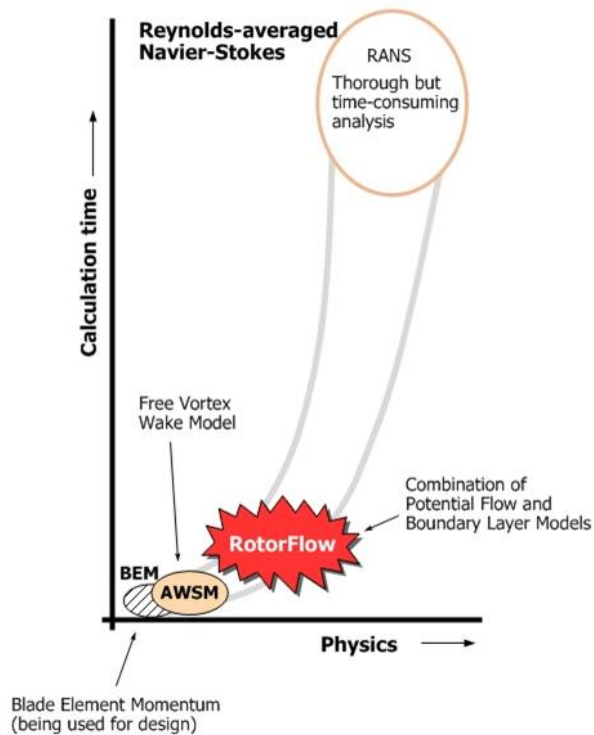


Figure 2.7: Classification of aerodynamic models, (Figure from H. Ozdemir)

scribed before, with a large number of engineering add-ons, see [Lindenburg and Hegberg \(1999\)](#).

The emphasis in the thesis lies on the aerodynamic modelling but in principle PHATAS is a full aero-elastic code which includes a structural model, different generator and control models and an interface for an external controller. The wind field can be provided from a stochastic wind generator but it is also possible to prescribe a constant and/or uniform wind speed with or without wind shear and yaw misalignment.

2.3.2 AWSM

The AWSM code, see [van Garrel \(2003\)](#), is based on a non-linear lifting line vortex wake model. It basically calculates the induction in the rotor plane from the vorticity in the wake using the law of Biot and Savart where the vorticity in the wake is trailed from the rotor blades which are modelled as lifting lines. This implies that, similar to BEM codes, aerodynamic profile data should be prescribed as function of the angle of attack. The vorticity of the lifting lines (i.e. the bound vorticity) is calculated from the lift forces with the Kutta-Joukowski theorem. The code is of a free wake character but for distances larger than 4 rotor diameters downstream of the rotor, the wake is often assumed to be 'frozen'.

All AWSM calculations as presented in this thesis were made under the following assumptions:

- The construction is assumed to be rigid and mass induced loads are neglected;
- The wind speed is constant in time and homogenous. The aerodynamic tower shadow effect has been neglected;
- The rotor speed and pitch angle are constant;

2.4 Concluding remarks on rotor aerodynamic models

The main subject of the present chapter is to give a brief description of the Blade element momentum (BEM modelling). This consists of an axial relation (equation 2.26) and a tangential relation (2.35). Furthermore the auxiliary expressions 2.36, 2.37, and 2.38 are used which together with the airfoil coefficients ($c_l(\alpha)$ and $c_d(\alpha)$) close the equations.

More advanced aerodynamic models (Computational Fluid Dynamic (CFD) models and intermediate methods between BEM and CFD) are briefly touched upon. However, the present thesis mainly pays attention to the engineering methods at the left bottom part of figure 2.7. Such methods consist of a BEM model with several add-ons which are described in the next sections. Results from more advanced methods are mainly used to support and interpret the analysis from engineering methods. Figure 2.7 shows how the engineering

methods should be distinguished from the more advanced models. In this respect it is important to note that although engineering methods are considered to be very different from Computational Fluid Dynamic methods, this does not prevent them to compute the dynamics of the fluid too!

Chapter 3

Uncertainties and assumptions in Blade Element Momentum theory and engineering add-on's

As explained in chapter 2 a basic BEM model consists of the equations 2.26, 2.35 and the auxiliary expressions 2.36, 2.37 and 2.38. Airfoil coefficients ($c_l(\alpha)$ and $c_d(\alpha)$) should be prescribed as input to the BEM model. In the derivation of the BEM equations a large number of assumptions and simplifications have been made. Furthermore it is important to realize that the airfoil coefficients are generally measured (or calculated) under 2D and steady conditions. This 2D, steady environment differs considerably from the situation on a wind turbine blade in the free atmosphere which is highly 3-dimensional and unsteady. In order to overcome these deficiencies several engineering methods have been developed which need to be added to the BEM model or to the airfoil data.

In this chapter the main assumptions and simplifications from the BEM theory are described together with the way how they are covered in nowadays design codes. Where possible some words are spent on the practical importance of the simplifications. It is meant to be a general overview. In the next sections several assumptions and engineering models with their validations

are described in more detail using results from projects in which the author was involved (note that the precise involvement of the author is described in Appendix C).

It must be noted that the models which are applied as corrections to the 2D, steady airfoil characteristics obviously rely on the validity of these 2D, steady characteristics. However these basic characteristics are often only measured for a limited angle of attack range around zero angle of attack and at Reynolds numbers which are (much) lower than the Reynolds number on modern wind turbine blades, see e.g. the discussions from [Timmer and van Rooij \(2001\)](#) and [Timmer and van Rooij \(2003\)](#). A method to extend the basic airfoil data for the entire angle of attack range from -180 to +180 degrees and to find data at the actual Reynolds number is offered by the ATG program ([Bot \(2001\)](#)), where flat plate data are used at high angles of attack.

3.1 Assumption of incompressible flow

The assumption of incompressibility (i.e. constant density) is made in both the momentum theory as well as in the blade element theory.

In principle compressibility corrections on airfoil characteristics are known, e.g. the Prandtl-Glauert correction using a compressibility factor $\sqrt{1 - M^2}$ with M the Mach number. Alternatively the airfoil characteristics can be calculated with a compressible airfoil design code like RFOIL, see [Montgomerie et al. \(1997\)](#) and [van Rooij \(1996\)](#). With this code the airfoil characteristics can be calculated for the actual free stream Mach number.

However, compressibility corrections to airfoil characteristics are hardly applied because the tip speed (which is the maximum relevant velocity for wind turbine applications) is generally limited to around 80 m/s (mainly due to noise consideration), by which the free stream Mach number remains lower than 0.25. This Mach number makes the compressibility corrections small enough to be neglected. For future off-shore wind turbines, the tip speed may become higher (in view of the fact that noise does not play a role) but even then the compressibility corrections may be limited in relation to other uncertainties.

3.2 Assumption of inviscid flow

Viscous effects are accounted for in the blade element theory through the drag coefficient. As a matter of fact drag losses are one of the reasons why the power production of a wind turbine will always be below the Betz limit.

Viscous effects will also disturb the simplified streamtube concept from figure 2.1 and the accompanying text in section 2.1.1. This concept goes together with a constant low velocity in the streamtube and a higher velocity outside. The fact that the momentum theory is generally applied on annular ring level does allow some radial variation in induced velocity but it does not prevent an (unrealistic) discontinuity in velocity (and pressure) at the edge of the stream tube. The resulting high shear at that position will lead to production of turbulence. Nevertheless wind tunnel measurements from the project Mexico (see section 6.3.3) still confirm that the velocity in the near wake follows this streamtube concept well, at least in the near wake which is determinant for the induced velocities. They show the velocity in the wake to be constant at a lower value than the free stream velocity, where the tip vortices induce a rather abrupt increase towards the free stream velocity at the edge of the wake more or less in agreement the streamtube concept

Hence although the inviscid assumption in the momentum theory is difficult to assess, it is not expected to be a significant source of deviations. As a matter of fact viscous mixing in the wake is mainly believed to be a parabolic process, i.e. it influences the downstream flow but its upstream effect on the induction in the rotor will be limited. As such the impact of viscosity mainly lies on the field of wind farm aerodynamics and less on the field of rotor aerodynamics.

3.3 Assumption of annular independency, axi-symmetry

A main assumption in the momentum theory is the division of the streamtube in independent annuli. For helicopter flows, [Bramwell \(1974\)](#) finds on basis of calculations with a more detailed flow model, that the induced velocity mainly depends on the local pressure jump in the annular ring which then confirms the annular independency. However this is not expected to be true when small (and inevitably) yaw errors occur since this will lead to a radial flow component along the blade. Furthermore, in [Sørensen and van Kuik \(2011\)](#) the equations

of motions are analyzed showing a large radial pressure gradient in particular at low rotational speeds and resulting large tangential induced velocities. This radial pressure gradient obviously violates the assumption of annular independence.

Moreover the induced velocities within an annular ring are assumed to be azimuth angle independent. This assumption is violated by the finite number of blades which leads to a non-uniform flow between the blades. This is explained in more detail in section 3.4. The 2D assumption is also violated by wind shear and yaw. Part of this problem is addressed by [Snel et al. \(2008\)](#). He points out that, for three bladed rotors, BEM methods should account for the effect of the inflow at a blade induced by the bound vortex of the other blades. For axi-symmetric flow the net effect is zero, because the other blades have equal but opposite effects. However for wind shear and yaw the bound vortex depends on the azimuth, hence there is a non-zero effect. In [Snel et al. \(2008\)](#) a clear non-negligible velocity is induced by the other 2 blades for a yaw angle of 30 degrees and recommendations are given to include this effect in BEM methods.

Also yaw leads to an azimuthal dependency of the induced velocity. This is discussed in more detail in section 3.8.

3.4 Assumption of actuator disc concept

One of the most important simplifications in the momentum theory is the representation of the rotor by an actuator disc. Such actuator disc is a hypothetical concept which to some extent can be seen as a rotor with an infinite number of blades since the flow in the rotor plane is assumed to be uniform. However, the fact that a real rotor has a finite number of blades makes the actual flow in the rotor plane non-uniform. This non-uniformity is generally covered with the Prandtl tip loss correction F , (or modifications to it, see e.g. [Shen et al. \(2005\)](#)). In its basis the Prandtl tip loss factor gives the ratio between the local axial induction factor at the blade (as applied in the blade element theory) and the azimuthally averaged axial induction (as applied in the momentum theory).

The Prandtl tip loss factor takes the following form:

$$F = \frac{2}{\pi} \arccos(\exp(-F_1)) \quad (3.1)$$

with:

$$F_1 = \frac{-B(R - r)}{2r\sin(\phi)} \quad (3.2)$$

There exist different implementations of the Prandtl tip loss factor into the BEM equations but usually it changes equation 2.26 into:

$$4aF(1 - aF)V_w^2 = \sigma V_{\text{eff}}^2 c_l(\alpha) \cos(\phi) \quad (3.3)$$

The left hand side of equation 3.3 (i.e. the momentum theory term) uses the annulus averaged induction factor aF . In the right hand side (i.e. the blade element term) the effective velocity, the angle of attack and the inflow angle are based on the local axial induction factor a .

Prandtl derived the factor in the pre-computer era (1919). This necessitated the use of a very simplified vortex wake concept by which it was possible to derive equation 3.1 analytically (even though virtually all wind turbine aerodynamic text books state that the derivation of the Prandtl tip correction is outside the scope of the book (...)).

The simplified model from Prandtl consisted of vortex planes which move with a constant transport velocity $V_w(1 - a)$, i.e. the velocity in the rotor plane based on the local axial induction factor. Flow 'wipes' in and out from the free stream into the streamtube, see figure 3.1. This brings the actual wake velocity to $(V_w(1 - aF))$, i.e. a value between the 'inner' wake velocity $(V_w(1 - a))$ and the free stream velocity (V_w) .

Hence, the averaged induction factor is decreased or, vice versa, the local axial induction factor at the blade, is increased, see also figure 3.2. This then reduces the local inflow angle according to equation 2.37 and hence the angle of attack and the resulting aerodynamic loads. As the name tip loss factor already indicates the correction is stronger at the tip. This is consistent with equations 3.1 and 3.2 which show the Prandtl tip loss factor to approach zero towards the tip. The correction is less strong for a shorter distance between the vortex planes (i.e. for a large number of blades and a high tip speed ratio). This is again consistent with equations 3.1 and 3.2 which show F to approach 1 for an infinite number of blades, in agreement with the actuator disc concept. The same happens for a fast rotating turbine (i.e. $\lambda \rightarrow \infty$ which implies $\phi \rightarrow 0$ according to equation 2.37). The Prandtl factor was derived to model tip effects but a similar effect occurs at the blade root. Thereto the same loss factor is often used where the tip radius R in equation 3.1 is replaced by the

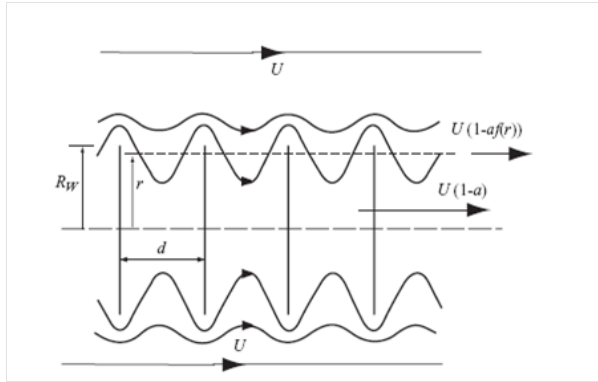


Figure 3.1: Wake model used to derive the Prandtl tip correction, from [Burton \(2001\)](#) (U denotes the free stream wind speed and d the distance between the vortex planes)

root radius. It should then be noted that such root radius is less well defined than the tip radius.

In section 6.3.4 a validation of the Prandtl tip loss factor is described on basis of Mexico flow field measurements in the rotor plane and on basis of AWSM free vortex wake calculations. It will be found that the inflow angle dependency in equation 3.1 might be improved. Moreover the location of maximum chord was found to be a good measure for the root radius when the Prandtl factor is used as root loss factor.

3.5 Turbulent wake

The conservation laws as discussed in section 2.1.1 assume positive flow velocities in the stream tube of figure 2.1 or in other words the flow direction in this figure should be from left to right. This is however not true anymore for $a > 0.5$ which yields negative values for U_4 according to equation 2.7. This situation is called the turbulent wake state. The invalidity of the stream tube concept for large values of the axial induction factor can be illustrated by considering the situation at $a = 1.0$ which implies the velocity in the rotor plane (U_d) to be 0, i.e. a fully blocked flow in the rotor plane. Nevertheless this goes

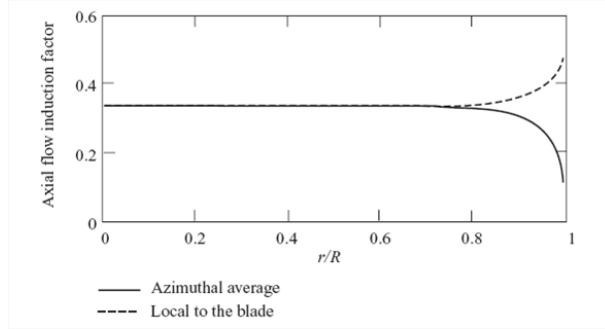


Figure 3.2: Local and azimuthally averaged induction factor, from [Burton \(2001\)](#)

together with a zero axial force coefficient according to equation 2.10. This leads to a controversy since a zero axial force coefficient implies no blockage at all!

For this reason the momentum relation 2.10 is generally replaced by an empirical turbulent wake relation between the axial force coefficient and the axial induction factor. A large number of these relations have been proposed, e.g. [Wilson \(1981\)](#) who applies the following relation for $a > 0.38$:

$$C_{D,ax} = 0.96aF + 0.58 \quad (3.4)$$

Another turbulent wake relation is given in [Anderson \(1982\)](#):

$$C_{D,ax} = 1.93aF + 0.425 \quad (3.5)$$

Also the correction from [Glauert \(1935\)](#) is well known:

$$C_{D,ax} = 4aF[(1 - (0.25(5 - 3a)a)] \quad (3.6)$$

This equation is applied for $a > 0.33$

The fact that there exists such a large variety of turbulent wake corrections is seen as an indication for a big uncertainty in these models. However this uncertainty may be of less relevance since the practical importance of the turbulent wake state is limited. Thereto it should be realized that high axial induction factors go together with high tip speed ratios which are uncommon for

variable speed turbines (such turbines generally operate near the optimal tip speed ratio which implies that $a \approx 1/3$). Constant speed turbines may operate at high tip speed ratios but this then corresponds to very low wind speeds which contribute little to the energy production and load spectrum. As a matter of fact the main reason for including a turbulent wake model in a BEM code is to guarantee its robustness since a standard BEM model without it will face convergence problems at high axial induction factors. Turbulent wake corrections may also be important near the tip of the blade, where the Prandtl tip loss effect, as described in section 3.4, yields very high local induction factors.

Some more information on the aerodynamics at the turbulent wake state can be found in section 6.3 where IEA Task 29(Mexnext) PIV measurements are presented at very high axial induction factors. A comparison is made with results from several CFD codes.

3.6 Assumption of stationary conditions

Wind turbines operate at a very unsteady environment due to e.g. turbulence, wind shear, deflections, control actions etc. Nevertheless the BEM theory is derived for stationary conditions.

The assumption of steady flow is made in the blade element theory through the use of (calculated or measured) steady airfoil data and in the momentum theory. Unsteady phenomena are most conveniently explained in terms of a vorticity representation of the wake (and the blades). The wake vorticity exists of shed vorticity and trailing vorticity, both time dependent. Unsteady effects in the momentum theory depend mainly on the trailing vorticity (i.e. the vorticity related to the spanwise variation of the bound vortex) which is transported with a velocity in the order of the wind speed. The characteristic length scale for the bound vorticity is in the order of the rotor diameter. Unsteady effects on the airfoil aerodynamics depend on the shed vorticity (i.e. the vorticity related to the unsteady variation of the bound vortex). This vorticity is transported with a velocity in the order of V_{eff} and it has a characteristic length scale of the chord length. This makes the time scale of unsteady airfoil effects in the order of c/V_{eff} ($\approx c/(\Omega r)$) where the time scale of unsteady effects in the momentum theory is in the order of D/V_w . Hence the time scale of unsteady effects in the momentum theory is much slower than the time scale of the unsteady airfoil aerodynamics, by which the phenomena can be considered as independent.

3.6.1 Unsteady airfoil aerodynamics

Unsteady effects on the airfoil characteristics are especially important at high angles of attack where dynamic stall occurs but even at attached conditions there is an unsteady effect.

- The unsteady effects at attached conditions can be modelled with the model from [Theodorsen \(1935\)](#). This model can be seen as an unsteady extension of thin airfoil theory which implies that it has been derived for inviscid conditions. It basically describes the effects associated to the acceleration of the flow around the airfoil and the angle of attack variations as induced by the shed vorticity.

The classical Theodorsen model is however of a 2D character where the shed vorticity is represented by infinite long vortex lines. For a wind turbine situation the shed vorticity can more realistically be represented by vortex 'spokes', see [Snel \(2004\)](#). Lack of good validation material hampers the further development of such model as pointed out by [Hur \(2011\)](#).

- Dynamic stall is a viscous phenomenon which is initially caused by an accumulation of vorticity near the leading edge of the airfoil as the angle of attack increases and the separation point approaches the leading edge. This causes an overshoot in lift followed by an abrupt decrease in the lift when the vortex is convected downstream of the airfoil. It altogether leads to a hysteresis loop on the $c_l(\alpha)$ curve with high c_l in the upstroke and a low c_l in the downstroke. It goes together with very large moment variations due to centre of pressure movements.

In the EU-Joule project Dynamic Stall and Three Dimensional Effects, (see [Björck \(1995\)](#)) an overview is given of engineering dynamic stall models. Dynamic stall effects are often expressed as a (time dependent) correction to the steady state $c_l(\alpha)$ in the form of an ordinary differential equation in time

$$\tau \frac{dc_l}{dt} + f(\alpha)c_l = g(c_l, \alpha, \frac{d\alpha}{dt}, \frac{d^2\alpha}{dt^2}) \quad (3.7)$$

Dynamic stall models of this form are generally developed and validated using steady 2-dimensional $c_l(\alpha)$ coefficients as a basis. In section 3.7 it will be explained that the time averaged airfoil coefficients on a wind turbine blade (in particular at stalled conditions) are exposed to

strong rotational effects for which several correction methods are invented. Therefore dynamic stall effects for wind turbine situations are often modelled according to equation 3.7 but applied to rotationally corrected steady state $c_l(\alpha)$ characteristics.

In section 5.6 dynamic stall hysteresis loops will be shown from the IEA Task 14/18 field measurements as analyzed in the project 'Dynamic Stall and Three Dimensional Effects'. It is found that the unsteady and stochastic field environment makes the excitation unknown by which these measurements are not very useful for the study of dynamic stall.

Wind tunnel measurements at yaw are more useful since they are exposed to a very well defined excitation. Thereto section 8.4 analyzes the NREL's Phase VI(Nasa-Ames) wind tunnel measurements at yawed conditions. In Santos Pereira et al. (2011) the Mexico wind tunnel measurements at yaw are used to validate and tune dynamic stall models. A complicating factor when using yawed wind tunnel measurements for the interpretation of dynamic stall effects lies in the interference of dynamics stall with the (partly unknown) effects from yaw, see section 3.8.

The practical importance of unsteady airfoil aerodynamics lies on the impact it has on load variations (i.e. fatigue loads). Perhaps even more important is the impact on the aerodynamic damping. Aerodynamic damping is determined by the energy transfer between the blade and the airflow for a vibrating blade. During a flapping motion in stall the use of steady airfoil characteristics may lead to negative aerodynamic damping, which is not observed in measurements, see e.g. Björck (1995). These instabilities are then prevented by dynamic stall which changes the phase of the aerodynamic forces during a flapping cycle.

A different effect from the turbulent wind field on the airfoil aerodynamics may be through the transition point, i.e. the location where the transition from a laminar to a turbulent boundary layer takes place. Some commonly used airfoils have a large part of laminar flow along the airfoil, at least when they are measured in the low turbulence environment of a wind tunnel. The question can be asked whether the turbulent environment in which a wind turbine operates causes 'by-pass transition' i.e. a significant forward shift of the transition point on the suction side. This would yield a much higher drag and consequently a considerably lower power.

Unfortunately (and surprisingly) very little experimental data exist with which this hypothesis can be confirmed. However almost forgotten measurements on ECN's HAT-25 turbine as carried out by [van Groenewoud, Boermans and van Ingen \(1983\)](#) donot seem to confirm the hypothesis. Thereto it should first be realized that the turbulence intensity (defined as standard deviation of wind speed fluctuations divided by the mean wind speed) felt by a blade element is decreased through the higher mean wind speed from rotation. Furthermore the frequencies in the turbulent spectrum which are relevant for the transition of a laminar to a turbulent boundary layer on current wind turbine blades are estimated to be between 500 and 1000 Hz (personal communication with van Ingen, 2009, based on calculations with his e^m method, [van Ingen \(1956\)](#)). At these frequencies the rotating turbulent spectrum for a wind turbine blade hardly contains any energy. As such the effect from the ambient turbulence on the transition position could be expected to be very limited.

3.6.2 Dynamic Inflow

The steady assumption in the momentum theory is apparent through the fact that the induced velocity follows the load situation (i.e. $C_{D,ax}$) instantaneously. This is often called the equilibrium wake assumption. However when the loading situation changes (due to for example a change in pitch angle, wind speed or rotor speed), the induced velocity will lag behind, since an appreciable amount of air must be accelerated or decelerated. In such cases the wake behind the turbine, and consequently the induction will achieve steady state conditions after a certain delay. This phenomenon is commonly called 'dynamic inflow' (Alternatively, the names 'dynamic wake' or 'dynamic induction' are sometimes used).

In figure 3.3 the dynamic inflow effect is explained by means of a (trailed) vorticity representation. The trailed vorticity is formed at the blade and convected downstream with the local total velocity, partly wake induced. Then a change in $C_{D,ax}$ (e.g. through a change in pitch angle) modifies the bound vorticity and hence the trailed vorticity. Due to the fact that the trailed vorticity is convected with a finite velocity, the resulting wake becomes a mixture of 'old' and 'new' vorticity. Consequently the velocity induced by such wake includes a contribution from the 'old' and the 'new' situation. As soon as the 'old' vorticity has travelled a distance of some 2 to 4 diameters behind the rotor, its influence is hardly felt anymore in the rotor plane and the new equilibrium situation is reached. However, before the vorticity has travelled this distance,

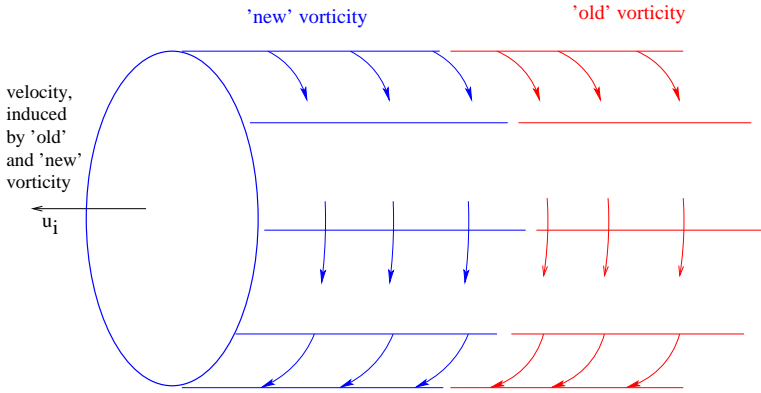


Figure 3.3: Wake with 'mixed' vorticity as a result of e.g. a pitch angle step

a gradual change of the induced velocity takes place from its old equilibrium value to its new equilibrium value. It is this gradual change in induced velocity which is the essential characteristic of the dynamic inflow phenomenon.

It was studied extensively in two European 'Dynamic Inflow' projects, see [Snel and Schepers \(1994\)](#) and [Schepers and Snel \(1995\)](#) where it was shown that the delay in induction is the cause of a temporary enlargement of the forces, in particular during fast pitching steps.

Dynamic inflow is generally modelled by adding a first order time derivative on the axial induced velocity to the momentum theory relation 2.10, i.e.

$$\tau \frac{du_i}{dt} + 4u_i(1 - u_i) = V_w C_{D,ax} \quad (3.8)$$

with τ a time constant which decreases towards the tip and increases with rotor diameter.

Note that in an equilibrium situation this equation returns to equation 2.10. A similar equation has been derived for the inplane component, see [Snel and](#)

[Schepers \(1994\)](#).

Section 7 describes several results from research on Dynamic Inflow, e.g. the derivation of equation 3.8 is explained using a simplified vortex wake method and results from several validations are presented (mainly based on IEA Task 20(NASA-Ames) measurements).

In order to assess the practical importance of dynamic inflow it must first be noted that it is driven by a change in axial force coefficient. This happens during a pitch angle transient. Therefore dynamic inflow effects are often described for pitch angle variations indeed, see e.g. the results from section 7. Moreover dynamic inflow effects can be expected during a change in wind speed and/or rotor speed. Section 7.4 shows Mexico measurements which confirm that dynamic inflow effect appear during a rotor speed transient. However, opposite to common belief a change in free stream velocity hardly leads to any dynamic inflow effects. This is a result of the fact that, although the axial induction factor changes with wind speed, the induced velocity itself is hardly affected. This is shown in [Snel and Schepers \(1994\)](#) on basis of a linearized BEM model and with measurements at wind speed changes carried out by the University of Delft in their Open Jet Facility.

In the assessment of the importance of dynamic inflow effects for modern state of the art turbines it should be acknowledged that most results from section 7 are not very representative in view of the unrealistically large rotor speed and pitch angle steps. On the other hand the dynamic inflow effect on a modern state of the art turbine will be enhanced by the very large scale. Thereto it is recalled that the time constant from equation 3.8 increases with diameter. It is then not surprising to find in [van Engelen and van der Hooft \(2004\)](#) that the dynamic inflow effects have a large practical importance, not only in view of the higher dynamic loads on a turbine but also because of its impact on the aerodynamic damping characteristics and in particular in the design of pitch control algorithms.

3.7 Assumption of 2D airfoil aerodynamics

The airfoil characteristics as used in the blade element theory are generally based on 2D wind tunnel measurements. Blade rotation and three dimensional geometrical effects (taper, twist, different airfoils) violate this two dimensional assumption.

- The main effect from rotation on the airfoil coefficients is a so-called stall delay as first noted by [Himmelskamp \(1950\)](#) who carried out experiments on propellers. It was found that rotation postpones the separation of the boundary layer in particular at the inner part of the blade. Hence the lift increases until a larger angle of attack than expected from 2D experiments.

The practical importance of stall delay for wind turbine situations mainly lies in the fact that power and loads are higher as predicted with 2D airfoil data for conditions where the inner part of the blade is stalled. This may happen at gusts for pitch controlled turbines and at high wind speeds for stall controlled turbines.

In [Snel et al. \(1993\)](#) the stall delay effect is explained by considering the rotating boundary layer equations:

$$\frac{\delta u}{\delta s} + \frac{v}{r} + \frac{\delta v}{\delta r} + \frac{\delta w}{\delta z} = 0 \quad (3.9)$$

$$u \frac{\delta u}{\delta s} + v \frac{\delta u}{\delta r} + w \frac{\delta u}{\delta z} = -\frac{1}{\rho} \frac{\delta p}{\delta s} + \frac{1}{\rho} \frac{\delta \tau_s}{\delta z} + 2\Omega v - \frac{uv}{r} \quad (3.10)$$

$$u \frac{\delta v}{\delta s} + v \frac{\delta v}{\delta r} + w \frac{\delta v}{\delta z} = -\frac{1}{\rho} \frac{\delta p}{\delta r} + \frac{1}{\rho} \frac{\delta \tau_r}{\delta z} + \frac{(u - \Omega r)^2}{r} \quad (3.11)$$

The first equation gives the continuity equation (in which s , r and z denote the coordinates in chordwise, radial and 'boundary layer direction' respectively, and u , v and w denote the corresponding velocities). The second equation denotes the momentum equation in chordwise direction and the third equation denotes the momentum equation in radial direction. The latter equation includes the radial pressure gradient (dp/dr) and centrifugal force $[(\Omega r)^2/r]$ which act on the boundary layer giving it an outward radial velocity component v (on the suction side). For an attached boundary layer, an order of magnitude analysis showed the v component to be much smaller (order (c/r)) than the u component. However in a separated boundary layer the u component is much smaller by which the 'residence time' of the air is sufficient to give the boundary layer particles a large radial velocity v , directed outward. Since at a more outboard station, the blade moves faster in chordwise direction (i.e. Ωr is larger), the boundary layer particles that are radially transported from the inboard stations get a relative velocity in chord direction, towards the trailing edge. This relative acceleration is present in the chordwise

momentum equation (equation 3.10) as the Coriolis force $2\Omega v$ which works in line with the pressure gradient dp/ds along the chord. As such the Coriolis force works as a 'favourable' pressure gradient, i.e. it reduces the adverse pressure gradient along the chord leading to a thinner boundary layer and an increased lift. An order of magnitude analysis showed the local solidity (c/r) to be the dominant parameter for this effect, i.e. the largest increase in lift is found at the root.

A method to generate rotating $c_l(\alpha)$ curves from the 2D characteristics is introduced in the same reference from Snel, Houwink and Bosschers using a factor f_{cl} . This factor is the ratio of the actual increase in c_l (i.e. $c_{l,3D} - c_{l,2D}$) and Δc_l with Δc_l the difference between the non-viscous $c_{l,inviscid}$ (with 'inviscid' slope $dc_l/d\alpha = 2\pi$) and the 2D value of $c_{l,2D}$, see figure 3.4. Hence

$$f_{cl} = \frac{c_{l,3D} - c_{l,2D}}{c_{l,inviscid} - c_{l,2D}} = \frac{c_{l,3D} - c_{l,2D}}{\Delta c_l} \quad (3.12)$$

and

$$c_{l,3D} = c_{l,2D} + f_{cl}(c_{l,inviscid} - c_{l,2D}) = c_{l,2D} + f_{cl}\Delta c_l \quad (3.13)$$

[Snel et al. \(1993\)](#) propose the following value for f_{cl} :

$$f_{cl} = 3(c/r)^2 \quad (3.14)$$

Equation 3.14 shows the strongest rotational correction at the inboard stations where the chord c is large and the radial position r is small.

Since then many alternative formulations for f_{cl} have been proposed. As an example [Chaviaropoulos and Hansen \(2000\)](#) found, by matching results of CFD calculations:

$$f_{cl} = 2.2(c/r)\cos^4(\epsilon + \theta) \quad (3.15)$$

The term $\epsilon + \theta$ can be understood by realizing that this is the angle between the rotor plane and the chord. Hence the coriolis term in equation 3.10 should in principle be multiplied with $\cos(\epsilon + \theta)$. Experimental evidence for the dependency of stall delay on $\epsilon + \theta$ is given in section 5.7.4. As an alternative to equation 3.13, or in the absence of any 2D airfoil data, the rotating airfoil data can be calculated with the aforementioned airfoil design code RFOIL (see [Montgomerie et al. \(1997\)](#) and

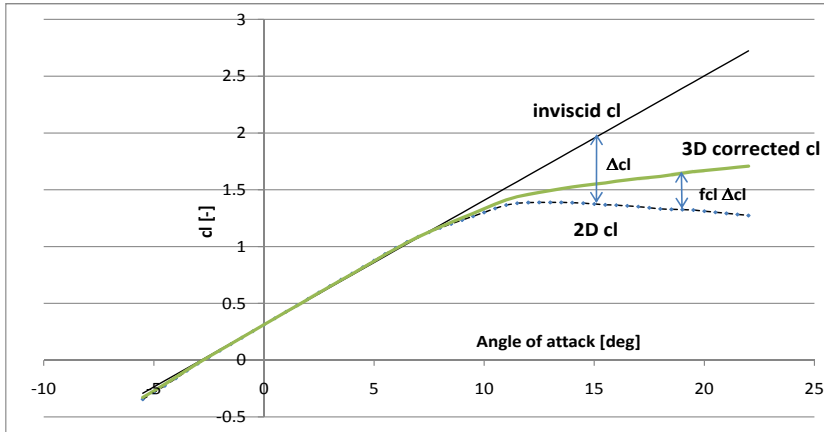


Figure 3.4: Correction to rotational effects on lift coefficient

van Rooij (1996)).

RFOIL calculates airfoil characteristics from the airfoil geometry and the local solidity c/r as input. It is a modification of the 2D airfoil design code XFOIL from Drela (1989). RFOIL is based on the 3D rotating boundary equations as presented above but written into an integral boundary layer formulation. An order of magnitude analysis is performed on the equations by which rotational effects are again accounted for through c/r . This makes it possible to apply the model in a quasi-2D way. The advantage of using RFOIL above equation 3.13 lies in the fact that no measured airfoil characteristics need to be available. However it also implies that any measured information is ignored. Therefore, instead of using equation 3.13, RFOIL is sometimes used to determine the increment on c_l and then this increment is added to the measured 2D lift

coefficient.

It must be noted that equation 3.12 only models the rotational effects on the lift coefficients. A rotational effect on the drag coefficient was proposed in the above mentioned reference from [Chaviaropoulos and Hansen \(2000\)](#). They found the drag to increase. This drag increase was modelled through a factor f_{cd} and the difference between the 2D drag coefficient and the minimum drag coefficient:

$$c_{d,3D} = c_{d,2D} + f_{cd}(c_{d,2D} - c_{d,2D,min}) \quad (3.16)$$

In the same reference f_{cd} was proposed to be similar to f_{cl} see equation 3.15, hence:

$$f_{cd} = 2.2(c/r)\cos^4(\epsilon + \theta) \quad (3.17)$$

In section 5 several studies are presented in which the expressions for f_{cl} and f_{cd} are validated and refined on basis of detailed aerodynamic measurements from IEA Task 14/18 and IEA Task 20(NASA-Ames).

- Apart from the 3D effects from blade rotation, there are 3D geometrical effects (due to taper and twist). These mainly play a role at the tip of the blade. This is shown in section 5 where a comparison is made between calculated and measured tip loads from IEA Task 14/18 and IEA Task 20(NASA-Ames). A significant over prediction of the tip loads is found when using the Prandtl tip correction from section 3.4 only. Thereto it should be emphasized that the Prandtl tip correction addresses the flow non-uniformities from the finite number of blades. As a result hereof the local axial induction factor is increased (by which the angle of attack and the aerodynamic loads are decreased). However it does not affect the airfoil coefficients in itself which remain 2D (i.e. the lift slope $dc_l/d\alpha \approx 2\pi$ at attached flow conditions according to thin airfoil theory). As such an additional tip correction should be added to the airfoil coefficients. A suggestion for such tip correction is done by [Shen et al. \(2005\)](#). In chapter 5 it is shown that the inclusion of this correction leads to an improvement in results. Moreover a suggestions for a more physical tip correction is done in chapter 5.

3.8 Yawed flow

The expressions in the Blade Element Theory as well as the expressions in the momentum theory have been derived under the assumption that the rotor

plane is perpendicular to the wind direction. This is generally only true on a time averaged basis. The inevitable wind direction fluctuations around the mean wind direction implies the wind turbine to be in a continuous yawed situation. An inventory of 5 years measurements in the ECN Wind Turbine Test Site EWTW showed the standard deviation of the turbine yaw errors (based on 10 minute time series) to vary between 2 and 10 degrees, although much higher values were found in wake operation. Failure of the yaw system might also lead to high yaw errors.

The practical importance of yaw partly lies in the fact that the power is expected to decrease with yaw which implies an economical loss. Equally important is the fact that yaw causes an azimuthal variation of the loads on a wind turbine. This affects the power quality but in particular the loads. It is found in e.g. [Schepers et al. \(2002c\)](#), that yaw can even be design driving in terms of extreme and fatigue blade loads.

The importance of yaw aerodynamics has nowadays even become more prominent by the idea that yaw can be applied as a wake reducing concept see e.g. [Machielse \(2011\)](#). Thereto the upstream turbine in the farm is put under yawed conditions. This results in a deflection of the wake behind this upstream turbine. This could most easily be understood by assuming that the lateral velocity component in the skewed wake remains $V_w \sin \phi_y$ where the axial component is decreased with the induced velocity, see e.g. [Snel and Schepers \(1994\)](#). This leads to a so-called wake skew angle (χ), which differs from the yaw angle:

$$\tan \chi = \frac{V_w \sin \phi_y}{V_w \cos \phi_y - u_i} \quad (3.18)$$

The deflection can then be used as a way to control the wake such that the downstream turbine is exposed to less wake effects by which the overall wind farm production can be increased.

The power loss due to yaw is often thought to be proportional to $\cos^3(\phi_y)$ (with ϕ_y the yaw angle). Such cubic dependency is expected from the idea that the power behaves as V_{axial}^3 and the axial velocity component is $V_w \cos(\phi_y)$. However, this would only be true if the induction is unaffected by yaw. Measurements analyzed by [Dahlberg \(2005\)](#) and [Schepers \(2001\)](#) proved this to be incorrect. This is further explained in section 8.2 where an analysis of NASA-Ames measurements shows that yaw can even lead to a power increase!

The effect of yaw on the load (variations) was until the beginning of the 1990's only modelled through the advancing and retreating blade effect in combination with stationary lift and the drag coefficients.

The advancing and retreating blade effect is explained in Figure 3.5 (top). In this figure, the definitions of yaw angle and azimuth angle are also given.

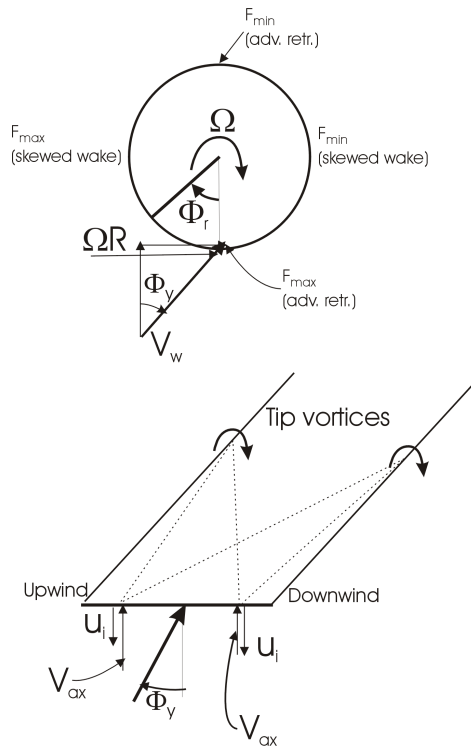


Figure 3.5: Advancing and retreating blade effect (top) and unbalance in inflow induced by the skewed wake (bottom):

For positive yaw, the blade will be retreating in the upper half plane and advancing in the lower half plane with respect to the inplane wind component (V_{\tan}). This gives a 1P variation of angle of attack and effective inflow velocity, with $\phi_{\max, \alpha}$ (i.e. the azimuth angle where the angle of attack is maximum)

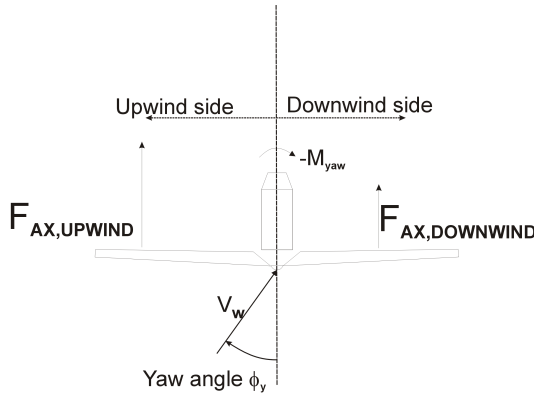


Figure 3.6: Load unbalance between upwind and downwind side of the rotorplane at yawed condition, and sign of yawing moment defined such that a negative moment is restoring

at the 12 o' clock position ($\phi_r = 180$ degrees) and $\phi_{max, V_{eff}}$ (i.e. the azimuth angle where the effective inflow velocity is maximum) at the 6 o' clock position ($\phi_r = 0$ degrees). It is found, see e.g. [Schepers \(2007b\)](#) that the effect of the effective velocity on the loading dominates the effect from the angle of attack by which the maximum loading, for positive yaw, occurs at the 6 o'clock position.

The advancing and retreating blade effect is symmetric around zero azimuth. Therefore it will, averaged over a rotor revolution, not lead to a restoring yaw moment as is measured in reality.

This problem was covered in the EU JOULE projects 'Dynamic Inflow' see [Snel and Schepers \(1994\)](#) and [Schepers and Snel \(1995\)](#). In these projects the azimuthal variation of the induced velocity at yawed conditions has been investigated. This variation is a result of the skewed wake geometry on the inflow distribution, see Figure 3.5 (bottom): The proximity to the rotor plane of the vortices in the wake strongly influences the inflow. The trailing tip vorticity is on the average closer to the downwind side of the rotor plane, which according to the Biot-Savart law results in a larger value of the axial induction velocity u_i . The higher induced velocity means a lower value of the total axial velocity for the downwind half of the rotorplane and (under the assumption of

linear aerodynamics) lower blade loads in this part. The resulting load unbalance yields a restoring yaw moment, as illustrated in figure 3.6.

The research in the Dynamic Inflow projects was followed by a Dutch National project in which the velocities in the rotor plane of a yawed rotor placed in the Open Jet Facility of TUDelft were investigated, see [Schepers \(1999\)](#). From these results and supporting calculations from more advanced models as described by [van Bussel \(1995\)](#) and [Voutsinas, Belessis & Huberson \(1993\)](#), it became clear that it is not only the tip vorticity which leads to an azimuthal variation of the induced velocity but also the root vorticity. The root vorticity then yields a destabilizing yawing moment at the inner part of the blade. At a later stage this conclusion was confirmed by [Madsen \(1999\)](#) and [Hansen, Mikkelsen and Øye \(2010\)](#) on basis of CFD calculations. A further confirmation also came from a more detailed experimental study of the flow field in the TUDelft Open Jet Facility as recently published by [Haans \(2011\)](#).

[Schepers \(1999\)](#) used the TUDelft measurements to derive a model for the overall variation of the induced velocity around its mean value. It is expressed in the following way:

$$u_i = u_{i,0}[1 - A_1 \cos(\phi_r - \psi_1) - A_2 \cos(2\phi_r - \psi_2)] \quad (3.19)$$

In this equation $u_{i,0}$ is the disk (or annulus) averaged induced velocity (see below) and the amplitudes A_1 and A_2 and the phases ψ_1 and ψ_2 have been modelled as a function of radial position and yaw angle.

It must also be noted that the two tip vortex lines in the bottom figure 3.5 are thought to be parallel and both trailed under the wake skew angle from equation 3.18.

However equation 3.18 shows that the azimuthal variation in induced velocity goes together with a variable wake deflection. The large induced velocities in the downwind side of the rotor plane lead to a stronger wake deflection. The opposite happens at the upwind side where the induced velocity is small. An experimental confirmation of this variable wake deflection has come from measurements presented in [Haans \(2011\)](#) and also from measurements taken in the Mexico project, see e.g. [Schepers, Pascal and Snel \(2010\)](#). As such the aerodynamics of a yawed rotor is complicated by the fact that the wake geometry is determined by the azimuthal variation in induced velocities where the wake geometry determines this azimuthal variation.

Further complications appear from the azimuthal variations in angle of attack and effective velocity which are a result of the azimuthal variation of induced velocity and the advancing and retreating blade effects. If these variations are fast enough, the boundary layer around the airfoil cannot follow them instantaneously. As a consequence the steady relation between the c_l (c_d) and α does not hold anymore and unsteady airfoil effects appear as explained in section 3.6.1.

The Dynamic Inflow projects showed that the importance of the 'skewed wake effect' mainly lies at relatively high tip speed ratios (i.e. low wind speeds), where the advancing and retreating blade effect becomes more important at lower tip speed ratios. Thereto it should be realized that the skewed wake effect works on the induced velocities which generally speaking are larger at a high tip speed ratio. On the other hand, a high tip speed ratio limits the advancing and retreating blade effect since the inplane component of the wind speed ($V_w \sin(\phi_y)$) is relatively small compared to the rotational component. It is furthermore noted that a high tip speed ratio generally means a small angle of attack by which the dynamic stall effects are limited

At low tip speed ratios (high wind speeds) the opposite is true: The high wind speed leads to a large value of V_{tan} and consequently to a strong advancing and retreating blade effect, where the low induction factor makes the variation in induced velocity less visible in the load distribution. The large angles of attack lead to strong dynamic stall effects.

A further uncertainty in the modelling of yawed conditions lies in the determination of the disk averaged induced velocity ($u_{i,0}$). This value is generally calculated with the model from [Glauert \(1926\)](#):

$$F_{ax} = \rho A_r |\tilde{V}_w + \tilde{u}_{i,0}| u_{i,0} \quad (3.20)$$

where V_w and $u_{i,0}$ have to be added vectorially, and next normed. Glauert applied the model on disc level but in wind turbine BEM codes the model is generally applied on annular ring level.

The Glauert model is based on the fact that (3.20) is the correct expression for a gyrocopter at fast forward flight i.e. a yaw angle of 90 degrees. The rotor disk is then seen as a circular wing on which the resultant force works as a lift, see e.g. [Bramwell \(1974\)](#).

Furthermore equation 2.9, which represents the situation for an actuator disc

at aligned condition, is a special form of equation 3.20 since it can be written as:

$$F_{ax} = \rho A_r (V_w - u_{i,0}) 2u_{i,0} \quad (3.21)$$

Hence equation 3.20 is valid for 90 degrees and 0 degrees yaw misalignment, and it is supposed to be true for in between values. However, the flow situation for an actuator disc at aligned flow and the flow situation around the circular wing is substantially different. At aligned flow the axial force acts as a drag force where it works as a lift force in the case of a helicopter at fast forward flight.

Nevertheless [Haans \(2011\)](#) finds on basis of TUDelft OJF measurements that equation 3.20 yields a reasonable result for the induced velocity in yaw, also when it is applied on annular ring level.

In section 8 some more details on the research of yaw aerodynamics is given. Amongst others it is described how the measurements in the TUDelft OJF are analyzed by [Schepers \(1999\)](#), [Sant \(2007\)](#) and [Haans \(2011\)](#). Also the full model description from equation 3.19 is given. Furthermore NREL's Phase VI (NASA-Ames) measurements are used to study the power dependency on yaw and the azimuthal variation of local aerodynamic loads. The same is done using the IEA Task 29(Mexnext) measurements. The IEA task 29(Mexnext) PIV measurements are also used to understand the flow field and the tip vortex trajectories around a wind turbine at yawed conditions.

3.9 Cone angle, tilt angle, unconventional blade shapes

The expressions in the Blade Element Momentum Theory have been derived for zero cone and tilt angle. The effects from cone angle and tilt angle (and deformations and unconventional blade shapes (e.g. aft swept)) can relatively easy be included in the blade element theory by means of geometrical corrections. In principle there is also an effect from the tilt angle in the momentum theory since a tilt angle leads to an azimuthal variation of the induced velocity, similarly to the variation of induced velocity from a yaw angle as described before. Such correction is rarely included in BEM where it should be realized that for common values of the tilt angles (< 5 degrees) the practical impact of this variation will be limited. It must be noted that the 3D flow effects which may be expected from geometric 'deviations' are not taken into account

(e.g. the undisturbed wind vector will have a component along the blade in case of cone and tilt angle).

3.10 Tower effects

Although in principle the BEM model should be seen as a rotor theory the effects from tower shadow can relatively easily be included, at least for the common situation where the rotor is placed upwind of a cylindrical (or almost cylindrical) tower.

Thereto the cylinder is represented by a dipole around which the (inviscid) velocity field is known from the following stream function:

$$\Psi = V_w(1 - a)y[1 - \frac{R_{\text{tower}}^2}{(x^2 + y^2)}] \quad (3.22)$$

Where $V_w(1 - a)$ is assumed to be the undisturbed velocity 'felt' by the tower and the origin of the x, y coordinate system lies in the tower centre.

Then the axial and tangential velocities induced by the tower ($d\Psi/dy$) and $(-d\Psi/dx)$ are added to the 'undisturbed' velocity diagram from figure 2.6.

The less common situation of a downwind rotor is much more difficult to model since the rotor passes the strongly turbulent wake behind the tower for which the above mentioned inviscid expression of the flow field around a cylinder is invalid. Also the shadow effects from a lattice tower are more difficult to determine but at the same time these effects will generally be more limited.

Tower shadow models formed the subject of the EU project ROTOW, see [Graham and Brown \(2000\)](#). It was found that generally speaking tower effects were overpredicted from a standard dipole model. Amongst other things IEA Task 14/18 measurements were used in the assessment of tower shadow models, see section 5.6.

3.11 Benchmarks, impact of uncertainties on design loads

In section 1 it is mentioned that a main aim of this thesis is to assess the progress made on the field of engineering rotor aerodynamic models in the last 25 years. Thereto the status of the aerodynamic models in wind turbine design codes in the mid 1980's should be established first. This status was assessed by [van Grol et al. \(1991\)](#) in the EU project 'Wind Turbine Benchmark Exercise on Mechanical Loads, WTBE/ML' in which most wind turbine design codes of that time participated. Many of these codes were still under development and they were mentioned to be 'first generation codes'. They all applied the BEM theory in a very basic form with only a few of the above given engineering models. Most codes applied a Prandtl tip loss correction, a turbulent wake correction and a tower shadow model based on a dipole model. A 'geometric' correction for cone and tilt angle was also included and yaw was modelled with the advancing and retreating blade effect only. It was considered very difficult to establish generalized numbers for uncertainties but roughly speaking the uncertainty in blade forces was determined to be 20% and the uncertainty in blade root flap moments and rotor shaft bending moments was determined to be in the order of 35%. It should be noted that the WTBE/ML validation was not very challenging from a 2011 point of view: The validation was only based on one turbine with a rotor diameter of 20 meter and with relatively stiff blades. A limited number of verification cases were considered. These were more or less randomly chosen and did not include many off-design cases.

Since then engineering models have been added for instationary effects on the airfoil characteristics (at attached flow and dynamic stall), dynamic inflow, rotational effects on the airfoil characteristics, tip effects on the airfoil characteristics, an induction correction at yawed conditions and a Prandtl correction at the root. Many of these models could be developed and validated on basis of detailed aerodynamic measurements.

In a more recent (though still outdated) benchmark exercise on wind turbine design codes, see [Schepers et al. \(2001\)](#), a better defined validation approach was followed. Thereto measurements of turbine(blade) loads were considered on three different turbines at conditions which were, if possible, chosen to be 'design driving'. However it was concluded that some fundamental problems appear when establishing generalized numbers for un-

certainties based on a comparison between calculated and measured turbine(blade) loads in atmospheric conditions. This is partly due the fact that a generalization of the very many comparisons between calculations and measurements was far from straightforward. Moreover many design driving load cases can in practice not be measured on commercial wind turbines. Most important is the role of the external conditions. In a validation as performed in [Schepers et al. \(2001\)](#) the wind field should inevitably be based on information from a limited number of meteorological measurements. The generated wind field from that is then undoubtedly different from the real wind field leading to an unknown uncertainty. This makes these validation calculations fundamentally different from design calculations where the external conditions are prescribed by the regulations. Last but not least a validation on basis of global turbine(blade) loads does not give a decisive answer on the accuracy of aerodynamic models due to the fact that 'compensating errors' may occur, see section 5.7.5.

Nevertheless a rough estimate for the discrepancies between calculations and measurements at design conditions was reported to be 5-20% which indicates an improvement compared to the observations from the WTBE/ML. However, the uncertainty in tower and shaft loads (not considered in the WTBE/ML) was sometimes found to be larger than 20%. The discrepancies at off-design conditions or at stalled conditions (not considered in the WTBE/ML) still turned out to be very large (50% or even more).

Finally it is important to note that the improvements in aerodynamic models from the last 25 years are largely abolished by the increased complexity of nowadays design problems. This is due to the larger blade deflections and the use of new concepts (e.g. winglets, aft swept blades etc) which are more difficult to model from an aerodynamic point of view than conventional, rigid wind turbine blades. Also the increased size of the wind turbines and the placement of turbines in a wind farm add to the complexity: The wind field which enters a large wind turbine is less coherent than the wind field which enters a small wind turbine. The 3D shear which is found in wind farm operation (section 9.3) makes the prediction of the aerodynamic response even more difficult.

Chapter 4

Field and wind tunnel measurements on rotor aerodynamics as performed in IEA Tasks

4.1 Introduction on rotor aerodynamic measurements from IEA Tasks

A large part of this thesis is devoted to analyzes of advanced aerodynamic measurements. Most (but not all) of the measurements on rotor aerodynamics were performed within four subsequent IEA Tasks: IEA Tasks 14, 18, 20 and 29. IEA Tasks 14 and 18 were carried out in the 1990's and considered field measurements. These projects were followed by IEA Tasks 20 and 29 which considered wind tunnel measurements.

The background of the first IEA Tasks (14 and 18) lied in the fact that within all experimental programs on wind turbines which were carried out until the end of the 1980's, global loads, i.e. total (blade or rotor) loads were measured only. These loads consist of an aerodynamic and a mass induced component and they are integrated over a certain spanwise length. Various projects had been performed in which wind turbine design codes were validated on basis

of such global measurements, see e.g. the European 'Benchmark exercise' as described in [van Grol et al. \(1991\)](#). In the late 1980's and in the beginning of the 90's it was realized that such global measurements do show differences between calculations and measurements but they donot explain the cause for these discrepancies. This is only possible from more direct measurements of detailed aerodynamic properties along the blade. For this reason several institutes initiated experimental programs in which the pressure distributions at different radial positions were measured on full scale turbines in the free atmosphere. These pressure distributions are integrated to sectional forces, i.e. the normal and tangential forces (denoted by 'n' and 't' respectively) where the normal and tangential direction refer to the orientation of the chord. As such the normal and tangential forces differ from the lift and drag through the angle of attack. In the period from 1992 to 2001 these institutes cooperated within IEA Task 14 and its follow up project IEA Task 18, see [Schepers et al. \(1997\)](#) and [Schepers et al. \(2002a\)](#). The main aim of these IEA tasks was to exchange information and experiences on these, at that time, new innovative and specialized measurement techniques

Furthermore a common IEA Task 14/18 database of aerodynamic measurements has been created. The fact that the measurements were taken on a large number of facilities gave the resulting insights and models more general validity than those obtained from the experimental programs independently.

One of the conclusions from IEA Task 14 and 18 was that the free stream environment in which the measurements were taken led to a large uncertainty in the interpretation of many results (as is the case in all field measurements) This was due to the instationary, inhomogeneous and uncontrolled wind conditions. The free stream conditions were usually measured with a mast some distance away from the turbine (not necessarily upstream of the turbine). This mast was instrumented with only a few anemometers. In the best case this yields a reasonable estimate for the mean wind conditions at the rotor plane but it anyhow does not provide the instantaneous inflow conditions at every position in the rotor plane which is needed to study high frequency, local, effects e.g. dynamic stall. Therefore the inflow angles and velocities were sometimes measured ahead of of the airfoil with a five hole pitot probe or a wind vane but these devices too donot yield the exact instantaneous velocity with a sufficient spatial resolution.

This problem was overcome in NREL's Phase VI (NASA-Ames) experiment which was carried out in 2000, see [Hand et al. \(2001\)](#). In this experiment

a heavily instrumented rotor with a diameter of 10 meter was placed in the world's largest wind tunnel, i.e. the NASA-Ames ($24.4 \times 36.6 \text{ m}^2$) facility. As such measurements could be performed at stationary, known and homogeneous conditions which enormously facilitated the interpretation of measurement results. The huge size of the wind tunnel allowed a rotor diameter of 10 m, with little blockage effects.

The instrumentation of this turbine was largely similar to the instrumentation of the turbine which NREL used in IEA Tasks 14/18. Amongst other things measurements have been taken of the pressure distributions at 5 radial positions from which the resulting normal and tangential forces were derived.

NREL made the measurements from this experiment available to other institutes and they were analyzed within IEA Wind Task 20, IEA Task 20 started in 2003 and ended in december 2007, see [Schreck \(2008\)](#).

The measurements from IEA Tasks 14/18 and 20 were mainly focussed on blade aerodynamics and they hardly delivered information on induction aerodynamics. This problem was overcome with the measurement taken within the EU project Mexico. These experiments concern pressure and load measurements on a wind turbine model with a diameter of 4.5 m, which was placed in the largest European wind tunnel, the Large Low Speed Facility (LLF) facility of the German Dutch Wind Tunnel, DNW with a size of $9.5 \times 9.5 \text{ m}^2$. However, in addition to these pressure and load measurements, detailed flow field data were taken with the Particle Image Velocimetry (PIV) technique. As such a comparison can be made between calculated and measured loads where the underlying flow field which drives these loads can also be assessed.

The Mexico project was completed in 2007, see [Schepers and Snel \(2007\)](#). Thereafter its results were analyzed in IEA Task 29 'Mexnext' which ended in 2011, see [Schepers, Boorsma et al. \(2011\)](#).

In the sequel of this chapter more information is given on the IEA tasks and the experimental facilities.

4.2 Measurement uncertainties

An important item within the different IEA Tasks was the assessment of measurement uncertainties. An example of an uncertainty analysis is given in

[Schepers, Boorsma et al. \(2011\)](#) for the Mexico experiment, where results have been checked by visual inspection, consistency, reproducibility etc. In this respect it is important to know that within all experiments frequent calibrations were carried out (in the Mexico experiment the Kulite transducers required zero-calibrations only, in the other experiments both gain and offset were calibrated). Generally speaking the uncertainties introduced by the measurement equipment itself (in particular the pressure sensors) were found to be limited. An exception is formed by the measurements at standstill where the low pressure levels are within the lower part of the measurement range leading to a poor accuracy. Moreover some of the pressure measurements at the inner stations (25% and 35% span) of the Mexico experiment showed irregularities [Schepers, Boorsma et al. \(2011\)](#). Therefore the runs as analyzed in IEA Task 29 were as much as possible selected on smooth, 'regular' pressure distributions. Generally speaking the effect from these irregularities on the local aerodynamic forces were estimated to be small.

Most of the results presented in this thesis are averaged over a number of samples. In some cases the standard error (defined as the standard deviation of the mean values divided by the square of the number of samples) is plotted around the mean. However it turned out that, generally speaking, the standard error for the wind tunnel measurements was limited (in the order of the symbol size!), although this is less true in stalled conditions.

However this doesn't imply that the results as supplied within the different IEA tasks should be considered as the 'truth'. In the wind tunnel experiments an uncertainty is introduced from tunnel effects. Also the processing of data may introduce uncertainties, e.g. errors can be made in the integration of pressure distributions into normal and tangential forces. The use of processed data like angle of attack and dimensionless airfoil characteristics require careful interpretation as will be explained in the sections 5.2 and section 5.3.

In the sequel several discussions take place on consistency and compatibility checks see e.g. the sections 4.5, 5.4, 5.5, 6.3.1, 6.3.4. These checks form, at least to some extent, an indication for the measurement uncertainty.

4.3 IEA Task 14 and 18: Field Rotor Aerodynamics: Description of projects, experimental set-up and measurements

As explained in section 4.1, the IEA Tasks 14/18 established a cooperation between various institutes which carried out aerodynamic field measurement programs. This cooperation resulted in a common database of aerodynamic measurements from the facilities of the different participants. The projects started in 1992 and ended in 2001 and the following organisations participated:

- Energy Research Center of the Netherlands, ECN, The Netherlands (Operating Agent, i.e. coordinator of the project).
- Delft University of Technology, TUDelft, The Netherlands
- Imperial College, IC and Rutherford Appleton Laboratory, RAL, United Kingdom:
- National Renewable Energy Laboratory, NREL, USA:
- Mie University, Japan:
- RISØ National Laboratory, Denmark

Note that the the Center for Renewable Energy Systems, CRES from Greece was also participating in IEA Task 18, but they did not provide any data.

The 'common denominator' in (almost) all of these programs was that, apart from the measurement of 'conventional' rotor(blade) loads, the pressure distributions and the resulting aerodynamic segment forces were measured along the rotor blades. This was established by drilling pressure holes into the blade surface along the chord. The diameter of these pressure holes was generally in the order of 1 mm. The number of pressure holes per section varied between 25 and 50, where the highest concentration of holes was applied near the leading edge, since this is the area with the strongest pressure gradients. The pressure holes were connected by means of tubes to (one or more) electronic pressure scanners inside the blade. Special attention had to be paid to the tube length and diameter to minimize the distortion on the frequency response from these tubes to a fluctuating pressure signals, see e.g. [Spath and Stefanatos \(1995\)](#). The pressure scanners could incorporate a number of pressure ports (say 10-30) which were scanned very rapidly

(>10 kHz). In this way the entire pressure distribution around an airfoil could be measured almost instantaneously. From these pressure distributions the resulting normal and tangential forces have been determined by integrating the pressure forces along and perpendicular to the chord.

It is important to realize that all of the pressure scanners measured differential pressures relative to a reference pressure. This reference port was generally connected to the hub of the rotor where the pressure was assumed to be close to the (known) atmospheric pressure. It nevertheless implied an uncertainty in the precise absolute level of the pressures.

Apart from pressure distributions around the airfoil most facilities also measured the inflow angle and inflow velocity, often by means of a 5 hole pitot probe which was placed ahead of the airfoil's leading edge.

In Appendix A the facilities from the participants and their instrumentation are described in some detail. In summary the experiments and facilities of the various participants can be characterized by mentioning the following differences and resemblances:

- The diameter of the facilities in the project ranged between 10 m (NREL, TUD, Mie) and 27 m (ECN) where the Reynolds number at the 70% radius section varied roughly between $0.5 \cdot 10^6$ to $1.8 \cdot 10^6$.
- The number of blade was two (TUDelft, ECN) or three (NREL, RISØ, IC/RAL, Mie).
- The blades of four facilities (ECN, RISØ, IC/RAL, Mie) were twisted and tapered. The blades of two facilities (TUDelft, NREL) were untwisted and untapered. In addition, NREL supplied measurements on a blade which is twisted only. The NREL measurements on the untwisted untapered blade are denoted as Phase II, where the twisted untapered measurements are denoted as Phase III or Phase IV.
- The following aerodynamic airfoils were applied on the various turbines:
 - NACA 44xx (ECN)
 - NACA 632xx (RISØ and IC/RAL)
 - NLF 0416 (TUDelft)
 - NREL S809 (NREL)

– DU91-W2-250 and DU93-W-210 (Mie)

For all of these airfoils, 2D steady $c_l - \alpha$ and $c_d - \alpha$ characteristics are available, either from literature or from own experiments. For the NREL and DU airfoils pressure distributions are measured in a 2D environment too. The 2D pressure distributions from the NLF airfoils were measured by placing the entire instrumented TUDelft rotor blade into a wind tunnel. The untwisted, untapered blade shape then enables the measurement of a 2D pressure distribution which can straightforwardly be related to the rotating results, without uncertainties from airfoil deviations, different pressure tap locations etc.

- Most participants measured the pressure distribution around the profiles from which the aerodynamic forces are derived. RISØ measured the aerodynamic forces directly by means of balances, which includes the measurement of the skin friction.
- All participants have instrumented at least three radial stations, i.e. a root station (around 30% span), a mid station (around 60% span) and a tip station (around 80% span). TUDelft and Mie have instrumented 4 stations. NREL has instrumented 4 (Phase II) or 5 (Phase III) stations. IC/RAL has instrumented 6 stations. At most facilities the different radial stations were measured simultaneously. At the IC/RAL turbine two stations were measured simultaneously, at the TUDelft and Mie turbine every station was measured separately.
- The number of pressure taps per station was 25 for IC/RAL, 32 for NREL, 47 for ECN, 60 for Mie and 59 for TUDelft
- The IC/RAL, NREL and RISØ measurements were all made at the same rotor speed and the same pitch angle. The angle of attack was set by means of the wind speed. In the TUDelft experiments the angle of attack was usually set by means of the rotor speed (and the wind speed). In Mie's experiments, the angle of attack was usually set by means of the pitch angle (and the wind speed). In ECN's experiments, the angle of attack was set in various ways; by means of the wind speed, the rotor speed or the pitch angle.
- The measurement of the ambient free stream conditions was done in the following way:
 - NREL applied a vertical plane array, heavily instrumented with many anemometers in Phase II. This array was placed $\approx 1D$ upstream in

the dominant wind direction. In the Phase III and IV experiments the inflow was measured in a slightly less extensive way. Nevertheless there were still three masts available with anemometers at different heights. These were placed $\approx 1D$ upstream in the dominant wind direction;

- Mie University also measured the inflow through three masts with anemometers at different heights. They were placed $\approx 1D$ upstream in the dominant wind direction;
- TUDelft measured the inflow conditions at hub height with a mobile mast which was placed $1D$ upstream;
- ECN measured the inflow conditions at three heights with a meteorological mast, which was located $\approx 2D$ from the turbine.
- RISØ measured the wind speed at hub height with a mast which was placed $\approx 2D$ from the turbine;
- IC/RAL measured the inflow conditions from two meteorological masts, which were placed at different locations, $2D$ from the turbine;

The participants of IEA Task 14/18 agreed on a joint measurement program with which rotating measurements were supplied for:

- Mean yaw angle \approx zero. This yields a more or less constant angle of attack.
- Mean yaw angle \neq zero; In these campaigns the angle of attack variations are deliberately triggered.

Thereto the test matrix from table 4.1 served as a guideline for measurement campaigns (time series) to be supplied in the database. Generally the time series had a length of 30-60 seconds. However, RISØ measured the aerodynamic forces directly by means of balances, which reduced the amount of data considerably. Therefore RISØ could supply time series with a length of 10 minutes. Moreover some parties supplied measurements for non-rotating conditions.

Apart from times series, measurements of airfoil coefficients (2D values as well as rotating values) as function of angle of attack were also added to the database. However, it should be realized that these rotating airfoil characteristics suffer from an uncertainty in the angle of attack and dynamic pressure as explained in section 5.2 and 5.3

	Re *) (-)	α_{mean} (°)	yaw angle (°)
ECN	$1.8 \cdot 10^6$	-5 to + 40	± 30 à 40
TU Delft	$0.9 \cdot 10^6$	-5 to + 40	± 30 à 40
NREL	$0.7 \cdot 10^6$	-5 to + 40	± 30 à 40
IC/RAL	$1.0 \cdot 10^6$	-5 to + 40	
RISØ	$1.0 \cdot 10^6$	-5 to + 40	± 30 à 40
Mie	$0.5 \cdot 10^6$	-5 to + 40	± 30 à 40

*) Reynolds number at rotating conditions at 70% R;

Table 4.1: Test matrix from IEA Task 14.18 measurement. Numbers are indicative only

The database is freely available from the internet under the condition that user give feedback about the experiences with the database to the IEA Task 14/18 participants. On basis of these experiences it has been possible to improve the quality of the database.

4.4 IEA Task 20: NREL's Phase VI (NASA-Ames) measurements: Description of project, experimental set-up and measurements

The main aim of IEA Task 20 was to analyse the so-called Phase VI measurements as performed by NREL on a wind turbine placed in the large NASA-Ames wind tunnel. The measurements were carried out in the year 2000. A large number of measurements were stored into a database and made accessible to the IEA task 20 participants.

The project was coordinated by NREL. The following institutes participated:

- National Renewable Energy Laboratory, NREL, USA (Operating Agent)
- École de technologie supérieure, Montréal, Canada
- RISØ-DTU, Denmark
- Center for Renewable Energy Systems, CRES and National Technical University of Athens, NTUA, Greece

- Energy Research Center of the Netherlands, ECN and Delft University of Technology, TUDelft the Netherlands
- Institute for Energy Technology, IFE, Norway
- National Renewable Energy Center, CENER, Spain
- University of Gotland, HGO, Sweden

A detailed description of the experimental set-up and the available measurements is given by [Hand et al. \(2001\)](#). A picture of the wind turbine placed in the NASA-Ames wind tunnel test section is shown in Figure 4.1. The tunnel is open loop with a closed test section of 24.4x36.6 m. The tunnel speed is variable between almost zero and 50 m/s, where the minimum speed for the present measurements was 5 m/s and the maximum speed was 25 m/s. As noted in [van Rooij \(2005\)](#) the turbulence levels decrease with tunnel speed. At a tunnel speed of 5 m/s the turbulence intensity is in the order of 2.5 % and it decreases to 0.2% at a tunnel speed of 24 m/s. The characteristics of the



Figure 4.1: NREL Phase VI turbine in NASA Ames wind tunnel

turbine and the instrumentation is largely based on the characteristics and instrumentation of the Phase II/III and IV turbines used in IEA Tasks 14/18.:

- The rotor diameter is 10 m. This implies that 9% of the test section area is covered by the rotor swept area. This is below the 10% which is commonly considered to be acceptable for closed wind tunnel test sections. In [Hand et al. \(2001\)](#) it is noted that the maximum blockage

can be in the order of 2% but for the majority of the cases, the blockage is less than 1%;

- Opposite to the NREL Phase II/III/IV turbines as employed in IEA Tasks 14/18, the NREL Phase VI turbine is 2-bladed (with blade numbers given as number 1 and 3).
- Opposite to the blades used in the Phase II/III/IV experiments, the blades of the present experiment have a linear taper with a maximum chord of 0.737 m at 25% span and 0.356m at 100% span. As pointed out by [Lindenburg \(2003\)](#) this results in a relatively low aspect ratio and high solidity compared to modern (2 bladed) wind turbines.
- The blades have a non-linear twist of 22.5 degrees over the blade.
- The airfoil is the S809 profile over the entire span.
- The turbine has an asynchronous generator with a rated rotor speed of 72 rpm. This results, roughly speaking, in a blade Reynolds number in the order of 1 Million.

One of the blades (blade number 3) was heavily instrumented at 5 radial positions with 22 pressure taps each connected by means of tubes to pressure scanners, similar to the instrumentation of the NREL Phase II to IV experiments as described in Appendix A. The measurement sections (relative to the rotor centre) are located at 30%, 47%, 63%, 80% and 95% span, i.e. at $r = 1.510$ m, 2.343 m, 3.185 m 4.023 m and 4.780 m. The resulting pressure distributions are integrated to normal forces and tangential forces.

In addition the inflow velocities and inflow angles are measured from five hole probes. These probes were placed 4% outboard of the pressure taps, i.e. at $r = 1.710$ m, 2.5653m, 3.370 m and 4.225 m and 4% inboard of the outer station, i.e. at $r = 4.5773$ m. Moreover measurements of blade and rotor loads were taken.

NREL performed measurements at very different conditions and very different configurations (unyawed/yawed conditions, upwind/downwind rotor, teetered/fixed hub, with/without transition strips). Most of the analyzes in IEA Task 20 were focussed on measurements for the upwind rotor with fixed hub and without transition strips. The tunnel speed generally ranged between 5 and 25 m/s and pitch angles between 0 and 6 degrees were considered. The rotor speed of 72 rpm yields relatively low tip speed ratios and axial induction factors. Results from the PHATAS code, presented in [Schepers \(2007a\)](#),

show that substantial induction factors (0.33 or higher) are only found at a tunnel speed of 5 m/s and a pitch angle of zero degrees. At a tunnel speed of 10 m/s the axial induction factors are between 0.1 and 0.15 and at 15 m/s the induction factors are smaller than 0.1. Moreover the calculated angles of attack already exceed the (2D) stall angle of attack over a large part of the blade at a tunnel speed of 10 m/s.

The length of the measurement campaigns was generally 30 seconds.

4.5 IEA Task 29 (Mexico) measurements: Description of project and experimental set-up

In IEA Task 29(Mexnext) measurements are analyzed which have been taken in the European Union project 'Mexico' (Model Rotor Experiments In Controlled Conditions, see [Schepers and Snel \(2007\)](#)). In the Mexico project 10 institutes from 6 countries cooperated in doing experiments on an instrumented, 3 bladed wind turbine of 4.5 m diameter placed in the Large Low-speed Facility (LLF) of DNW in the Netherlands. The measurements were performed in December 2006 and resulted in a database of combined blade pressure distributions, loads and flow field measurements. Although the Mexico project can to some extent be seen as the successor of the NREL Phase VI (NASA-Ames) experiment from section 4.4 it was designed to be complementary. An obvious difference between the two experiments lies in the larger size of the NASA-Ames experiment but on the other hand the NASA-Ames experiment only contained rotor measurements where the Mexico experiment also included extensive flow field measurements using the stereo PIV technique. As a matter of fact, to the author's knowledge, the Mexico experiment is the only experiment which combines pressure/load measurements AND flow field measurements. Furthermore the Mexico model is three bladed, whereas the NREL model is two bladed. Finally, the majority of the NREL measurements concern stalled flow, while the entire operational envelope is covered in the Mexico measurements.

A thorough analysis of the Mexico data has been performed within IEA Wind Task 29 'Mexnext'. In this project 20 parties from 10 different countries participated:

- Energy Research Center of the Netherlands, ECN, the Netherlands (Operating Agent)

- École de technologie supérieur, Montréal, ETS and University of Victoria, UVic, Canada
- RISØ-DTU and the Technical University of Denmark DTU-MEK, Denmark
- University of Stuttgart, Ustutt, University of Applied Sciences at Kiel and ForWind, Germany
- Technion, Israel
- Mie University/National Institute of Advanced Industrial Science, Japan
- Korea Institute of Energy Research KIER, and Korea Aerospace Research Institute, KARI, Korea
- Delft University of Technology, TUDelft Suzlon Blade Technology, SBT and University of Twente, UTwente, Netherlands
- Institute for Energy Technology/Norwegian University of Science and Technology, IFE/NUST, Norway
- National Renewable Energy Center, CENER and National Institute for Aerospace Technology, INTA, Spain
- Royal Institute of Technology/University of Gotland, KTH/HGO, Sweden
- National Renewable Energy Laboratory, NREL, USA

The LLF facility of DNW is shown in figure 4.2 where the setup of the Mexico experiment is given in figure 4.3. The turbine is placed in an $9.5 \times 9.5 \text{ m}^2$ open jet configuration with a measurement section of 20 meter length. The rotor plane of the turbine is located 7 meter downstream of the nozzle and 13 meter upstream of the collector. Pressure distributions on the blades were obtained from 148 Kulite pressure sensors, distributed over 5 sections at 25, 35, 60, 82 and 92% radial position respectively. In view of conflicting requirements between structural needs on one hand, and the required space for the data acquisition units in the model blade on the other hand, it was not possible to mount all pressure sensors into 1 blade. For this reason they were divided over all three blades (where blade 1 has the instrumented sections at 25% and 35% span, blade 2 is instrumented at 60% span and blade 3 is instrumented at 82 and 95% span). The number of sensors per section ranged between 25 to 28. A limited number of pressure sensors were mounted at similar locations at the other blades to check the reproducibility of the pressure measurements on the different blades. An illustrative result for such

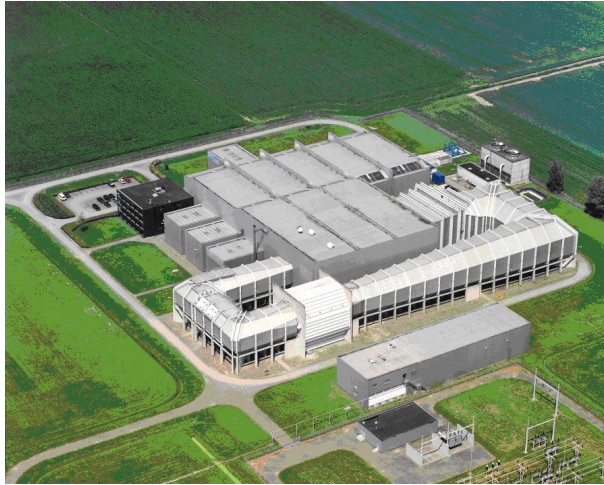


Figure 4.2: LLF (Large Scale Low Speed Facility) of DNW (German Dutch Wind Tunnel) (Picture from <http://www.twanetwerk.nl>)

check is shown in figure 4.4. Generally speaking the level of disagreement between the results of the different blades turns out to be small. The cause of the slight disagreement could be either a geometrical offset (slightly different position of the sensor) or a signal offset from the sensors.

It is noted that opposite to the instrumentation of the IEA Task 14/18 facilities and NREL's Phase VI (NASA-Ames) experiment the pressure transducers in the Mexico experiment measured absolute instead of relative pressures. This eliminates an uncertainty from the unknown reference pressure which will be described in section 5.3.

Apart from the pressure measurements, blade loads were monitored at each blade root and tower loads were measured with the external six component balance i.e. the blue structure beneath the model in figure 4.3. This balance, amongst other things, measured the forces and moments in rotor shaft direction. Even though these loads are measured at the tower foot they were meant to be an indication for the rotor shaft torque and rotor axial force (this is explained further in sections 5.4 and 5.5). Pressures and blade loads were sampled at 5.5 kHz where the tower loads were supplied as static values. The measurement period of a datapoint was 5 seconds (i.e. 35 revolutions for a

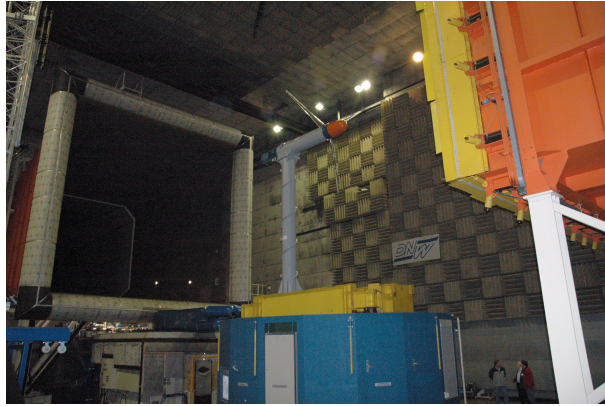


Figure 4.3: Setup of Mexico turbine in the measurement section of the DNW LLF

rotor speed of 7 Hz).

The rotor blades were twisted (over 16 degrees) and tapered (with a maximum chord of 24 cm). Three different aerodynamic profiles (DU91-W2-250, RISØ-A1-21 and NACA 64-418) were used in the design. The DU91-W2-250 airfoil was applied from 20 to 45.6% span, the RISØ-A1-21 airfoil from 54.4% to 65.6% span and the NACA 64-418 airfoil outboard of 74.4% span. Hence a constant airfoil is applied over a considerable radial extension around the instrumented sections in order to assure known conditions at each of these sections, where the remaining length is used for the transition from one airfoil to another. The rotational speed was either 424.5 rpm or 324.5 rpm, leading to a tip speed of 100 m/s and 76 m/s respectively.

At 424.5 rpm a chord based Reynolds number of approximately 0.8 Million was reached without entering into noticeable compressible conditions; the blades were tripped to avoid possible laminar separation phenomena. Pressure and load measurements were done at different tunnel speeds ranging from 10 m/s to 30 m/s, yielding tip speed ratios between 3.3 and 10. Note that the design tip speed ratio is 6.67, which corresponds to $V_{\text{tun}} = 15 \text{ m/s}$ at 424.5 rpm. Different yaw angles and pitch angles were covered, including the design pitch angle of -2.3 degrees.

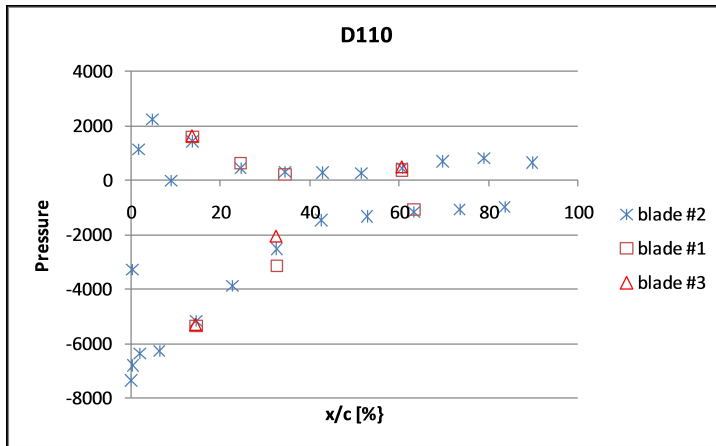


Figure 4.4: Mexico: Pressure distribution at 60% span measured on blade 2 compared with a limited number of corresponding pressure data on blades 1 and 3

Flow field mapping of all three velocity components was done by DNW by means of stereo PIV. These flow field measurements were combined with measurements of the pressures and the blade root moments. The PIV measurements were performed in the following way:

- Two cameras are mounted on a traversing tower. They focus on a PIV sheet with a size of 337*394 mm². The PIV sheet is located horizontally in the symmetry plane of the rotor at the '9 o' clock' position, see figure 4.5. The PIV tower is moveable in the horizontal streamwise (x) and radial (y) direction;
- The flow field is 'seeded' with small bubbles which are brought into the settling chamber, upstream of the rotor;
- The seeded PIV sheet is illuminated with a laser flash, and two digital photographs are taken with a short delay of approximately 200 micro-seconds;
- Then the actual seeding of the second photo is compared with the expected seeding for different velocity vector fields using the seeding of the first photo as a basis. The actual velocity vector field is the one which gives the maximum cross correlation between the expected and

the real seeding field. Thereto the PIV sheets are subdivided into small interrogation windows (with a size of $4.3 \times 4.3 \text{ mm}^2$).

The PIV samples were taken rotor-phase locked with a frequency of 2.4 Hz. Each PIV data point consists of 30-100 samples. Although all individual samples are stored, it is mainly averaged results which are investigated within Mexnext.

The PIV flow field measurements are only done at a rotational speed of 424.5 rpm at both non-yawed and yawed flow at different tunnel speeds. Basically three types of PIV measurements were carried out:

- Radial traverses from 52 to 122% span with PIV sheets just upstream and just downstream of the rotor plane (and a small overlap in the rotor plane), see figure 4.6. The radial traverses were done at 6 positions of blade 1 (denoted with ϕ_r) using a 20 degrees interval, see figure 4.7. In this way the non-uniformity of the flow field is measured. It is important to note that the definition of azimuth angle in the Mexico experiment assumed zero azimuth for blade 1 at the '12 o' clock' position. In chapter 8 the Mexico measurements at yawed conditions have been transformed to a zero azimuth angle at 6 o'clock in order to comply with the definitions used in other experiments.
- Axial traverses from $x = -4.5 \text{ m}$ to $x = 5.9 \text{ m}$ (i.e. from 1.D upstream of the rotor to 1.31 D downstream of the rotor), see figure 4.8. The azimuthal position of blade 1 was 0 degrees, i.e. blade 1 was pointing vertical upwards in the '12 o' clock position';
- Tip vortex tracking experiments in which the position of the tip vortex is searched by 'trial and error'. The position of blade 3 was 270 degrees, i.e. the '9 o' clock position'.

More detailed information on the measurement procedure can be found in [Schepers and Snel \(2007\)](#).

4.5.1 Mexico: Tunnel effects

The Mexico model is placed in the open test section of DNW-LLF with a nozzle and collector where the collector has a closed connection with the nozzle. The distance between collector and nozzle is 20 m. It is well known that tunnel effects in such open configuration will be less severe than those in a closed tunnel section, see [Barlow, Rae and Pope \(1999\)](#). As a consequence, the solid blockage by the model can be estimated to be less than a percent, see

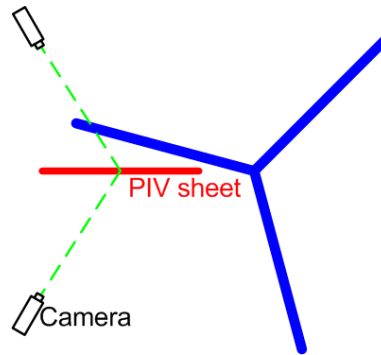


Figure 4.5: Mexico: PIV sheet with cameras

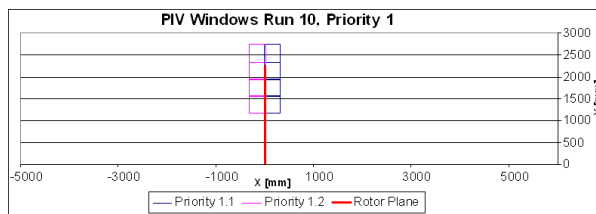


Figure 4.6: Mexico: PIV measurement sheets at radial traverses as seen from above

[Ewald \(1998\)](#). The axial distance between model location and the nozzle amounts to 7 m which is regarded as a safe margin to prevent nozzle blockage (model interference with the static and dynamic pressure sensors located in the nozzle which determine freestream tunnel velocity).

The exact tunnel effects are difficult to quantify due to the free shear layer between the tunnel flow and the outer flow. The presence of the collector which captures the wind turbine wake flow and which is closed with the nozzle adds to the complexity. As such standard tunnel correction methods cannot be applied. It must be noted that the DNW-LLF rarely employs the $9.5 \times 9.5 \text{ m}^2$ nozzle. The collector size approximately has the same cross-sectional area, which does not allow for much expansion of the free jet emerging from the nozzle.

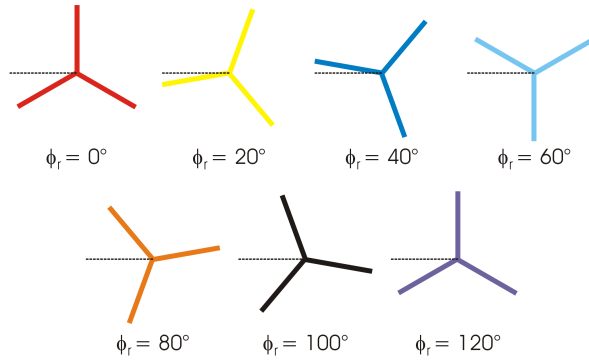


Figure 4.7: Mexico: Position of blade 1 at $\phi_r = 0, 20, 40, 60, 80, 100, 120$ deg

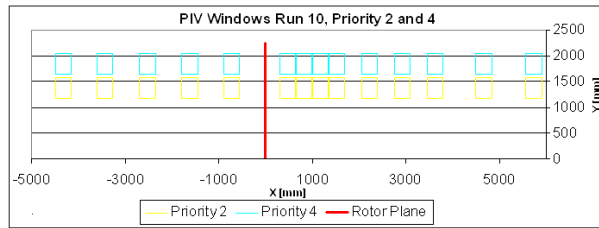


Figure 4.8: Mexico: PIV measurement sheets at radial traverses as seen from above

Within the Mexico project the wind tunnel effects were first studied with a qualitative flow model from [Snel \(2002\)](#) based on 1D axial momentum theory. The model is largely similar to the classical axial momentum theory but the flow from the nozzle to the collector has been divided into two stream tubes: An inner stream tube containing the flow passing through the rotor and an outer stream tube which contains the remaining flow, see also figure 4.9.

In a closed system between collector and nozzle, mass is conserved meaning that the lower velocity in the wake should be compensated with a higher velocity in the flow outside the wake. This also accelerates the wake flow. As a result of these phenomena, the collector inlet pressure is smaller than the nozzle outlet pressure. The simple model showed that, compared to the unbounded situation, the wind tunnel situation yields a higher axial force on the turbine at the same velocities in the rotor plane (i.e. at the same axial induced

velocity). Vice versa, a similar axial force coefficient gives a higher rotor velocity (i.e. a lower axial induced velocity) in a wind tunnel situation. The severeness of the tunnel effects obviously increases with axial force coefficient.

In a later stage detailed CFD analyses were carried out within the Mexico project, see [Voutsinas et al. \(2003\)](#). They confirmed the results from the simple model, i.e. they showed tunnel effects in the form of a higher velocity in the rotor plane for the same axial force on the rotor (or alternatively: a higher axial force on the rotor at the same induction). Nevertheless in quantitative terms, the disturbance from the tunnel on the flow in the rotor plane was generally speaking limited. This is exemplified in figure 4.10 from [Shen et al. \(2010\)](#). The figure shows the axial force coefficient with and without tunnel calculated with CFD. Maximum differences in axial force coefficient remain limited to approximately 5%.

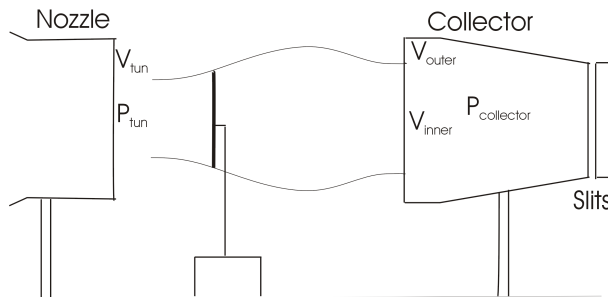


Figure 4.9: Mexico: Tunnel configuration

All of these investigations assumed a fully closed connection between collector and nozzle. The real wind tunnel has slits with a width of 250 mm at the end of the collector see figure 4.9. These slits reduce the tunnel effects since the suction in the collector generates a mass flow from the outer flow field through this opening into the collector. This mass flow was found to be significant in measurements which were carried out in a scaled down version of the LLF tunnel, see [Rozendal \(2003\)](#).

Within the Mexnext project [Rethoré et al. \(2011a\)](#) (see also [Rethoré et al. \(2011b\)](#)) performed CFD calculations using a tunnel geometry including slits. The investigation confirmed a reduction of the tunnel effects from slits. The

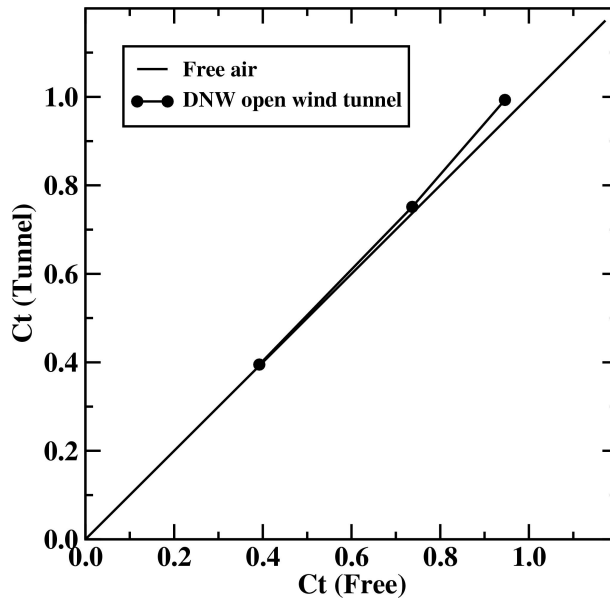


Figure 4.10: Axial force coefficient from [Shen et al. \(2010\)](#) with and without tunnel

practical importance of this reduction was limited since the tunnel effects without slits were already found to be small. However, simulations with a DES approach showed that there could be an oscillation of the wind tunnel jet interface that might create a significant oscillation of the wake. No indications for this effect have been observed in the Mexico measurements.

It is noted that all studies on wind tunnel effects within the Mexico and Mexnext project were still based on an estimate of the tunnel geometry since the exact geometry was supplied at the end of the Mexnext project only. Hence, although most studies on tunnel effects which have been performed until now indicate little disturbance, further CFD calculations are still to be performed. These need to be based on the exact tunnel geometry, where they should consider more conditions (e.g. yaw).

Chapter 5

Progress in blade aerodynamics using the aerodynamic field and wind tunnel measurements from IEA tasks

5.1 Introduction on blade aerodynamics

In this chapter several studies related to blade aerodynamics are presented. Most of these results have been obtained from the detailed aerodynamic measurements as carried out in IEA Tasks 14/18, IEA Task 20 and IEA Task 29. Before starting these discussions in some detail the sections 5.2 and 5.3 address two important problems which are related to the analysis of wind turbine aerodynamic measurements, i.e. the determination and definition of the angle of attack and dynamic pressure.

Next in section 5.4 the correlation between the local aerodynamic loads and the overall blade and rotor loads is established by integrating the measured segment loads along the blades. The integrated loads are then compared with the directly measured rotor loads. This comparison serves as a consist-

ency, i.e. quality, check on the measurements. It furthermore relates the local segment loads to overall rotor(blade) loads which are quantities of direct importance for designers

One of the main subjects in the analyzes carried out on the IEA Task measurements was the modelling of 3D stall effects. It is then somewhat surprising to find from section 3.7 that, despite the fact that these models describe a 3D **rotational** correction, they are usually considered to be independent of the rotational speed. For this reason the sensitivity of aerodynamic coefficients on the rotational speed has been investigated by means of Mexico measurements complemented with measurements from the Korean Aerospace Laboratory KARI. This study is described in section 5.5.

Next section 5.6 discusses an inventory of analyzes as performed by various parties on the IEA Tasks 14/18 field measurements. This inventory was made at the start of the the so-called Annexlyse project in 2003. Annexlyse was a Dutch national project, carried out by ECN and TUDelft. Its objective was a further analysis of the aerodynamic field measurements from IEA Tasks 14/18. The inventory showed that one of the main problems in the analysis of IEA Task 14/18 measurements lies in the fact that the data were commonly assessed on basis of non-dimensional airfoil characteristics (i.e. c_n , c_t , c_l and c_d) as function of the angle of attack α .¹ The determination of these measured characteristics was far from straightforward due to the above mentioned uncertainty in angle of attack and dynamic pressure. To avoid these uncertainties, the Annexlyse project also applied aerodynamic data from the IEA Task 14/18 database in a different way. Thereto ECN's aero-elastic code PHATAS was used to simulate time series from the database. Then the calculated and measured, time averaged, dimensional, aerodynamic segment loads are compared. Moreover, the comparison on aerodynamic segment loads is related to the comparison on the overall blade and rotor loads (flat-wise moments, rotorshaft torque and axial force). The main advantage of the comparisons performed in this way lies in the fact that the dimensional forces are not obscured by the uncertainties in dynamic pressure nor angle of attack, which do effect the comparison on dimensionless characteristics, where furthermore the local aerodynamic effects are directly related to design loads. This comparison is presented in section 5.7.1.

¹ c_n and c_t denote the normal and tangential force coefficients where the normal force is oriented perpendicular to the chord and the tangential force is oriented along the chord. These forces make an angle α with the lift and drag forces.

In section 5.7.2 the same is done for the IEA Task 20 wind tunnel measurements on NREL's Phase VI (NASA-Ames) experiment where the wind tunnel environment obviously facilitated the comparison because the calculations could be performed under constant conditions without the need for averaging the stochastic atmospheric effects. In this comparison results from ECN's free wake code AWSM code are also included.

The comparison between calculated and measured loads from the Mexico experiment is shown in section 5.7.3. This comparison does not only include results from ECN codes but also results from other participants.

The comparisons using these detailed aerodynamic measurements gave good insight into the most important sources of discrepancies and they formed the basis for model improvements in particular for the modelling of 3D stall effects, (not only on the lift but also on the drag) and for the modelling of tip effects. These model improvements are described in the sections 5.7.4. The results from the updated models are given in section 5.7.5.

It is noted that the present chapter largely builds upon results presented in [Schepers, van Rooij and Bruining, \(2003\)](#), [van Rooij et al. \(2003\)](#), [Schepers et al. \(2004a\)](#), [Schepers et al. \(2004b\)](#), [Schepers and van Rooij \(2005\)](#), [Schepers \(2007a\)](#), and [Schepers, Boorsma et al. \(2011\)](#).

5.2 Angle of attack in wind turbine experiments

The angle of attack is a crucial quantity in most aerodynamic models for 3D rotating wind turbines. It should be realised however that its definition is based on the definition of the angle of attack in a 2D wind tunnel situation and that such definition becomes hypothetical in a 3D rotating environment. Hence the resulting angle of attack is not a physical quantity and it cannot be measured straightforwardly.

In the 2D wind tunnel environment, the angle of attack is defined as the angle between the chord and the undisturbed wind vector which is aligned with the wind tunnel walls. Now suppose (Figure 5.1) that it is attempted to measure the angle of attack with a measuring device (i.e. a 5 hole pitot probe, wind-vane etc.) which is placed ahead of the airfoil. The figure shows that this measured local inflow angle is different from the real angle of attack, due to the 'bending' of the streamlines. This is caused by the presence of the profile

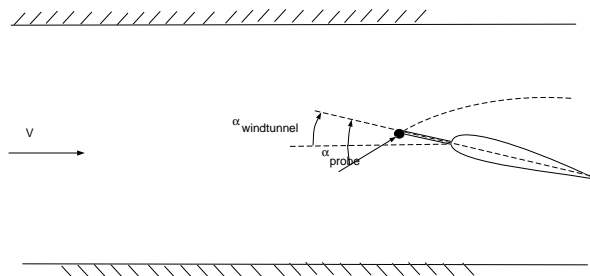


Figure 5.1: Angle of attack in wind tunnel environment

itself, i.e. from the upwash which is induced by the bound vorticity. In order to derive the angle of attack from this local inflow angle, the upwash from the bound vorticity (i.e. the vorticity related to the lift force on the airfoil) should be subtracted.

In a rotating wind turbine environment, the wind tunnel definition of the angle of attack becomes hypothetical, because no equivalent of the undisturbed wind vector, aligned with the wind tunnel walls is known. The undisturbed wind vector at infinity is not a good measure, since it does not include the wake induced velocities. The wake induced velocities are present in the vicinity of the rotor and consequently the angle of attack should be measured near the airfoil itself. As described in sections 4.3 and 4.4 some IEA Task 14/18 experiments and the NREL Phase VI(Nasa-Ames) experiment employed a five hole pitot probe or a wind vane to measure the local inflow angle ahead of the airfoil. However, similar to the probe measurement of the inflow angle in a wind tunnel environment, this inflow angle differs from the angle of attack: In order to find the angle of attack, the upwash from the inflow angle needs to be subtracted. The correction due to the upwash is far from obvious since it is induced by the bound vorticity all along the blade which is not a-priori known. Therefore the upwash was often determined from 2D wind tunnel measurements or from calculational methods. The drawback of using

calculational methods lies in the fact that the measurements are corrected with the same theoretical models which were supposed to be validated with these measurements. The drawback of using 2D wind tunnel measurements lies in the 3D flow situation on a rotating wind turbine blade which makes 2D measurements less valid.

Apart from the determination of the angle of attack from probe measurements, other methods have been attempted in IEA Task 14/18. A popular method was to derive the angle of attack from the stagnation point or from some measure of the pressure distributions. The stagnation point or pressure distribution was then compared with the 2D wind tunnel stagnation point or pressure distribution, and the corresponding 2D angle of attack was assumed to be valid for the 3D situation. It is obvious that this assumption is doubtful, in particular at high angles of attack, where significant 3D effects may occur.

More recently three methods for the determination of the angle of attack have been assessed by Shen see his contribution to the final Mexnext report ([Schepers, Boorsma et al. \(2011\)](#)). The three methods are:

1. **Inverse BEM method**

The inverse BEM method employs the measured normal and tangential force on the blade sections obtained from the pressure measurements. Then the axial and tangential BEM equation are used iteratively to establish the axial and tangential induction factors at the blade. When the code converges, the angle of attack can be found from the velocity triangle at the blade. For more details about the technique, the reader is referred to [Hansen and Johansen \(2004\)](#) or [Guntur \(2011\)](#).

2. **Inverse free wake method**

The inverse free wake method again employs the measured normal and tangential force on the blade sections. These forces are decomposed into the lift forces using an initial spanwise distribution of the angle of attack along the blade. From the lift, the bound circulation along the blades is determined with the Kutta-Joukowski law and this bound vortex is trailed into the wake. The vorticity in the wake then induces a velocity at the blades which is used to calculate a new angle of attack. The process is repeated until convergence in the angle of attack is achieved. The method is inspired by the inverse free wake model as described by [Sant et al. \(2006\)](#) although the method from Sant is meant to derive the loads along the blade from the measured flow field.

3. Direct method

The direct method can only be employed when both surface pressure and velocity measurements are available as is the case in the Mexico experiment for the outer part of the blade. First, the blade is divided into a number of cross-sections, where the local blade forces are known. Second, a number of monitor points is chosen within the PIV sheets (i.e. in the horizontal '9 o' clock' plane see section 4.5) where the velocity is known. The method again starts with determining the bound circulation from the measured normal and tangential forces using an initial angle of attack distribution. This bound circulation induces a velocity at the monitor points. Next a velocity (vector) is determined by subtracting this induced velocity from the PIV measured velocities. From the resultant velocity a new angle of attack is determined. This procedure is repeated until convergence is obtained.

For more details about the technique, the reader is referred to [Shen et al. \(2009a\)](#) or [Yang et al. \(2011\)](#).

It is noted that Shen compared the three angle of attack methods on basis of Mexico measurements. However, it was not possible to draw a firm conclusion on the 'best' method.

5.3 Dynamic pressure and non-dimensionalization of aerodynamic coefficients in wind turbine experiments

The measured data from IEA Tasks 14/18, 20 and 29 are often presented in the form of aerodynamic coefficients, i.e. they are non-dimensionalized with the dynamic pressure.

However, the determination of aerodynamic coefficients is far from obvious. A first problem lies in the establishment of the dynamic pressure. Thereto it is recalled from section 4.3 that the experiments from IEA Task 14/18 and IEA Task 20 generally measure differential pressures, relative to a reference pressure.

In many experiments the dynamic pressure was defined as the maximum

value in the pressure distribution, i.e.:

$$q = p_{\max, \text{relative}} = p_{\max, \text{absolute}} - p_{\text{ref}} \quad (5.1)$$

with $p_{\max, \text{relative}}$ the actually measured maximum pressure (i.e. the differential value) and $p_{\max, \text{absolute}}$ the maximum absolute pressure. Note that $p_{\max, \text{relative}}$ may be based on a curve fit around the measured maximum value but this does not fundamentally change the method.

An alternative way of determining the dynamic pressure is offered by the 5 hole pitot probe measurements which are added to many experimental facilities, see sections 4.3 and 4.4. The resulting pitot pressure (which is again measured relative to the reference pressure) has then been used as an estimate for the dynamic pressure:

$$q = p_{\text{pitot}, \text{relative}} = p_{\text{pitot}, \text{absolute}} - p_{\text{ref}} \quad (5.2)$$

Now the expressions 5.1 and 5.2 are only correct under the assumption that the reference pressure is equal to the static pressure at the blade section. However, this assumption is doubtful in view of the fact that the static pressure at the rotor plane is unknown, see figure 2.2! On the other hand it should be acknowledged that this uncertainty in static pressure is expected to be relatively small. At design conditions ($a=1/3$), the pressure p_2 in figure 2.2 is according to the law of Bernoulli: $p_2 = p_1 + 5/9 \cdot (0.5\rho V_w^2)$. Similarly the minimum pressure p_3 is found to be: $p_3 = p_1 - 3/9 \cdot (0.5\rho V_w^2)$. The maximum uncertainty in static pressure is then the difference between p_3 and p_2 . Since V_w is generally much smaller than Ωr (possibly with the exception of the very inner stations) this uncertainty is small compared to the dynamic pressure which is in the order of $0.5\rho(\Omega r)^2$

Alternatively some institutes determined the dynamic pressure by writing it as $0.5\rho V_{\text{eff}}^2$ where several procedures were followed to estimate the value of V_{eff} . However all of these methods are subject to an uncertainty. Sometimes V_{eff} was determined straightforwardly as the vectorial sum of the free stream wind velocity and the rotational speed. Then it should be realized that for field experiments the value of the free stream wind velocity is not precisely known due to the stochastic atmosphere. Another uncertainty lies in the induced velocities. They are sometimes neglected or they are determined from an analytical model e.g. from an inverse BEM or from an inverse free wake method as described in section 5.2. It should then be noted that a calculational method is used to process the measurements, where the resulting

experimental data form validation material for more or less the same calculational methods.

An additional uncertainty, related to the unknown static pressure, appears in the determination of the pressure coefficients. In many experiments the nominator of these pressure coefficients is based on the actually measured pressure difference at a pressure tap, hence:

$$C_p = \frac{p_{\text{tap}} - p_{\text{ref}}}{q}$$

Again this is only the correct definition if p_{ref} equals the static pressure.

Note that in the Mexico experiment where absolute pressures are measured, the static pressure could be found from $p_{\text{max}} - q$ where q was determined from the tunnel speed and rotational speed and (sometimes) the induced velocities from an analytical method.

Fortunately the knowledge of the absolute pressures is not needed for the determination of dimensional aerodynamic segment forces. This can be illustrated by the integration of the pressure distribution into the normal force which for simplicity is written as an integration along the chord:

$$N = \int_{x=0}^{x=c} (p_{\text{pressure}} - p_{\text{suction}}) dx = \int_{x=0}^{x=c} (p_{\text{pressure}} - p_{\text{ref}}) - (p_{\text{suction}} - p_{\text{ref}}) dx$$

where the index 'pressure' denotes the pressure side of the airfoil and the index 'suction' denotes the suction side. Hence under the assumption of a constant reference pressure during the measurement of the pressure distribution, the absolute value of the normal force can be determined from the pressure differences and it is not disturbed by the uncertainty in the reference pressure.

5.4 Relation between local aerodynamic loads and global rotor loads

The common denominator in the IEA Annex 14/18, 20 and 29 experiments is formed by the pressure measurements at different radial positions. These pressure measurements improve the understanding of the aerodynamic behavior at local blade element level which then in turn should lead to a more

accurate prediction of the rotor(blade) design loads. For this reason it was considered interesting to investigate the relation between the local aerodynamic loads and the rotor loads (which in some experiments were measured additional to the pressure measurements). The investigation can also be seen as a consistency check, and hence a quality check, on the measurements.

For the ECN facility from IEA Task 14/18, see section 4.3, rotor loads have been calculated by fitting a blade load distribution to the measured segment loads at different locations along the blade, see also Feigl (2003). The resulting rotor loads (in the sequel they are denoted as 'pressure' loads) were compared with the 'directly' measured loads, i.e. the loads measured with a balance.

To this end, eight campaigns were considered. The time averaged conditions of the campaigns are given in table 5.1. The values for α_{80} , only served as an indication for the mean angle of attack at 80% span. It can be seen that the main difference between the campaigns is in the pitch angle, which varied from +9.7 to -12.6 degrees between campaign 1 to 8.

campaign	α_{80} deg	U_{hub} m/s	Power kW	θ deg	Ω rpm
1	0.08	9.15	29.17	9.7	36.7
2	2.58	9.70	64.56	6.5	37.3
3	5.01	10.36	65.89	2.5	37.3
4	10.39	10.39	76.06	-0.7	37.5
5	19.44	10.97	94.35	-4.6	37.8
6	19.84	8.52	49.77	-7.0	37.0
7	25.35	9.71	30.20	-10.3	36.7
8	31.57	9.96	10.94	-12.6	36.3

Table 5.1: Global conditions of ECN measurement files

The 'pressure' axial force and the 'pressure' torque were derived from a load distribution which was fitted to the measured segment forces, i.e. to the normal and tangential forces at the 3 instrumented stations at 30% span, 60% span and 80% span. In the load distribution, the forces were assumed to vary linearly between the instrumented sections and they drop linearly to zero towards the tip and the root.

A graphical comparison of time series is given in the figures 5.2 and 5.3, where the campaigns are plotted in sequential order. The agreement between

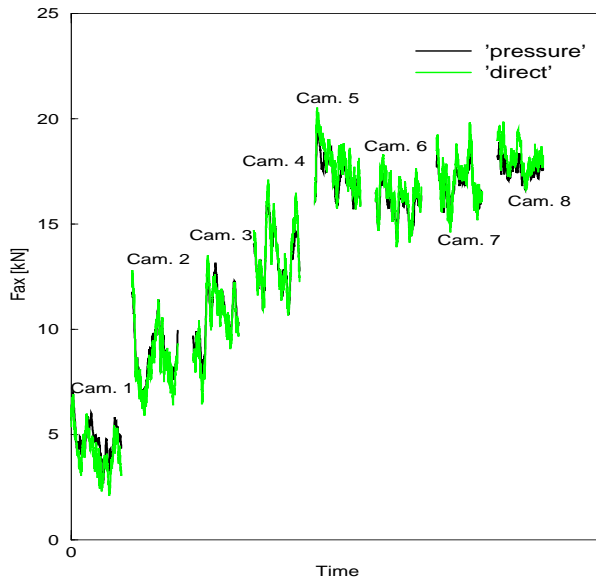


Figure 5.2: ECN field Measurements from IEA Task 14/18: 'Pressure' and 'direct' axial force as function of time for 8 campaigns

'pressure' and 'direct' axial force is extremely good, both in terms of variations as well as in terms of level. This is a remarkable observation since the 'pressure' and 'direct' axial forces are obtained in very different ways.

In figure 5.3, the 'pressure' torque is compared with the 'direct' torque. The agreement in 'shape' of the time series turns out to be very well except for campaign 8. The agreement in absolute levels gets poorer with increasing campaign number (i.e. with decreasing pitch angle and increasing angle of attack). It should be noted that the directly measured torque is believed to be accurate. This is among others confirmed by the fact that it compares very well with the torque derived from the measured generator power. As

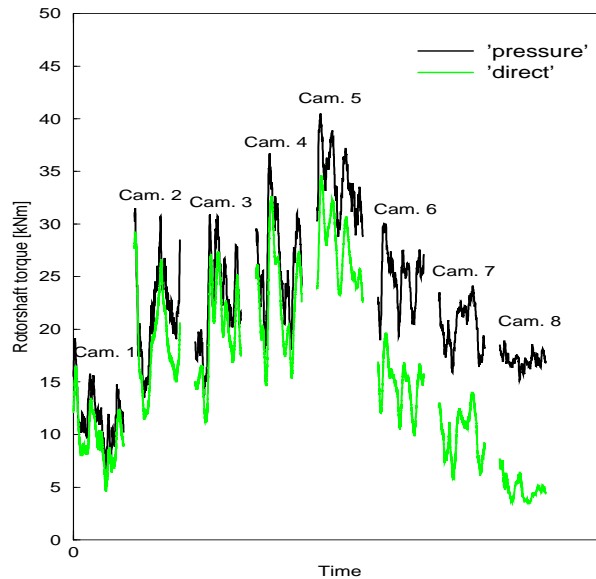


Figure 5.3: ECN field Measurements from IEA Task 14/18: 'Pressure' and 'direct' rotorshaft torque as function of time for 8 campaigns

such it is the 'pressure' torque which is less accurate. Many explanations for the differences between the 'direct' and 'pressure torque' at decreasing pitch angles were investigated but the final conclusion is that the differences are caused by the inaccuracy in measured tangential force. Thereto it should be realized that the local tangential force is derived from integration of the pressure distribution and small errors in pressure tap positions and small errors in the surface direction will have a large effect on this quantity. For campaign 1, the contribution of the tangential force to the torque can be shown to be small compared to the contribution of the normal force, but its contribution increases with decreasing pitch angles. Hence the possible inaccuracy in

measured tangential force plays the largest role in campaign 8. It is noted that the tangential force hardly contributes to the axial force and as such the good agreement between 'pressure' and 'direct' axial force is not affected.

It is noted that the same observations are found in the NREL Phase IV measurements (where only the rotor shaft torque has been measured): For positive pitch angles there is a good agreement between 'pressure' and 'direct' torque (differences in mean value are in the order of a few percents or even lower). For negative pitch angles the 'pressure' torque is much higher (at a pitch angle of -8.9 degrees, the 'pressure' torque is even twice the 'direct' torque)

In figure 5.4 a comparison is made between 'pressure' and 'direct' loads from the Mexico experiment. Thereto the axial force coefficient is presented as function of tip speed ratio. The results are given for two rotational speeds: 324 rpm and 424 rpm. The directly measured axial force is determined from the balance at the tower foot where a correction for tower drag has been applied to determine the rotor axial force. Note that the tower drag could be determined from the tower foot axial force and fore-aft moment by assuming a uniform tower drag. It should be acknowledged however that this assumption is not fully true in view of the fact that the upper part of the tower is affected by the rotor flow and the lower part not.

It can be seen that the differences between the 'pressure' and 'balance' axial force are very small giving confidence in both the pressure and balance measurements.

Furthermore it can be seen that the dependency of axial force coefficient on the rotational speed is limited. This will be discussed in more detail in section 5.5. In summary, the extreme good agreement between 'direct' and 'pressure' rotor loads gives confidence in the quality of the measurements considered. It also shows that these loads can be predicted accurately (on a time averaged basis) by integrating the correct sectional aerodynamic loads along the blade. Furthermore the results lead to the belief that there is a large uncertainty in tangential force as integrated from the pressure distribution. However this conclusion was contradicted by a later study from [Timmer \(2010\)](#) in the Mexnext project. He derived the tangential force by integrating an (almost) continuous pressure distribution on the DU-91-W2-250 airfoil as calculated with RFOIL. He then compared this value with the tangential force obtained from a discrete pressure distribution which would result from the 25 pressure sensors as employed in the Mexico experiment. Large differences

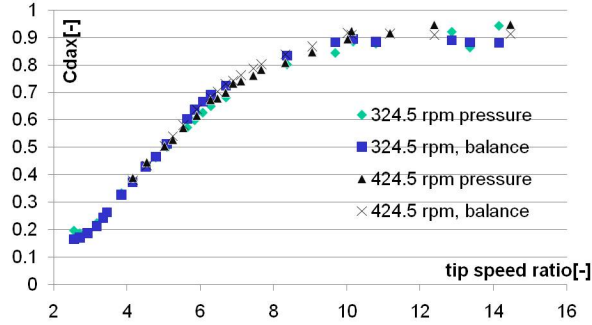


Figure 5.4: Mexico experiment: Axial force coefficient from pressure distributions and balance as function of tip speed ratio for two rotational speeds: 324.5 and 424.5 rpm

(in the order of 300%) were found at zero degrees angle of attack but at 5 and 7.5 degrees angle of attack, the differences were only 3 and 7%.

5.5 Influence of rotational speed and scale on aerodynamic coefficients

One of the main uncertainties in blade aerodynamics lies in the effects from blade rotation on the airfoil coefficients. In section 3.7 it is described that these corrections are driven by the effect from the coriolis force on the chordwise pressure gradient. The main parameter to describe these rotational effects was found to be the local solidity c/r where the rotational speed itself, somewhat surprisingly is generally not included. A model which does model the rotor speed dependency is developed by the University of Illinois, [Du and Selig \(1999\)](#). Thereto, f_{cl} , i.e. the factor in equation 3.13 which accounts for stall delay is assumed to depend on a modified tip speed ratio Λ :

$$\Lambda = \frac{\Omega R}{\sqrt{(\Omega R)^2 + U_{hub}^2}}. \quad (5.3)$$

For all measurements which are considered in the sequel of this project, this factor is approximately 1 which leads to negligible variations in f_{cl} .

In order to confirm this expectation the influence of rotational speed on the aerodynamic coefficients of the Mexico rotor has been investigated by considering the axial force coefficients as function of tip speed ratio, see figure 5.4.

By presenting the axial force coefficient as function of tip speed ratio the results become independent of the rotational speed unless the airfoil coefficients depend on the rotational speed. Such dependency could be a result of a different stall delay effect. However another reason for a rotor speed dependency of airfoil coefficients could originate from a different Reynolds number. Figure 5.4 anyhow shows the rotor speed dependency on the axial force coefficients to be very limited.

Another indication for the rotor speed sensitivity is found by comparing the power coefficients C_P at different rotor speeds. Thereto it should be realized that the axial force coefficients from figure 5.4 are mainly influenced by the lift coefficients, but the power coefficients are also influenced by the drag coefficients which are generally more sensitive to Reynolds number effects. Unfortunately the power has not been measured directly on the Mexico rotor and attempts to derive the power from the moments and loads at the tower foot balance were not successful (see [Schepers et al. \(2011\)](#)).

For this reason the rotor shaft torque has also been derived from the pressure forces along the blade even though it is acknowledged that this excludes the effect of viscous drag, which is one of the main drivers for a Reynolds number dependency.

The resulting power coefficients at 324 and 424 rpm could be compared with measurements at different rotational speeds which have been taken on a 'daughter' of the Mexico rotor. This daughter has been built by the Korean Aerospace Research Institute KARI and it is a perfect look alike of the Mexico rotor but scaled down to a rotor diameter of 2 meter, see figure 5.5. The model is placed in an open measurement section of a KARI wind tunnel with a size of $5 \times 3.75 \text{ m}^2$, where the Mexico rotor has a diameter of 4.5 m and was placed in an open measurement section with a size of $9.5 \times 9.5 \text{ m}^2$. The KARI test was conducted at various tip speeds, including the value of 76 m/s, which was used in the Mexico test. The maximum tip speed was 90 m/s (where the maximum tip speed in the Mexico experiment was 100m/s). Transition was fixed at 5% chord line at both the suction and pressure side, to match the Mexico experiment. The torque was directly measured with a torque sensor

installed in the rotating axis. In figure 5.6 the power coefficient as function of tip speed ratio is compared for the KARI and Mexico experiment at tip speeds of 76 m/s and 90 m/s (KARI) and 76 m/s and 100 m/s (Mexico).

First it is interesting to find the maximum C_P near a tip speed ratio of 6.6 in both the KARI and the Mexico experiment. The $C_{P,max}$ of the KARI wind turbine ≈ 0.33 which is lower than the $C_{P,max} \approx 0.38$ of the Mexico rotor. A lower value for the KARI rotor could be expected, in view of its lower Reynolds number and resulting higher drag value: The Reynolds number near the tip of the KARI rotor varies between 1.8 to $3.2 \cdot 10^5$, where the Reynolds number near the tip of the Mexico rotor varies roughly between 6 and $8 \cdot 10^5$. Apart from this, as mentioned above, the viscous drag is not included in the Mexico results. This had led to a higher power coefficient as well. At low tip speed ratios (large angles of attack) pressure drag will be dominant above viscous drag but at high tip speed ratios the contribution of viscous drag is larger.

In figure 5.6 the influence of rotational speed turns out to be small for both the Mexico as well as the KARI experiment. This is not true however in figure 5.7 in which the KARI measurements are presented for 5 tip speeds speeds, not only for 76 and 90 m/s but also for 50, 60 and 70 m/s. The results are given in terms of a torque coefficient using the blade tip speed as a reference velocity in order to compare the test results for various rotating speeds:

$$C_{\text{torque}} = \frac{\text{Torque}}{0.5\rho V_{\text{tip}}^2 \pi R^3} = \frac{C_P}{\lambda^3} \quad (5.4)$$

The KARI measurements at low tip speeds (50 to 70 m/s) do indicate a clear rotor speed dependency in particular near stall ($\lambda \approx 4$, i.e. $\lambda^{-1} \approx 0.25$ in figure 5.7). The fact that the rotor speed dependency is mainly found near stall indicates a different stall delay effect despite the fact that the factor Λ from equation 5.3 at the stalling point is still larger than, or equal to 0.97 for all rotational speeds. Nevertheless the explanation of a Reynolds number sensitivity might not be fully excluded either, since the Reynolds number sensitivity is known to be strongest at low values of the Reynolds number, i.e. at a small wind turbine. Finally figure 5.8 shows a very interesting result. It presents the local aerodynamic force coefficients from the Mexico pressure distributions, according to a procedure from [Verhoef \(2011\)](#). Thereto the resultant force coefficient (C_{res}) is plotted versus the resultant force angle γ for both 324 and 424 rpm. The resultant force coefficient is the resultant aerodynamic force non-dimensionalized with $0.5\rho V_{\text{eff}}^2 c$, see figure 5.9. Note that V_{eff} has been determined as the sum of the tunnel speed and the rotational speed without



Figure 5.5: KARI wind tunnel with scaled down model of Mexico rotor, compare with figure 4.3

induced velocities. The angle γ is the angle between the resultant aerodynamic force and the chord. Again very little effect of the rotational speed is found. Figure 5.8 presents the result for 82% span but similar results were obtained for the other instrumented sections. Figure 5.8 also presents the resultant force coefficient from the 2D wind tunnel measurements. These results compare well with the 3D measurements (although the study showed this to be less true at more inboard locations where clear 3D effects are apparent).

5.6 Inventory of analyzes on IEA Task 14/18 data

In 2003 an inventory has been made of the analyzes which have carried out on the IEA Task 14/18 measurements until that date, see [Schepers, van Rooij and Bruining, \(2003\)](#). Thereto it should be known that the measurements from the IEA Task 14/18 database are freely available to third parties under the condition that the IEA Task 14/18 participants should be informed on experiences with the database.

At that moment some 32 users of the database were registered. Apart from that the measurements were used in several European Research Projects, e.g. the EU project VISCEL, see [Chaviaropoulos et al. \(2001\)](#), the EU-Joule project Dynamic Stall and Three Dimensional Effect, see [Björck \(1995\)](#) and

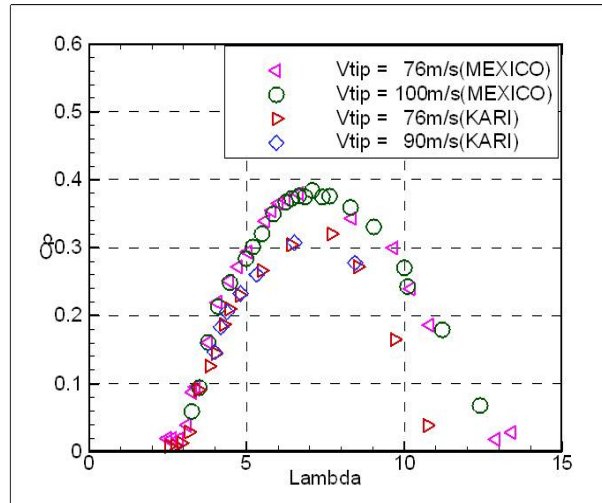


Figure 5.6: Power coefficients as function of tip speed ratio for KARI and Mexico experiment at different tip speeds

the EU project ROTOW, see [Graham and Brown \(2000\)](#). The aim of the first project (VISCEL) was to validate a large number of European 3D viscous CFD codes. In the second and third project (Dynamic Stall and Three Dimensional Effects and ROTOW) several of the engineering methods discussed in section 3 were developed and/or assessed. The aim of the project 'Dynamic Stall and Three Dimensional Effects' was to develop and validate engineering models for dynamic stall and three dimensional effects and the aim of the ROTOW project was to investigate the validity of aerodynamic tower shadow models.

The main conclusions from the inventory were:

- The measurements taken within IEA Task 14/18 revealed the aerodynamic details of wind turbine blade segments. This enabled many successful activities, e.g.:
 - The measurements of rotating (mean) airfoil characteristics, were compared with 2D airfoil characteristics. However the determination of airfoil characteristics was not straightforward due to the uncertainty in angle of attack and dynamic pressure, see the sections 5.2 and section 5.3. Nevertheless a clear stall delay could be ob-

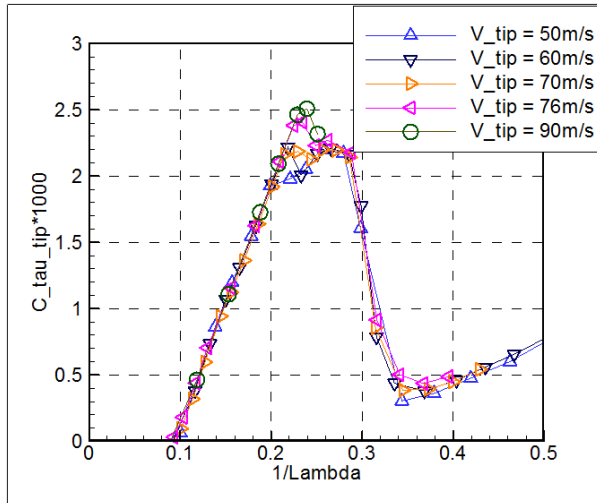


Figure 5.7: Torque coefficient as function of (tip speed ratio)⁻¹ for KARI experiment

served at the inner sections of all measurement facilities. Models have been developed which calculate this stall delay.

- The IEA Task 14/18 measurements have been used extensively for validation of models, e.g. engineering models, free wake methods, airfoil design tools and CFD methods at both aligned and yawed flow conditions. The validation of the latter tools was not only based on local segment loads but also on pressure distributions. Most comparisons between calculations and measurements showed a good to reasonable agreement below stall, but above stall the agreement became poor.
- Tower effects were found to be overpredicted when a standard potential dipole model from section 3.10 was used.
- For validation of some CFD methods the modelling of transition turned out to be a problem (no experiments with fixed transition are included in the IEA Task 14/18 database)
- A main uncertainty lies in the field environment which complicates the

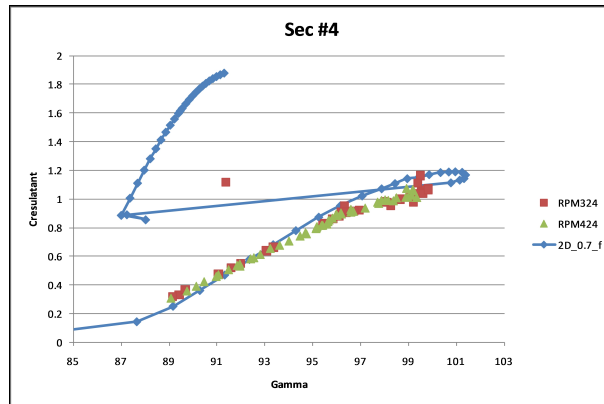


Figure 5.8: Mexico experiment: Resultant force coefficient as function of resultant force angle γ (see figure 5.9) for 82% span measured at two rotational speeds and compared with 2D measurements, from [Verhoef \(2011\)](#)

interpretation of the measurements. It was found that this uncertainty (together with the uncertainty on angle of attack) made the measurements less suitable for a direct validation of dynamic stall models. An example is given in figure 5.10 and 5.11. They show measurements on the RISØ test facility of the normal force coefficients at 68% span as function of angle of attack (around a low and a high angle of attack). The angle of attack is derived from a local flow angle as measured with a pitot probe and corrected for upwash. A very disorderly pattern can be observed at high angle of attack by which these measurements cannot be used for a direct validation of dynamic stall models.

To some extent the latter problem is overcome by selecting data according to the baseline criterion as applied by TUDelft and NREL, [Bruining \(1993\)](#) and [Shipley et al. \(1995\)](#). This technique aims to select measurements which are taken at conditions which are as steady as possible. Thereto data sets are selected in which the variations in wind speed and yaw error are limited over three subsequent rotations. The middle cycle data has been averaged for all the azimuth positions and is the final baseline result. The baseline data generally show less scatter than the data from the full base of measurements.

It is obvious that the NASA-Ames and Mexico wind tunnel measure-

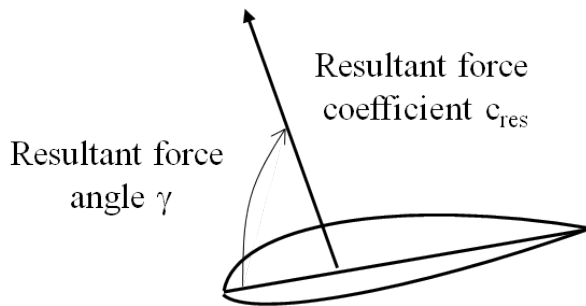


Figure 5.9: Resultant force coefficient and resultant force angle γ

ments as used in IEA Tasks 20 and 29 do not suffer from these uncertainties in the inflow.

In the next sections more analyzes on the IEA Task 14/18 data, as performed by the author, are described.

5.7 Comparison between calculated and measured local aerodynamic loads

5.7.1 IEA Task 14/18: Comparison between calculations and field measurements

As mentioned in section 5.6 the IEA Task 14/18 measurements were often analyzed in the form of airfoil characteristics but the determination of these measured characteristics was far from straightforward due to the uncertainty in angle of attack and dynamic pressure. In order to overcome these problems, ECN's aero-elastic code PHATAS was applied to study the deficiencies of aerodynamic engineering models. Thereto calculated time averaged dimensional loads are compared with the corresponding measured values. In such comparison the uncertainty in measured angle of attack and dynamic pressure is avoided.

Comparisons have been made with measurements from the IEA Tasks 14/18

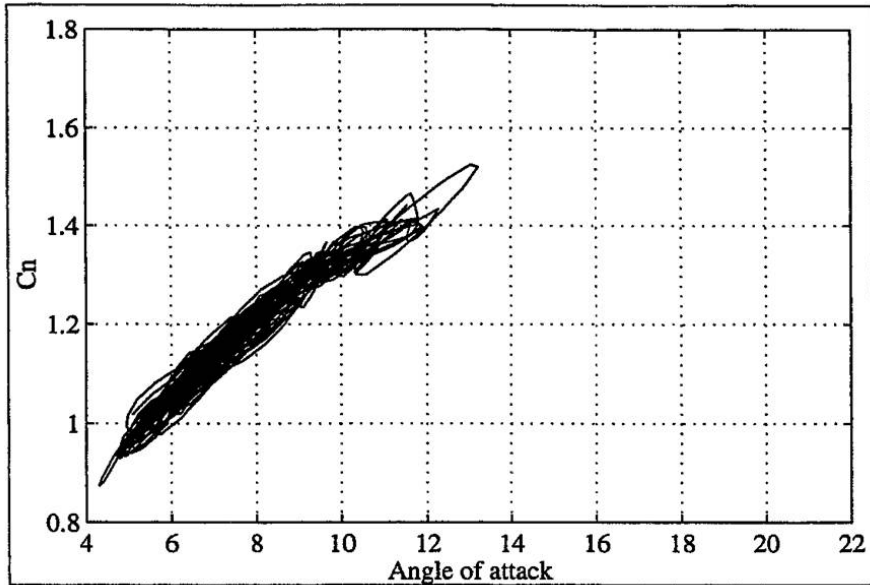


Figure 5.10: Normal force as function of attack (low angle of attack) as measured by RISØ in IEA Task 14/18

facilities from TUDelft, ECN, NREL (both the twisted as well as the untwisted blade) and RISØ, at more or less aligned conditions see [Schepers \(2004a\)](#). The airfoil coefficients as prescribed to PHATAS were generated with the ATG, [Bot \(2001\)](#). The ATG is a database with measurements of 2D airfoil characteristics with inter(extra) extrapolations to generate performances for a wide range of angles of attack, thicknesses and Reynolds numbers. The 2D $c_l(\alpha)$ curves have been corrected for rotational effects according to the model from Snel, see equations 3.13 and 3.14. Structural dynamic effects were included based on the model descriptions of the turbines given in [Schepers et al. \(2002a\)](#). In the calculations, the wind speed was assumed to be constant (with wind shear included). Thereto the time averaged wind conditions from the measurements were prescribed.

In the analysis, emphasis is put on time averaged data of dimensional sectional aerodynamic forces, blade loads, and rotor loads.

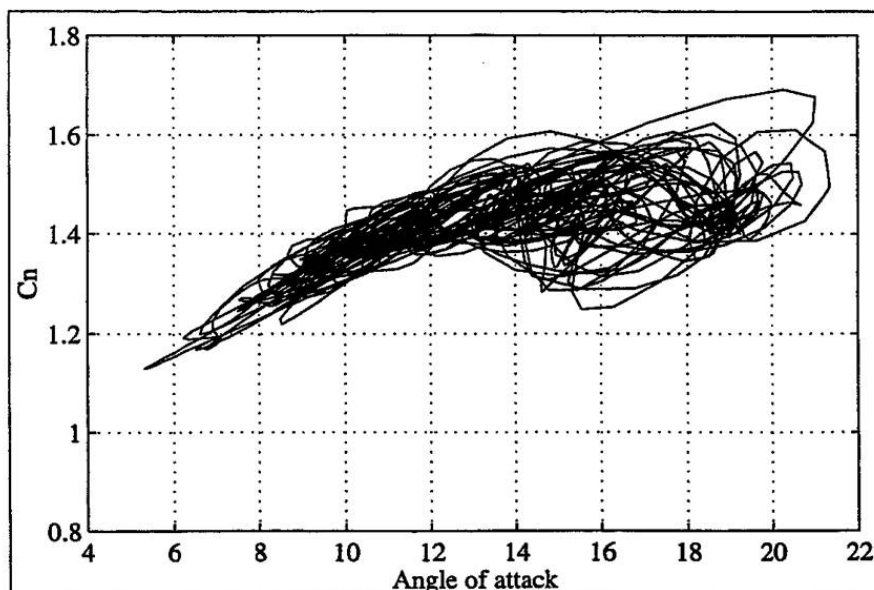


Figure 5.11: Normal force as function of attack (high angle of attack) as measured by RISØ in IEA Task 14/18

This chapter highlights some results and the comparison with measurements on the NREL rotor with twisted blades (Phase IV) will be discussed in more detail. These results often turned out to be representative for the results obtained on the other IEA Task 14/18 facilities.

For the Phase IV turbine, 5 campaigns were selected at (more or less) aligned flow conditions. They are denoted as case 1 to 5. The averaged conditions of these cases are given in table 5.2. Note that α_{95} denotes the mean angle of attack at 95% span as supplied by NREL and the rotor speed is almost constant at 72 rpm. The main difference is in wind speed which is lowest for campaign 1 and highest for campaign 5. The measurement period is 1 minute.

As mentioned in Appendix A the sections where the aerodynamic forces are measured (relative to the rotor centre) on this turbine are located at 30%, 47%, 63%, 80% and 95% span.

case	α_{95} deg	U_{hub} m/s	Power kW	θ deg
1	4.3	7.1	3.3	3.0
2	9.4	10.4	9.7	3.0
3	12.1	12.9	11.1	2.6
4	15.2	15.9	9.4	2.7
5	18.4	19.3	10.1	2.9

Table 5.2: Global conditions of NREL measurement files

In the figures 5.12 and 5.13, the ratios between calculated and measured normal forces and tangential forces (i.e. the calculated value divided by the measured value) for the different cases and the different radial positions are presented as function of mean wind speed. In figure 5.14 the ratios between calculated and measured root flapwise moments and rotorshaft torques are given. The ratios which are presented in the figures hide the sign information of the underlying loads. The normal force and flatwise moment were usually directed in 'downwind' direction, where the tangential force is pointing towards the leading edge.

The following comments can be made to the comparison (where it is emphasized that the comments for the other IEA Task 14/18 facilities from TUDelft, ECN, NREL (untwisted blade) and RISØ) are largely similar:

- Normal forces, see figure 5.12:
For the low wind speed cases 1 and 2 the agreement in normal forces is generally good but a large underprediction of the normal force at 30% span is found at the high wind speeds (the cases 4 and 5). This is related to an underpredicted 3D stall delay effect from equation 3.14.

The value of the normal force at 80% span is overpredicted at the low wind speeds, but at the high wind speeds this force is underpredicted. The value of the normal force at the very outer station (95% span), is always overpredicted. This is explained in section 3.7: By default the tip effects are modelled according to the Prandtl tip correction, which only corrects the non-uniformity from the finite number of blades. It reduces the inflow angle and the resulting lift but not necessarily fully to zero. An explicit tip loss, due to the finite length of the blade is not taken into account.

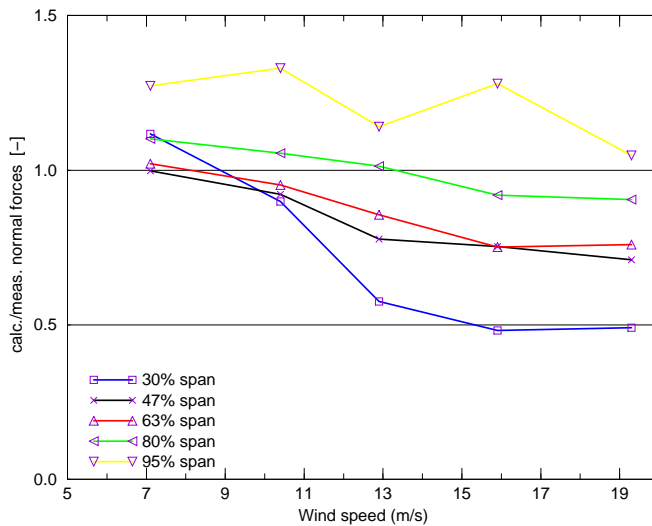


Figure 5.12: Ratio between ECN calculated and measured normal forces of NREL phase IV field measurements from IEA Task 14/18 (Time averaged)

- Tangential forces, see figure 5.13:
For the low wind speeds cases 1 and 2 the agreement in tangential forces is generally good but at high wind speeds the differences are large. Most times the value of the tangential force is overpredicted, i.e. the ratio is (far) above 1, although this is less true for the inner station for the present NREL measurements (For most other IEA Task 14/18 turbines it was also found to be true at the inner station). This implies the prediction of a too strong force towards the leading edge. The stronger force towards the leading edge can be a result of an overpredicted lift force but it can also be a result of an underpredicted drag force. The latter is in principle always true due to the neglect of the skin friction but this contribution is not significant.
- Correlation between local aerodynamic loads and overall rotor load

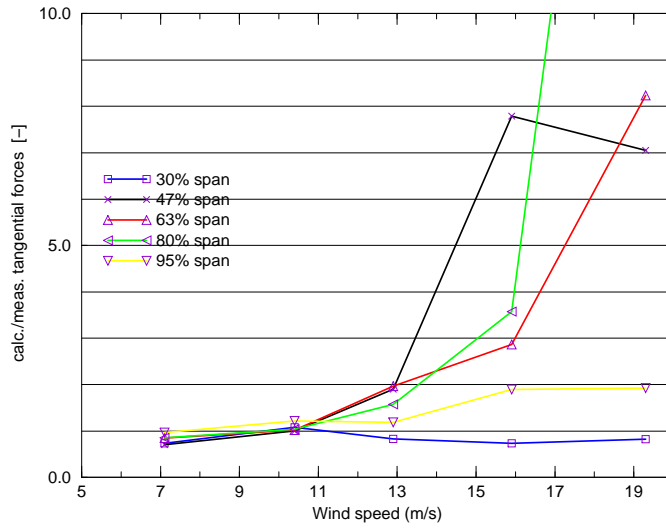


Figure 5.13: Ratio between ECN calculated and measured tangential forces of NREL phase IV field measurements from IEA Task 14/18 (Time averaged)

see figure 5.14:

The differences between calculated and measured torque are very small also at high wind speeds. This is a surprising result, in view of the large discrepancies between the normal forces and tangential forces. Note that at least the measurements of the normal force and the torque are believed to be accurate, see section 5.4. Then the good agreement in torque seems to be due to compensating 'errors' between normal and tangential forces: The normal force is generally underpredicted (yielding a lower torque) and the tangential force is overpredicted (yielding a higher torque). Hence a good agreement in rotor loads is found even if the associated segment forces are predicted very poorly. It is again emphasized that similar observations are found for the other turbines in IEA Task 14/18, where, additionally, it was found that 'errors' between

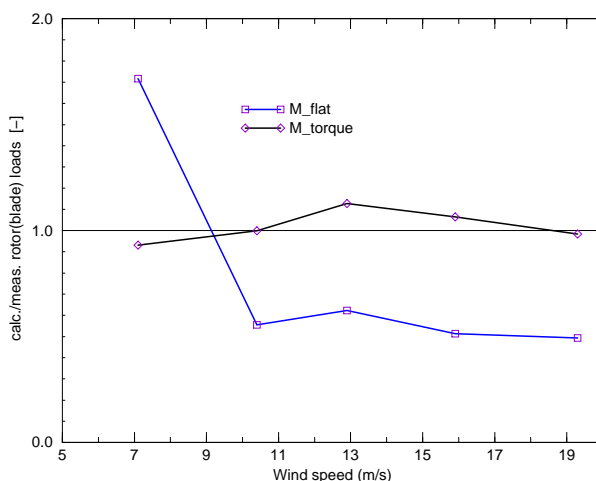


Figure 5.14: Ratio between ECN calculated and measured flatwise moments and torque of NREL phase IV field measurements from IEA Task 14/18 (Time averaged)

loads on the inner part of the blade could be compensated by 'errors' on the outer part of the blade.

The largest underprediction of the flatwise moments is found for campaign 4 and 5, which also shows the largest underprediction of the normal forces.

5.7.2 IEA Task 20: Comparison between calculations and NREL Phase VI (NASA-Ames) measurements

In IEA Task 20 PHATAS calculations have been compared with NREL Phase VI (NASA-Ames) measurements. Some calculations from ECN's free wake code AWSM were also added. It is noted that within IEA Task 20 many more

institutes used the NASA-Ames measurements to validate their codes. In this respect it should be mentioned that CFD codes (in particular the RISØ-DTU Ellipsys code) obtained very good results, also at stalled conditions.

In [Schepers \(2007a\)](#) a comparison is made between the ECN calculated and measured dimensional loads from the NREL Phase VI(NASA-Ames) experiment. In this reference the results are presented similarly to those in section 5.7.1. Also the calculations are performed in a very similar way, i.e. the calculations are made with the PHATAS code for constant wind conditions (where the wind tunnel conditions in the present case make this assumption much more plausible). The basic 2D airfoil data were supplied by NREL and slightly adjusted and extended. The 3D correction from Snel (equations 3.13 and 3.14) is again included. Structural dynamic effects are also taken into account. The resulting PHATAS input is described by [Lindenburg \(2003\)](#)

In section 5.7.1 it is again concluded that at the inner part of the blade, at high wind speeds the normal forces are underpredicted where the forces at the outer part of the blade are overpredicted. As a result the flatwise moment at high wind speeds is underpredicted. The comparison on basis of tangential forces again indicates the prediction of too strong a force towards the leading edge.

Moreover figure 5.15 shows the normal forces measured along the blade in comparison with calculated results from PHATAS and AWSM for a (low) tunnel speed of 5 m/s and a pitch angle of 3 degrees. The results are plotted as function of radial position. It can be concluded that the normal forces calculated with AWSM are usually very close to the normal forces calculated with PHATAS, where the agreement between the PHATAS results and the measurements is also very good. An important improvement from the AWSM code is visible at the 95% station. At this station the PHATAS calculated normal force is considerably overestimated, where AWSM overpredicts the normal force to a smaller extent. This can be a result of the simplifications from the Prandtl tip correction as implemented in PHATAS. Section 3.4 explains that this Prandtl tip correction is based on an analysis from a simplified vortex wake model. Since AWSM models the flow around the tip with a complete, numerical, free wake model this will lead to a more realistic angle of attack. However, it does not fully prevent the overprediction of the normal force which can be explained by the fact that AWSM, similar to PHATAS uses the two dimensional airfoil characteristics. This is incorrect near the very tip as already found in section 5.7.1.

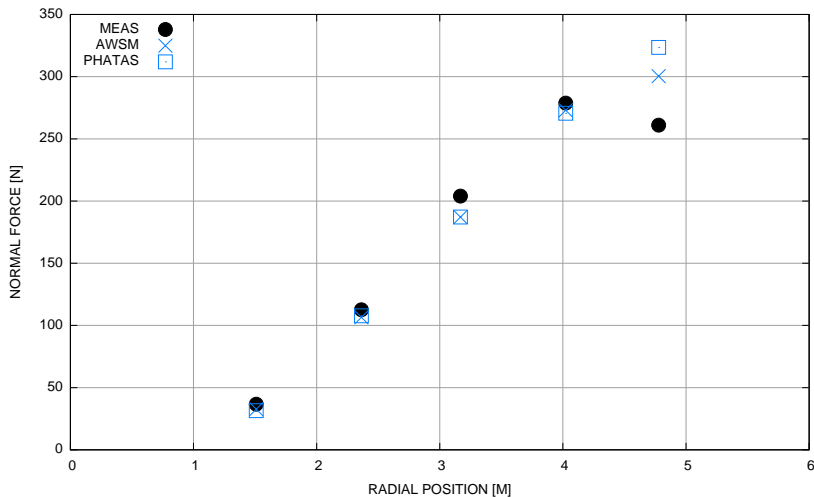


Figure 5.15: NREL Phase VI (NASA-Ames): Comparison between calculated and measured normal force as function of radial position at $V_{\text{tun}} = 5$ m/s and $\theta = 3$ degrees (Note that blade length is 5 m)

5.7.3 IEA Task 29 (Mexnext): Comparison between calculations and Mexico measurements

Within IEA Task 29(Mexnext) an elaborate comparison is made between calculated and measured results. Calculations have been supplied by almost all IEA Task 29 participants with a large variety of codes ranging from simple lifting line models to more advanced CFD codes. The results of the normal forces as function of the radial position are presented in the figures 5.16 to 5.18. They show the results for tunnel speeds of 10, 15 and 24 m/s (where the pitch angle is -2.3 degrees and the tip speed is 100 m/s). The tunnel speed of 15 m/s represents design conditions, a tunnel speed of 10 m/s represents turbulent wake conditions and a tunnel speed of 24 m/s represents stalled conditions. Similar to the results on the IEA Tasks 14/18 turbines and the NREL Phase VI(Nasa-Ames) turbine it is found that the lifting line codes underpredict the normal force at the inner part of the blade at stall (24 m/s) where the agreement at 10 and 15 m/s is better. This again indicates an underprediction of stall delay even though this effect is modelled with a large variety of different 3D corrections. The corresponding results from the CFD

codes are generally in better agreement, which was also found in IEA Task 20 for the NREL Phase VI(Nasa-Ames) turbine. At 60, 82 and 92% span and tunnel speeds of 10 and 15 m/s almost all codes overpredict the normal force. At 92% span an overprediction from the lifting line codes is consistent to the overprediction of tip loads in sections 5.7.1 and 5.7.2, which was explained by the use of 2D airfoil data near the tip. However this does not explain the overprediction at 60 and 82% span. It also does not explain the overprediction from the CFD codes at 92% span since these codes do not apply airfoil characteristics. However it is interesting to note that generally speaking the overprediction from the CFD codes is less than the overprediction from the lifting line codes.

The lifting line results for $V_{\text{tun}}=15$ m/s show a shift in normal force roughly between $r=1.3$ and $r=1.7$ m. This is attributed to the discontinuity in airfoil distribution, since the RISØ profile, which is applied mid-span has a different zero lift angle of attack compared to the surrounding DU and NACA profiles. In addition to that the validity on the 2D airfoil data of the RISØ profile has been questioned, since this data was obtained in a wind tunnel which features rather high turbulence intensity levels. The fact that this jump is most pronounced at $V_{\text{tun}}=15$ m/s can be attributed to the difference in lift coefficients being larger for the angle of attack corresponding to this operating condition.

In section 6.3.2 these results will be related to those of the flow field. It will then be found that none of the calculations from the Mexnext group can predict both the velocities AND loads in a correct way, where the discontinuity in airfoil distribution leads to vortex shedding which is not predicted by any of the codes.

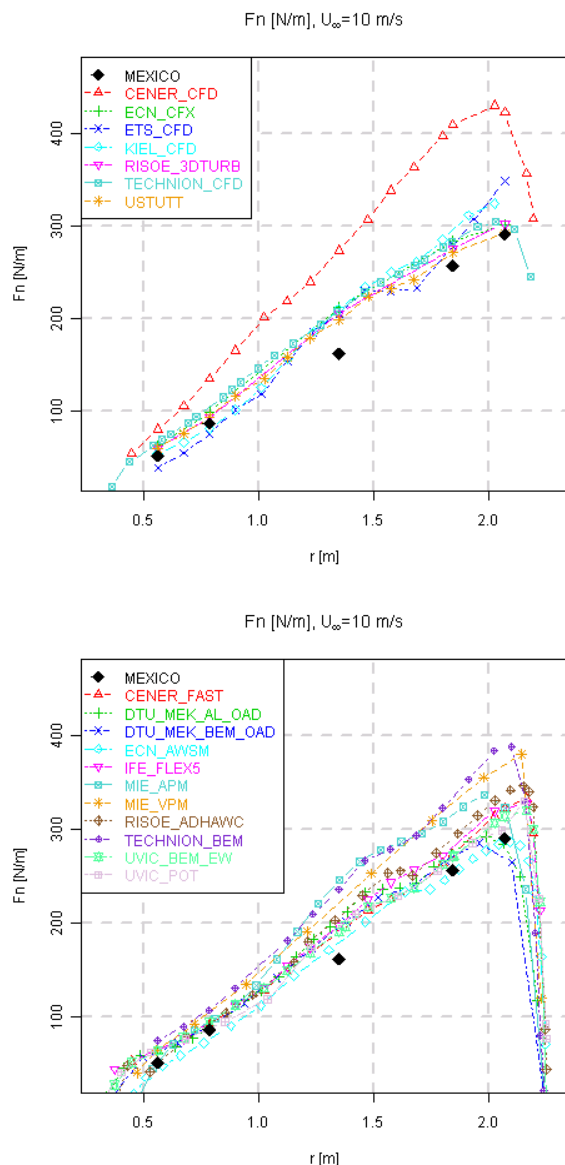


Figure 5.16: IEA Task 29 (Mexnext): Comparison between measured and calculated normal force on the Mexico rotor blade, at $V_{tun} = 10$ m/s. Calculations from CFD codes are in upper figure, calculations from lifting line codes are in lower figure.

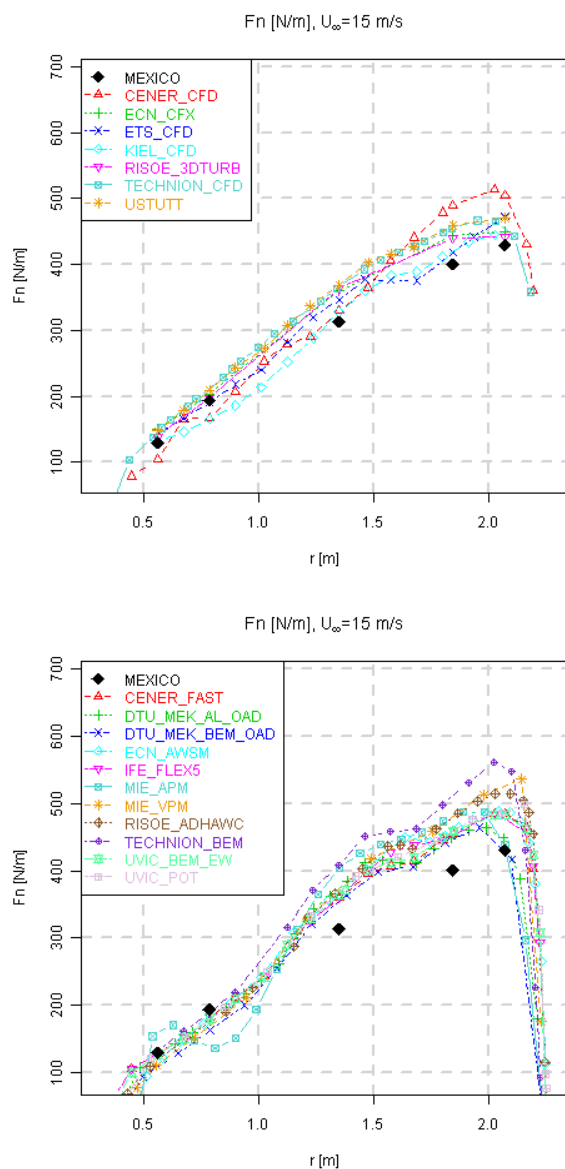


Figure 5.17: IEA Task 29 (Mexnext): Comparison between measured and calculated normal force on the Mexico rotor blade, at $V_{\text{tun}} = 15$ m/s. Calculations from CFD codes are in upper figure, calculations from lifting line codes are in lower figure.

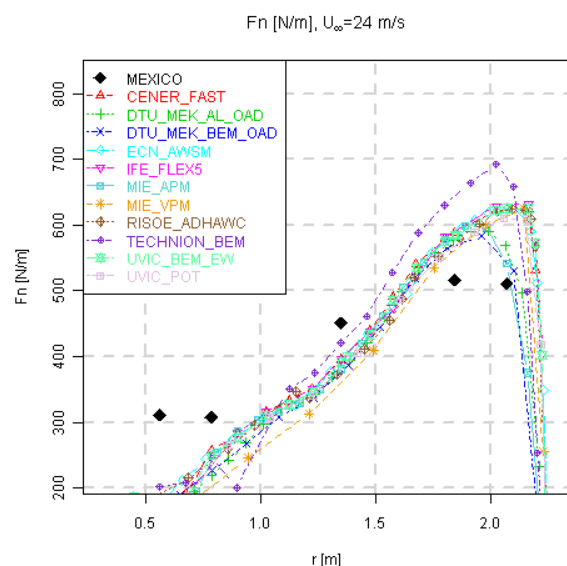
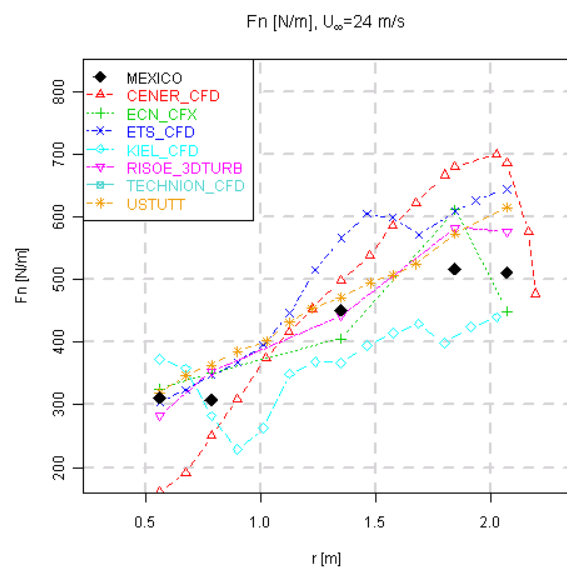


Figure 5.18: IEA Task 29 (Mexnext): Comparison between measured and calculated normal force on the Mexico rotor blade, at $V_{tun} = 24$ m/s. Calculations from CFD codes are in upper figure, calculations from lifting line codes are in lower figure.

5.7.4 Improved model for 3D effects at airfoil aerodynamics, using measurements from IEA Task 14/18/20

In this section a new model for rotational effects is described. It was originally developed in the Annexlyse project, [Schepers et al. \(2004a\)](#), to reduce the differences between calculated and measured results from IEA Task 14/18, as presented in section 5.7.1. At a later stage it also helped to improve the agreement between the calculated and measured IEA Task 20 (NASA-Ames) results from section 5.7.2.

First the considerations which led to the improved model are described followed by the actual description of the model.

Background for improved model

The most promising and most appropriate improvements to reduce the disagreement between calculated and measured IEA Task 14/18 results were believed to be possible by correcting the basic 2D airfoil characteristics. Thereto it is recalled from section 3.7 that stall delay (i.e. the increase in c_l due to rotation) is usually modelled by considering a factor f_{cl} according to equation 3.13 (This equation is copied to equation 5.5):

$$c_{l,3D} = c_{l,2D} + f_{cl}\Delta c_l \quad (5.5)$$

with:

$$\Delta c_l = c_{l,inviscid} - c_{l,2D} = c_{l,0} + 2\pi\alpha - c_{l,2D} \quad (5.6)$$

Drag can, according to equation 3.16 (copied to equation 5.7) be modelled by applying a factor f_{cd} to the difference between the 2D drag coefficient and the minimum drag coefficient: Hence:

$$c_{d,3D} = c_{d,2D} + f_{cd}(c_{d,2D} - c_{d,2D,min}) \quad (5.7)$$

The factors f_{cl} and f_{cd} have then been tuned to the measured results from IEA Tasks 14/18.

Obviously, part of the differences between calculated and measured rotor(blade) loads will not be covered in this way. This holds for differences which originate from the calculation of induction, from the uncertainties in the basic 2D airfoil characteristics or from the uncertainties in turbine and wind descriptions. It should also be realized that the proposed model improvements are based on generalizations on which many exceptions can be found.

Before explaining the new model it is good to repeat and extend some observations which were given by [Schepers, van Rooij and Bruining, \(2003\)](#) on the IEA Task 14/18 airfoil characteristics. Although these characteristics are subject to the uncertainty on angle of attack and dynamic pressure, they remain valuable. As a matter of fact several observations on the characteristics are consistent to the previously made observations on the dimensional loads as addressed in the sections 5.7.1 and 5.7.2.

- In figure 5.19, $f_{\text{meas}}(\alpha)$ is given for the NREL Phase IV turbine where f_{meas} is the value of f_{cl} derived from the measured $c_l(\alpha)$ curve. The measured values are compared with model results: f_{ECN} denotes the ECN model 3.14.

$$f_{\text{ECN}} = 3(c/r)^2 \quad (5.8)$$

This model was used in the PHATAS calculations as described in the previous sections.

f_{CRES} denotes the value from equation 3.15, as derived by CRES ([Chaviaropoulos and Hansen \(2000\)](#)) which takes the following expression:

$$f_{\text{CRES}} = 2.2(c/r)\cos^4(\epsilon + \theta) \quad (5.9)$$

Figure 5.19 shows that initially, f_{meas} increases with α . A maximum is reached near $\alpha \approx 20$ degrees. Thereafter the factor decreases again. The models from CRES nor ECN include a dependency on the angle of attack. Furthermore, figure 5.19 shows f_{ECN} to be too low, where f_{CRES} is more realistic (at least near an angle of attack of 20 degrees). This observation turned out to be valid for the measurements of the other IEA Task 14/18 facilities as well. It is consistent with the underpredicted dimensional root normal forces from the previous sections, which are based on f_{ECN} ;

- In figure 5.20 the values of f_{cl} are presented as function of c/r . Some explanatory comments should be given to this figure: The factor f_{cl} is determined from a large number of $c_l(\alpha)$ IEA Task 14/18 measurements: To this end, the measurements on all instrumented sections of the two NREL rotors, the RISØ rotor and the TUDelft rotor are considered. Some slight adjustments have been made to the measured angle of attack in order to fit the 3D $c_l - \alpha$ curve to the 2D curve. This results in a large number of figures, similar to figure 5.19. Then the factor f_{cl} at $\alpha \approx 20$ degrees is approximated visually and these values are plotted as function of c/r in figure 5.20.

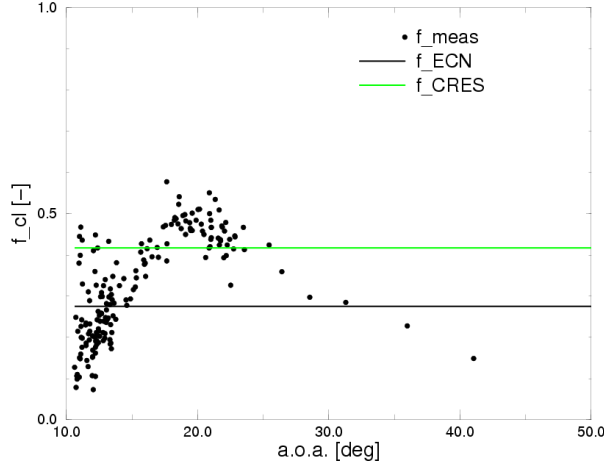


Figure 5.19: Factor f_{cl} as function of α for the NREL, Phase IV field measurements at 30% span

As a matter of fact, the results from TUDelft and NREL Phase II are most suitable to derive the c/r dependency, since these turbines have untwisted blades (see Appendix A). For all other turbines a different c/r goes together with a different twist, which, according to equation 5.9, is expected to influence the factor f_{cl} as well. Therefore the values of f_{cl} for the RISØ and NREL Phase IV turbine, have been corrected for the twist under the assumption that f_{cl} varies according to $\cos^4(\theta + \epsilon)$, consistent with equation 5.9.

The measurements from TUDelft yield the following c/r dependency:

$$f_{cl} = 1.56(c/r)^{0.56} \quad (5.10)$$

The NREL Phase II measurements yield:

$$f_{cl} = 4.93(c/r)^{1.54} \quad (5.11)$$

The best fit on all measurement points (including the NREL Phase IV and RISØ measurements with a pitch angle correction) is found to be:

$$f_{cl} = 2.93(c/r)^{1.178} \quad (5.12)$$

Expression 5.12 is not too different from relation 5.9 for zero pitch angle:

$$f_{\text{CRES}} = 2.2(c/r)$$

The large differences between the expressions 5.10, 5.11 and 5.12 throws some doubt on the assumption that a generally valid expression for the c/r dependency exists. It should be realized however, that the expressions are determined in a rather crude way due to the uncertainties in the angle of attack, the basic 2D characteristics, the visual averaging etc.;

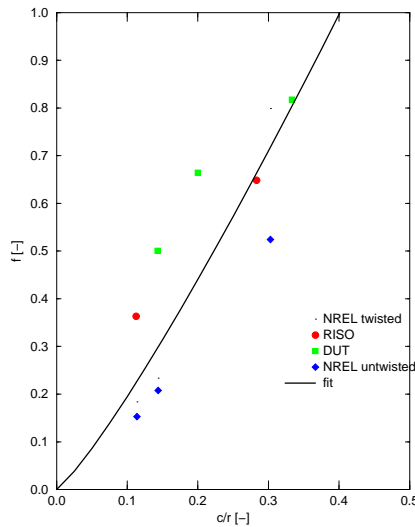


Figure 5.20: Factor f_{cl} as function of c/r from the available IEA Task 14/18 field measurements

- In [Schepers, van Rooij and Bruining, \(2003\)](#) it is shown that the $c_n - \alpha$ curves as measured by ECN and NREL in IEA Task 14/18 depend on the pitch angle (θ). Later this was also found to be true for the NREL Phase VI(Nasa-Ames) measurements. This is exemplified in figure

5.21, which shows the $c_n(\alpha)$ measured in the NREL Phase IV experiment at 47% span. Stall delay effects appear much stronger at negat-

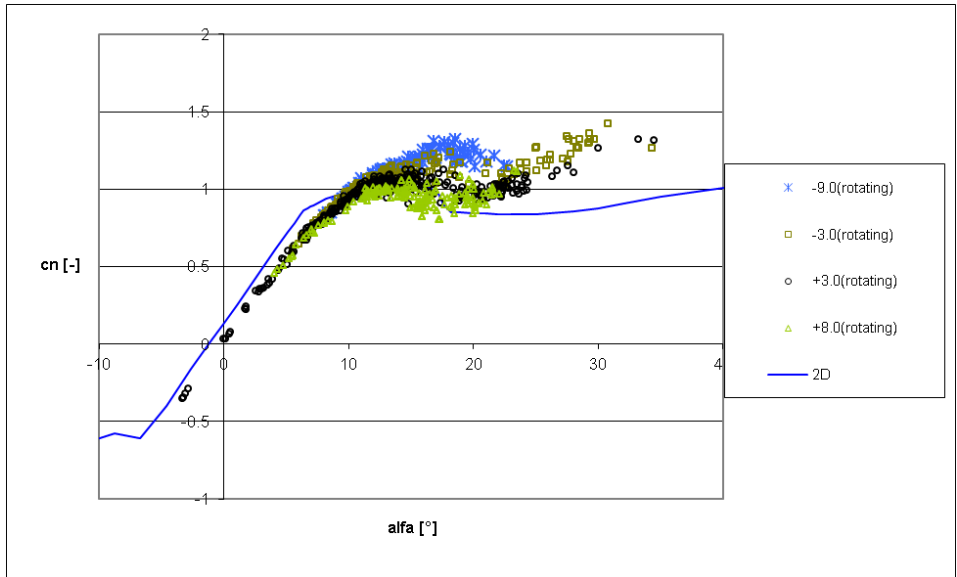


Figure 5.21: Normal force coefficient as function of angle of attack for the NREL Phase IV field experiment (47% station) for pitch angles from -9.0 to +8.0 degrees and 2D measurements

ive pitch angles, which due to the positive twist (ϵ) implies a small total blade angle: $\epsilon + \theta$.

The only 3D model known to the author which does include a pitch angle dependency is the model from CRES, equation 5.9.

In figure 5.22 the measured values of f_{cl} (at $\alpha \approx 20$ degrees) are shown as function of $\epsilon + \theta$ for three instrumented sections of the NREL Phase IV rotor. The factor f_{cl} is normalized to its maximum value at every instrumented section which, in agreement with equation 5.9, is found at $\epsilon + \theta$ closest to zero indeed. A comparison is made with a $\cos^4(\epsilon + \theta)$ behavior as applied in the model from CRES. The measurements show the dependency to be stronger than $\cos^4(\epsilon + \theta)$.

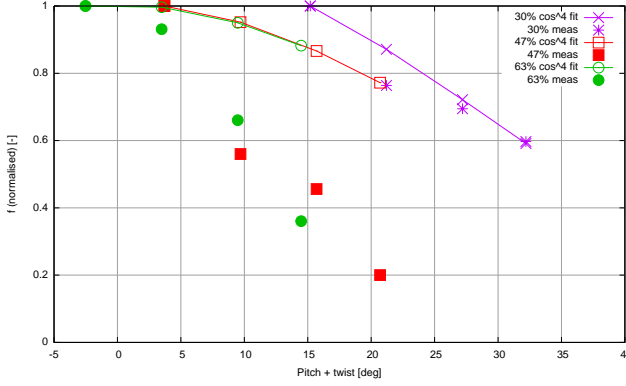


Figure 5.22: Normalised factor f_{cl} as function of pitch angle (+twist) for the NREL, Phase IV field measurements

- In [Schepers, van Rooij and Bruining, \(2003\)](#), it is shown that most c_t - α curves are overpredicted when using 2D drag data. This led to the suspicion that the drag coefficients are underpredicted. This is consistent with the overpredicted dimensional tangential forces from sections 5.7.1 and 5.7.2. The model from CRES does forecast an increase in drag coefficient on basis of equation 5.7 in which the value of f_{cd} is assumed to be similar to the value of f_{cl} :

$$f_{cd} = 2.2(c/r)\cos^4(\epsilon + \theta) \quad (5.13)$$

The increase in lift due to rotation is associated to the increased suction pressures. Since viscous drag is negligible at high angles of attack, the increased drag should also be apparent from the pressure distribution, but this is less transparent than it is for the lift. This is due to the fact that the drag forces are related to the pressure differences between the 'front' and 'rear' part of the airfoil. As such increased suction pressures at the rear part of the airfoil increase the drag, but this is opposed by increased suction pressures at the leading edge. Now, from a physical point of view it can anyhow be doubted whether the f -factor in the drag modelling should be similar to the f -factor in the lift modelling, as is the case in the model from CRES. This would imply that the modified pressure distribution effects the resulting force in normal direction similar as the force in tangential direction, which is difficult to comprehend.

Although measurements of c_d have been supplied to the IEA Task 14/18 (and Task 20) database, they are not expected to be a reliable basis for an engineering relation of the drag (if such relation exists at all). This is a result of the uncertainty in the tangential force (section 5.4) which, multiplied with the very uncertain $\sin(\alpha)$ term, forms an important contribution to the drag force. Nevertheless the NREL Phase IV c_d measurements have been analysed in a qualitative way. They show f_{cd} to depend on α where the maximum in f_{cd} seems to appear near $\alpha \approx 15$ degrees and is much (> 6 times) higher than the factor from equation 5.13;

- In [Schepers, van Rooij and Bruining, \(2003\)](#) it is shown that near the tip section ($r/R > 9$) both the $c_n(\alpha)$ and the $c_t(\alpha)$ curves are considerably overpredicted. This is consistent with the observations on the over-predicted dimensional normal and tangential forces at the tip section in section 5.7.1 and 5.7.2.

The considerations given above together with those from section 5.7.1 led to the following recommendations:

- A model should be developed which, compared to the original PHATAS modelling, yields higher normal forces at the root sections. Furthermore the tangential forces (i.e. the force towards the leading edge) should be decreased for all sections. For the tip sections ($r/R > 0.9$) both the normal as well as the tangential force should be decreased. Finally the dependency of f_{cl} on the pitch angle and angle of attack should be taken into account where the dependency on c/r should be as close as possible to the behavior found in equation 5.12;
- The model from CRES could form the basis for most of these improvements. This model had already included the pitch angle dependency and a c/r dependency which is close to equation 5.12. The relative high values for f_{cl} which result from the CRES model are expected to yield higher values of the normal force, closer to the measured data. Moreover the increased drag from the CRES model will reduce the tangential forces in agreement with the measured results.

Description of improved model

The model from CRES has been used as starting point, but some further refinements by means of 'trial and error' were applied. Thereto several para-

meters were varied systematically until the resulting local aerodynamic loads as calculated by PHATAS, showed an acceptable agreement with most measured loads.

- Lift modelling (i.e. f_{cl})

- Pitch angle and c/r dependency: The $\cos^4(\epsilon + \theta)$ dependency is enhanced to a $\cos^6(\epsilon + \theta)$ dependency, since the measurements from figure 5.22 indicate a stronger $(\epsilon + \theta)$ dependency. The c/r dependency was enhanced to a $(c/r)^{1.4}$ dependency;
- Angle of attack dependency: It was attempted to reproduce the measured behavior from figure 5.19. The maximum value of f_{cl} was assumed to appear at $\alpha=20$ degrees.

$$f_{cl, \alpha=20} = 3.8(c/r)^{1.4} \cos^6(\epsilon + \theta) \quad (5.14)$$

The angle of attack dependency has then been modelled in the following way: An initial increase in f_{cl} until $\alpha = 20$ degrees is modelled. This increase is assumed to be proportional to Δc_l . This difference increases with angle of attack. Hence:

$$f_{cl} = \frac{\Delta c_l}{\Delta c_l(\alpha = 20)} \cdot f_{cl}(\alpha = 20) \quad (5.15)$$

by which, see equation 5.5, the actual value of $c_{l,3D}$ becomes proportional to $(\Delta c_l)^2$. Between 20 and 25 degrees the factor f_{cl} remains constant. Between 25 and 60 degrees, the factor f_{cl} drops linearly to zero.

- Drag modelling (i.e. f_{cd}): The drag model is written in the form of equation 5.7. Because, as mentioned above, direct measurements on c_d are rather inaccurate most dependencies in the drag model were just copied from the lift model, where only information on the angle of attack dependency from the NREL PHASE IV c_d measurements was used in an indicative way. Then multiplication factors have been determined by means of trial and error. In summary this gave the following model:

- Pitch angle and c/r dependency: The dependency on the pitch angle and c/r remained similar to the dependency from equation 5.14, i.e. a $(c/r)^{1.4}$ dependency and a $\cos^6(\epsilon + \theta)$ dependency;
- Angle of attack dependency: The factor f_{cd} is assumed to be maximum at $\alpha = 15$ degrees. This maximum is defined to be:

$$f_{cd, \alpha=15} = 6.0 \cdot 3.8(c/r)^{1.4} \cos^6(\epsilon + \theta) \quad (5.16)$$

Hence the maximum value of f_{cd} is 6 times the value of the maximum f_{cl} . The value of f_{cd} increases until $f_{cd,\alpha=15}$ by making it proportional to $(c_{d,2D} - c_{d,2D,min})$. Between $\alpha = 15$ degrees and $\alpha = 20$ degrees the value of f drops linearly to

$$f_{cd,\alpha=20} = 2.5 \cdot 3.8(c/r)^{1.4} \cos^6(\epsilon + \theta) \quad (5.17)$$

Between $\alpha = 20$ degrees and $\alpha = 30$ degrees, f_{cd} remains constant to the value from equation 5.17 and between $\alpha = 30$ degrees and $\alpha = 45$ degrees, f_{cd} drops linearly to zero.

- Tip modelling. The tip loss model developed by [Shen et al. \(2005\)](#) has been applied. This model is based on the NREL Phase VI (Nasa-Ames) and FFA ([Ronsten \(1994\)](#)) wind tunnel measurements on 2-bladed turbines. It explicitly reduces the lift force coefficient and the resultant normal forces and tangential force coefficients to zero at the tip. For the three bladed rotors from IEA Task 14/18 the tip correction modelling has been modified, since the original model from [Shen et al. \(2005\)](#) was derived for 2-bladed rotors.

5.7.5 Comparison between calculations from modified model and measurements

In the figures 5.23, 5.24 and 5.25 the ratios between calculated and (IEA Task 14/18) measured normal forces, tangential forces, flatwise moments and rotorshaft torques are presented in a similar way as in section 5.7.1. It is recalled that the conditions of the different campaigns can be found in table 5.2. The following observations can be made:

- The normal forces at 30%, 47% and 63% span are predicted more accurately in particular at the high wind speed cases 4 and 5 (compare figure 5.12 with figure 5.23). The better prediction of the normal forces is reflected into a more accurate prediction of the flatwise moments, compare figure 5.25 with figure 5.14;
- The normal forces at the very tip (the 95% section) are predicted more accurately
- The tangential forces are still overpredicted at the high wind speeds (compare figure 5.13 with figure 5.24). This is a result of the higher values of the lift, which are only partly compensated by the higher drag from equation 5.16. As a consequence, the rotorshaft torque is slightly

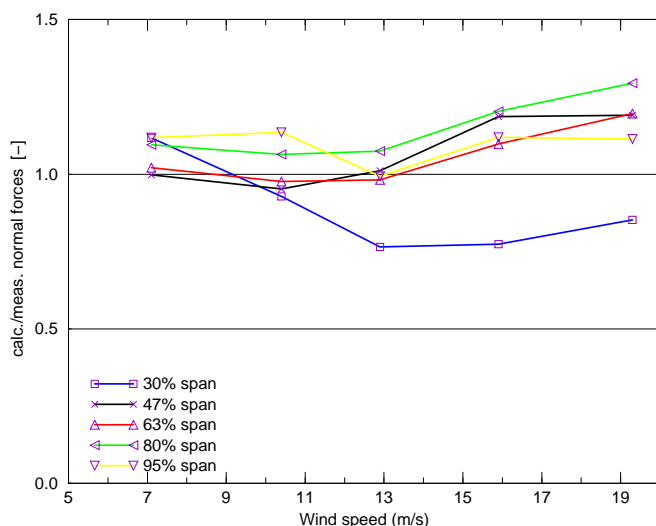


Figure 5.23: Modified ECN modelling: Ratio between calculated and measured values of the normal forces for the NREL phase IV field measurements from IEA Tasks 14/18 (time averaged)

overpredicted. It should be noted however, that the good agreement in torque from the original modelling is very misleading, since it is the result of two compensating errors: An underpredicted normal force in conjunction with an overpredicted tangential force. It might be tempting to increase the drag from equation 5.16. This did improve the agreement with the NREL Phase IV measurements indeed, but the agreement with the measurements on the other facilities became poorer.

The present model was developed in the Annexlyse project and should be considered as a 'common denominator' to all IEA Task 14/18 data. At a later stage it also improved the predictions at the inner and the very outer part of the NREL Phase VI (Nasa-Ames) blade but the results at 67% became somewhat poorer. On the other hand the Mexico measurements were pre-

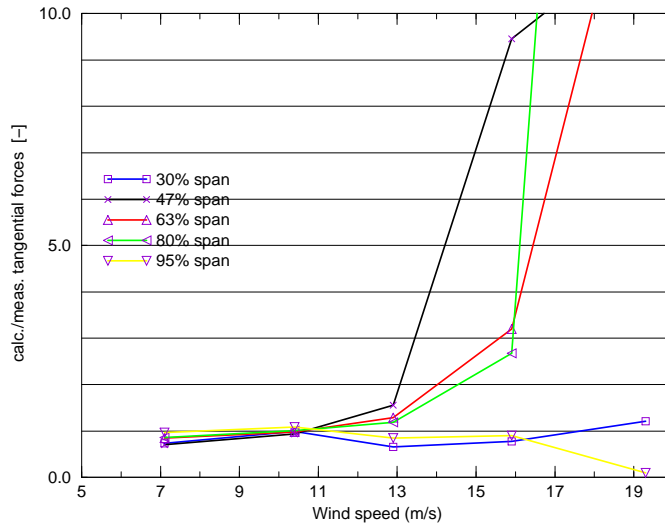


Figure 5.24: Modified ECN modelling: Ratio between calculated and measured values of the tangential forces for the NREL phase IV field measurements from IEA Tasks 14/18 (time averaged)

dicted best with equation 3.14 indicating that aerodynamic engineering methods sometimes perform well but in other cases the agreement may be poorer.

5.8 Conclusions and recommendation on blade aerodynamics

- The most important conclusion from the analysis of the present chapter is that the data from IEA Tasks 14/18, 20 and 29 enabled a detailed validation of blade aerodynamic models on basis of local aerodynamic loads. The large amount of data on different facilities made that trends and dependencies in the models could be confirmed, investigated and/or

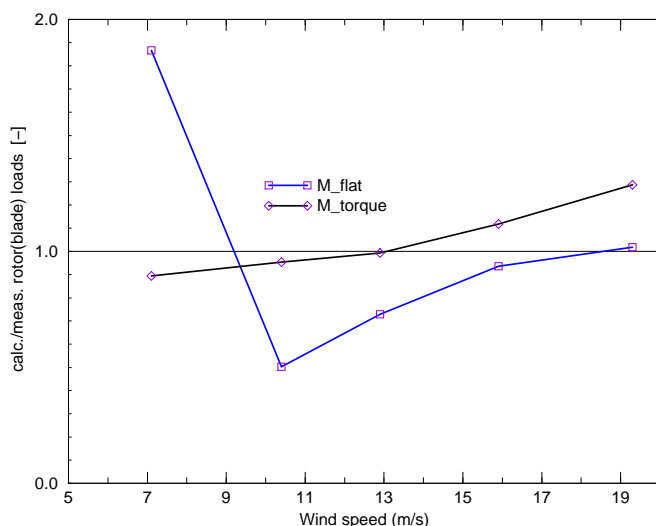


Figure 5.25: Modified ECN modelling: Ratio between calculated and measured values of the flatwise moment and the rotor shaft torque for the NREL phase IV field measurements from IEA Tasks 14/18 (time averaged)

discovered. Differences between calculated and measured blade and rotor loads were found to have a very complicated origin and only measurements of the underlying sectional loads can help to understand this origin. Examples were found where the overall rotor(blade) loads were predicted in good agreement with the measured values but the agreement of the underlying local loads was very poor. The good agreement in overall loads was then a result of 'compensating errors'. However, the complexity of the phenomena and the large number of dependencies makes that even (much) more measurements are needed. Moreover good drag measurements are urgently needed.

- The validation of aerodynamic models with the measurements from the IEA tasks was complicated by an uncertainty in angle of attack and

dynamic pressure. By comparing calculated and measured dimensional local loads this uncertainty could be avoided. A comparison of data on basis of a resultant force coefficient versus resultant force angle is another way of avoiding the uncertainty in angle of attack.

- The overall rotor(blade) loads have been determined by integrating the local loads along the blade. This yields rotor(blade) loads which agree extremely well with the directly measured loads as long as the contribution of the tangential force is small;
- All measurements indicate a clear stall delay at the inner part of the blade at high angles of attack. Hence the loads are under predicted when they are calculated with 2D airfoil coefficients. CFD codes were found to predict the stall delay effect in better agreement than engineering methods.
- The effect of the rotational speed on the aerodynamic load coefficients was generally found to be small. Only for very small rotors at low rotational speeds a rotor speed dependency is visible near stall.
- A new model is developed to correct the 2D airfoil data for rotational stall effects. The model can be considered as a common denominator of the measurements from this chapter. It uses the model from CRES ([Chaviaropoulos and Hansen \(2000\)](#)) as a basis. The advantage of the CRES model lies in a stronger stall delay effect on the lift coefficient than the model from equation 3.14. This was found to be correct in most (but not all!) measurements. Moreover the CRES model has included a dependency of the stall delay effect on the pitch angle which was also observed in the measurements. Finally it forecasts the increase in drag in agreement with the measurements from this chapter. Nevertheless some modifications still needed to be made to the CRES model in order to improve the general agreement with the measurements. Among others, a dependency on the angle of attack has been implemented and the drag modelling needed to be adjusted.
- The normal and tangential forces at the tip (say $r/R > 0.9$) are over predicted when using 2D airfoil characteristics as input to a BEM code in which the tip effects are only covered by the Prandtl tip loss factor. This is due to a 3D effect on the airfoil characteristics which is not taken into account in the Prandtl tip loss factor. A correction to the 2D airfoil data at the tip was applied in order to reduce the loads. Thereto a slightly modified version of the model from [Shen et al. \(2005\)](#) was used. It is

recommended to derive a more physical model for these tip effects. This could be based on the well known thin airfoil theory, see e.g. [Katz and Plotkin \(2001\)](#). This theory is commonly applied for 2D airfoils, where the airfoil is represented by vorticity distributed on a thin 2D camber line along an infinitely long 'blade'. A more physical representation of the flow near the tip can be obtained by a semi-infinite blade model, in which vorticity is only present in the direction of the root. This will reduce the gradient $dc_1/d\alpha$ to values $< 2\pi$ and hence the resultant tip loads are reduced as well.

Chapter 6

Progress on induction aerodynamics, based on flow field measurements from IEA Task 29

6.1 Introduction on induction aerodynamics

In this chapter the progress is described which has been made on understanding the flow field in and around the rotor based on the flow field measurements from the Mexico experiment. As explained in chapter 2.1.1 this flow field is determined by the induced velocities, i.e. the disturbances to the free stream wind field as generated by the wind turbine. These induced velocities can be calculated with the momentum theory from the loads on the rotor. In its basic form this momentum theory is applied on an actuator disc under the assumption of steady and non-yawed conditions. The present chapter is then devoted to a validation of the basic aspects of the momentum theory which is offered by the PIV measurements of the flow field in and around the rotor plane from the Mexico experiment. This includes an assessment of the velocity behavior in streamwise and radial direction and a relation between the velocities and the loads on the rotor. The measurements are also compared with results from a simplified vortex wake method. This model was already briefly touched upon in section 2.1.1, where it was mentioned that the results

from the model are fully compatible to those from the momentum theory. The advantage of the cylindrical vortex wake model lies in the fact that the entire velocity decay from $x = -\infty$ to $x = +\infty$ is covered, where the momentum theory only considers the velocities in the rotor plane and far downstream. The cylindrical vortex wake model is described in more detail in section 6.2.

The wake vorticity in such vortex wake methods is calculated from the bound circulation along the blade which is determined by the aerodynamic blade loads. In the Mexico experiment both the tip vortices in the wake as well as the aerodynamic loads on the blades are measured. This makes it interesting to relate the results from both types of measurements which is done in section 6.3.1.

Then the sections 6.3.2 and 6.3.3 present an analysis of the axial and radial velocity traverses. This includes a comparison with calculational results from the cylindrical vortex wake method and from CFD codes as employed within IEA Task 29(Mexnext).

This is then followed by an analysis of the flow non-uniformities in the rotor plane due to the finite number of blades in section 6.3.4. The results are used to assess the Prandtl tip loss factor, which covers these flow non-uniformities in momentum theory, see section 3.4.

Furthermore the following remarks can be made on the results of the present chapter:

- All measurements have been taken at a rotational speed of 424 rpm and a pitch angle of -2.3 degrees;
- The present chapter only considers induction effects at non-yawed and steady conditions. Induction effects at unsteady (Dynamic Inflow) and yawed conditions are described separately in the chapters 7 and 8;
- Unless otherwise stated, the present chapter only considers the u component, i.e. the velocity in streamwise direction;
- The present chapter applies the definition of ϕ_r according to figure 4.7, i.e. zero azimuth angle corresponds to blade 1 at the 12 o'clock position).
- Many of the results from the present chapter have already been reported in [Schepers, Snel and Boorsma \(2010\)](#), [Schepers, Pascal and Snel](#)

(2010) and Schepers et al. (2011)

6.2 Cylindrical vortex sheet method

The cylindrical vortex wake sheet method as described in Snel and Schepers (1994) has the following features and assumptions:

- The blade is modelled as a vortex line from the rotor axis to the tip with a constant bound vortex strength Γ along the radius. This implies that all the vorticity which is trailed into the wake is concentrated at the tip and the root. The vorticity which is trailed at the tip is 'smeared out' over a cylindrical vortex sheet, see below.

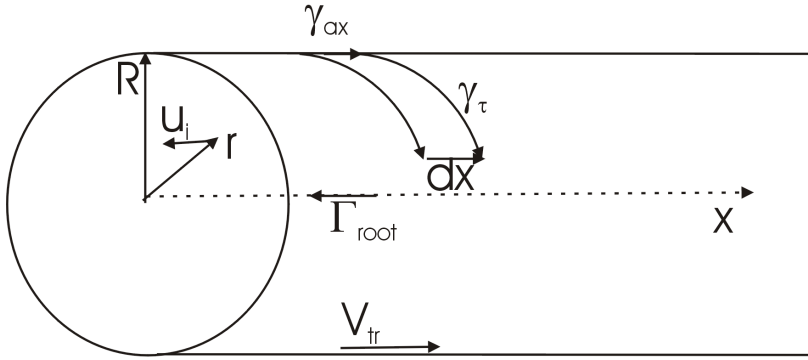


Figure 6.1: Simplified vortex wake model

- The bound vortex strength is related to the axial force coefficient $C_{D,ax}$ of the rotor. Using the Kutta-Joukowski theorem:

$$\tilde{\mathbf{F}} = \rho \tilde{\mathbf{V}} \times \tilde{\Gamma} \quad (6.1)$$

this gives (for the axial force on the blade ($F_{ax,blade}$)):

$$F_{ax,blade} = \rho \Gamma \int_0^R \Omega r dr = 0.5 \rho \Gamma \Omega R^2 \quad (6.2)$$

in which the tangential induced velocity is neglected. The axial force on the blade can also be written as the axial force on the rotor divided by

the number of blades, hence:

$$F_{\text{ax,blade}} = \frac{C_{D,\text{ax}} 0.5 \rho V_w^2 \pi R^2}{B} \quad (6.3)$$

which yields the following relation between the bound vortex strength and the axial force coefficient of the rotor:

$$\Gamma = \frac{\pi C_{D,\text{ax}} V_w^2}{\Omega B} \quad (6.4)$$

- The bound vortex which is trailed from the tip of the blade is distributed over a semi-infinite cylinder sheet with radius R equal to the rotor radius. This implies that deformation (expansion) of the tip vortex wake is neglected. The trailed vorticity is decomposed into an axial and tangential component of the wake vorticity where it is the tangential component (γ_t) which induces the axial velocities in the rotor plane. The tangential vorticity density is found by distributing the bound vortex strength over the distance which the vortex has transported until the next blade passes. The vorticity is assumed to be transported with a constant velocity equal to the velocity with which it is trailed at the blade tip ($V_{\text{tr}} = V_w - u_i$).

Hence

$$\gamma_t L = B \Gamma \quad (6.5)$$

with L = the length over which the vorticity is transported during one revolution:

$$L = V_{\text{tr}} \frac{2\pi}{\Omega} \quad (6.6)$$

This gives the following relation between the bound vortex Γ and the wake vorticity γ_t .

$$\Gamma = \frac{\gamma_t V_w (1 - a) 2\pi}{B \Omega} \quad (6.7)$$

- The axial velocities are calculated from the tangential vorticity density with the law of Biot-Savart. The resulting equation for the axial induced velocity in the rotor plane at a radial position r , is an integral over the cylinder surface (with x the streamwise and ϕ_r the azimuthal coordinate):

$$u_i = \frac{R}{4\pi} \int_{x=0}^{\infty} \int_{\phi_r=0}^{2\pi} \frac{\gamma_t(x) [R - r \cos \phi_r]}{[x^2 + R^2 + r^2 - 2rR \cos \phi_r]^{3/2}} d\phi_r dx \quad (6.8)$$

- For equilibrium conditions (i.e. constant wind speed and $C_{D,ax}$) the bound vortex strength and the resulting wake vorticity are constant. Hence γ_t can be placed outside the integral in equation 6.8. This makes it possible to solve equation 6.8 analytically. The final solution of equation 6.8 (also using equations 6.7 and 6.4) turns out to be the well known momentum theory equation (see [Snel and Schepers \(1994\)](#) for more details):

$$C_{D,ax} = 4a(1 - a) \quad (6.9)$$

Furthermore equation 6.8 yields the following relation for the induced velocity in the cylindrical vortex sheet:

$$\frac{u_i(x)}{u_i(x = \infty)} = 0.5 + \frac{0.5f}{(f^2 + 1)^{0.5}} \quad (6.10)$$

with f the downstream distance to the rotor, non-dimensionalized with the rotor radius, i.e. $f = x/R$. The velocity is independent of radial position. Equation 6.10 shows the induced velocity at infinity to be twice the induced velocity in the rotor plane, which is again in agreement with momentum theory (equation 2.7). Note that for unsteady conditions the γ_t term should be placed inside the integral by which the solution of the equation becomes much more complicated. This is of relevance for the modelling of dynamic inflow effects, as discussed in section 7.2.1.

- The tangential velocities are induced by the axial vorticity components. It can then be shown that it is only the root vorticity which induces these tangential velocities. The law of Biot and Savart then dictates that the tangential induced velocity is large at the root where it decreases towards the tip. In [Snel and Schepers \(1994\)](#) the velocities induced by the root vorticity are found to resemble very closely the tangential induced velocities from the conservation of angular momentum.

6.3 IEA Task 29(Mexnext): PIV measurements at non-yawed conditions

6.3.1 Tip vortex strength in relation to blade circulation

In this section the pressure measurements from the Mexico experiment are translated into the bound vortex strength along the blade (i.e. the blade circulation) which is then compared with the tip vortex strength as derived from the

PIV measurements. The results are also described in [Schepers, Pascal and Snel \(2010\)](#).

The bound vortex strength along the blade is determined from the Kutta-Joukowski theorem (equation 6.1). $\Gamma = \frac{L}{\rho V_{\text{eff}}}$

Where L is the lift force per unit length which is found from the pressure distribution and V_{eff} is the resultant velocity at the blade section, see figure 2.4. This velocity includes the induced velocities. Thereto the tangential induction is neglected. The axial induction is found by assuming it to be half the value at the most downward position from the PIV measurements (i.e. 1.3D behind the rotor) in agreement with momentum theory (Note that this axial induction factor was also used to determine the angle of attack which was needed in the determination of the lift force from the pressure distributions). The tip vortex

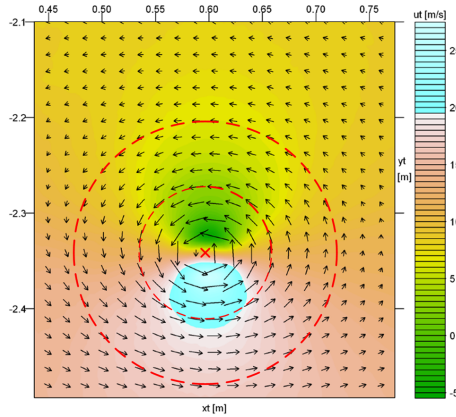


Figure 6.2: Measured velocity field at 0.6 m behind the rotor containing a tip vortex. The circles were used for the integration to vortex strength

strength in the wake is found from the integral: $\Gamma = \oint \tilde{V} d\tilde{s}$ along circles of different radii in the flow field, see figure 6.2.

In figure 6.3 the tip vortex strength at different wake positions is given as function of integration radius at design conditions (i.e. $V_{\text{tunn}} = 15$ m/s). It can be seen that the tip vortex strength reaches an asymptotic value with increas-

ing integration radius. Also indicated is the maximum bound vortex strength along the blade as derived from the pressure measurements. In [Schepers, Pascal and Snel \(2010\)](#) it was found that the maximum vortex strength for these conditions occurs at 35% span but as a matter of fact it varied only between 3.73 to 4.1 m²/s (with the exception of the 92% station where the bound vortex strength, due to tip effects is lower (3.58 m²/s)). Such (almost) constant bound vortex strength is expected at the present (design) conditions since it goes together with a constant induction along the entire blade which was one of the design targets for the Mexico blade.

It is then interesting to see a good agreement between the asymptotic value of the tip vortex strength in figure 6.3 and the bound vortex strength which indicates a very good correlation between the results from these two very different types of measurements (pressure measurements and PIV measurements).

Similar studies have been done at $V_{\text{tun}} = 10$ m/s and $V_{\text{tun}} = 24$ m/s by [Pascal \(2009\)](#). At these conditions a much stronger variation in bound vortex strength along the blade is found. This could be expected from the fact that these measurements are done at off-design conditions. Nevertheless the bound vortex strength at 82% span still compares well with the tip vortex strength.

6.3.2 Axial velocity traverses

In the figures 6.5 to 6.6 the measured axial velocity decay at 61% and 82% span is shown for different rotor loadings ($V_{\text{tun}} = 10$ m/s i.e. $\lambda = 10.0$, $V_{\text{tun}} = 15$ m/s, i.e. $\lambda = 6.67$ and $V_{\text{tun}} = 24$ m/s, i.e. $\lambda = 4.17$).

As explained in section 4.5, these measurements are done in the horizontal plane at the '9 o'clock position' in a phase locked way (with blade 1 at the 12 o'clock position). They are averaged over several samples. The velocity measurements in many upstream PIV sheets show some similar 'wiggles'. This might possibly be caused by the 1P trigger sensor (from which the blade position is derived). This trigger was sometimes found to behave unstable during the experiments. Also indicated are the results from the cylindrical vortex sheet method as described in section 6.2.

At design conditions i.e. $V_{\text{tun}} = 15$ m/s, the axial force coefficient in the cylindrical vortex sheet method was set to the expected value of 0.89. At $V_{\text{tun}} = 10$ m/s and $V_{\text{tun}} = 24$ m/s they have been calculated with the ECN BEM

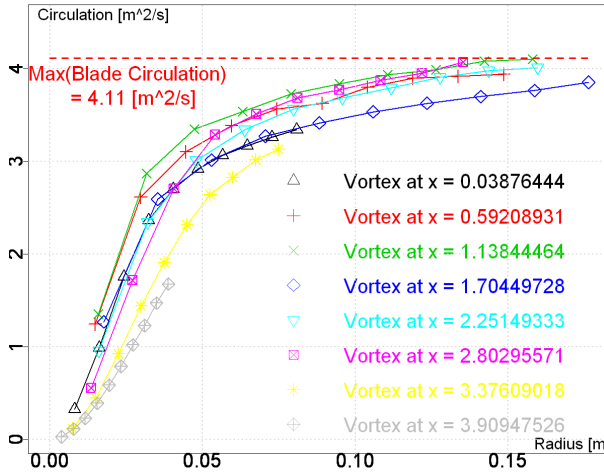


Figure 6.3: Tip vortex strength as function of integration radius for different x-positions in the wake (x-position indicated in meters). Also indicated is the maximum blade circulation.

model BOT (Bot and van Langen (2006)) which yielded $C_{D,ax} = 1.04$ and 0.433 respectively. It should then be noted that a value of $C_{D,ax} > 1$ is not possible in the cylindrical vortex sheet method since it is not capable of modelling the turbulent wake state (a discussion of the turbulent wake state is given in section 3.5). For this reason a slightly lower value of $C_{D,ax} = 1.0$ was prescribed for the calculations at $V_{tun} = 10$ m/s.

The high value of $C_{D,ax}$ at $V_{tun} = 10$ m/s leads to a very strong deceleration of the wake, i.e. the velocity is reduced to $V < 1$ m/s at $x = 5.9$ m and 82% span. Since the conditions are anyhow very close to the so-called turbulent wake state it could be expected that back flow in the wake occurs. The present measurements indicate very low, but still positive, velocities with a smooth flow although there is still a deceleration at the most downstream position.

At $V_{tun} = 24$ m/s, the blades are stalled (This was confirmed from the pressure measurements) and the velocity decays show a more chaotic behavior which is a result of vortex shedding from the stalled boundary layer into the

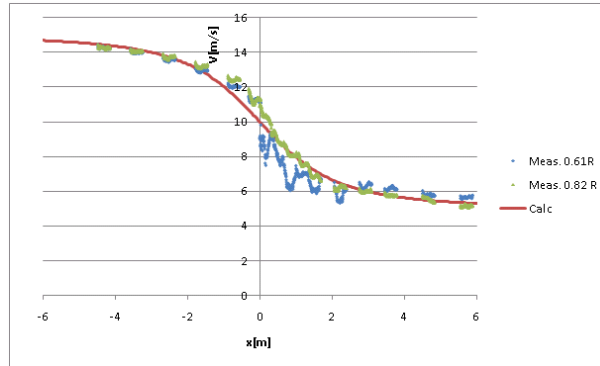


Figure 6.4: Mexico: Measured axial velocity decay at 61% and 82% span at $V_{tun} = 15$ m/s compared with results from a cylindrical vortex sheet method, $\phi_r = 0$ degrees.

wake.

At $V_{tun} = 15$ m/s (i.e. design conditions) the axial velocity decay downstream of the rotor at 61% span is striking in the sense that velocity fluctuations appear near the rotor plane. These are most likely a result of the transition from the DU airfoil to the RISØ airfoil near that position, see section 4.5. Since the RISØ airfoil has a different zero lift angle of attack compared to the surrounding DU and NACA airfoils this leads to a change in bound vortex strength near this location. As explained in section 5.7.3 this change is largest at $V_{tun} = 15$ m/s.

Generally speaking a good agreement is found between the measured decay and the decay from the cylindrical vortex wake model. This is in particular true at the locations upstream of the rotor plane and at more downstream positions in the wake. The discrepancies near the rotor plane are partly explained by the actuator disc assumption in the cylindrical vortex wake model which implies a uniform flow in the rotor plane, opposite to the real flow field situation, where the finite number of blade yields a strong non-uniformity, see section 6.3.4. Moreover the velocity fluctuations due to stall cannot be reproduced in the cylindrical vortex wake model, since this model does not include stall. Also the velocity fluctuations at 61% span and $V_{tun} = 15$ m/s due to the transition in airfoils cannot be reproduced since the model assumes a con-

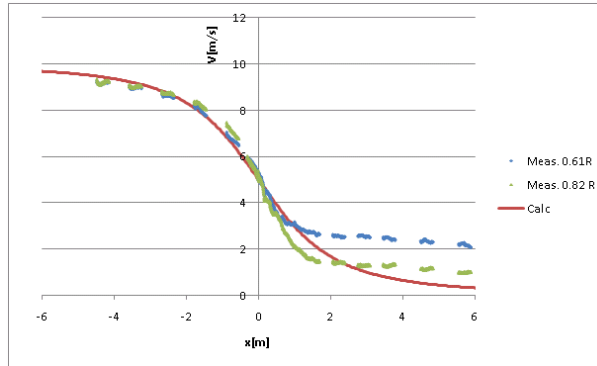


Figure 6.5: Mexico: Measured axial velocity decay at 61% and 82% span at $V_{\text{tunn}} = 10$ m/s compared with results from a cylindrical vortex sheet method, $\phi_r = 0$ degrees.

stant bound vortex strength along the blade.

The cylindrical vortex wake model finds the velocity to be independent of radial position. This assumption is to some extent confirmed by the present measurements, in particular at the locations upstream of the rotor and at the more downstream positions in the wake. An exception is found in the results at $V_{\text{tunn}} = 10$ m/s where the velocity in the wake and at 82% span is predicted well but the velocity at 61% span is underpredicted. It is recalled that this measurement is done at a condition very close to the turbulent wake situation, which is an extreme case in the sense that the momentum theory (and the cylindrical vortex wake model) are expected to break down, going together with a large non-uniformity of the flow.

Hence the measured velocity decay at design conditions agrees very well with the momentum theory but it is recalled that the C_{Dax} was set to the expected value of 0.89. It is then very striking to note that the measured C_{Dax} from figure 5.4 at a design tip speed ration of 6.67 only seems to be 0.72! Such low C_{Dax} yields much lower axial induced velocities and hence a higher velocity level, see figure 6.7 The first logical explanation would be that the C_{Dax} measurements from figure 5.4 are incorrect. Although the uncertainties in the rotor axial force as determined from the balance and the pressure integration are acknowledged, this is still difficult to comprehend since the val-

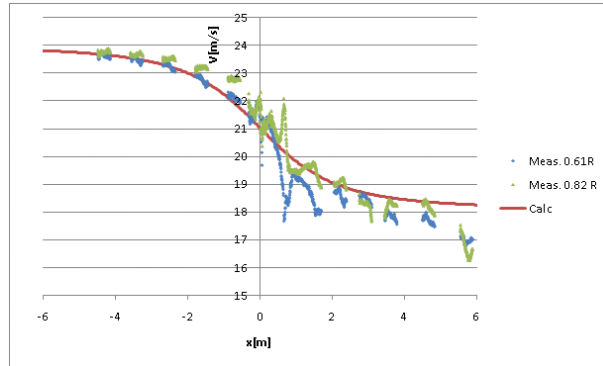


Figure 6.6: Mexico: Measured axial velocity decay at 61% and 82% span at $V_{\text{tun}} = 24$ m/s compared with results from a cylindrical vortex sheet method, $\phi_r = 0$ degrees.

ues are determined with two fully independent measurement techniques, the results of which agree very well at all data points with different tunnel speeds and different rotational speeds.

Another explanation for the anomalies could be tunnel effects. An extensive investigation on the impact of these effects took place within the Mexnext project on basis of CFD calculations, see also section 4.5.1. Until now the impact of these effects seems to be small at design conditions, and the limited effect which has been found points in the opposite direction: When the induction in the tunnel is the same to the induction in the free stream, the $C_{D_{\text{ax}}}$ is higher in the tunnel situation. This implies that the free stream $C_{D_{\text{ax}}}$ would even be lower than 0.72.

A logical consequence is that none of the calculations produced within IEA Task 29(Mexnext) can predict both the velocities AND loads in a correct way. The comparison between calculated and measured normal forces was already discussed in section 5.7.3, where it was found that most codes overpredict the loads at design conditions. The comparison between the CFD calculated and measured velocity decay at 80% span is shown for all three tunnel speeds in the figures 6.8 to 6.10. Most of the codes overpredict the velocities (i.e. they underpredict the axial induced velocity). For those codes which donot overpredict the velocities it is found that they overpredict the loads to a larger

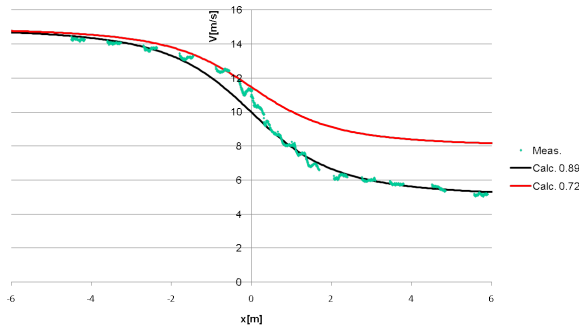


Figure 6.7: Mexico: Axial velocity decay for 82% span from cylindrical vortex sheet method at $C_{Dax} = 0.89$ and 0.72

extent. Hence the prediction of loads and velocities of the Mexico experiment seems to act as communicating vessels: A better prediction of velocities goes together with a larger overprediction of the loads and vice versa. Despite this puzzling observation it is encouraging to see a good qualitative prediction of the velocity decay even at $V_{tun} = 24$ m/s where the velocity fluctuations due to stall are predicted very well.

6.3.3 Radial velocity traverses

In figure 6.11 the measured radial velocity traverse at a distance of 0.3 m downstream of the rotor plane is presented. It is compared with CFD calculations from IEA Task 29(Mexnext). As explained in section 4.5 the radial traverses are measured in a horizontal PIV plane at the 9 o' clock position at different blade positions. Then figure 6.11 shows the result for the blade at $\phi_r = 60$ degrees

In figure 6.12 the corresponding result is shown at a distance of 0.3 m upstream of the rotor plane.

A first general observation is again an overprediction of the velocities in agreement with the results from section 6.3.2.

Figure 6.11 shows, in both measurements and calculations a low velocity in the wake where the velocity increases at the edge of the wake (i.e. near r

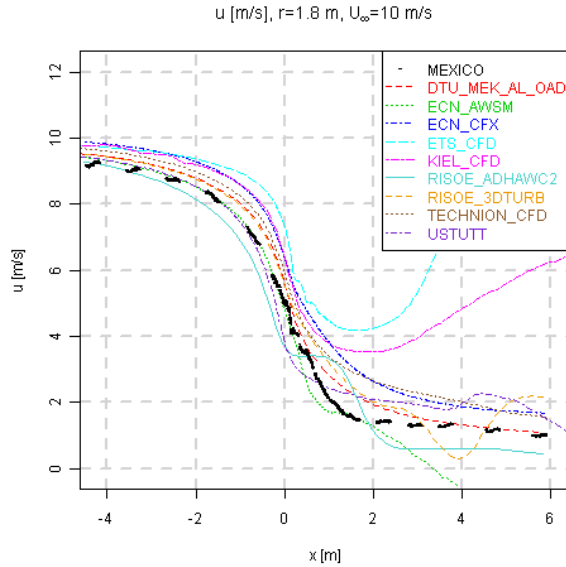


Figure 6.8: IEA Task 29(Mexnext): Axial velocity decay at 80% span, measured and calculated with CFD codes, $V_{\text{tunn}} = 10$ m/s, $\phi_r = 0$ degrees.

≈ 2.25 m). This increase is associated to the presence of the tip vortex. As such it confirms to some extent the stream tube concept from the momentum theory with a constant low velocity in the wake and a sudden abrupt change towards the free stream velocity at the edge of the wake. It can be observed that many CFD codes predict the increase in velocity to be less abrupt than the measured increase. The significant drop in velocity towards the inboard positions is most likely a result of the vorticity due to the transition in airfoils (with different zero lift angles of attack), which leads to a change in bound vortex strength along the blade. It is interesting to note that the CFD calculations, though they do predict a small change in bound vortex strength at that location have not been able yet to predict the drop in velocity. The vorticity is also present in figure 6.13 in which the PIV sheets in this region are concatenated. The figure shows an unexpected velocity discontinuity which could very well be attributed to this phenomenon. The agreement between calculations and measurements is qualitatively very good at the upstream position, figure 6.12. The lowest velocity is found inboard from where it increases gradually towards

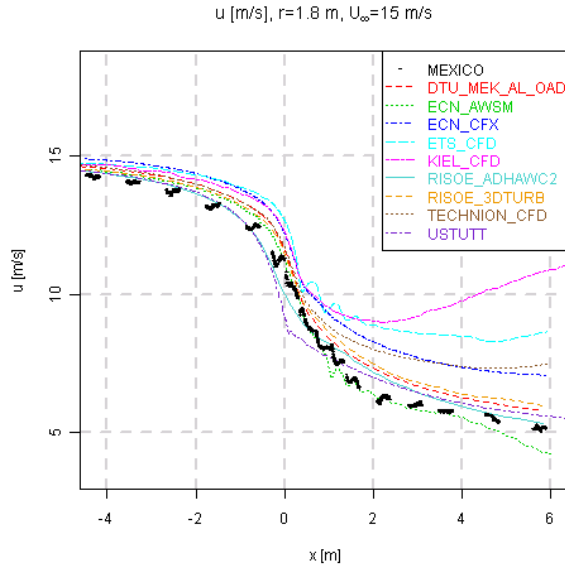


Figure 6.9: IEA Task 29(Mexnext): Axial velocity decay at 80% span, measured and calculated with CFD codes, $V_{\text{tun}} = 15 \text{ m/s}$, $\phi_r = 0$ degrees.

the free stream velocity, although this value is not reached yet at the edge of the measurement range at 122% span. This is obviously different from the momentum theory concept which assumes a lower velocity in the streamtube (with radius smaller than the rotor radius) and a discontinuous jump towards the free stream velocity at the edge of the streamtube.

6.3.4 Flow non-uniformities in the rotor plane

In the figures 6.15 to 6.17 the velocities as measured very near the rotor plane are presented. The results are extracted from the radial velocity traverses. They are plotted along the x-range of the two PIV sheets, just upstream and just downstream of the rotor plane at $r/R = 80\%$, 92% and 120% . The two PIV sheets have a small overlap in the rotor plane, see figure 4.6. The tunnel speed is 15 m/s . The different lines represent different blade azimuth positions, the colour legend of which is indicated in figure 6.14. It is again recalled that the present chapter defines the zero azimuth angle of blade 1 to be at

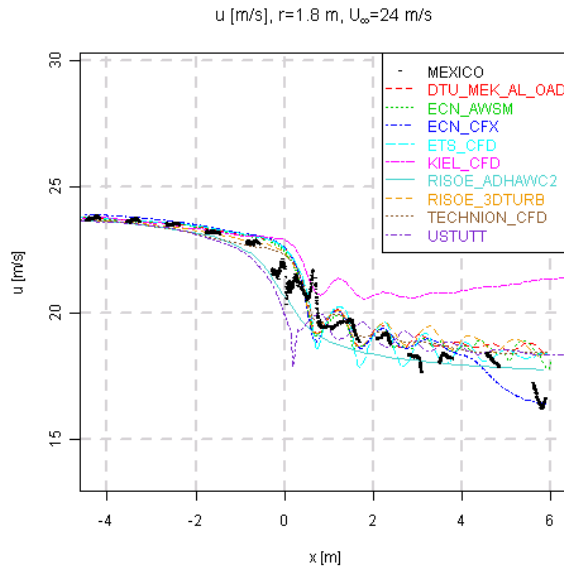


Figure 6.10: IEA Task 29(Mexnext): Axial velocity decay at 80% span, measured and calculated with CFD codes, $V_{\text{tunn}} = 24$ m/s, $\phi_r = 0$ degrees.

'12 o' clock'. This implies that the other blades are generally closer to the PIV sheet at '9 o' clock'.

First it is interesting to note the multi-valued curves near $x=0$, which are a result of the overlapping PIV sheets at this position. The results are usually (but not always) very compatible indicating a good quality of the data. This is also confirmed by the (generally) good compatibility of the results at $\phi_r = 0$ and 120° . Thereto it should be realized that the flow situation at $\phi_r = 0$ and 120° should be similar for a 3-bladed rotor (at least when the blade geometries (and settings) are similar). The flow similarity between $\phi_r = 0$ and 120° degrees then confirms this to be true.

Outboard section

At the outboard station (viz. 120% span, see figure 6.15) a clear maximum is visible in the velocity traverse $u(x)$, the magnitude and location of which

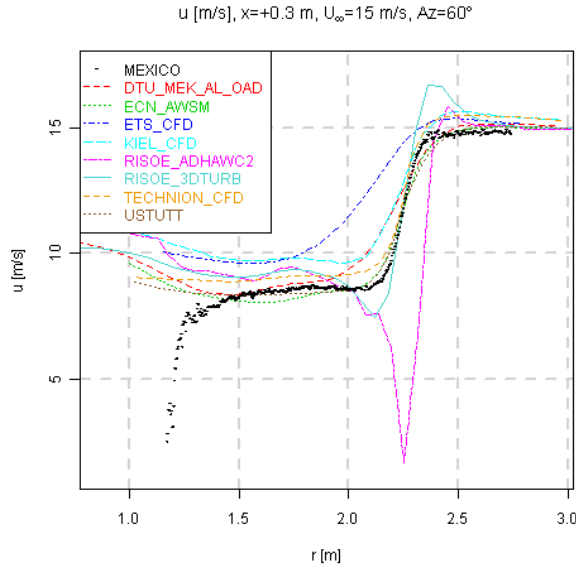


Figure 6.11: IEA Task 29(Mexnext): Radial velocity traverse, 0.3 m downstream of the rotor, measured and calculated with CFD codes. $V_{tun} = 15$ m/s, $\phi_r = 60$ degrees

depends on the blade azimuth position. This maximum velocity is induced by the tip vortex at the x -location where it crosses the horizontal plane, i.e. the position where the tip vortex is as close as possible to the PIV sheet, see figure 6.19. This figure shows the tip vortex to induce a positive x -velocity at outboard positions. The x -location where the tip vortex crosses the PIV sheet depends on the tip vortex travel speed. In [Snel et al. \(2009\)](#) the tip vortex tracking measurements have been analyzed which resulted in a vortex travel speed in the order of 11.86 m/s, constant throughout the wake. As noted in the same reference this is smaller than the often assumed averaged value of the free stream and wake velocity (which would give 12.5 m/s in the rotor plane based on $V_{tun} = 15$ m/s and an axial induction factor of 1/3). On basis of the present analysis, an even lower transport velocity of 11.2 m/s is found near the rotor plane (since the tip vortex has travelled from $x= 0.0997$ m at $\phi_r = 40$ degrees to $x= 0.2774$ m at $\phi_r = 80$ degrees). It must be realized however that the maximum in the velocity traverse is very flat which makes it difficult

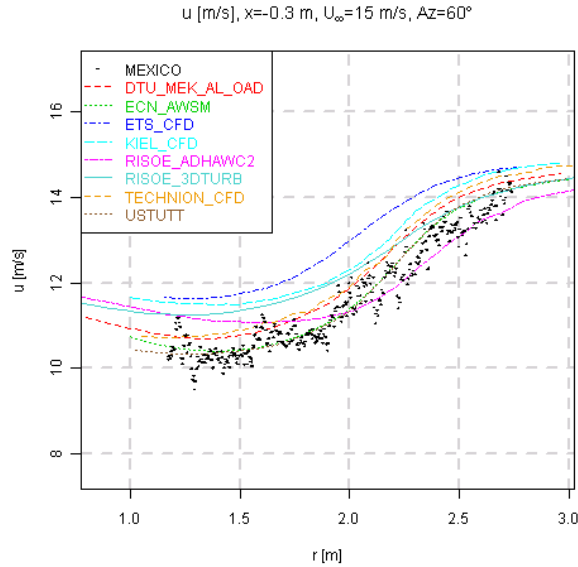


Figure 6.12: IEA Task 29(Mexnext): Radial velocity traverse 0.3 m upstream of the rotor, measured and calculated with CFD codes. $V_{\text{tun}} = 15\text{ m/s}$, $\phi_r = 60$ degrees

to determine the precise location of the tip vortex and resulting vortex travel speed.

Figure 6.15 shows the maximum velocity at $\phi_r = 40$ degrees to be smaller than the velocity at $\phi_r = 60$ degrees, where the velocity at $\phi_r = 60$ degrees is again smaller than the velocity at $\phi_r = 80$ degrees. This can be explained by the fact that the relevant tip vortex at $\phi_r = 40$ degrees is trailed from blade 3 at 280 degrees azimuth (since ϕ_r refers to the position of blade 1). Hence the tip vortex crosses the horizontal plane just downstream of the rotor plane. At this position the wake expansion is still limited by which the tip vortex is relatively far from the 120% span location. Consequently the velocity induced by the tip vortex at that position is relatively weak. At $\phi_r = 80$ degrees the tip vortex is trailed at 320 degrees by which it crosses the horizontal plane much further downstream. This goes together with a more outboard location, i.e. closer to the 120% span location, where the tip vortex induces a stronger velocity.

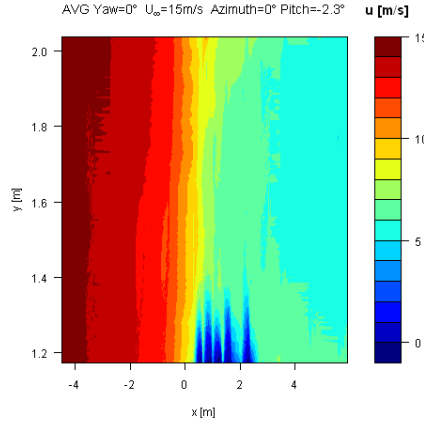


Figure 6.13: IEA Task 29(Mexnext): Contours of axial velocity from PIV (x in axial, y in radial direction, origin in rotor center) [‡]

[‡] Missing values between PIV sheets have been linearly interpolated

Inboard sections

At the inboard stations (viz. 80% and 92% span, figures 6.16 and 6.17) a strong non-uniformity in the rotor plane can be observed with a jump in velocity when the blade moves from $\phi_r = 20$ to $\phi_r = 40$ degrees. Thereto it should be realised that $\phi_r = 20$ degrees corresponds to a position of blade 3 at 260 degrees i.e. just below the PIV sheet at 270 degrees azimuth where its bound vortex increases the axial velocity, see figure 6.18. At $\phi_r = 40$ degrees the blade is just above the PIV sheet and the bound vortex decreases the axial velocity. The jump in velocity is slightly less at 92% span consistent with the observation of a smaller bound vortex strength at this location which was found in section 6.3.1 from the pressure measurements.

Even if these blade positions are excluded the non-uniformity in the flow remains large: At 80% span and $x=0$ m, the velocity varies from $u = 9.5$ m/s at $\phi_r = 60$ degrees to $u = 11.2$ m/s at $\phi_r = 120$ degrees. At 92% span, the velocity varies from $u = 11$ m/s at $\phi_r = 60$ degrees to $u = 12$ m/s at $\phi_r = 120$ degrees. The velocities induced by the tip vortex are visible in the form of a (relatively slight) minimum at those x-locations where the velocity at 120% span appears

to be maximum. This is as expected since the positive x-velocity as induced at positions outboard of the tip vortex, turns into a negative velocity at an in-board location.

It is interesting to average the velocities in the rotor plane over all azimuth angles in order to get an indication of the induction in the rotor plane. At 80% span, the averaged velocity is 10.37 m/s (where the velocity results at $\phi_r = 20$ and 40 degrees are not included in the averaging). This corresponds to an axial induction factor of 0.31 close to the expected value of $1/3$. At 92% span the averaged velocity is 11.5 m/s. This corresponds to an averaged induction factor of 0.23.

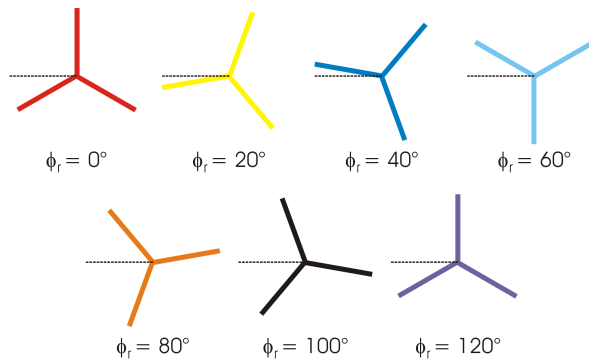


Figure 6.14: Position of blade 1 at $\phi_r = 0, 20, 40, 60, 80, 100, 120^\circ$

Tip effects

If the measurements from figures 6.15 to 6.17 are to be used for a direct assessment of the Prandtl tip loss factor it should be realised that this factor relates the local blade velocity to the annulus averaged velocity. The traverses from figures 6.15 to 6.17 have been made at 6 different blade positions but none of them correspond to 270 degrees, i.e. the position where the blade is in the PIV sheet. Such measurements are however available from the so-called tip vortex tracking experiments. This experiment is explained in section 4.5 where it is described that it measures the flow field near the blade tip at a blade position of 270 degrees.

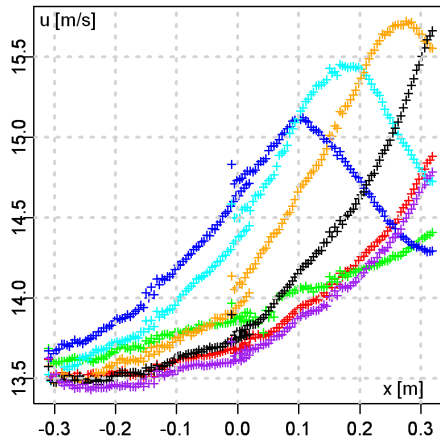


Figure 6.15: IEA Task 29(Mexnext): Velocities near the rotor plane as function of axial coordinate at 120% span and $V_{\text{tun}} = 15 \text{ m/s}$. Different lines represent different blade positions, see figure 6.14

The assessment of the Prandtl tip loss factor is further supported by AWSM calculations. Thereto it is recalled from section 3.4 that the Prandtl tip loss factor has been determined in the pre-computer era (1919) with a very simplified vortex wake model. At present numerical full vortex wake methods like AWSM have been developed which open the door to estimate the tip loss factor in a more accurate way.

In this respect it is important to know the accuracy with which AWSM predicts the flow field in the rotor plane. Thereto a comparison between the AWSM calculated and the Mexico measured flow field was carried out in [Grasso and van Garrel \(2011\)](#). This comparison generally shows a good agreement.

Moreover figure 6.20 shows the measured axial velocities from figure 6.16 compared with calculations from AWSM. It can be observed that generally speaking the agreement between the measured and AWSM calculated velocities is reasonable, where the agreement is poorest close to the blade positions. This can be explained by the lifting line approximation in AWSM which in the vicinity of the blade leads to a poor representation of the flow around the actual blade geometry.

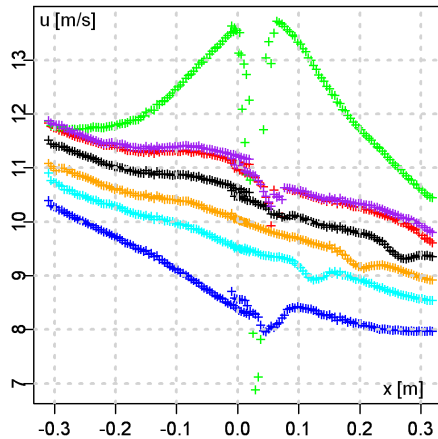


Figure 6.16: IEA Task 29(Mexnext): Velocities near the rotor plane as function of axial coordinate at 80% span and $V_{tun}=15\text{m/s}$. Different lines represent different blade positions, see figure 6.14

Then, from the measurements (and AWSM calculations), an idea can be formed of the flow non-uniformity between the rotor blades with which the validity of the Prandtl tip correction can be assessed. Thereto the figures 6.21 to 6.23 present the velocity measurements and calculations near the tip in the rotor plane at $V_{tun} = 10, 15$ and 24 m/s in the form of azimuthally averaged velocities and local velocities at the blade.

The azimuthally averaged measured values are averaged over the 6 blade positions from figure 4.7 where the AWSM calculations are averaged over 12 blade positions.

It should be recalled that the results from the figures 6.21 to 6.23 are derived from data which include the upwash from the bound vortex and which was found to add considerably to the flow non-uniformity as discussed above. The non-uniformity from this upwash is obviously not included in the Prandtl tip correction. At first sight one may think that this makes the results inapplicable for an assessment of the Prandtl tip correction. However, the present way of processing filters out the effect from the upwash. This is due to the fact that the data are azimuthally averaged over different blade positions which are all symmetrically positioned around the PIV sheet at 270 degrees. As

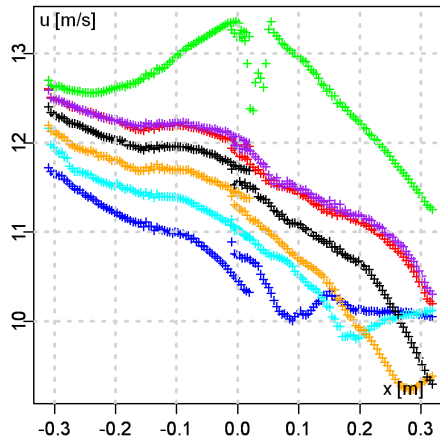


Figure 6.17: IEA Task 29(Mexnext): Velocities near the rotor plane as function of axial coordinate at 92% span and $V_{\text{tunn}} = 15 \text{ m/s}$. Different lines represent different blade positions, see figure 6.14

an example: the upwash at 280 degrees is opposite to the upwash at 260 degrees (at least when the bound vortex is thought to be concentrated in a vortex line). Also the local axial induced velocity, i.e. the axial velocity in the PIV plane with the blade located in this plane, is not disturbed by this upwash since a horizontal bound vortex line in the PIV plane does not induce a velocity in axial direction.

An important observation from the figures 6.21 to 6.23 is the very good agreement between measured and AWSM predicted azimuthally averaged velocities in the rotor plane. This can be seen as a further confirmation of the ability of AWSM to calculate the flow field in the rotor plane accurately.

Another observation is the good qualitative agreement between the calculated and measured local blade velocities in the sense that the drop in velocity, followed by an increase in velocity towards the tip (which is a result from the tip vortex), is present in both calculations and measurements. It is noted however that the increase in velocity takes place at a more inboard position than predicted by AWSM. This is a result of the fact that the so-called tip vortex tracking experiments showed the tip vortex to be trailed slightly inboard where AWSM assumes this vortex to be trailed at the tip. Furthermore it can

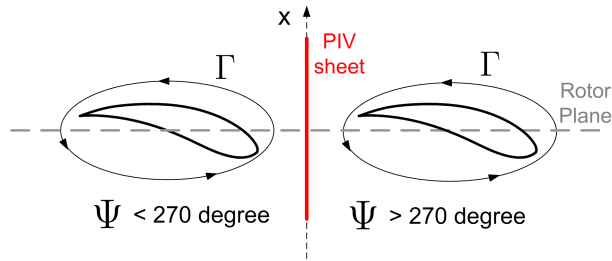


Figure 6.18: Blade crossing the PIV sheet at 270 degrees azimuth

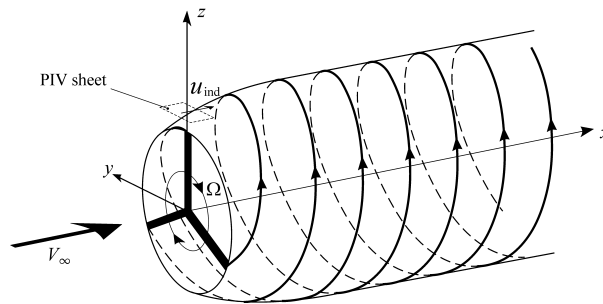


Figure 6.19: PIV sheet outside helical wake vortex system

be seen that the measured local blade velocities do not tend to coincide with the azimuthally averaged velocity at more inboard positions which the AWSM calculations do. This would also be expected from the Prandtl tip loss factor which approaches a value of 1 at inboard positions (A Prandtl tip loss factor of 1 implies the azimuthally averaged velocity to be equal to the local velocity at the blade). It must be noted however that AWSM assumes a lifting line approach where the real blade is obviously having a finite chord and thickness. Also the blade position might slightly differ from 270 degrees, because, as explained before, the 1P trigger sensor was sometimes found to behave unstable during the experiments. Since the velocities local to the blade are very sensitive to the precise value of the blade position the results can be disturbed heavily by a relatively small off-set in position.

Despite the discrepancies the comparisons between AWSM results and measurements are considered convincing enough to propose AWSM as a basis for

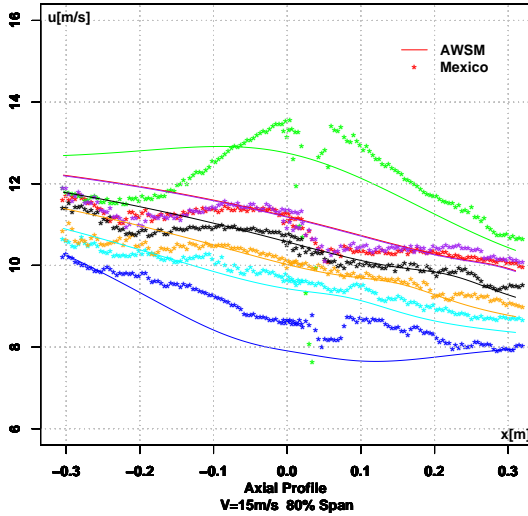


Figure 6.20: IEA Task 29(Mexnext): Axial traverse near the rotor at 80% span and $V_{\text{tun}} = 15$ m/s, different blade positions. Measured and calculated with AWSM

a refinement of the tip loss factor, also because the discrepancies are partly a result of measurement uncertainties and because the original tip loss factor is based on a much less physical realistic vortex wake model. Thereto the figures 6.24 to 6.26 compare the tip loss factors from AWSM (i.e. the ratio between the azimuthally averaged induction factor and the local blade induction factor) with the Prandtl tip loss factors. Most interesting is the behavior of these factors near the tip (the wiggles at the mid-span positions are most likely a result of intermediate vortex shedding).

A striking difference between the Prandtl tip loss factor and the ASWM tip loss factor can be seen at the very tip. The Prandtl tip loss factor decreases to 0 but the AWSM factor increases before the tip. This is consistent with the results from the figures 6.21 to 6.23 which show that the local blade velocity exceeds the azimuthally averaged velocities already inboard from the tip. In order to understand this, it needs to be realized that the AWSM tip vortex is a singularity which in principle yields an infinite induced velocity and hence a

negative infinite total velocity at the tip. This however assumes the flow to be inviscid where viscosity will prevent such a singularity to exist in the real flow. Consequently AWSM applies a so-called cut-off radius, the default value of which is 5%. This means that if the distance between a point and a segment of the wake is less than 5% of the segment length, the velocity induced by the segment is neglected. As a result of this cut-off radius, the velocity local to the blade increases towards the tip.

A sensitivity study showed only a significant effect of the cut-off radius at the very tip, i.e. at the outer 2% of the blade radius. Together with the fact that the qualitative agreement between the AWSM results with 5% cut-off radius and measured results is good, it is believed that this default cut-off radius can be used with sufficient confidence for a better assessment of the tip loss effects.

Apart from the deficiencies at the very tip it can then be seen that the AWSM tip loss factor follows the Prandtl tip loss factor very closely but the AWSM tip loss factor is higher at high tip speed ratio (10 m/s) and lower at low tip speed ratio (24 m/s). At the intermediate wind speed of 15 m/s a good agreement is found. This might indicate that the tip speed ratio dependency (i.e. the inflow angle dependency) in the Prandtl tip loss correction factor could be improved.

Another interesting observation is the behavior of the loss factor near the root. In the figures 6.24 to 6.26 the Prandtl tip loss factor has, despite the name **tip** loss factor, also been applied at the root. Thereto the tip radius in the original tip loss factor has been replaced by a root radius which is obviously less well defined than the tip radius. In the figures 6.24 to 6.26 the root radius has been set as the location of the maximum chord which seems to be a reasonable choice.

6.4 Summary, conclusions and recommendations on the field of induction aerodynamics

In the present chapter induction aerodynamics has been studied on basis of Mexico measurements.

- The PIV measurements as carried out in the Mexico experiment gave a very detailed mapping of the flow field around the rotor. Within IEA Task 29(Mexnext) these measurements were analyzed on basis of which insights were gained on the flow behavior upstream of the rotor, in the

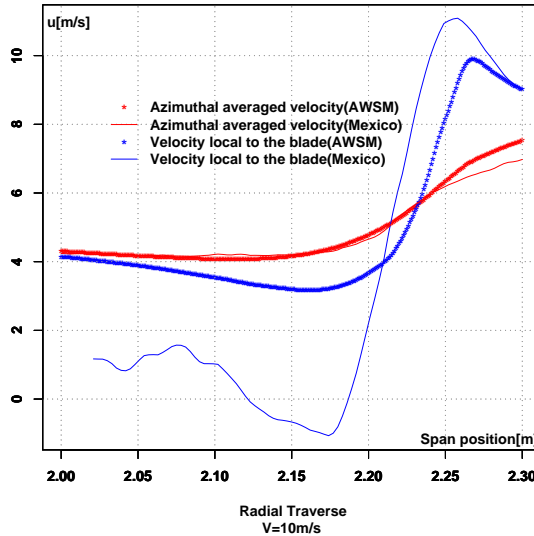


Figure 6.21: IEA Task 29(Mexnext): Local blade velocity and azimuthally averaged velocity, as function of radial position, measured and AWSM calculated, $V_{\text{tun}} = 10 \text{ m/s}$

rotor plane and in the near wake.

- A good correlation is found between the bound vortex strength as derived from pressure measurements at 82% span and the tip vortex strength derived from the PIV measurements
- Generally speaking the measurements confirm the expectations from the momentum theory and from the cylindrical vortex wake method: The velocity defect far downstream is twice the velocity defect in the rotor plane. Moreover the velocity decay is generally speaking independent of radial position. Furthermore the averaged values of the velocities in the rotor plane agree well with the expected value from momentum theory. Nevertheless some discrepancies have also been observed:
 - The measured velocity decay at design conditions only agrees well with the velocity decay from the momentum theory as long as the

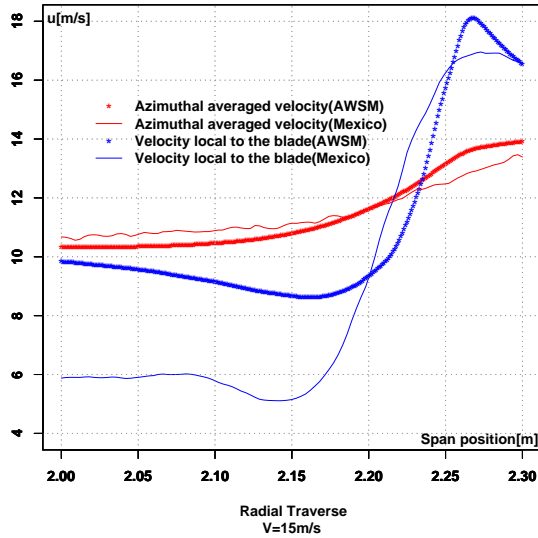


Figure 6.22: IEA Task 29(Mexnext): Local blade velocity and azimuthally averaged velocity, as function of radial position, measured and AWSM calculated, $V_{\text{tun}} = 15 \text{ m/s}$

axial force coefficient is set to the expected value of 0.89. The measured axial force coefficient however only amounts to 0.72. Until now all investigations on measurement quality indicate that the measurements are sufficiently accurate to make this inconsistency at least to some extent true. Moreover tunnel effects point in an opposite direction. Also striking at these conditions is a vortex shedding near 60% span which might be explained by the change in airfoils near that position.

- At off-design conditions where the blades are stalled a vortex shedding is clearly visible in the wake.
- The flow field measurements at the lowest tunnel speed still show positive flow velocities at the most downstream position even though the $C_{D,ax}$ value is 1.04. At these conditions the velocities are dependant on the radial position

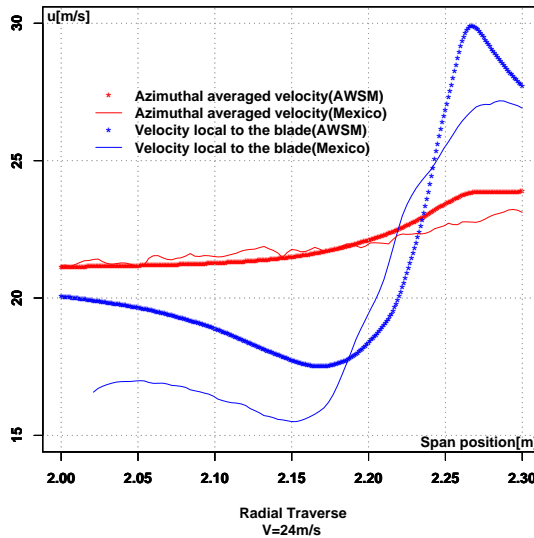


Figure 6.23: IEA Task 29(Mexnext): Local blade velocity and azimuthally averaged velocity, as function of radial position, measured and AWSM calculated, $V_{\text{tun}} = 24 \text{ m/s}$

- Generally speaking the CFD methods as employed in IEA Task 29 Mexnext showed a good qualitative (and sometimes quantitative) agreement with measurements. Amongst other things the vortex shedding at stalled conditions is predicted very well. At design conditions none of the CFD codes has been able to predict both the velocities and the loads in a correct way. The vortex shedding due to the transition in airfoils is not predicted either.
- A strong non-uniformity has been found in the flow in the rotor plane due to the passage of the bound vortex. The velocities as measured near the tip show a behavior consistent with the concept used in the Prandtl tip loss factor and with results from AWSM. The results from AWSM indicate that the dependency of the Prandtl tip loss factor on inflow angle can be improved.

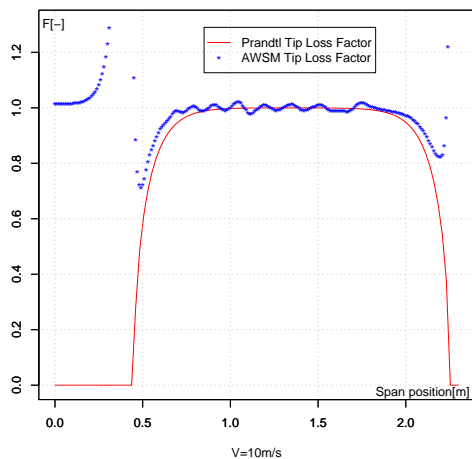


Figure 6.24: IEA Task 29(Mexnext): Prandtl tip loss correction as function of radial position, compared with AWSM tip loss factor, $V_{tun} = 10$ m/s

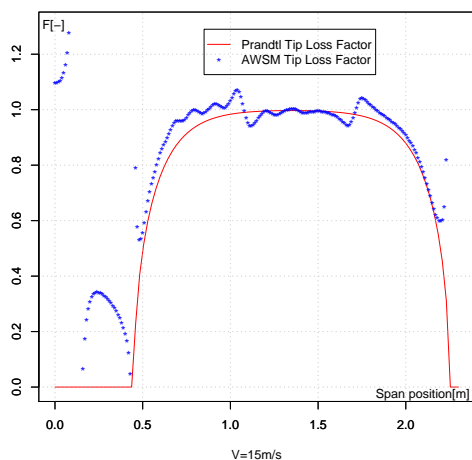


Figure 6.25: IEA Task 29(Mexnext): Prandtl tip loss correction as function of radial position, compared with AWSM tip loss factor, $V_{tun} = 15$ m/s

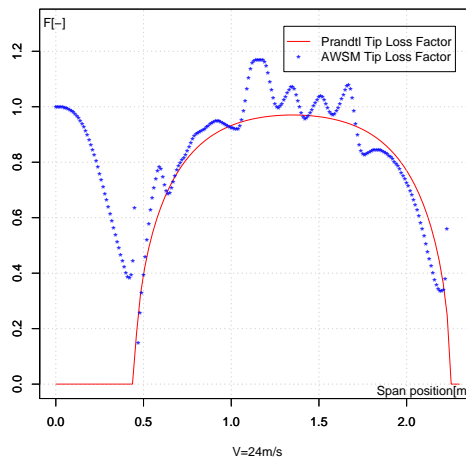


Figure 6.26: IEA Task 29(Mexnext): Prandtl tip loss correction as function of radial position, compared with AWSM tip loss factor, $V_{\text{tun}} = 24 \text{ m/s}$

Chapter 7

Progress on Dynamic Inflow based on measurements from the EU Dynamic Inflow projects and IEA Tasks 20 and 29

7.1 Introduction on Dynamic Inflow

The momentum theory has been derived for steady conditions. This implies that the induced velocity follows a change in axial force coefficient instantaneously. Such instantaneous change in induced velocity is often called the equilibrium wake assumption. The equilibrium wake assumption is however not valid for situations where the axial force coefficient changes suddenly due to e.g. a sudden change in pitch angle, rotor speed or wind speed. In such cases the wake behind the turbine, and consequently the induction in the rotor plane will respond with a certain delay. This phenomenon is discussed in section 3.6.2 where it was mentioned that the effect is commonly called 'Dynamic Inflow'. Dynamic inflow was the subject of several research projects, the results of which will be discussed in some detail in the present chapter. The most extensive study on Dynamic Inflow took place in two European pro-

jects, see [Snel and Schepers \(1994\)](#) and [Schepers and Snel \(1995\)](#). In these European 'Dynamic Inflow projects' several models have been developed and implemented in design codes. One of these models, i.e. the ECN model, will be described in section 7.2.1. In its basis this model does not differ much from the models as developed by other participants i.e. it is a first order differential equation on the induced velocity as described in section 3.6.2. It is however derived as an unsteady version of the cylindrical vortex wake method from section 6.2 which gives it a physical basis.

The models from the Dynamic Inflow projects were validated with very useful measurements during fast pitching transients which were performed by the Technical University of Denmark on the 60 m diameter Tjæreborg turbine, see section 7.2.2. At a later stage a more detailed validation of the model could be carried out on basis of NREL's Phase VI(NASA-Ames) measurements. In this validation results from the AWSM code have also been included. This validation is reported in detail by [Schepers \(2007c\)](#). A summary of the observations from that reference will be given in section 7.3. Finally section 7.4 will show dynamic inflow effects from the Mexico experiment at rotor speed steps. It is recalled from section 3.6.2 that opposite to common belief, a change in free stream velocity hardly leads to any dynamic inflow effects. This is a result of the fact that, although the axial induction factor changes with wind speed, the induced velocity itself is hardly affected.

7.2 EU projects 'Dynamic Inflow'

7.2.1 Engineering model for dynamic inflow

The engineering model for dynamic inflow as developed by ECN and implemented in PHATAS is described in [Snel and Schepers \(1994\)](#).

- The model is derived from an integral relation which is extracted from the simplified cylindrical vortex wake sheet model as discussed in section 6.2 for steady conditions. The steady conditions make that $\gamma_t(x)$ can be placed outside the integral in equation 6.8 and the equation can be solved analytically. The final solution turned out to be equivalent to the well known momentum theory equation:

$$C_{D,ax} = 4a(1 - a) \quad (7.1)$$

where the axial induction factor a is constant along the rotor plane.

- For non-equilibrium situations, the term $\gamma_t(x)$ should be placed inside the integral of equation 6.8. Then using the relation between the stream wise position x of the vorticity and its transport velocity (which is assumed to be constant at $V_w - u_i$) a time dependant integral relation is derived. This relation cannot be solved analytically. However, by differentiating the resulting integral relation and under the condition that the correct steady state solution should be fulfilled, a heuristic reasoning (see Appendix L from [Snel and Schepers \(1994\)](#)) yields the following solution for the axial induced velocity at radius r :

$$4Rf_a \frac{d}{dt}(u_i) + 4u_i(V_w - u_i) = \sigma V_{\text{eff}}^2 c_n$$

In all cases which are analyzed in the present thesis, the wind speed is assumed to be constant. For these conditions the expression can be written as a first order differential equation in time on the axial induction factor:

$$\frac{R}{V_w} f_a \frac{da}{dt} + a(1 - a) = dC_{D,ax}/4 \quad (7.2)$$

with $dC_{D,ax}$ the axial force coefficient on a rotor annulus at radius r .

The time constant of this equation (denoted as τ) is found to be:

$$\tau = \frac{R}{V_w} f_a(r) \quad (7.3)$$

which contains the term f_a . This term is a function of the radial position and was found to be:

$$f_a = 2\pi / \int_0^{2\pi} \frac{[1 - (r/R) \cos \phi_r]}{[1 + (r/R)^2 - 2(r/R) \cos \phi_r]^{3/2}} d\phi_r \quad (7.4)$$

It can be noted that:

- The first order differential equation makes that the induced velocity reacts gradually on a change in axial force coefficient. For equilibrium conditions, equation 7.2 returns to the stationary momentum equation 6.9;
- In figure 7.1 the term f_a is plotted as function of r/R . It can be seen that its value is 1 in the rotor center leading to a time constant of $\tau = R/V_w$. The time constant gets shorter towards the tip. This is due to the fact that the outer portions of the blade are close to the tip vortex. The

outboard positions of the blade are then, through the law of Biot and Savart, more sensitive to a change in tip vorticity.

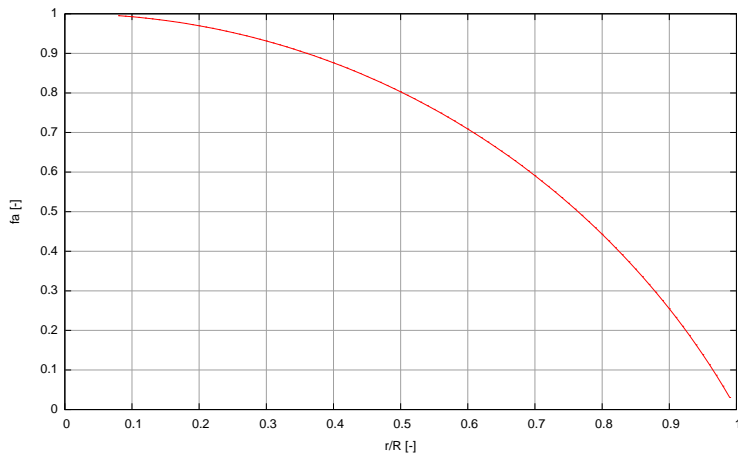


Figure 7.1: Factor f_a as function of radial position

7.2.2 Measurements on Tjæreborg turbine

The model from the previous section (together with the models from other participants in the Dynamic Inflow project) has been validated with measurements of blade root flapping moment and rotor shaft torque during fast pitching transients. These measurements were performed by the Technical University of Denmark (DTU) on the Tjæreborg turbine, see Øye (1991). This turbine was pitch regulated and it had a constant rotor speed and a diameter of 60 meter. The rated power was 2MW.

In the pitching transients, after an initial period, the blade pitch angle is first increased at a fast rate, next maintained constant for some period and then decreased to its initial value at a fast rate. In order to reduce the influence of turbulence, wind shear and tower shadow in the measured response, DTU synchronized nine time series with respect to the pitch angle change. These nine time series were averaged. Some typical results are shown in Figures 7.2 and 7.3. Figure 7.2 shows (qualitatively) the time series for a step on

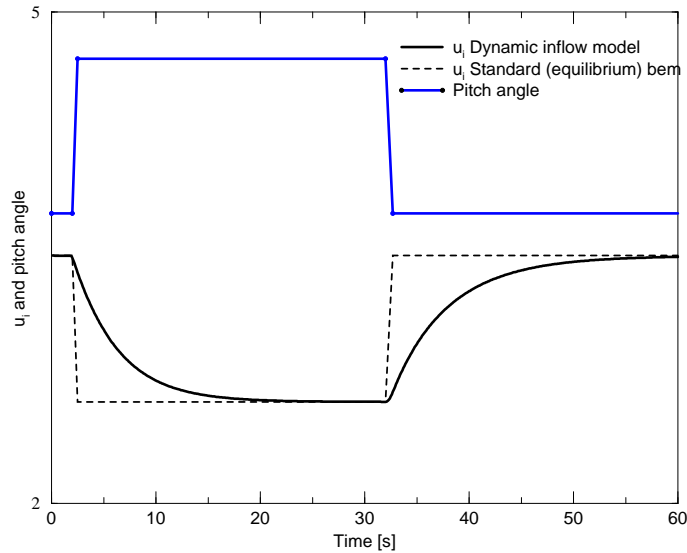


Figure 7.2: Induced velocity (qualitatively) in response to pitch angle step

the pitch angle together with the calculated response of the induced velocity. The induced velocities are calculated from a conventional equilibrium blade element momentum theory and from ECN's engineering model for dynamic inflow as described in the previous section. The equilibrium BEM model gives an instantaneous response of the induced velocity where the dynamic inflow model shows a gradual behavior in which the new equilibrium value is reached only after a certain period.

Figure 7.3 shows the response of the calculated and measured rotorshaft torque. The calculated results in Figure 7.3 are again obtained from ECN's dynamic inflow model and from a conventional equilibrium wake model. Figure 7.3 clearly shows the improved prediction from the dynamic inflow model: A

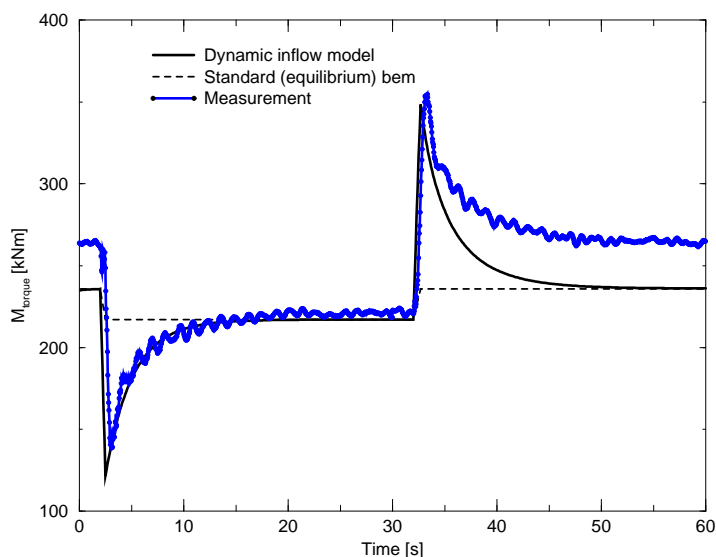


Figure 7.3: Rotor shaft torque on Tjæreborg turbine in response to pitch angle step

large overshoot in torque is visible after the step on the pitch angle which is not predicted at all with the conventional momentum theory. The load overshoot is a result of the lag in induced velocity. This can be understood by considering two effects (illustrated for the downward pitching step):

1. The first effect is a sudden increase in angle of attack due to the pitching motion of the blade itself. This leads to an almost instantaneous increase of the torque (a slight delay comes from unsteady airfoil aerodynamics but the time constant of that effect is very short (in the order of $c/(\Omega r)$, see section 3.6.1);
2. The second effect is the response of the rotorshaft torque to the induced velocity. In the new equilibrium situation, the induced velocity

is larger (Figure 7.2) and the axial wind speed through the rotor plane is lower. This reduces the rotorshaft torque, by which the increase in rotorshaft torque from effect 1 is partly compensated. As a result, the overall increase in rotorshaft torque turns out to be very limited in the new equilibrium situation.

However the compensating second effect only comes into play after a certain period in time, since the lag in induced velocity from Figure 7.2 takes place with a time scale in the order of R/V_w . Hence the rotorshaft torque will initially be determined by effect 1, causing a temporary enlargement of the rotorshaft torque. Thereafter the gradual increase of the induced velocity reduces the rotorshaft torque.

7.3 IEA Task 20: Dynamic Inflow effects in NREL's Phase VI(NASA-Ames) experiment

The measurements from the European Dynamic Inflow projects offered unique insights since they gave experimental evidence of dynamic inflow effects. Nevertheless the validation did suffer from a few shortcomings. Among others the field environment and the associated instationary, unknown and uncontrollable conditions gave uncertainties. Although this problem was partly overcome by averaging over a large number of measurement campaigns, some fluctuations from the field conditions remained in the averaged time series (partly because of the structural dynamic effects). These fluctuations interfere with the fluctuations from the 'pure' dynamic inflow effect.

Another, even more important, problem is the fact that the rotor shaft torque and the blade root flatwise moments 'hide' the dependency of the aerodynamic loads on the local radius, since they are a result of the integration of the load distribution along the entire blade span. This is a major drawback in the validation since the radial dependency of the dynamic inflow effect is expected to be very strong.

The measurements which are used in the present section are performed on the NREL Phase VI(NASA-Ames) turbine, see section 4.4. Again measurements have been taken at fast pitching steps. The pressure distributions at 5 positions have then been integrated to sectional loads by which these measurements offered the radial dependency of dynamic inflow with an additional

advantage that they are being taken in controllable and well defined wind tunnel conditions.

For this purpose NREL measured time series at fast stepwise pitch changes, similar to the ones which were measured by DTU in the Dynamic Inflow projects.

The pitching steps have been performed at different tunnel speeds. Now it should be realized that dynamic inflow effects are expected to be most pronounced at relatively high values of the axial induction factor. As pointed out in section 4.4 a significant axial induction factor (in the order of 0.3) is for the present turbine (at the design pitch angles) only found at the lowest available tunnel speed, which is 5 m/s. Hence, the measurement series at this wind speed has been requested at NREL and used in the dynamic inflow analysis. Figure 7.4 shows the measured time series of the pitch angle. The measurement period is 600 seconds and within this period 200 pitch angle steps are performed. Thereto a repeated upward pitching step is performed with a fast pitching speed from approximately -5.90 degrees to 10.02 degrees, after which it remains constant for some 15 s. Thereafter a downward step is performed by decreasing the pitch angle again to -5.90 degrees.

The axial induction factors at the instrumented sections at these equilibrium pitch angles of -5.9 and 10.02 degree are calculated by PHATAS, see table 7.1. It can be noted that the rotor is heavily loaded at a pitch angle of -5.90 de-

pitch angle (deg)	a_{30} [-]	a_{47} [-]	a_{63} [-]	a_{80} [-]	a_{95} [-]
-5.90	0.32	0.42	0.58	0.68	1.06232
10.02	0.039	0.005	0.008	-0.0168	-0.03

Table 7.1: NREL's Phase VI(NASA-Ames): Axial induction factor at a pitch angle of -5.9 degrees and 10.02 degrees. The 5 radial positions are given in percentage of the span in the subscript

grees but at a pitch angle of 10.02 degrees the rotor is only very lightly loaded. As such the pitch angle steps should be considered as rather artificial but they are very suitable for validation purposes. It should be realized that even in the NASA-Ames wind tunnel environment some fluctuations appear in the measured response which are not caused by dynamic inflow. These undesired fluctuations mainly result from (turbine dependent) structural dynamics.

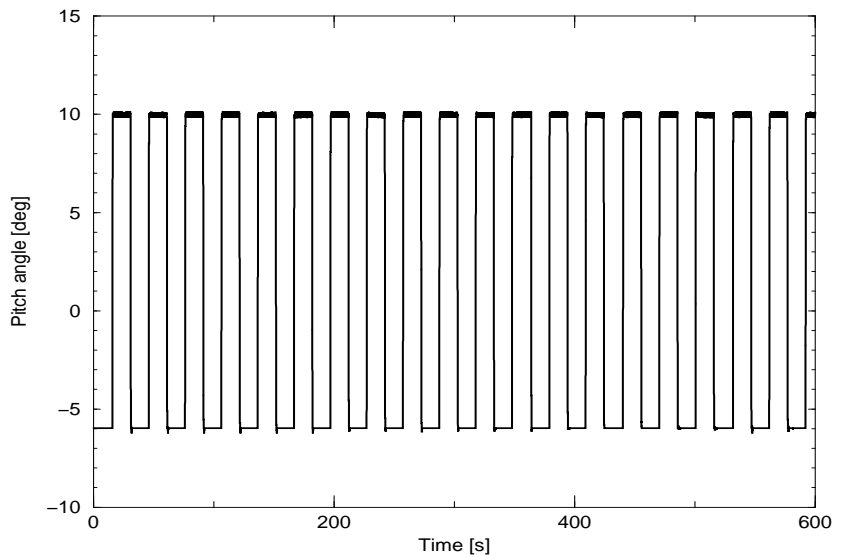


Figure 7.4: NREL's Phase VI(NASA-Ames): Pitch angle variation during 600 seconds

Apart from the interference with structural effects, there are fluctuations from the tower shadow and from slight, inevitable instationarities in the wind tunnel conditions (as mentioned in section 4.4, the turbulence intensity increases with decreasing tunnel speed where the current measurement series is selected at the lowest possible tunnel speed of 5 m/s). In order to smoothen the load signals an averaging procedure has been applied similar to the one from the Dynamic Inflow project, see section 7.2.2. Thereto the different pitching steps are synchronized and initialized to the start of the pitching step transient. The resulting, synchronized, time series are then averaged in order to filter out the fluctuations as good as possible.

The averaged upward and downward pitching steps are given in Figures 7.5 and 7.6. Note that the pitching step starts at $t = 0$ s.

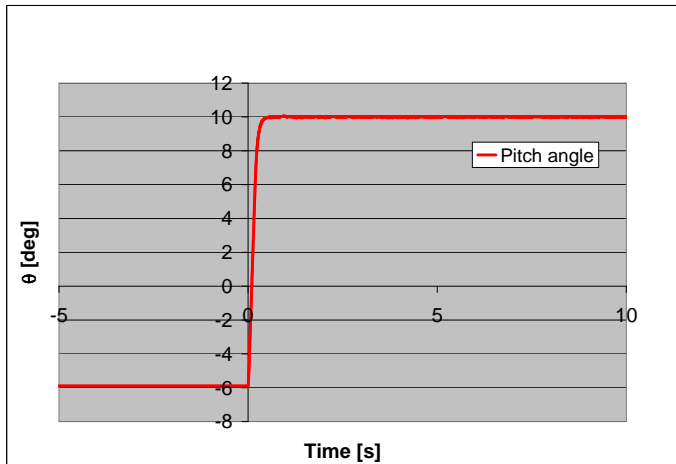


Figure 7.5: NREL's Phase VI(NASA-Ames): Upward pitching step (Averaged over 10 realizations)

7.3.1 Comparison between calculations and measurements

In [Schepers \(2007c\)](#) the NREL Phase VI(Nasa-Ames) measurements are compared with calculational results from the aero-elastic code PHATAS (which includes the engineering model from section 7.2.1) and the free wake lifting line method AWSM. The pitch angle transients as prescribed to these calculations are based on the measured pitch angle transients from figures 7.5 and 7.6.

Amongst other things a comparison is made between calculated and measured blade and rotor loads (i.e. the flatwise moment and rotorshaft). A representative example is copied into figure 7.7. In this comparison the results from the AWSM-code are not presented. In [Schepers \(2007c\)](#) it was shown that

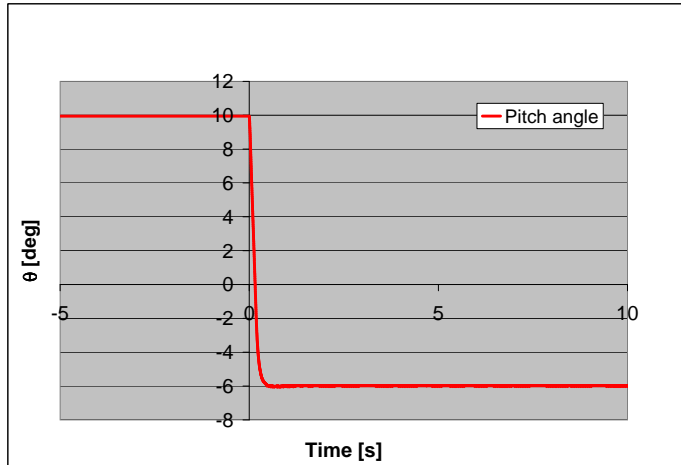


Figure 7.6: NREL's Phase VI(NASA-Ames): Downward pitching step (Averaged over 10 realizations)

these loads are strongly influenced by structural dynamic effects, but these effects are not included in the AWSM code.

Even more interesting is the comparison in terms of local normal forces. Some representative examples are shown in figures 7.8 and 7.9. The following observations can be made:

- In all (measured and calculated) transients, the effects from dynamic inflow are clearly visible. Just after the pitching step a load overshoot appears, after which it takes a certain period in time before the new equilibrium value is reached. This resembles very much the behavior of the loads which was measured in the European Dynamic Inflow projects, see section 7.2.2. The dynamic inflow effects donot only appear in the rotor(blade) loads see e.g. figure 7.7 but also in the sectional normal forces, see figures 7.8 and 7.9. The 'high frequency' fluctuations which appear in the rotorshaft torque are a result of the rotor shaft flexibility, as shown in [Schepers \(2007c\)](#). Qualitatively speaking they are reproduced

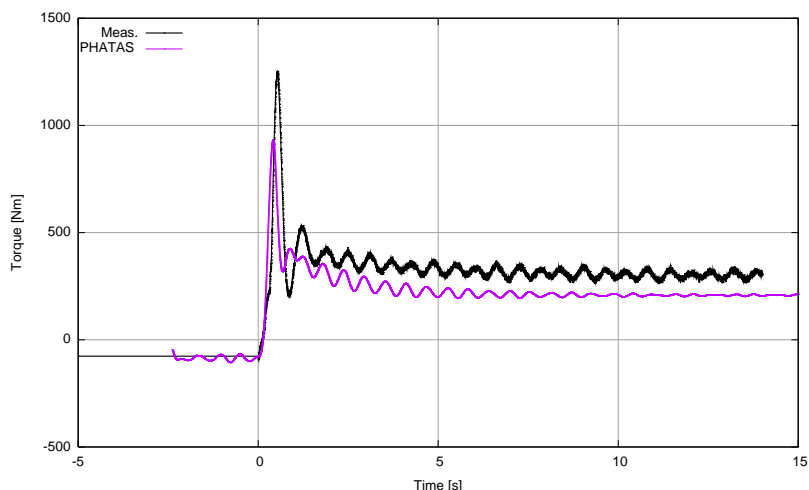


Figure 7.7: NREL's Phase VI(NASA-Ames): Torque: Comparison between measured and PHATAS calculated results: Downward pitching step

well by PHATAS, although the overshoot is underpredicted.

- At first sight it might be expected that the dynamic inflow effects for the downward pitching step are the 'reverse' of the dynamic inflow effects for the upward pitching step. However, the dynamic inflow effects for the downward pitching step seem to be less pronounced (in terms of load overshoots). This may be a result of the overshoot in angle of attack just after the downward pitching step which gives values above the stall angle of attack ($\alpha_{\text{stall}} \approx 9.5$ degrees (Figure 7.10). At these angles of attack the $c_l(\alpha)$ curve is relatively flat by which the overshoots are damped. At the upward pitching step (Figure 7.11), the angle of attack remains within the linear $c_l(\alpha)$ range. Another difference between the upward and downward pitching step is given by the fact that prior to the upward pitching step the axial induction factor is high, see table 7.1. This implies significant wake expansion and a relatively low downward convection velocity of the vorticity in the wake. This is followed by an increase in pitch angle which yields a gradual decrease of induced velocity. At the end of the transient the axial induction factor is very low which implies little wake expansion and a rapid convection of the 'new'

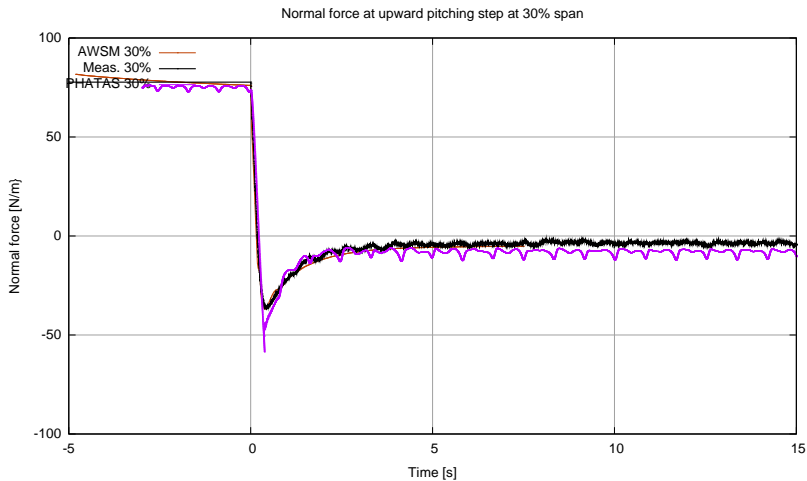


Figure 7.8: NREL's Phase VI(NASA-Ames): Upward pitching step: normal force at 30% span: Comparison between measured and calculated results

vortices. As such the upward pitching step starts with a 'slow' dynamic inflow process. For a downward pitching step the situation is opposite. It starts with a 'rapid' dynamic inflow process with little wake expansion but at the end of the transient the convection velocity is low and the wake is more strongly expanded.

- For the upward pitching step, the agreement between measured and AWSM calculated results is excellent. It is not only the equilibrium levels which are predicted very well (this was already expected from the comparison between AWSM results and measurements at 'standard' conditions, see section 5.7.2) but the load overshoot and the time constant are also predicted well (note that the time constant is still assessed from visual inspection. A quantitative assessment of the time constant is carried out in chapter 7.3.2). For the downward pitching steps it is concluded that the agreement is less good ([Schepers \(2007c\)](#)). Thereto it should be realized that modelling of stalled conditions is more difficult than modelling of attached flow conditions, due to strong 3-dimensional and instationary effects as explained in section 3. This then explains the poorer agreement for the downward pitching step, where the stalling

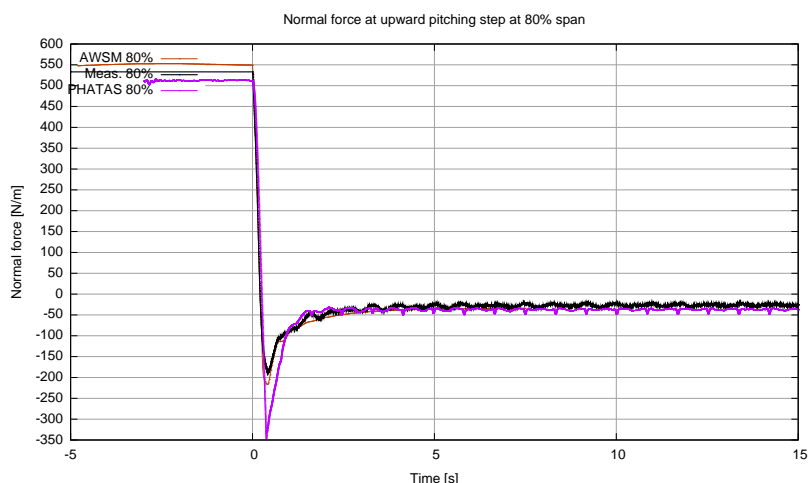


Figure 7.9: NREL's Phase VI(NASA-Ames): Upward pitching step: normal force at 80% span: Comparison between measured and calculated results

angle of attack is exceeded. Note that AWSM has not included a model for stall effects (and structural dynamic effects).

7.3.2 Time constant (time scale) analysis

The time constant is a very important parameter in the dynamic inflow process. A short time constant implies that the new equilibrium value is reached shortly after the change in rotor state and as such the event can still, with a reasonable agree of accuracy, be predicted with an equilibrium wake model. A longer time constant implies a longer response time by which the actual response will deviate from the response calculated with an equilibrium wake model.

Therefore a reliable assessment of the time constant is of utmost importance but the quantification of a time constant from the measured signals is not straightforward. Among other things, the definition of the time constant needs to be clarified. As a starting point, the induced velocity (i.e. the axial induction factor) is assumed to behave according to equation 7.2. By neglecting the

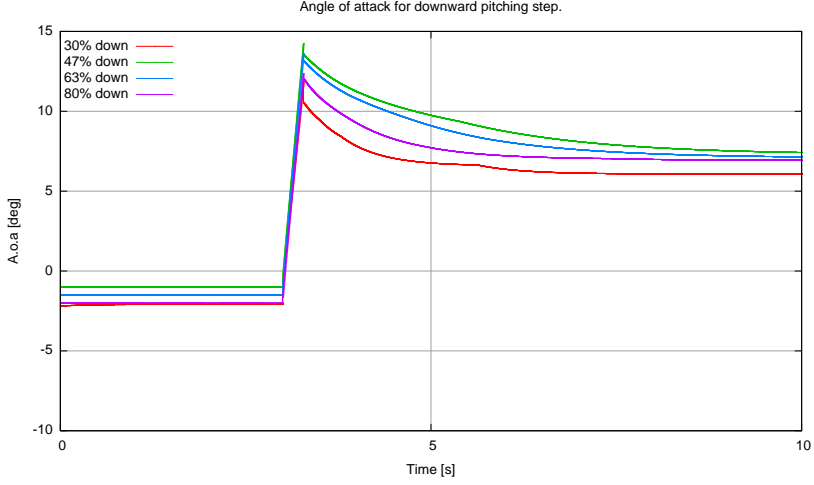


Figure 7.10: NREL(Phase VI (Nasa-Ames): Downward pitching step, Angles of attack calculated by PHATAS

quadratic a^2 term, this equation becomes:

$$\tau da/dt + a = \frac{1}{4}dC_{D.ax,2} \quad (7.5)$$

with τ the time constant and $dC_{D.ax,2}$ the axial force coefficient on the annulus after the step in pitch angle. In addition it is assumed that $dC_{D.ax,2}$ is reached instantaneously after the step on the pitch angle (i.e. $dC_{D.ax,2}$ is independent of time).

Then equation 7.5 yields:

$$\frac{da}{0.25dC_{D.ax,2} - a} = \frac{dt}{\tau} \quad (7.6)$$

from which the axial induction factor as function of time reads:

$$a(t) = a_2 - \Delta a \cdot \exp^{-(t-t_1)/\tau} \quad (7.7)$$

In this expression $a_1 = a(t_1)$ i.e. the initial value of a at $t = t_1$, a_2 is the new equilibrium value for the axial induction factor ($a_2 = 0.25dC_{D.ax,2}$) and $\Delta a =$

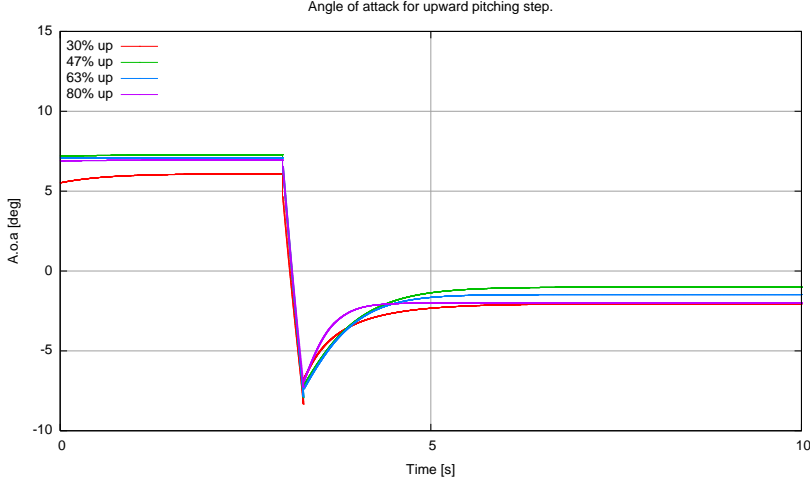


Figure 7.11: NREL(Phase VI (Nasa-Ames)): Upward pitching step, Angles of attack calculated by PHATAS

$a_2 - a_1$. In figure 7.12 the behavior of the axial induction factor as function of time is shown for $a_1 = 0.2$, $a_2 = 0.5$ and $t_1 = 1$ s. Finally it is assumed that the variations in the blade loads are fully driven by the change in the axial induction factor. Then the transient of the load $F(t)$ can be expressed in a form similar to equation 7.7:

$$F(t) = F_2 - \Delta F \cdot \exp^{-(t-t_1)/\tau} \quad (7.8)$$

In this equation F_2 is the new equilibrium value of the load and ΔF the load overshoot, i.e. the difference between F_2 and F_1 , with F_1 the load just after the pitching step. Then equation 7.8 gives the following expression for the time constant:

$$\tau = -\frac{t - t_1}{\ln[(F_2 - F(t))/\Delta F]} \quad (7.9)$$

Hence equation 7.9 shows that the time constant can be determined from the actual value of the load $F(t)$, the final equilibrium value F_2 and the 'starting value' F_1 (at t_1). All these values can in principle be extracted from the measured data. It should be realized however, that the determination of the time constant requires a very smooth and well defined dynamic inflow transient where even the present signals, though filtered and measured in the relatively stable wind tunnel environment, do show some fluctuations. This is in

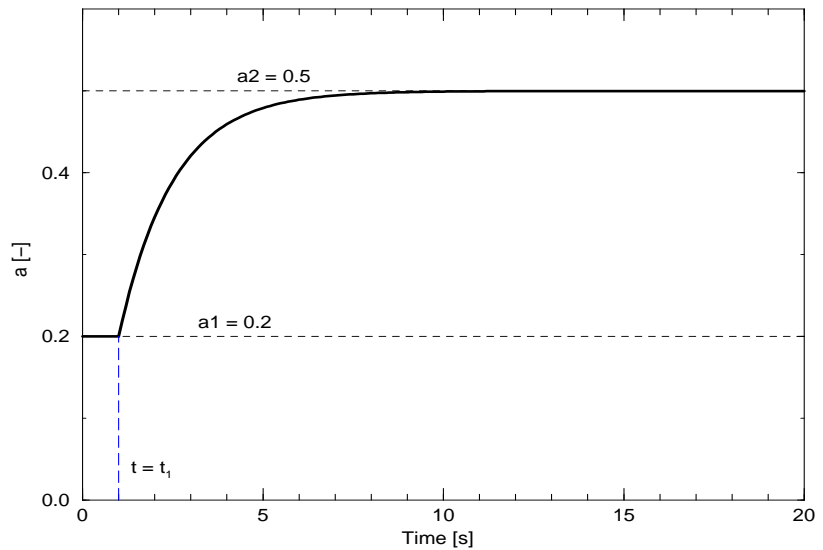


Figure 7.12: Assumed exponential behavior of the axial induction factor

particular true for the rotorshaft torque and (to a smaller degree) the flatwise moment, see e.g. figure 7.7. For this reason it is only the time constant of the normal forces which are determined in the present research. Furthermore equation 7.9 assumes τ to be a time constant. However, the assumptions which have been made to arrive to equation 7.8 are too crude for τ being a constant. For this reason the factor τ is replaced by a time scale $f(t)$, which is a function of time.

In table 7.2 the time scales for the upward and downward step are given. The measured results are compared with the time scale which is derived from the AWSM results and with the time scale from the engineering model, see equation 7.4. The measured and AWSM time scales are averaged over the

period from $t = 0.7$ s to 3.7 s. In this period the time scale is assumed to be most accurate. Thereto it should be realized that the time scale needs to be determined in a period which is not too short and not too long after $t = t_1$: In the period very shortly after $t = t_1$, equation 7.9 gives non-sensible results with almost zero value in nominator and denominator. On the other hand, for $t \gg t_1$, the value of $F(t)$ approaches F_2 and the argument in the log function approaches zero.

A graphical presentation of the measured time scale in the period from $t = 0.7$ s to 3.3 s is given in Figure 7.13 for the normal force at 30% span and the upward step. Within this period the time scale turns out to be reasonable (though not completely) constant. A check on the validity of the resulting time scale is given in figure 7.14 where the measured transient is compared with the transient from equation 7.8 using the time scale from table 7.2. The figure shows a very good fit.

Table 7.2 shows a good agreement between the measured time scale and the time scale from the engineering model at the 30% and 47% section for the upward step.

For the upward step, the most important conclusion from table 7.2 is that the rapid decrease of the time scale towards the tip from the engineering model appears to a much smaller extent in the measured time scale. The decrease in time scale towards the tip from the AWSM calculated transients is qualitatively in very good agreement with the measurement although the AWSM time scale is consistently longer (in the order of 0.25 s) at all radial positions.

As expected, the calculated and measured time scale results for the downward pitching step, show a poor agreement, see table 7.2. This is expected from the fact that the dynamic inflow effects are much less well defined at this downward step.

7.4 IEA Task 29(Mexnext): Rotor speed steps from Mexico experiment

Within the Mexico project 4 time series have been measured at fast rotor speed steps. The difference between the time series lied in the tunnel speed which was 10, 15, 18 and 22 m/s (note that the pitch angle was always -2.3

r/R	$f_{up,meas}$	$f_{up,AWSM}$	$f_{up,e.m.}$	$f_{down,meas}$	$f_{down,AWSM}$	$f_{down,e.m.}$
[-]	[s]	[s]	[s]	[s]	[s]	[s]
0.30	0.95	1.12	0.93	1.07	1.98	0.93
0.47	0.83	1.04	0.83	1.09	1.61	0.83
0.63	0.77	1.01	0.68	1.10	n.r. *)	0.68
0.80	0.74	1.00	0.44	1.13	1.14	0.44
0.95	0.78	1.03	0.14	1.53	2.36	0.14

* too strong deviation from exponential behaviour

Table 7.2: Time scale from NREL Phase VI(Nasa-Ames) measurements, AWSM calculations and engineering model (e.m.) for upward and downward pitching step

degrees, i.e. the design pitch angle). Figure 7.15 shows the rotor speed variations as measured during the dynamic inflow transients. The rotor speed varies between 424.5 rpm to 324.5 rpm and vice versa. Note that one realisation was measured per wind speed, leading to some fluctuations from structural dynamic effects after the pitching steps. The downward 'spike' in rotor speed prior to the upward rotor speed step was an unintentional result from the control but makes the transient only interesting. As for the NREL Phase VI (NASA-Ames) experiment dynamic inflow effects only occurred at the lowest tunnel speed (see the study from [Pascal \(2009\)](#)). This is again explained by the fact that dynamic inflow is an effect on the induced velocities where the induced velocity increase with decreasing tunnel speed. Therefore the results at $V_{tun} = 10$ m/s are presented only. The resulting axial force as measured by the balance at the tower foot (uncorrected for tower drag) is shown in figure 7.16, where the normal forces at 25%, 60% and 92% span are presented in figures 7.17. The figures show clear dynamic inflow effects.

Until now there hasn't been an opportunity for a further analysis of these measurements, but they anyhow proof that dynamic inflow effects donot only occur at pitching steps but also at rotor speed steps.

7.5 Summary, conclusions and recommendations on Dynamic Inflow

In this section an engineering model for dynamic inflow is described as developed in the EU Joule projects Dynamic Inflow. Moreover measurements

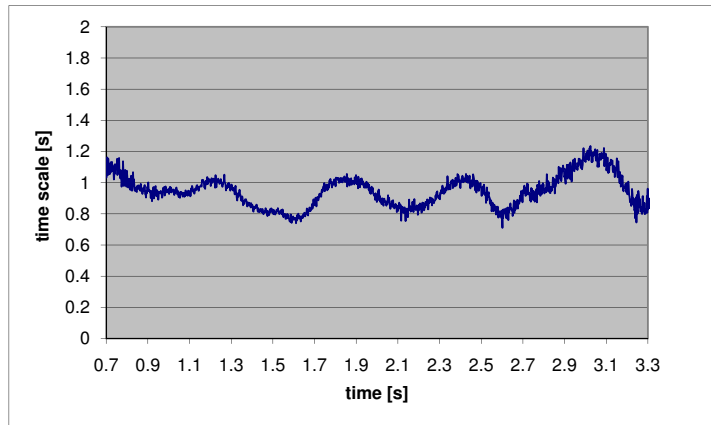


Figure 7.13: NREL Phase VI(Nasa-Ames): Time scale for normal force at 30% span (upward pitching step)

are presented with which the dynamic inflow effect is studied. The most important conclusions are:

- Strong dynamic inflow effects are found at fast pitching steps and rotor speed steps in the form of a significant overshoot in rotor(blade) loads and power after the step in pitch angle or rotor speed. The dynamic inflow effect from wind speed variations turns out to be limited.
- The NREL Phase VI(NASA-Ames) measurements allowed a detailed assessment of the dynamic inflow effect.
 - The agreement between the NREL Phase VI(NASA-Ames) measured results and the calculational results from AWSM (for the upward pitching step) was found to be very good in terms of:
 - * Overshoots in normal forces in reaction to the step in blade pitch angle

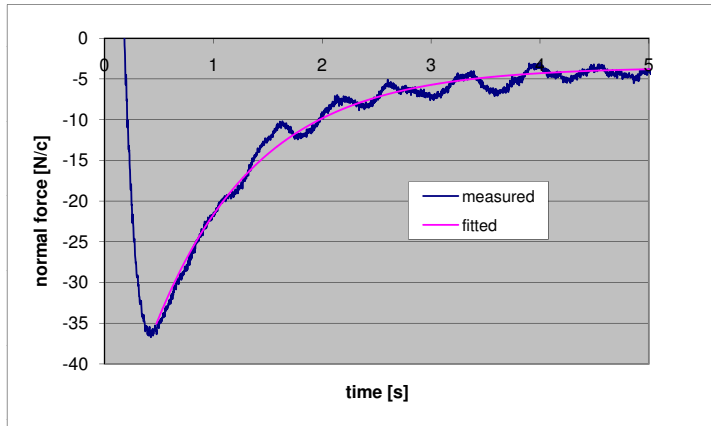


Figure 7.14: NREL Phase VI(Nasa-Ames): Fitted normal force at 30% span (upward pitching step)

* Time constants.

- However, it was found that the time constant hardly reduces towards the tip. This is opposite to the results from former theoretical consideration as implemented in the engineering models from the EU Dynamic Inflow project. For this reason it is recommended to reconsider the models in this respect. This could be done on basis of an extensive study in which AWSM (or a similar code) is used to calculate dynamic inflow events for a large number of configurations.

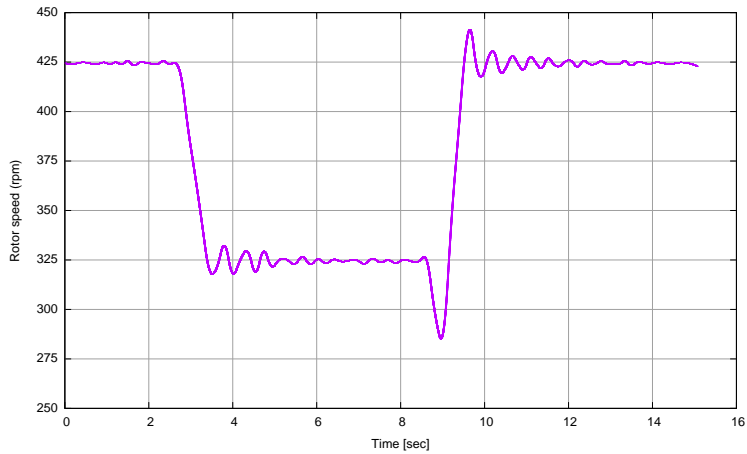


Figure 7.15: Rotor speed transient in the Mexico experiment

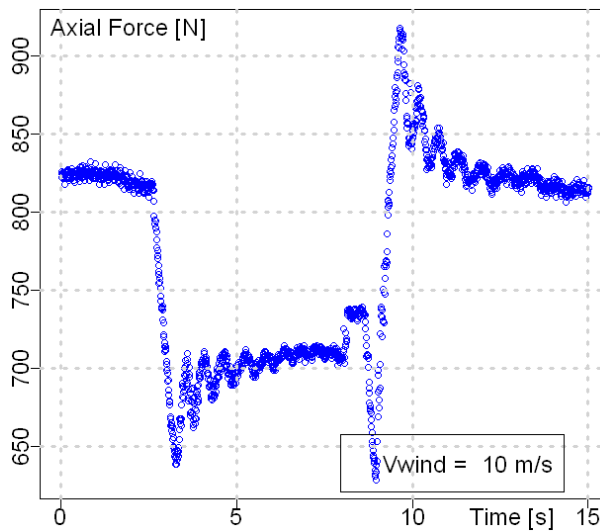


Figure 7.16: Mexico: Axial force from balance at rotor speed transient at $V_{tun} = 10 \text{ m/s}$

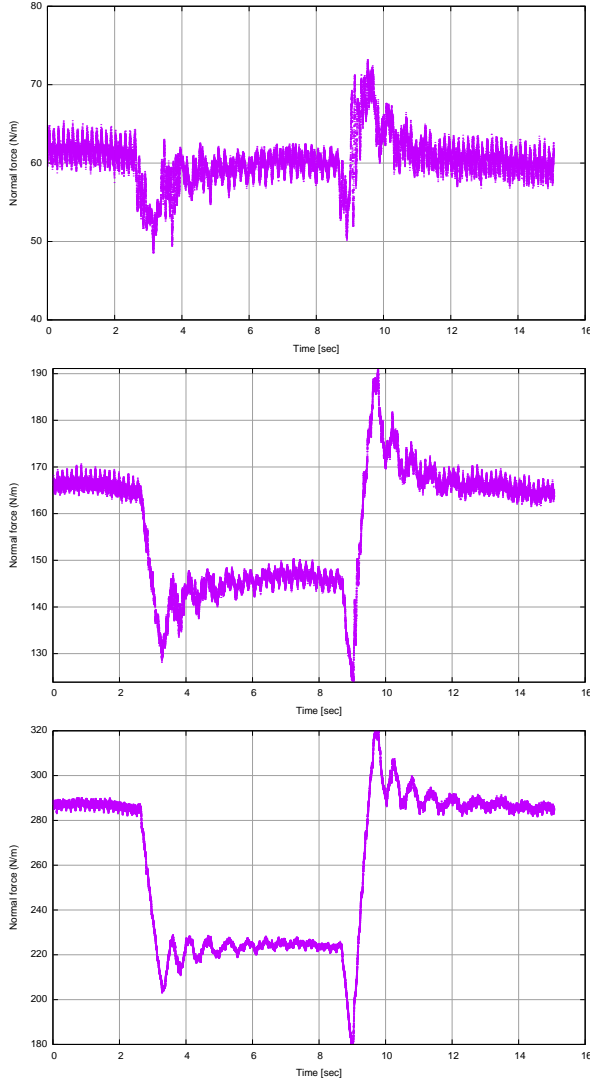


Figure 7.17: Mexico: Normal force at 35 % (top figure), 60 % and 92% span (bottom figure) for rotor speed transient at $V_{tun} = 10$ m/s

Chapter 8

Progress on yaw aerodynamics based on measurements from national, EU and IEA projects

8.1 Introduction on yaw aerodynamics

Modelling of yawed conditions is known to be a very difficult topic in wind turbine aerodynamics. At the same time it can be stated that the practical importance of yaw is very large, since the wind direction fluctuations in the stochastic atmosphere lead to a continuous yawed operation.

In section 3.8 it is explained that yaw leads to a power loss and to an azimuthal load variation. The azimuthal load variations are largely driven by two, more or less distinct, phenomena:

- The load variation which results from the so-called advancing and retreating blade effect. The advancing and retreating blade effect refers to the cyclic variation in angle of attack and inflow velocity due to the skewed inflow vector. The effect is mainly 'felt' at high wind speeds and

low tip speed ratios, i.e. low induced velocities which makes the below mentioned skewed wake effect of less importance. At high wind speed, the angle of attack is generally large by which the advancing and re-treating blade effect is often accompanied with instationary effects on the lift (and drag) of an airfoil, i.e. dynamic stall.

- The azimuthal load variation due to the variation in induced velocity which in turn is caused by the asymmetric, skewed, wake geometry. The resulting load distribution determines the yawing stability of a wind turbine, because it yields a load unbalance between the 'upwind' and 'downwind' side of the rotor plane.

As such the correct prediction of this type of load variation is not only very important for the calculation of fatigue and extreme loads but also for the prediction of the yawing moments and the stability of free yawing turbines.

The variation of the induced velocity is mainly 'felt' at high induced velocities i.e. at relatively high tip speed ratios and low wind speeds.

In this chapter yaw aerodynamics is mainly studied by means of wind tunnel measurements. Although several studies of yaw are known which are based on field measurements (e.g. the study in [Schepers \(2004b\)](#) and in [Snel and Schepers \(1994\)](#)), these analysis were complicated by the variable and uncertain yaw misalignment from the field environment. A further complication from the field environment comes from the (rather uncertain) wind shear which leads to a load variation which interferes with the load variation from yaw. Wind tunnel measurements are done under known, stationary and uniform conditions by which they do not suffer from these uncertainties and hence they are expected to be much more helpful in understanding yaw aerodynamics.

Thereto section 8.4 describes a study which was carried out on yawed measurements from the NREL Phase VI(Nasa-Ames) experiment where section 8.5 describes an analysis on the Mexico measurements in yaw. Prior to that a qualitative description of the load variation in yaw is given in section 8.3, using TUDelft wind tunnel measurements. Section 8.2 describes the yaw angle dependency of the power.

For a good understanding of the different aspects it is extremely important to absorb the definitions of yaw angle (ϕ_y) and azimuth angle (ϕ_r) as applied in this chapter. Thereto the definitions are used from figures 3.5 and 3.6. The

figure shows the positive sign of the yaw angle and it shows that a stabilizing yawing moment is negative in case of positive yaw. Furthermore, the blade azimuth angle is defined as zero for the (instrumented) blade pointing down in vertical position. i.e. the '6 o'clock' position. The rotor is assumed to rotate clock-wise. Hence for positive yaw, an 'upwind side' of the rotor plane can be defined between 0 and 180 degrees azimuth where for negative yaw this 'upwind side' is between 180 and 360 degrees azimuth. It is noted that this chapter also uses measurements from NREL's Phase VI(Nasa-Ames) experiment. The present definitions differ from the NREL definitions where zero azimuth was at 12 o'clock and where the yaw angle has opposite sign. Furthermore the actual rotor, placed in the NASA-Ames tunnel rotated anti-clockwise. The present definition also differs from the original Mexico definition where zero azimuth was at 12 o'clock, see figure 4.7. Consequently the measurement data from the NREL Phase VI(Nasa-Ames) and the Mexico experiment have been transformed to the definitions of the figures 3.5 and 3.6.

Many results from the present section have already been published in [Schepers \(1999\)](#), [Schepers \(2007b\)](#), and [Schepers, Pascal and Snel \(2010\)](#).

8.2 Yaw angle dependency of power

One of the most important effects from yaw is the expected decrease of power from it. It is then surprising to note that the precise relation between (time averaged) power and yaw angle got relatively little attention in the wind energy society. An exception forms the research carried out by [Dahlberg \(2005\)](#). He summarized the results from several measurements campaigns (both in the field as well as in the wind tunnel). He assumed the power to behave according to

$$P = P_0 \cos^x(\phi_y) \quad (8.1)$$

with P_0 the power at zero yaw and x the exponent to be determined. Dahlberg found the exponent x to vary between 1.88 and 5.14

The decrease of power due to yaw has also been investigated from DNW-LLF wind tunnel measurements obtained in the EU-JOULE project DATA, see [Schepers \(2001\)](#). The DATA project focussed on aero-acoustic effects but in addition the power (at non-yawed and yawed conditions) was measured. Several 2 bladed model rotors have been considered (a reference rotor and 2 rotors with acoustically optimized airfoils). All rotors had a rotor diameter

of 4.5 m. Measurements have been carried at a large variety of conditions (different tip speeds, tunnel speeds, pitch angles, clean and tripped blades). Figure 8.1 shows results from the reference rotor at 'clean' design conditions (which corresponds to tip speed of 100 m/s and a tunnel speed of 14 m/s). In this figure the results from PHATAS calculations are also added.

The following observations can be made:

- At aligned conditions PHATAS overpredicts the power with $\approx 8\%$;
- The measured drop in power due to yawed conditions is in the order of $\cos^{1.8} \phi_Y$;
- The calculated drop in power due to yawed conditions is less;
- As a result the overprediction in power increases rapidly with the yaw angle. Similar overpredictions of the power at yawed conditions have been found by Dahlberg in his research using a different BEM code. The explanation for the overpredicted power hasn't been found yet. It might be caused by an overpredicted mass flow through the rotor at yawed conditions due to an incorrect prediction of the azimuthally averaged induced velocity ($u_{i,0}$). This azimuthally averaged value is found with the model from Glauert which could be incorrect as suggested in section 3.8. The subject of the azimuthally averaged value of the induced value is discussed further in section 8.3.1.

Important new insights on the relation between power and yaw angle can be obtained from the NREL Phase VI(NASA-Ames) measurements. Thereto the figures 8.2, 8.3, 8.4 show the measured power as function of yaw angle for three different pitch angles at tunnel speeds of 5, 10 and 15 m/s respectively. It is recalled from section 4.4 that tunnel speeds of 10 m/s already result in stalled conditions along a large fraction of the blade (even more so for small pitch angle).

It has again been attempted to cast the power versus yaw angle curve in the form of equation 8.1. At a tunnel speed of 5 m/s the exponent was found to vary from approximately 2.28 at $\theta = 0$ degrees to 6.57 at $\theta = 6$ degrees. Very surprising is the power increase due to yaw at a tunnel speed of 10 m/s and $\theta = 0$ degrees. For a tunnel speed of 15 m/s the power even increases at all pitch angles. These results seem to indicate a dependency of the exponent from equation 8.1 on the angle of attack: At low tunnel speed and large pitch angle (i.e. small angle of attack) the exponent is high but at higher tunnel speeds and smaller pitch angles (i.e. larger angles of attack) the exponent is

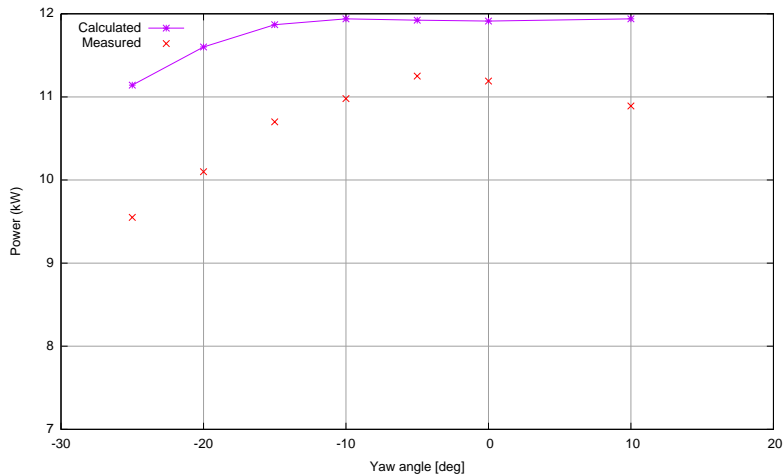


Figure 8.1: DATA project: wind tunnel measurements in DNW-LLF: Comparison between calculated and measured power for different yaw angles at design conditions

reduced or the power even increases with yaw angle! A possible explanation for the increase of power with yaw angle at large angles of attack is the occurrence of dynamic stall effects. Dynamic stall is a non-linear effect where the overshoot in lift (and hence power) may overcompensate the undershoots leading to an overall increase of power.

8.3 Azimuthal load variation at yaw

The azimuthal load variation at yaw is driven by the advancing and retreating blade effect and by the azimuthal variation in induced velocities. The first effect is relatively straightforward to model in the BEM equations and it was already included in the very first generation of BEM codes, see [van Groenou et al. \(1991\)](#). However the second effect requires a more fundamental understanding of the aerodynamics around the wind turbine.

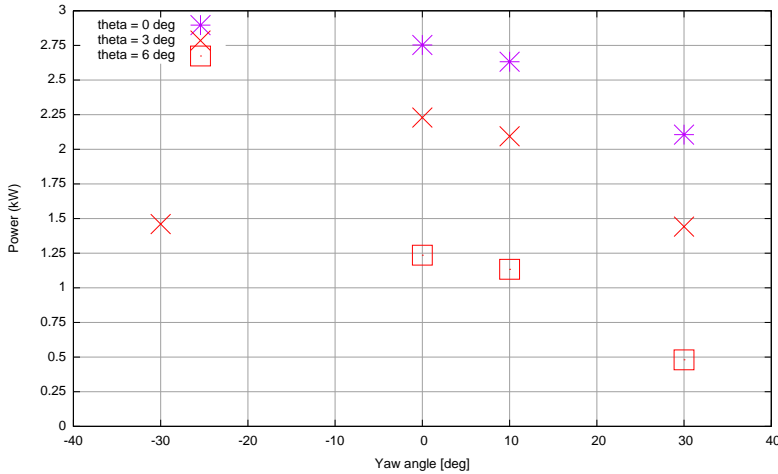


Figure 8.2: NREL Phase VI (NASA-Ames) wind tunnel measurements: power at different yaw and pitch angles for $V_{\text{tun}} = 5$ m/s

8.3.1 Azimuthal variation of induced velocity at yaw (skewed wake effect)

Results from EU projects 'Dynamic Inflow'

In section 3.8 it is explained that the azimuthal variation of the induced velocity is a result of the skewed wake geometry on the inflow distribution, In the EU JOULE projects 'Dynamic Inflow' see [Snel and Schepers \(1994\)](#) aerodynamic engineering models were developed which took this azimuthal variation of the induced velocity into account. All of these models assumed the variation in induced velocity to be purely sinusoidal according to Figure 8.5. This figure shows the qualitative behavior of the induced velocity and the resultant axial velocity for positive yaw. It is very important to note that such sinusoidal behavior is found from a vortex wake model which only considers tip vortices. Figure 8.5 shows $\phi_{\text{max,ui}}$ to be at 270 degrees (with $\phi_{\text{max,ui}}$ the azimuth angle where the induced velocity is maximum). This implies that the maximum induced velocity appears in the downwind part of the rotor plane (recall that the downwind part of the rotor plane is between $\phi_r = 180$ and 360 degrees).

The engineering models developed in the Dynamic Inflow projects, were val-

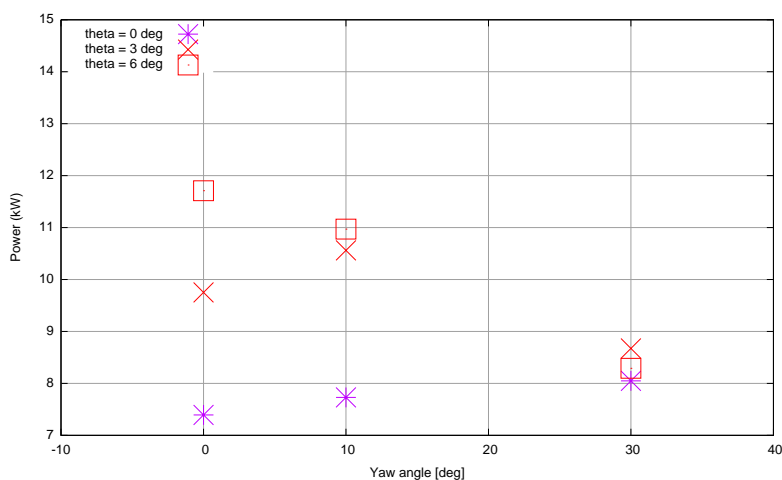


Figure 8.3: NREL Phase VI (NASA-Ames) wind tunnel measurements: power at different yaw and pitch angles for $V_{\text{tun}} = 10$ m/s

icated with load measurements at yawed conditions on the 3 bladed Tjæreborg turbine (with a diameter of 60 meter, see Øye (1992)) and on a 2 bladed model wind turbine (with diameter of 1.2 meter) placed in the open jet wind tunnel from Delft University of Technology. A major improvement was found: The calculated yawing moments turned out to be stabilizing in agreement with the measurements. These stabilizing yawing moments were not predicted by the former models, which only took into account the advancing and retreating blade effect.

Furthermore the projects showed that for yawed flow the root vortex also induces axial velocities by which the velocity behavior at the root deviates from the sinusoidal behaviour. This was found from theoretical models (e.g. the free wake model from the National Technical University of Athens, NTUA) a prescribed wake model from ECN and from an acceleration potential model from Delft University of Technology, see van Bussel (1995)). A further confirmation of these root vortex effects was found from velocity measurements behind the model wind turbine at yawed conditions in the TUDelft wind tunnel.

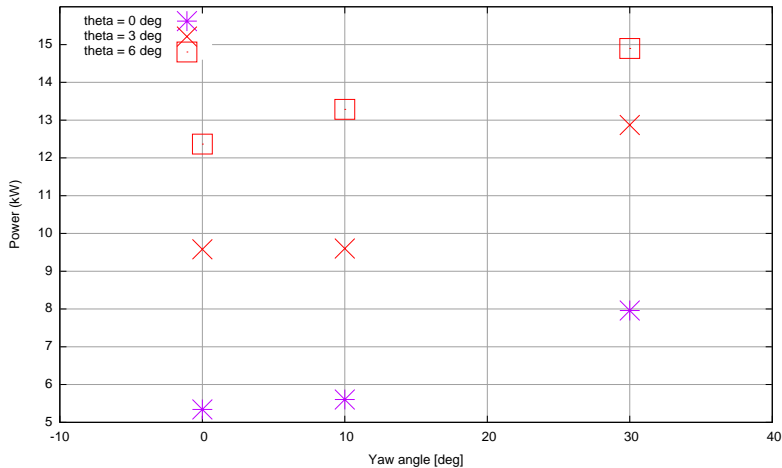


Figure 8.4: NREL Phase VI (NASA-Ames) wind tunnel measurements: power at different yaw and pitch angles for $V_{\text{tun}} = 15$ m/s

Results from Dutch National projects based on TUDelft wind tunnel measurements

In 1998 a Dutch national project has been performed, see [Schepers \(1999\)](#). In this project the inflow velocities were measured in the rotor plane of the model wind turbine placed in the TUDelft open jet wind tunnel. The project can be seen as a follow-up of the Dynamic Inflow projects and its main aim was a validation of the engineering models from the Dynamic Inflow projects by means of direct velocity measurements with hot wire velocimetry. Such measurements were to a limited extent already done in the Dynamic Inflow projects but the present project considered more detailed measurements at more positions where furthermore all three velocity components were determined instead of a resultant velocity. It was again found that the sinusoidal variation from the Dynamic Inflow projects was a rather crude simplification. This can be seen in Figure 8.6 which shows the measured axial velocity, just downstream of the rotor plane at 4 radial positions: $r/R = 0.5, 0.6, 0.7$ and 0.8 (Both the raw results as well as a curve fit on the raw measurements is shown). It is seen that the inflow distribution differs considerably from the sinusoidal distribution as plotted in Figure 8.5. This is in particular true at the inboard stations. A further illustrative confirmation for the root vortex effects

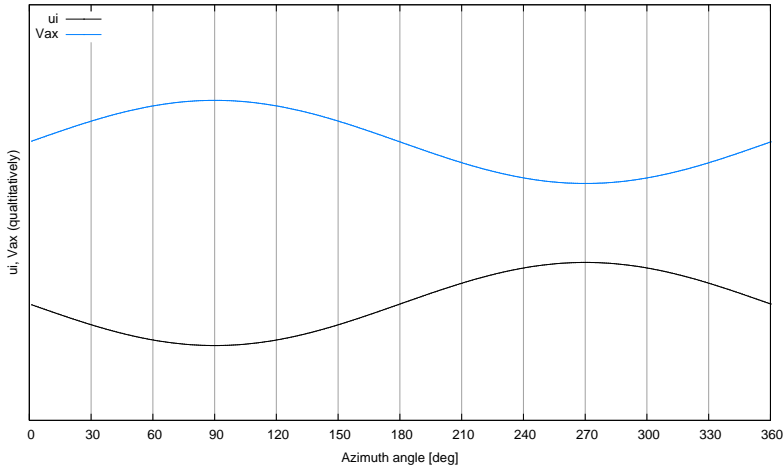


Figure 8.5: Sinusoidal (qualitative) behavior of induced velocity and resultant axial velocity (V_{ax}) in the rotor plane as induced by a tip vortex model

at yawed conditions comes from a calculation carried out with the free vortex wake code developed by [Voutsinas, Belessis & Huberson \(1993\)](#) from the National Technical University of Athens (NTUA), see Figure 8.7. In this figure the calculated axial velocity in the rotor plane of the Tjæreborg turbine (at 30%, 50% and 90% span) at a yaw angle of 32 degrees is shown. To distinguish the root vorticity effects, NTUA performed the calculations with two different models:

- The complete model (with identification 'with rv'). In this model the effect of the root vorticity is included automatically;
- A special version of the model (with identification 'without rv') in which root vorticity effects are excluded;

The calculations without root vorticity effects are qualitatively similar to the expected sinusoidal variation as induced by a tip vortex wake (Figure 8.5).

However the calculations with root vorticity effects show a clear radial dependency of the velocity variation: At $r/R = 0.9$, the variation in induced velocity is still similar to the sinusoidal variation as induced by a tip vortex wake but at the root the behavior is very different and the axial velocity has become

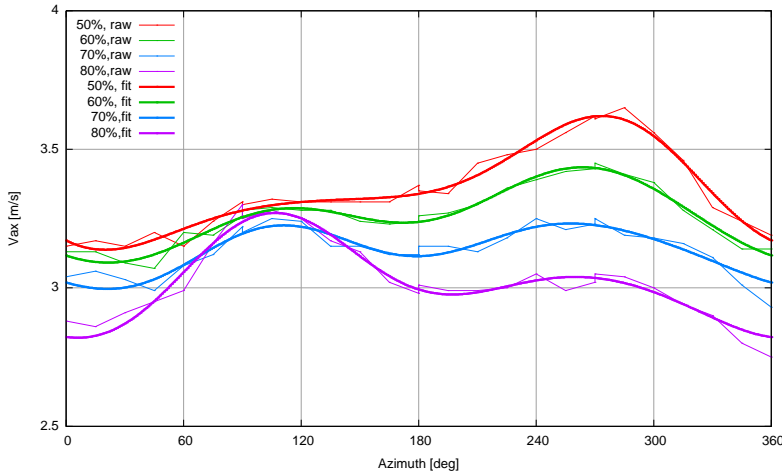


Figure 8.6: TUDelft Open Jet Facility measurements: Axial velocity (V_{ax}) at 4 radial positions, just behind the rotor plane at $\phi_y = +30^\circ$: Raw and smoothed data

maximum at $\phi_r = 270$ degrees. Hence the induced velocity is minimum at the downwind side (and maximum at the upwind side). Although the NTUA calculations have been performed on a different turbine than the TUDelft model turbine on which the velocity measurements were made, it is striking to see that the resulting radial dependency is, qualitatively speaking, very close to the measured dependency from Figure 8.6. This then strongly confirms the hypothesis that the deviations from the sinusoidal behavior are caused by root vortex effects.

On basis of the available velocity measurements, a new engineering model for the axial induced velocity could be developed. The model consists of a second order Fourier series. Thereto the amplitudes and phases of the $u_i(\phi_r)$ were fitted as function of radial position and yaw angle. The amplitudes are related to an azimuthal averaged induced velocity ($u_{i,0}$) which is calculated from the Glauert expression as discussed in section 3.8. It must be known that the velocity measurements from TUDelft were done with a hot wire system at several fixed azimuthal position. Then figure 8.6 shows the averaged velocities over a large number of revolutions. As such the measurements

from figure 8.6 do not represent the local velocities at a blade segment which are needed in the blade element theory. Therefore the fit on the TUDelft wind tunnel measurements only formed the basis for a final fit using the Tjæreborg load measurements from section 7.2.2 and load measurements carried out by the Aeronautical Research Institute of Sweden (FFA) on a 5.35 m turbine which was placed in the wind tunnel of the China Aerodynamic Research and Development Center (CARD C, see [Dahlberg et al. \(1989\)](#)).

For positive yaw the model reads as follows:

$$u_i = u_{i,0}[1 - A_1 \cos(\phi_r - \psi_1) - A_2 \cos(2\phi_r - \psi_2)] \quad (8.2)$$

A 'mirror image' gives for the induced velocity at negative yaw:

$$u_i = u_{i,0}[1 - A_1 \cos(360 - \phi_r - \psi_1) - A_2 \cos(360 - 2\phi_r - \psi_2)] \quad (8.3)$$

The amplitudes A_1 en A_2 and the phases ψ_1 en ψ_2 are a function of the relative radius ($r_{rel} = r/R$) and the yaw angle (ϕ_y). The amplitudes and phases are described in Appendix B.

It is noted that the measurements described in [Schepers \(1999\)](#) were taken at one condition only (more or less representing design conditions) and at one location (0.03 R behind the rotor plane). At a later stage a much more extensive experimental program was carried out on the same model in the same wind tunnel. These results are analyzed in [Sant \(2007\)](#) and [Haans \(2011\)](#). They performed measurements at more conditions and more locations. Moreover they developed a so-called inverse vortex wake model with which the load distribution along the blade could be derived from flow field measurements. Thereto it should be noted that the loads are not measured in the TUDelft experiment. The foundation for the inverse free wake model was laid by Sant where the application for yawed conditions was added by Haans. The method basically combines the conservation of circulation, the Biot and Savart law and the velocity measurements to solve the unknown bound circulation and inflow velocities. Note that a modified version of the model has been used to derive the angle of attack from the measured blade loads in e.g. the Mexnext project, see section 5.2.

Haans also used the inverse vortex wake model to find the flow field in the rotor plane from the measured flow field data, since these are only recorded behind the rotor plane (at a shortest distance of 0.035R). This is of importance since he observed a strong non-linear wake decay in the measurements

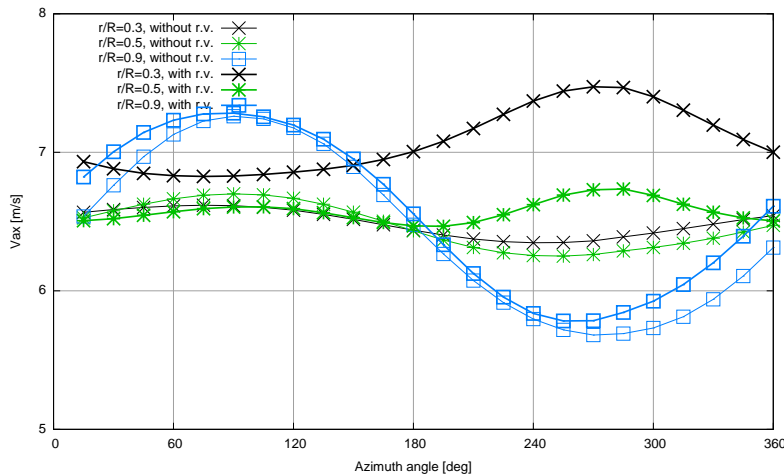


Figure 8.7: Axial velocity in the rotor plane (V_{ax}) of Tjæreborg turbine at $\phi_y = +32^\circ$ calculated with a free wake model from NTUA, with root vorticity (with r.v.) and without root vorticity (without r.v.)

(which were not only taken at 0.035 R but also at 0.06R and 0.09R behind the rotor) by which linear extrapolation is not valid.

The analyzes from Haans and Sant confirmed the deviations from the sinusoidal behavior of the induced velocity due to the root vortex. As a matter of fact Haans explicitly decomposed the experimental induction factors into the components from the tip and the root vortices. The tip vortices were found to induce a sinusoidal variation where the (inboard) velocities induced by the root vorticity are characterized by higher than 1P components. As such these results are fully consistent to the findings from [Schepers \(1999\)](#).

Haans' final recommendation is that the 'BEM modelling community is encouraged to implement nonuniformity correction methods that comply with given tip and root vortex effect'. Also Sant recommends the inclusion of higher harmonics in BEM yaw modelling. As a matter of fact these recommendations are already implemented in the model described in Appendix B. More important is therefore to assess the tip speed ratio dependency of that model since the model from Appendix B is mainly tuned on measurements near design

conditions.

Another interesting observation from Haans lies in a hysteresis effect on the airfoil coefficients as derived from the inverse vortex wake method. This variation even occurs at non-stalled conditions. As such these effects could not be reproduced with e.g. the dynamic stall model from [Leishman and Beddoes \(1998\)](#). Several explanations were offered e.g. a measurement error or a low Reynolds boundary layer effect. The author would like to add the explanation of a non-viscous 'Theodorsen' effect (see section 3.6.1). It anyhow implies that the load variation due to yaw is not only caused by the induced velocity variations but also by effects related to airfoil aerodynamics.

Finally Haans and Sant also looked into other yaw effects than the azimuthal variation of loads and induced velocity. Amongst other things the azimuthally averaged value of the induced velocity (to which the variations in induced velocities are related) is addressed. Haans and Sant draw opposite conclusions. Sant concludes that the Glauert momentum relation (see section 3.8) requires further tuning where Haans concludes that this is not needed. The explanation for the paradox lies in the fact that Haans derives the velocities in the rotor plane from the inverse wake method where Sant linearly extrapolates the measured wake decay, which as stated above, is not fully correct.

8.3.2 Global description of load variation at yaw

From the previous section it can be concluded that the commonly assumed sinusoidal variation of the induced velocity from Figure 8.5 is a too crude simplification and that the azimuthal variation of the induced velocity should depend on the radius. The impact of these effects on the normal force has been assessed by writing the normal force as $n \propto c_n(\alpha)V_{\text{eff}}^2$. For angles of attack below the stall angle of attack (i.e. at low tunnel speeds) it may be assumed that $c_n \propto \alpha$, hence

$$n \propto \alpha V_{\text{eff}}^2. \quad (8.4)$$

In BEM/lifting line codes like PHATAS and AWSM the angle of attack and the effective velocity are calculated from the velocity diagram and the angle between the chord and the rotor plane ($\epsilon + \theta$), see Figure 8.8.

$$\alpha = \text{atan}\left(\frac{V_w \cos \phi_y - u_i}{\Omega r + V_w \sin \phi_y \cos \phi_r}\right) - \epsilon - \theta \quad (8.5)$$

$$V_{\text{eff}}^2 = (V_w \cos \phi_y - u_i)^2 + (\Omega r + V_w \sin \phi_y \cos \phi_r)^2 \quad (8.6)$$

It is noted that the tangential induced velocity (u_t) is neglected in these for-

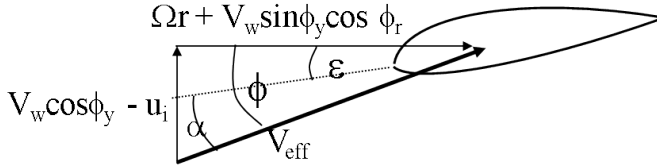


Figure 8.8: Velocity diagram and angle of attack at yawed conditions

mula. For aligned flow it is well known that the tangential velocity is generally only a minor fraction of the rotational speed. For yawed flow little knowledge on the tangential induced velocity is available but measurements analyzed in [Schepers \(1999\)](#) indicate a relatively small variation in the tangential induced velocity at yawed flow.

The equations 8.5 and 8.6 make clear that both the advancing and retreating blade effect as well as the skewed wake effect lead to an azimuthal variation of the effective velocity and the angle of attack. These variations are, according to equation 8.4, then straightforwardly reflected into a variation of the normal force. As such the azimuthal variation in normal force can originate from 4 sources:

- 1. The advancing and retreating blade effect on:
 - 1.a) The angle of attack (i.e. the term $V_w \sin \phi_y \cos \phi_r$ in equation 8.5).
 - 1.b) The effective velocity (i.e. the term $V_w \sin \phi_y \cos \phi_r$ in equation 8.6).
- 2. The azimuthal variation in induced velocity which effects:
 - 2.a) The angle of attack (see equation 8.5: The induced velocity appears in the term $V_w \cos \phi_y - u_i$).
 - 2.b) The effective velocity (see equation 8.6: The induced velocity appears in the term $V_w \cos \phi_y - u_i$).

In tables 8.1 and 8.2 a qualitative indication is given of the expected variation in normal force from these different sources: Thereto the values of $\phi_{\max, \alpha}$ and $\phi_{\max, V_{eff}}$ are listed, where $\phi_{\max, \alpha}$ denotes the azimuth angle at which α

is expected to be maximum and $\phi_{\max, V_{\text{eff}}}$ denotes the azimuth angle where V_{eff} is expected to be maximum. A distinction is made between the effects at the inboard and outboard part of the blade. In addition a quantitative indication of the different effects is given for the NREL Phase VI (NASA-Ames) configuration using the formula 8.5 and 8.6. Thereto the variations in α and V_{eff} are given as the \pm variation around the mean values. They are estimated for the 30% (inboard) span and the 90% (outboard) span under the following conditions:

- Tunnel speed (V_{tun}) = 5 m/s. This tunnel speed is sufficiently low to expect an effect from the variation in induced velocity. It is recalled that for higher wind speeds the effect from the variation in induced velocity is dominated by the advancing and retreating blade effect;
- Yaw angle (ϕ_y) = + 30 degrees;
- Mean axial induction factor (\bar{a}) = 0.2;
- A sinusoidal variation of the induced velocity is assumed, with an amplitude (Δu_i) = 1 m/s, where the phase at 30% span is opposite to the phase at 90% span. As a result, the variation in u_i at 90% span gives $\phi_{\max, u_i} = 270$ degrees and the variation at 30% span gives $\phi_{\max, u_i} = 90$ degrees, in line with the observations from section 8.3.

At a later stage, see the results presented in section 8.4, the actual variations in u_i have been calculated at more or less the same conditions. These calculations show the variations in u_i to be somewhat less than ± 1 m/s. As such the numbers for the skewed wake effect from table 8.2 could be a bit exaggerated. On the other hand, the axial induction factor on a representative turbine can be considerably larger (i.e. close to 0.33) than the assumed value of 0.2, by which this exaggeration is, at least, partly compensated.

The following comments can be given:

- Advancing and retreating blade effect, see table 8.1:
 - Effect on the angle of attack:

The advancing and retreating blade effect makes $\phi_{\max, \alpha} = 180$ degrees. This is true for both the inboard and outboard sections. However, the effect is more dominant at the inboard sections, since then the term $V_w \sin \phi_y \cos \phi_r$ is relatively large compared to the rotational speed. For the NREL Phase VI turbine at the conditions given above, the variation in angle of attack is found to be ± 0.4 degrees at 90% span and ± 3.5 degrees at 30% span.

- Effect on the effective velocity:
The advancing and retreating blade effect on the effective velocity works opposite to the effect on the angle of attack, since $\phi_{\max, V_{\text{eff}}}$ is found at 0 degrees for both the inboard and outboard section. Again, the effect is (relatively speaking) more important at the inner sections. For the NREL Phase VI turbine at the conditions given above, the variation in V_{eff} is estimated to be +/- 20% at $r/R = 0.3$ and +/- 7% at $r/R = 0.9$
- Skewed wake effect, see table 8.2:
 - Effect on the angle of attack:
The effect from the varying u_i is mainly 'felt' on the angle of attack. For the outboard stations, the induced velocity is minimum and the angle of attack is maximum near $\phi_r = 90$ degrees, i.e. at the upwind side of the rotor plane. The opposite happens at the inboard sections where the induced velocity is minimum and the angle of attack is maximum at the downwind side of the rotor plane.
For the NREL Phase VI turbine at the conditions given above, it is found that the angle of attack varies with ± 1.6 degrees at 90% span and with ± 4 degrees at 30% span.
 - Effect on the effective velocity.
The effect from the varying u_i on the effective velocity is in phase with the effect on the angle of attack (i.e. a maximum effective velocity goes together with a maximum in the angle of attack) but the effect from the effective velocity on the loads is small, in particular at the outboard section. At $r/R=0.3$ the variation in effective velocity for the NREL Phase VI turbine at the conditions given above turns out to be $\pm 3\%$ and at 90% span the variation is only $\pm 0.6\%$.

In summary, the above given analysis shows a considerable variation in angle of attack from the skewed wake effect which yields a load unbalance between the upwind and downwind side of the rotor plane, such that for the outer part of the blade, the normal force is maximum at the upwind part of the rotor plane. This yields a stabilizing yawing moment, see Figure 3.6. At the inner part of the blade the highest loading is found at the downwind part of the rotor plane which yields a destabilizing yawing moment. The advancing and retreating blade effect gives a symmetrical loading around the vertical ' $\phi_r = 0-180$ degrees line' by which it is neutral in terms of yawing stability.

	α	V_{eff}
inboard	max at $\phi_r = 180^0$ ($\pm 3.5^0$)	max at $\phi_r = 0^0$ ($\pm 20\%$)
outboard	max at $\phi_r = 180^0$ ($\pm 0.4^0$)	max at $\phi_r = 0^0$ ($\pm 7\%$)

Table 8.1: Phase of $\alpha(\phi_r)$ and $V_{\text{eff}}(\phi_r)$ at positive yaw due to the advancing and retreating blade effect. Furthermore an order of magnitude estimate is given for the variation in α and V_{eff} at the NREL Phase VI experiment at low tunnel speeds

	α	V_{eff}
inboard	max at downwind side ($\phi_r = 270^0$) ($\pm 4^0$)	in phase with α ($\pm 3\%$)
outboard	max at upwind side ($\phi_r = 90^0$) ($\pm 1.6^0$)	small ($\pm 0.6\%$)

Table 8.2: Phase of $\alpha(\phi_r)$ and $V_{\text{eff}}(\phi_r)$ at positive yaw due to the the skewed wake effect. Furthermore an order of magnitude estimate is given for the variation in α and V_{eff} at the NREL Phase VI experiment at low tunnel speeds

8.4 IEA Task 20: NREL's Phase VI(NASA-Ames) measurements in yaw

This section describes the analysis as carried out by the author in IEA Task 20 on the NREL Phase VI(NASA-Ames) measurements at yawed conditions. Measurements were analyzed at two yaw angles, 10 and 30 degrees for a large number of tunnel speeds and pitch angles, see [Schepers \(2007b\)](#). In this chapter only a selection of results is presented. Measurements have been selected at a yaw angle of 30 degrees and a low tunnel speed of $V_{\text{tun}} = 5$ m/s (and $\theta = 0$ degrees). At this low tunnel speed it is known from section 4.4 that the averaged angle of attack at non-yawed conditions is below 5 degrees where the axial induction factor is in the order of 0.3 in case of zero pitch angle. Such axial induction factor is sufficiently high to expect a considerable variation in induced velocity at yawed conditions.

Furthermore some results are presented for a tunnel speed of 15 m/s where the advancing and retreating blade effect is dominant and where significant dynamic stall effects occur.

The measurements are compared with calculational results from PHATAS and AWSM. For the modelling of yawed conditions it is important to know that PHATAS includes the following effects:

- The advancing and retreating blade effect and dynamic stall effects. The advancing and retreating blade effect is modelled straightforwardly by decomposing the skewed wind speed vector into an axial and tangential component, where the tangential component is added or subtracted from the rotational speed. The resulting dynamic stall effects (on the lift only) are modelled with the first order dynamic stall model from Snel (1997).
- The azimuthal variation of the induced velocities as a result of the skewed wake geometry. These effects are taken into account with the empirical model from section 8.3.1.

Results from the AWSM code are only shown for a tunnel speed of 5 m/s since AWSM code suffered from some convergence problems at high tunnel speeds. Since high tunnel speed are associated to low induced velocities, it is expected that the added value of AWSM is limited for these conditions anyhow. Furthermore AWSM does not include a dynamic stall model, but the effect from the shed vorticity (due to the unsteady bound vortex strength) is included. Dynamic stall effects are expected to play a minor role at the low tunnel speed which is considered by AWSM and where no convergence problems occurred.

Most of the presented graphs show the calculated and measured sectional normal forces binned as function of azimuth angle. Some results from the angles of attack and induced velocities are also discussed (even though they are only calculated values), since they largely determine the azimuthal variation of the normal force. In principle one could think of comparing the results from the angle of attack with the measured local flow angles. However, these angles are measured with the five hole pitot probes, which are located at positions, slightly different from the pressure taps (see section 4.4). Furthermore the local flow angles need to be corrected for upwash which is not straightforward on a rotating wind turbine blade, see section 5.2. In view of these uncertainties the measured inflow angle is not included in the comparison.

As a matter of fact, the figures of the normal forces do not present the actual normal forces but it is the value of $c_n q$ where c_n and the dynamic pressure q were stored in the database from NREL. This value differs from the actual

normal force by the (constant) chord which makes its unit N/m^2 .

8.4.1 Results at a tunnel speed of 5 m/s

The figures 8.9 show the normal forces at 47% and 95% span for a tunnel speed $V_{\text{tun}} = 5 \text{ m/s}$.

The expectations from section 8.3.2 are, at least to some extent, reflected into the calculated and measured $n(\phi_r)$ curves

- At the outboard section (95% span), the calculated and measured $n(\phi_r)$ curves are more or less sinusoidal with the maximum value of the normal force at the upwind side of the rotorplane (i.e. $0 < \phi_r < 180^\circ$), i.e. a stabilizing yawing moment contribution.

Figure 8.10, shows the underlying induced velocities calculated by PHATAS and AWSM. At 95% span, it can be seen that the actually calculated induced velocities behave more or less in line with the sinusoidal variation from Figure 8.5.

Although the global behavior of the normal force is mainly determined by the skewed wake effect, some disturbances are apparent, since the maximum in normal force does not occur at (precisely) $\phi_r = 90$ degrees, but at $\phi_r < 90$ degrees. This can be explained by the advancing and retreating blade effect on V_{eff} : According to tables 8.1 the variation in V_{eff} shifts the maximum towards $\phi_r = 0$ degrees indeed.

- At the inboard sections (47% span), the maximum normal force is found at the downwind side of the rotor plane (i.e. between $\phi_r = 180$ and 360 degrees). Such behavior is in line with the expected skewed wake effect at the inner part of the blade and it leads to a destabilizing yawing moment contribution. It is also consistent with the induced velocities calculated by PHATAS and AWSM at 30% and 47% span, see Figure 8.10, which shows the minimum induced velocity at the downwind side of the rotor plane.

The variation in the normal force is of course also determined by the advancing and retreating blade effect. As a matter of fact, tables 8.1 indicates a relatively large influence from this effect at the inboard sections (the 'advancing and retreating blade numbers' are of the same order of magnitude as the 'skewed wake numbers'). It should be realized however that the advancing and retreating blade effect on the V_{eff} opposes and (partly) compensates the effect on α by which the skewed wake

effect becomes the most prominent mechanism in the load variation.

- At the mid-span positions (63% span and 80% span, not presented in this report) the observations on the normal force are more or less a mixture of the observations given at the inboard and outboard sections.

Generally speaking there is a good agreement between the measured $n(\phi_r)$ curves and the ones calculated with PHATAS and AWSM: The maximum normal forces at the outboard sections are found at the upwind side, where they are shifted towards the downwind side at the inboard sections. The agreement between the AWSM results and the measurements is excellent in terms of shape of the normal force distribution (where it should be noted that it is this shape which determines the yawing moment). It is furthermore noted that the off-set in level at 95% span is consistent with the overpredicted normal force as discussed in 5.7.2. The agreement between the PHATAS results and the measurements is poorer but opposite to common (engineering) yaw models, as developed in the Dynamic Inflow projects based on the purely sinusoidal behavior of figure 8.5, PHATAS anyhow predicts the shift in maximum normal force towards the downwind part of the rotor plane at the inner part of the blade. This is in agreement with the measured results.

It is furthermore interesting to see that, generally speaking, the mutual agreement between the PHATAS and AWSM calculated curves of $u_i(\phi_r)$ at 30% and 47% span is good, even though they are derived from very different sources: The PHATAS model is based on wind tunnel measurements and the AWSM model is based on a free wake representation. It indicates that the engineering model as implemented in PHATAS is a good representation of the induced velocity variation at the root.

In order to assess the prediction of the skewed wake effect in a quantitative way, a comparison is made between the calculated and measured 'sectional yawing moments' (dM_{yaw}).

Thereto the $n(\phi_r)$ curves have been transformed into their contribution to the yawing moment:

$$dM_{yaw} = - \sum_{ibl} n_{ibl} \cdot r \cdot \sin(\phi_{r,ibl}) \quad (8.7)$$

In equation 8.7, index *ibl* denotes the blade number. Note that the NREL blade numbering is such that blade 3 is the instrumented blade and blade 1

	$dM_{yaw,30}$ [Nm/m]	$dM_{yaw,47}$ [Nm/m]	$dM_{yaw,63}$ [Nm/m]	$dM_{yaw,80}$ [Nm/m]	$dM_{yaw,95}$ [Nm/m]
Meas.	6.9	6.3	-6.6	-24.0	-39.8
AWSM	3.9	4.7	-4.9	-27.9	-41.0
PHATAS	8.0	15.0	5.7	-34.1	-102.0

Table 8.3: NREL Phase VI(NASA-Ames): Contribution of the instrumented sections to the yawing moment, measured and calculated with AWSM and PHATAS for $V_{tun} = 5$ m/s, $\phi_y = 30$ degrees and $\theta = 0$ degrees. The spanwise position is given as subscript

is the non-instrumented blade. Hence the $n_1(\phi_{r,1})$ curve has not been measured, but it is assumed to be similar to the measured $n_3(\phi_{r,3})$ curve. Equation 8.7 gives an indication whether or not the normal force distribution yields a stabilizing yawing moment contribution, since a negative value indicates a stabilizing yawing moment and a positive value indicates a destabilizing yawing moment.

The (rotor averaged) results from equation 8.7 are listed in table 8.3. The results are very consistent to the qualitative observations given above:

- The measured yawing moment contribution is stabilizing at the outboard sections (63% to 95% span), where it is destabilizing at the inboard sections. This is also predicted by PHATAS and AWSM.
- The agreement between AWSM calculated yawing moment and the measured values is good. The AWSM calculated yawing moment is generally closer to the measured values than the PHATAS calculated yawing moment.
- PHATAS strongly overestimates the yawing moment at the tip (95% span). This may again be an indication that BEM type of tip models need improvement.

8.4.2 Results at a tunnel speed of 15 m/s

In figure 8.11 the comparison is shown between measurements and PHATAS calculated results of the normal force at $V_{tun} = 15$ m/s and a pitch angle of 0 degrees. The skewed wake effect is expected to play a minor role at this high tunnel speeds by which the load variation is mainly determined by the

advancing and retreating blade effect. It is also known that the angle of attack at 15 m/s is much larger than the stall angle of attack it may be expected that dynamic stall effects are very prominent.

PHATAS is also equipped with a dynamic stall model from [Snel \(1997\)](#). In order to investigate whether this model improves the agreement with the measurements, Figures 8.11 show a comparison with PHATAS calculations with and without dynamic stall model.

It can be seen that the max-min values of the normal force are around 0-180 degrees azimuth respectively, consistent with the expectations from the advancing and retreating blade effect. The maximum normal force occurs near 0 degrees azimuth which shows the advancing and retreating blade effect on the effective velocity to dominate the effect on the angle of attack, see table 8.1.

Generally speaking the agreement between measurements and PHATAS calculations is moderate and it cannot be concluded that this dynamic stall model leads to an improvement. Differences are found in the amplitude and the phase of the $n(\phi_r)$ curve. In this respect is worthwhile to mention the study from [Santos Pereira et al. \(2011\)](#). He improved the prediction of loads at yawed conditions on the Mexico rotor using a refined version of the dynamic stall model from [Leishman and Beddoes \(1998\)](#).

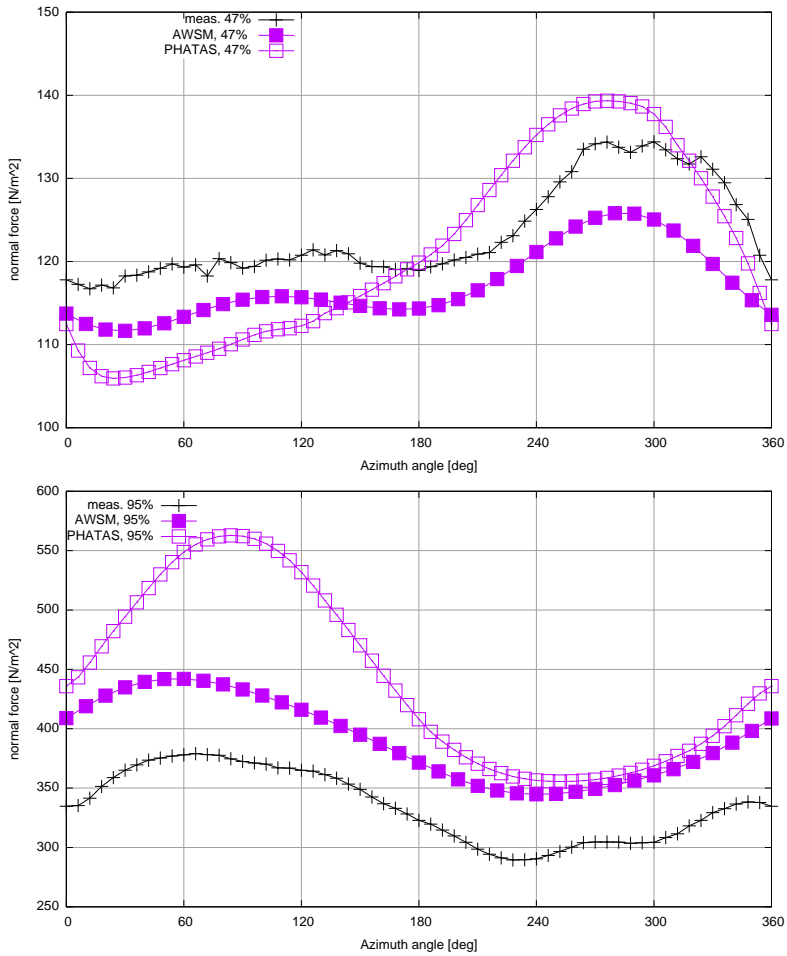


Figure 8.9: NASA-Ames: Azimuthal variation of normal force at 47% (upper figure) and 95% span (lower figure) for $V_{\text{tun}} = 5$ m/s, $\phi_y = 30$ degrees and $\theta = 0$ degrees. Measured and calculated with PHATAS and AWSM

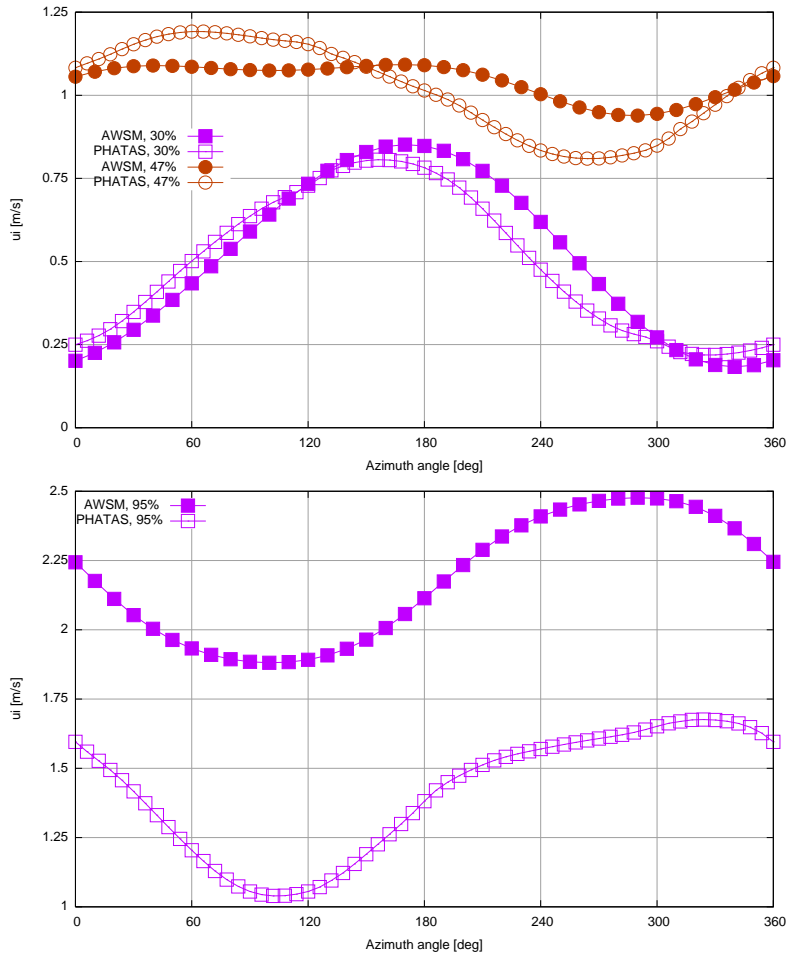


Figure 8.10: NASA-Ames: Azimuthal variation of induced velocity at 30% and 47% (upper figure) and 95% span (lower figure) for $V_{\text{tunn}} = 5$ m/s, $\phi_y = 30$ degrees and $\theta = 0$ degrees. Calculated with PHATAS and AWSM

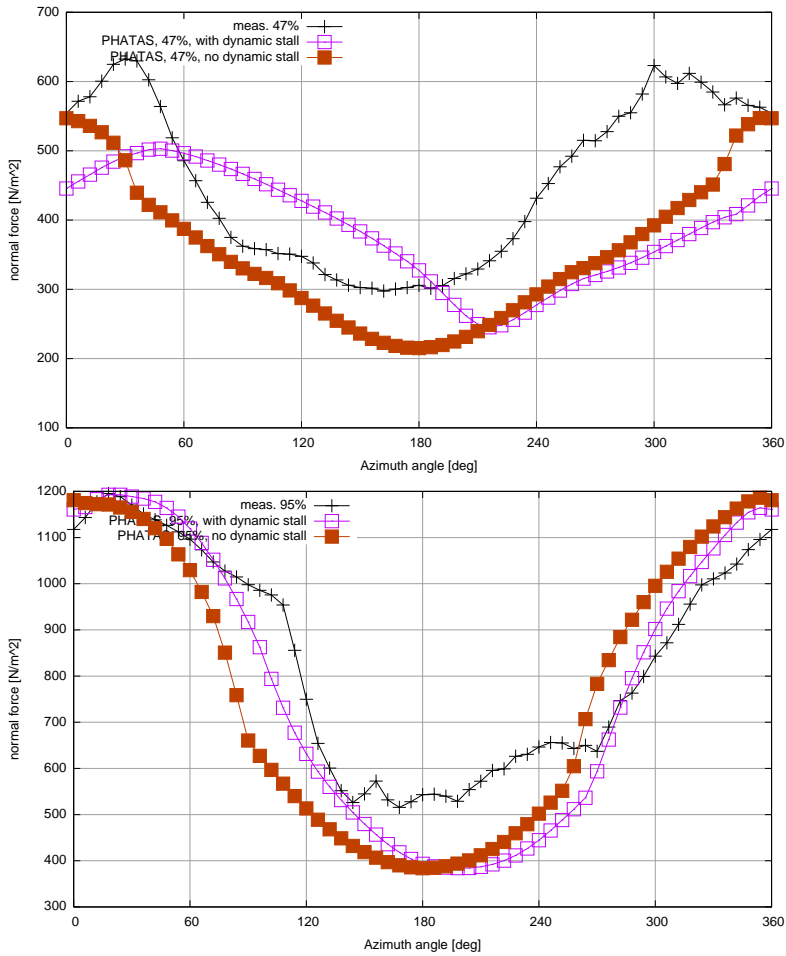


Figure 8.11: NASA-Ames: Azimuthal variation of normal force at 47% (top) and 95% span (bottom) at $V_{\text{tun}} = 15$ m/s, $\phi_y = 30$ degrees and $\theta = 0$ degrees. Calculated by PHATAS with and without dynamic stall

8.5 IEA Task 29(Mexnext): Mexico measurements in yaw

Within IEA Task 29(Mexnext) several analyzes have taken place on the Mexico measurements at yawed conditions. These results are reported in detail by [Schepers, Boorsma et al. \(2011\)](#). A selection of results is given in the present report: Section 8.5.1 analyzes the general character of the flow field at yaw from the PIV measurements. This analysis is of particular importance since the shape of the vortex wake determines the variation of induced velocities in the rotor plane. Moreover section 8.5.2 shows a comparison between calculated and measured results. The comparison considers both loads as well as velocities. All presented results are taken at design conditions, i.e. a tunnel speed of 15 m/s and a pitch angle of -2.3 degrees. The yaw angle is ± 30 degrees.

8.5.1 Flow field and tip vortices at yaw

In figure 8.12 the tip vortex trajectories at 30 degrees yaw are presented from the tip vortex tracking experiments. As a matter of fact these measurements have been performed for a yaw angle of +30 degrees and -30 degrees at the positive y-direction (where the positive y-direction is indicated in figure 8.12). Then the results for negative yaw angle are mirrored and interpreted as positive yaw but negative y-direction.

Figure 8.12 shows the wake deflection at the 'upwind side' of the rotor plane to be significantly different from the wake deflection at the 'downwind side'. At the upwind side the initial deflection is limited (the tip vortices travel at a constant radial position of $r \approx 2.25$ m) where a strong deflection appears at the downwind side.

These differences in deflection can be explained by the effect of the axial induced velocity on the wake skew angle (χ), see also section 3.8:

$$\tan\chi = \frac{V_w \sin\phi_y}{V_w \cos\phi_y - u_i} \quad (8.8)$$

Since the induced velocity at the downwind side of the rotor plane is high this yields a strong wake deflection. The opposite happens at the upwind side where the induced velocity is small. This implies a mutual interaction

between induced velocities and wake shape: The induced velocities determine the wake shape where the wake shape determines the induced velocities.

It is noted that calculations from the CFD code Fluent as carried out by ECN's daughter company NRG, show an additional effect on the wake deflection: This is caused by the blockage from the nacelle at the upwind side, see [Kuczaj \(2009\)](#). Figures 8.13 and 8.14 show the axial velocity as function of the axial

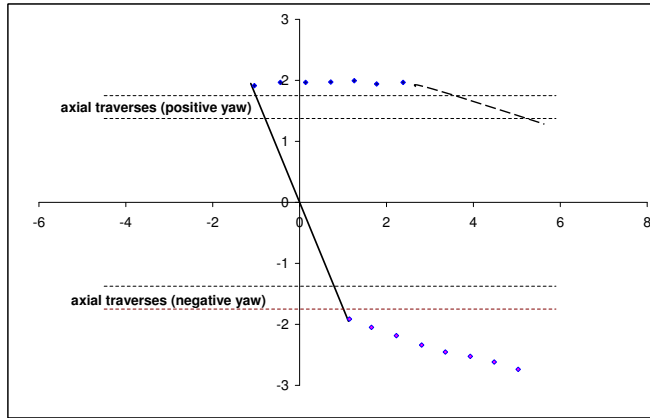


Figure 8.12: Mexico: Tip vortex positions seen from above at $V_{\text{tun}} = 15$ m/s, $\theta = -2.3$ degrees and $\phi_y = 30^\circ$. The actual measured tip vortex positions are indicated with diamonds. The dashed line indicates the expected tip vortex trajectory. Also indicated are the positions of the PIV sheets at two axial traverses

coordinate at two radial positions ($y = 1.374$ m and $y = 1.75$ m (61% and 78% span) for positive and negative yaw.

The corresponding results at zero yaw are also plotted. Note that results have been averaged over the axial extent of the PIV sheets. The zero velocity at 30 degrees yaw and $x=2$ m and $y = 1.374$ m is a result of the nacelle being present at that position.

The axial traverses at positive yaw initially show a reduced velocity behind the rotor followed by an abrupt increase to the free stream velocity of ≈ 15 m/s. This rapid increase is visible at both radial stations but it happens at earlier x for the inner station. It can be explained by considering the tip vortex trajectories and the locations of the axial traverses from figure 8.12: The PIV sheets at positive yaw are located at the upwind side from figure 8.12 where the initial wake deflection is limited with the edge of the wake at $y \approx 2.25$ m. The axial traverses at $y=1.374$ m and $y=1.75$ m then remain within the wake with consequent lower velocities. However at larger x -locations the wake may be expected to deflect downward, (this was also predicted with Fluent in Kuczaj (2009)), by which the traverse at $y = 1.75$ m crosses the edge of the wake and continues in the free stream where the velocity is 15 m/s. At an even further downstream location, where the wake edge is deflected more inboard, the inner PIV traverse will also cross the wake edge and the velocity will reach the free stream value.

The traverse at negative yaw corresponds to a traverse at the downwind side of figure 8.12. The wake deflection at this side makes that the entire traverse at both y -positions remain within the wake where the velocities are lower than the free stream velocities.

8.5.2 Comparison between calculated and measured results

In IEA Task 29, Mexnext, the loads at yaw are calculated with a large variety of codes e.g. BEM models, lifting line free vortex wake methods, and CFD codes. Similar to the discussion of the NREL PhaseVI (NASA-Ames) measurements in section 8.4, the normal force is presented as function of azimuth angle for one inboard and one outboard station (35% respectively 82% span) for a yaw angle of 30 degrees.

The velocities are calculated with CFD codes only. They are shown for a yaw angle of ± 30 degrees in the form of axial velocity traverses at $y = 1.4$ and 1.8 m (i.e. these results are very similar to the results in section 8.5.1, apart from a slightly different y -position). In addition the radial velocity traverses are discussed, 15 cm upwind and 15 cm downwind of the rotor plane (note that the radial direction is parallel to the rotor blade and not in a tunnel frame of reference). These traverses are made at blade azimuth angles which vary from 180 degrees to 280 degrees in steps of 20 degrees.

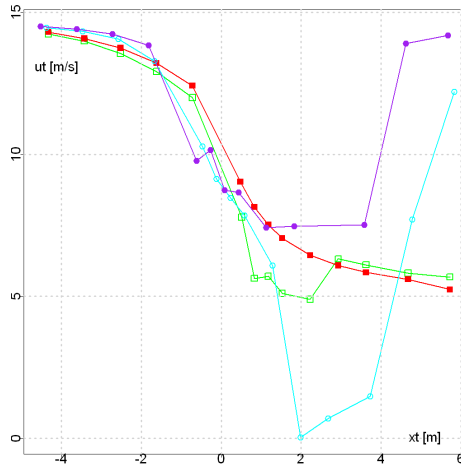


Figure 8.13: Mexico: Axial velocity at two radial position as function of stream wise coordinate x for $V_{\text{tun}} = 15\text{m/s}$ and $\phi_y = 0$ and 30° , $\theta = -2.3^\circ$

- At 61% span and $\phi_y = 0^\circ$; ■ At 82% span and $\phi_y = 0^\circ$;
 ○ At 61% span and $\phi_y = 30^\circ$; ● At 82% span and $\phi_y = 30^\circ$

This section highlights a few results: It only discusses the axial velocities (i.e. the velocities in a tunnel frame of reference in line with the tunnel speed) and the radial traverses are shown for a few blade azimuth angles only. The results of the other velocity components and the other blade azimuth angles can be found in [Schepers, Boorsma et al. \(2011\)](#).

Loads

In figures 8.15 and 8.16 the load variation is presented as a function of azimuth angle for the normal forces at 35% and 82% span. The standard deviation of the processed data points is displayed using a grey band. The grey band was generally found to be very small although the standard deviation at the 35% span station is slightly higher due to an intermittently malfunctioning pressure sensor. The measurements are compared with calculations from lifting line codes and CFD codes.

A phase shift is visible in the azimuthal load variation between the inner and

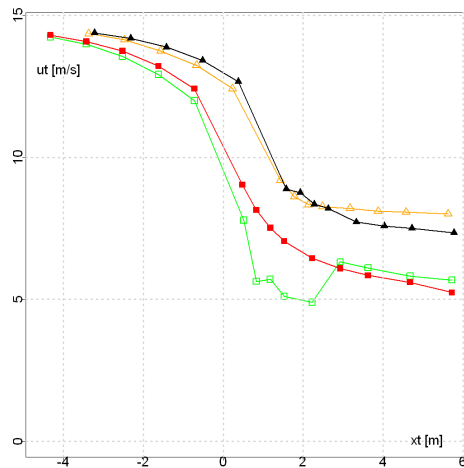


Figure 8.14: Mexico: Axial velocity at two radial position as function of stream wise coordinate x for $V_{\text{tun}} = 15\text{m/s}$ and $\phi_y = 0$ and -30° , $\theta = -2.3^\circ$

□ At 61% span and $\phi_y = 0^\circ$; ■ At 82% span and $\phi_y = 0^\circ$;
△ At 61% span and $\phi_y = -30^\circ$; ▲ At 82% span and $\phi_y = -30^\circ$

outer part of the blade, similar to the phase shift in the NREL Phase VI(NASA-Ames) measurements: At 82% span the maximum normal force is found at the upwind part of the rotor plane. This maximum shifts towards the downwind side at 35% section. It leads to a a stabilizing yawing moment contribution at the outer part and a destabilizing yawing moment at the inner part.

For the lifting line codes, the qualitative agreement is generally speaking better for the outboard sections compared to the inboard sections. This can be explained by the fact that the advancing and retreating blade effect is more dominant there and more straightforward to predict. For the inboard sections the aerodynamics becomes more complicated and the combination of a varying induction together with separated flow proves difficult to model. The inboard agreement for the CFD codes is better than for the lifting line codes.

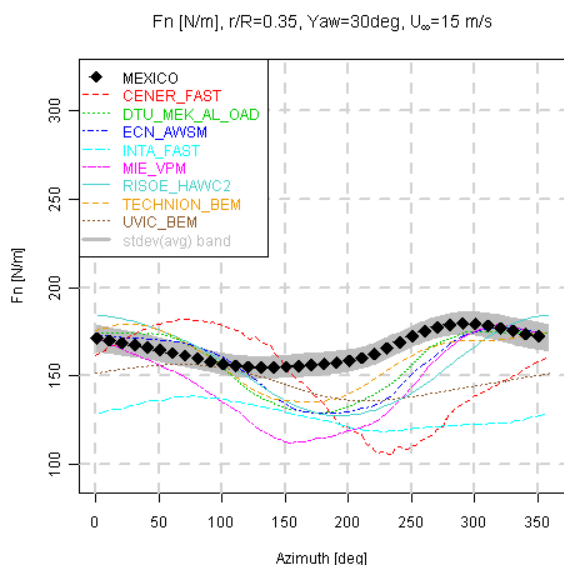
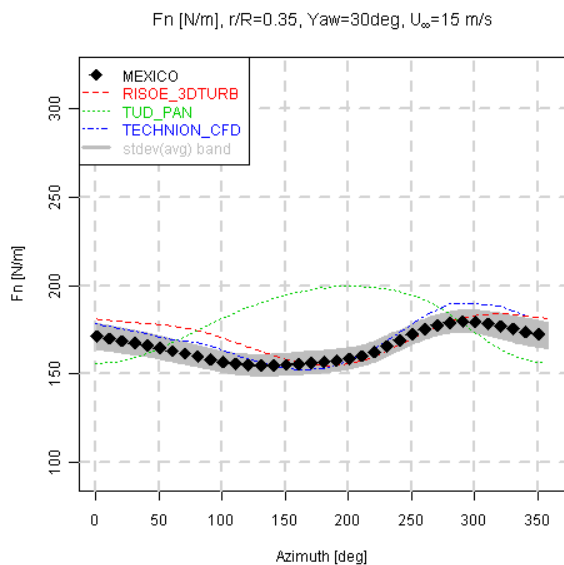


Figure 8.15: IEA Task 29 (Mexnext): Azimuthal variation of normal force at 35% (CFD codes (top) and lifting line codes (bottom)), $V_{\text{tun}}=15$ m/s, $\phi_y=30^\circ$, $\theta = -2.3^\circ$

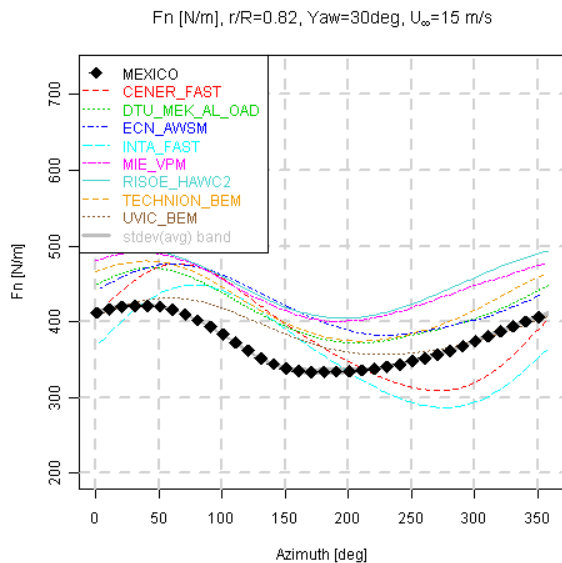
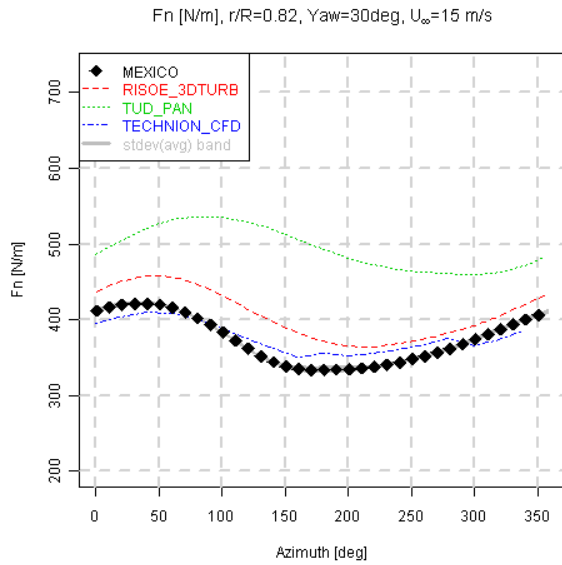


Figure 8.16: IEA Task 29 (Mexnext): Azimuthal variation of normal force at 82% span (CFD codes (top) and lifting line codes (bottom)), $V_{tun}=15$ m/s, $\phi_y=30^\circ$, $\theta = -2.3^\circ$

Axial velocity traverses

In figure 8.17 and 8.18 the calculated and measured axial velocity traverses are presented for positive and negative yaw.

Generally speaking the velocities are predicted in good agreement with the measurements, except from the near wake ($x \approx 1$ m).

For positive yaw, the wake deflection causes the traverse to move outside the wake for $x > 4$ m ($y = 1.4$ m) and $x > 3$ m ($y = 1.8$ m) as discussed in section 8.5.1. This is predicted by most codes.

As explained in section 8.5.1 the nacelle is causing the zero velocities near $x = 2$ m at the inboard section, but little codes included the nacelle by which most codes predict a finite velocity there. The sinusoidal fluctuations in the near wake for $y = 1.8$ m are caused by slicing through the tip vortices, which is often reproduced in good agreement.

Radial velocity traverses

In figure 8.19 and 8.20 the calculated and measured radial velocity traverses are presented just upstream and just downstream of the rotor plane. The results for negative yaw angle are mirrored and interpreted as positive yaw with negative radial positions. It is recalled that the radial direction is parallel to the rotor blade.

The radial traverses are predicted surprisingly good even for the downwind traverse. Dependent on the azimuth angle the traverse slices through the tip vortex, of which most codes are able to predict both position and strength accurately.

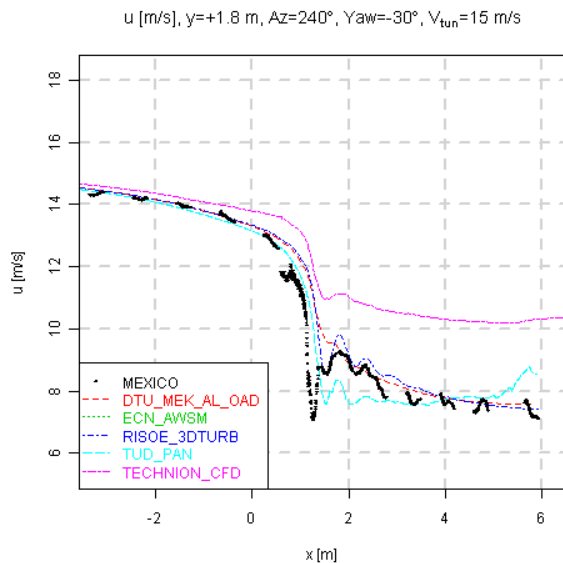
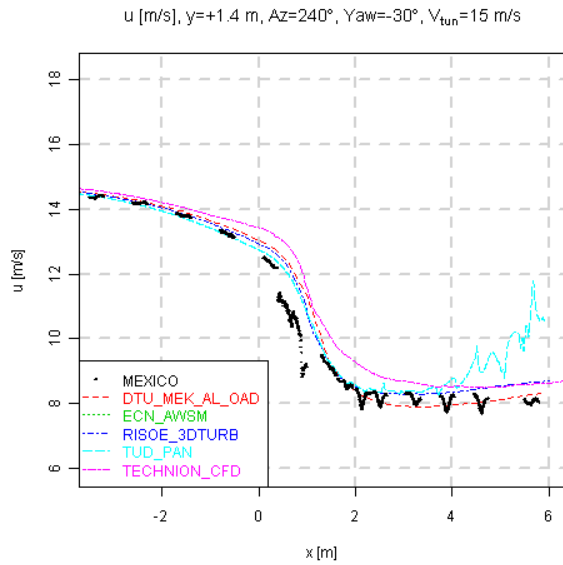


Figure 8.17: IEA Task 29 (Mexnext): Axial velocity as function of streamwise coordinate at two y-positions: $y=1.4$ m and $y=1.8$ m; The yaw angle is -30 degrees; $V_{\text{tun}}=15$ m/s, $\theta = -2.3^\circ$

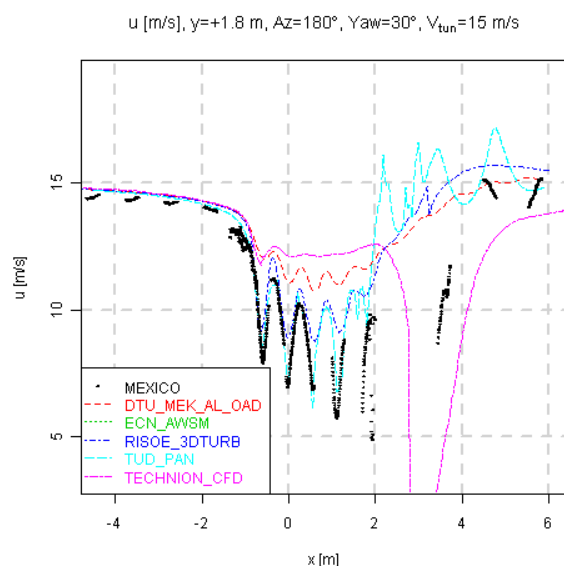
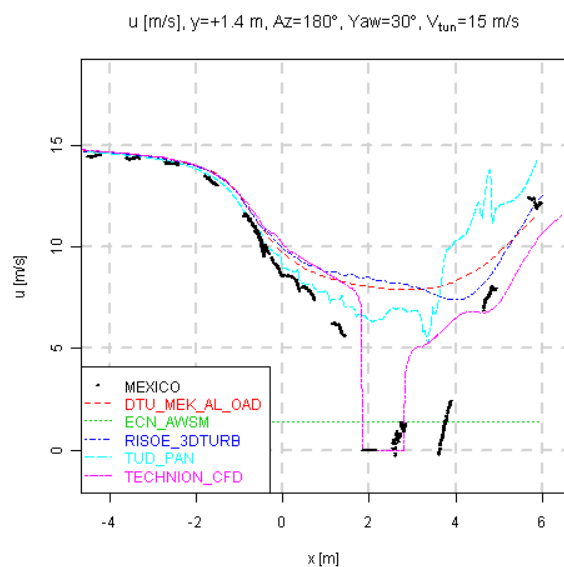


Figure 8.18: IEA Task 29 (Mexnext): Axial velocity as function of streamwise coordinate at two y -positions: $y=1.4$ m and $y=1.8$ m; The yaw angle is $+30$ degrees; $V_{tun}=15$ m/s, $\theta = -2.3^\circ$

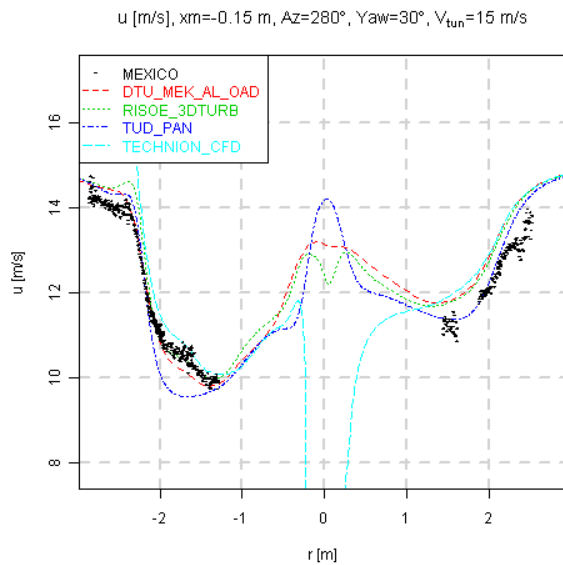
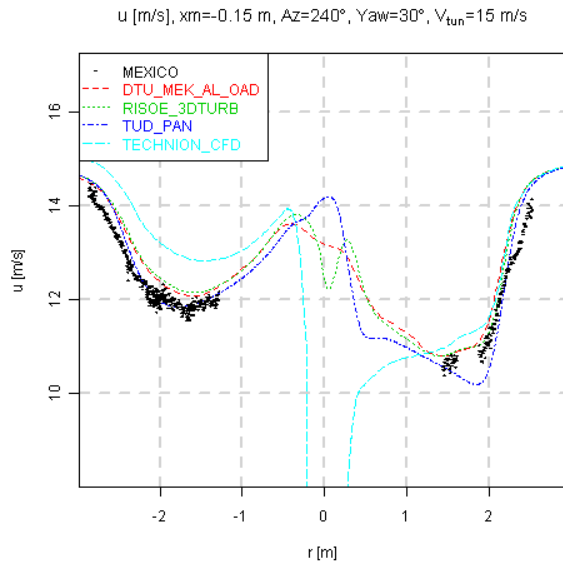


Figure 8.19: IEA Task 29 (Mexnext): Axial velocity as function of radial position upstream of the rotor, for two blade azimuth angles, $\phi_y = 30^\circ$, $V_{tun} = 15$ m/s, $\theta = -2.3^\circ$

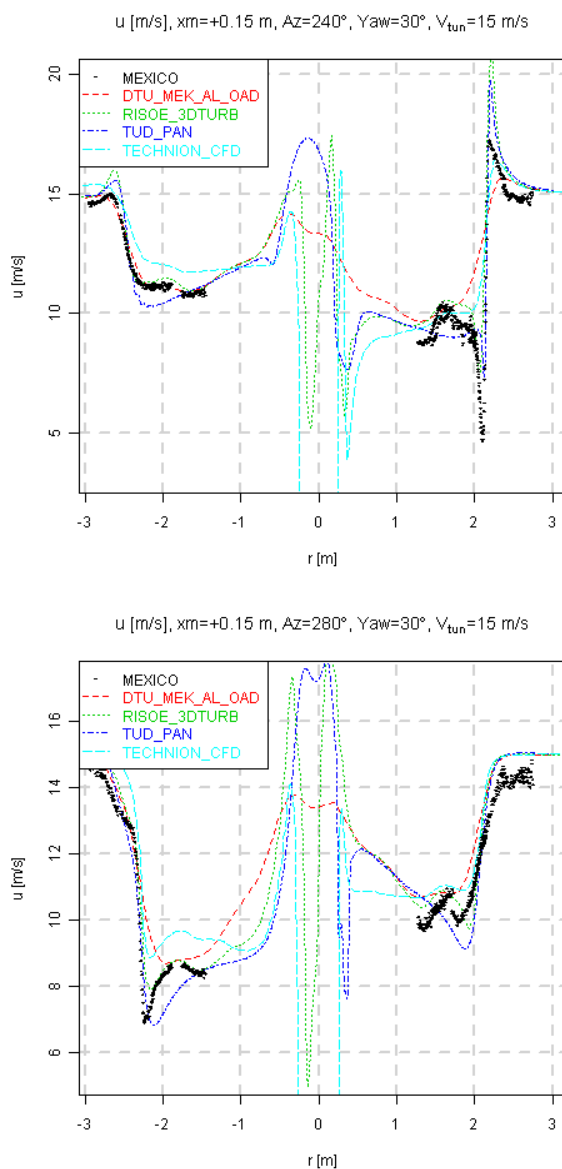


Figure 8.20: IEA Task 29 (Mexnext): Axial velocity as function of radial position downstream of the rotor, for two blade azimuth angles, $\phi_y = 30^\circ$, $V_{\text{tun}} = 15$ m/s, $\theta = -2.3^\circ$

8.6 Summary, conclusions and recommendations on yaw aerodynamics

- In this section several studies on yaw aerodynamics are discussed. The attention was focussed on the expected power decrease from yaw which implies an economical loss and on the increased load (fluctuations) which effect the design load spectrum and the power quality. Together with the fact that wind turbines operate under a continuous yaw operation, due the inevitable wind direction fluctuations around the mean wind direction, this makes the practical importance of yaw large.
- Wind tunnel measurements were found to be very suitable to study yaw aerodynamics: The wind tunnel environment avoids the common problem of field measurements where the interpretation of results is complicated by the uncertain and instationary atmospheric conditions.
- The TUDelft OJF measurements delivered direct velocity measurements from which an engineering model for the induced velocity could be derived. The NASA-Ames and Mexico wind tunnel measurements delivered the aerodynamic forces at different radial positions, which made it possible to assess aerodynamic yaw effects on a sectional level. Furthermore the Mexico PIV measurements helped to understand the flow field at yawed conditions.
- At low angles of attack the power decreases with yaw. It is very surprising to find the opposite at very large angles of attack. This might be due to non-linear dynamic stall effects. BEM predicts the dependency of the power with yaw poorly. It is recommended to investigate the yaw effect on the power more thoroughly also including CFD analyzes.
- Yaw leads to a cyclic load fluctuation which enhances the fatigue loads. This is caused by an azimuthal variation of induced velocities and by the advancing and retreating blade effects. The variation of the induced velocity was found to play a major role at high axial induction factors (i.e. relatively low wind speeds). The advancing and retreating blade effect is in particular important at high wind speeds, where it leads to strong dynamic stall effects.
- At high axial induction factors the variation of the normal forces is clearly influenced by the skewed wake effect by which a strong radial dependency is found on the azimuthal variation of the normal forces:

- At the outboard part of the blade the normal force varies more or less sinusoidally such that the maximum force occurs at the upwind part of the rotor plane. The resulting load variation leads to a stabilizing yawing moment. The variation is in line with the outcome of a conventional tip vortex wake model for the calculation of induced velocities;
- At the inboard sections of the blade, the maximum value of the normal force is found to shift towards the downwind side of the rotor plane. This was explained with wind tunnel measurements of the inflow velocity and with results from free vortex wake methods, which showed the inflow velocity at the inboard station to become maximum at the downwind side of the rotor plane. The shift is a result of velocities induced by the root vortex. The resulting load variation leads to a destabilizing yawing moment. Conventional engineering models for yaw only consider the tip vorticity and they do not predict this shift.
- The AWSM code does predict the above mentioned radial dependency in the azimuthal variation of the induced velocity and the resulting azimuthal variation in normal force agrees very well with the measured values. The agreement from the PHATAS code was slightly poorer. However, opposite to common (engineering) yaw models, PHATAS anyhow predict a destabilizing yawing moment near the inboard part of the blade in agreement with the measurements due to the fact that root vortex effects are taken into account.
- The mutual comparison of the induced velocities calculated with PHATAS and AWSM codes generally shows a good agreement even though the underlying models have very different bases.
- The calculational results at the higher tunnel speeds show a much poorer agreement with the measurements. Differences occur in amplitude and phase of the normal force variation. The most likely cause for these differences are dynamic stall effects which are widely known to be a source of differences between calculations and measurements. The use of a dynamic stall model leads to a minor improvement of the NREL Phase VI (NASA-Ames) results but the use of a Beddoes Leishman dynamic stall model helped to improve the agreement with Mexico measurements.
- CFD showed excellent prediction of the details of the flow field near the

rotor plane of a yawed wind turbine.

- The tip vortex trajectories in yaw differ significantly between the upwind and downwind side of the rotor plane. This is a result of the azimuthal variation of the induced velocities, which in turn is determined by the precise shape of the tip vortex wake. As such there is a mutual interaction between wake shape and azimuthal variation of the induction.
- The studies on yaw aerodynamics as described in the present chapter are limited to yaw angles of 30-45 degrees. Larger yaw angles have been measured in the NREL Phase VI (NASA-Ames) experiment. It is recommended to analyze these measurements in future studies.

Part III

Wind Farm Aerodynamics

Chapter 9

Wind farm aerodynamic models

9.1 Introduction on wind farm aerodynamics models

Opposite to the situation for rotor aerodynamics, where the BEM model can be appointed as the main model, the variety of models for wind farm aerodynamics is much larger, see for example the overview given by [Sanderse \(2009\)](#). This is partly due to the fact that a wind farm aerodynamic model should cover much more aspects: It should model both the aerodynamic behavior of the rotor (which generates the wake) as well as the turbulent wake downstream of this rotor where several interactions with the outer atmospheric flow and adjacent wakes should be taken into account. The fact that calculational time is such an extreme constraint adds to the diversity: This makes even the most simple wake models acceptable candidates for a wind farm design code. On the other hand there is a natural drive by researchers to include as much as possible physics into the model by which the other end of the spectrum (formed by very advanced CFD codes) also attracts a lot of attention. For this reason it is not easy to give a concise description of the differences in wind farm aerodynamic models in every detail. Nevertheless a global overview will be given in section 9.4.

The most simple class of models consists of analytical expressions which

are often based on self-similar velocity profiles. Despite the simplicity of such models, the self-similarity of wake profiles does have a physical basis as it can be derived from a simple eddy viscosity model as first done by [Schlichting \(2004\)](#). This is shortly explained in section 9.3.

Most of the wake models are however based on more advanced numerical field methods. Within this class of models a popular approach is formed by the parabolized Reynolds Averaged Navier Stokes models. Parabolized models are much less computational expensive than their counterparts (fully elliptic models). For this reason they are still considered to be engineering methods. However, a disadvantage of parabolized models lies in the fact that they usually donot model the physics of the near wake in an explicit way. This is explained in in section 9.2. The present thesis pays special attention to ECN's Wakefarm model (which at a later stage was implemented into the wind farm design code FarmFlow). This model has included a feature by which the near wake is modelled in a physical way where at the same time the parabolization is retained. In this way an optimal balance is found between computational efficiency and physical accuracy. The Farmflow/Wakefarm model is described in section 9.5.

9.2 Near wake versus far wake; Parabolization

Many wake aerodynamic models make a distinction between a near and a far wake where some models even add an intermediate wake. The distinction between the near and far wake is not always straightforward. Some researchers, see e.g. [Rethoré \(2009\)](#) relate it to the different turbulent processes in the wake which each have their own length scales. The turbulent processes in the near wake are then related to the blade induced vortex structures, the length scale of which is in the order of the chord length. The turbulent processes in the far wake are related to the mixing of the wake flow with the outer atmosphere, the length scale of which is in the order of the rotor diameter.

Another description for the near wake comes from [Vermeer, Sørensen and Crespo \(2003\)](#) who write that: 'The near wake is taken as the area just behind the rotor where the properties of the rotor can be discriminated so approximately up to one rotor diameter downstream.'

A more specific distinction can be made by defining the near wake as the region where the pressure gradient dp/dx (as a result of the velocity change

from $V_w(1-a)$ to $V_w(1-2a)$ see figure 2.2), can NOT be neglected in the flow equations. The analysis of equation 2.15 in section 2.1.1 shows that the wake expands (and hence the pressure increases) until approximately $2D$ behind the turbine. For larger distances behind the turbine, the pressure gradient dp/dx is very small and this region is then called the far wake.

The neglect of this streamwise pressure gradient enables the parabolization of the Reynolds Averaged Navier Stokes (RANS) flow equations. Parabolization basically implies that the flow properties are determined by the state of the upstream flow only where all 'flow-feedback' influences from a downstream location towards an upstream location, are neglected. In this way the flow equations can be solved in a fast space marching way by which it has become a widely accepted technique to reduce the calculational time of wake models.

However, the fact that the parabolization is only justified in the far wake makes that the near wake should be modelled in a separate way. As a matter of fact the near wake is usually fully excluded from the 'real' wake modelling. The solution procedure then starts at the end of the near wake, some distance behind the rotor. This location is denoted as $x = x_{nw}$, where the value of x_{nw} is generally in the order of $2D$, consistent with the observation above that the pressure gradient dp/dx has become very small at that location. Then at $x = x_{nw}$ a velocity profile is prescribed which serves as an initial condition for the far wake.

The initial velocity profile for the far wake is sometimes based on the fully expanded velocity from the momentum theory, equation 2.7. This velocity is then applied within the expanded rotor diameter from equation 2.8 leading to a 'hat shaped' velocity profile, as sketched in figure 9.1. The underlying assumption which is made in such approach is that the inviscid wake expansion from the momentum theory is almost completed at $x = x_{nw}$, by which the ignorance of this expansion is expected to have limited effects for $x > x_{nw}$. On the other hand it is assumed that the near wake basically develops according to the inviscid momentum theory by which all turbulent mixing in this region is neglected. The neglect of turbulent mixing in the near wake is to some extent justified by Smith (1990). There it is explained that the shear stress profile develops relatively slowly in the near wake. This slow development leads to a limited mixing of momentum from the ambient flow to the wake. It must be noted however that this observation is only valid for single wake conditions. For multiple wake the turbulent mixing in the near wake will be much stronger.

An approach based on an initial velocity profile from the momentum theory was followed by [Crespo et al. \(1985\)](#) in the UPMWAKE code. However, Crespo applied the fully expanded velocity deficit in the rotor plane already, i.e. at $x_{nw}=0$, despite the fact that momentum theory states that this velocity is reached at infinity only. ECN used the same UPMWAKE code but applied the initial velocity profile from the momentum theory at $x_{nw} = 2.25 D$, leading to a better agreement with measurements ([Adams \(1995\)](#)).

Alternatively the velocity profile at $x = x_{nw}$ is often based on a data fit, e.g. a Gaussian profile. The use of a Gaussian profile at the end of the near wake implicitly assumes that some turbulent mixing has already taken place before this position. A Gaussian profile was used by [Ainslie \(1988\)](#) who applied this profile at $x_{nw} = 2D$. The model from [Lange et al. \(2003\)](#) is largely similar to the model from Ainslie but the near wake length is made dependant on the ambient turbulence intensity due to the fact that the wake decays slower at lower ambient turbulence intensities. The fact that the wake decay is slower at lower ambient turbulence levels indeed, is proven experimentally in section 11.2.2 on basis of EWTW measurements. In [Schepers \(2003\)](#) a relatively good fit is found with measurements if a Gaussian profile was applied at $x_{nw} = 2.25 D$.

However the fact that the physics of the near wake is generally not modelled explicitly is still considered to be a weak point in all of these methods and it formed the motivation for the improvements in the Farmflow/Wakefarm program as described in section 9.5.2.

9.3 Global wake behavior

Before discussing ECN's Farmflow/Wakefarm model in some detail it is good to gain some general insight into the global wake behaviour. Thereto an analytical expression is derived for u_{def} which denotes the velocity deficit in the (far) wake. The model is described in [Schlichting \(2004\)](#). It has been used in the EU project Upwind to assess the scaling effects on wake aerodynamics, see [Schepers, Barthelmie, Politis \(2010\)](#). The model from Schlichting has been derived from the boundary layer equations under the following assumptions:

- The stream wise pressure gradient dp/dx is neglected (Hence it a parabolized method valid for the far wake only, see section 9.2).

- The wake deficit u_{def} is assumed to be axisymmetric around the rotor (wake) centre by which it can be expressed as function of r , i.e. the radial coordinate with respect to the wake centre;
- The analysis is based on the boundary layer equations in which the boundary layer assumption is made (i.e. the length scale in streamwise (x) direction is assumed to be long compared to the length scale in radial (r) direction)
- The rotor is modelled as an actuator disc with axial force coefficient $C_{D.\text{ax}}$. Only momentum exchange in axial direction is considered.
- The wake flow is turbulent, i.e. turbulent friction is much larger than laminar friction;
- The velocity deficit u_{def} is small compared to the free stream velocity.

With a simple mixing length eddy viscosity model, the analysis from [Schlichting \(2004\)](#) eventually shows that the velocity deficit takes a self similar velocity profile form, i.e.:

$$u_{\text{def}}(r) = u_{\text{max}} f(r/R_w) = u_{\text{max}} f(\eta) \quad (9.1)$$

with η the ratio between the radial position and the wake radius R_w , i.e. $\eta = r/R_w$. The self-similar solution $f(\eta)$ was found to be:

$$f(\eta) = [1 - \eta^{1.5}]^2 \quad (9.2)$$

Equation 9.2 can be shown to approach closely a Gaussian behaviour:

$$f(\eta) \approx \exp^{-\eta^2/0.27} \quad (9.3)$$

Hence the velocity deficits are characterized by the maximum velocity deficit u_{max} in the wake center and the wake radius (R_w) which are both a function of the streamwise coordinate x .

The wake radius and the velocity deficit are found from integration of the momentum deficit over the wake using equation 9.1 and the above mentioned assumption of small u_{def} .

$$\frac{u_{\text{max}}}{U_\infty} = k_{\text{um}} \frac{C_{D.\text{ax}} A}{R_w^2} \quad (9.4)$$

in which k_{um} is a constant ($= (\int 4\pi f(\eta) \eta d\eta)^{-1} \approx 0.6189$ (using equation 9.2)). Equation 9.4 shows the velocity deficit to decrease with the wake radius according to R_w^{-2}

Then the following considerations are made:

- The rate of increase of R_w is proportional to the transverse velocity v

$$\frac{DR_w}{Dt} \sim U_\infty \frac{dR_w}{dx} \sim v \quad (9.5)$$

- The transverse velocity v is approximated from a simple eddy viscosity mixing length model:

$$v \sim l \frac{du}{dr} \quad (9.6)$$

in which l is the mixing length which scales with the wake radius

$$l = \alpha R_w \quad (9.7)$$

Note that α is assumed to be constant.

- The average shear over the wake radius can be approximated as the maximum velocity deficit divided by the wake radius:

$$\frac{du}{dr} \sim \frac{u_{\max}}{R_w} \quad (9.8)$$

This yields:

$$dR_w/dx \sim \alpha \frac{u_{\max}}{U_\infty} \quad (9.9)$$

- Now the wake radius is solved from equations 9.4 and 9.9 which leads to:

$$\frac{R_w}{R} = k_{Rw} C_{D,ax}^{1/3} \left(\frac{x - x_0}{R} \right)^{1/3} \quad (9.10)$$

(with k_{Rw} a constant in which α is 'hidden'). The value of x_0 needs to be tuned from e.g. measurements and it is related to the length of the near wake length.

- From equation 9.10 and the momentum relation (equation 9.4) the relative maximum velocity deficit is derived:

$$\frac{u_{\max}}{U_\infty} = \lambda_2 C_{D,ax}^{1/3} \left(\frac{R}{x - x_0} \right)^{2/3} \quad (9.11)$$

(with $\lambda_2: k_{um}\pi \cdot k_{Rw}^{-2}$)

Hence, in global terms the velocity deficit in the wake takes a self similar form according to equation 9.1, where the velocity deficit u_{\max} in the wake centre decreases with downstream distance x according to $x^{-2/3}$ and the wake radius R_w increases with downstream distance according to $x^{1/3}$.

9.4 Classification of wake aerodynamic models

Although, as already mentioned in section 9.1, it is not easy to give a concise description of the differences in wind farm aerodynamic models, some classification can be made along the following lines:

- Differences in application:
 - Some wake models are merely devoted to the calculation of energy production and power. These models generally calculate the mean wind speed in the wake, in the form of a velocity deficit relative to the free stream velocities. Some of these models are of an analytical nature, see e.g. the models from [Lissaman and Bate \(1977\)](#) or [Vermeulen \(1980\)](#). They are often mentioned to be fully empirical. Nevertheless there is often still some physics hidden in these methods because they generally assume a self-similar velocity profile which is based on the physical model as described in section 9.3. Consequently they should be referred to as semi-empirical models.

The model described in section 9.3 also formed the basis for the often applied field method from [Ainslie \(1988\)](#) which in principle models the wake mean wind speed only. The model from Ainslie includes an additional eddy viscosity which is related to the ambient turbulence in view of the fact that wind turbine wakes decay slower in the case of low turbulent environments, see for example the measurements presented in section 11.2.2.

- Some wake models are merely devoted to the calculation of loads on a turbine in a farm. These methods should also model the turbulence in the wake. An example is the effective turbulence model from [Sørensen, Frandsen and Tarp-Johansen \(2007\)](#). It represents the wake effects in the form of an effective turbulence intensity which, when fed into an aero-elastic code yields a load increase.
- Most wake models can be used to calculate both the power and the loads. An example is the model from [Lange et al. \(2003\)](#). This model is almost similar to the model from Ainslie but in addition it calculates the turbulence intensity from the eddy viscosity. Other examples are the ECN Farmflow/Wakefarm model (see section 9.5) or the more advanced (but also more time consuming), fully elliptic CFD methods from CRES (the FlowNS-CFD code, see

[Chaviaropoulos and Douvikas \(1998\)](#)) or CENER (the CFD-Wake model, see [Cabezon et al. \(2008\)](#)). These models calculate a turbulent kinetic energy, either with a $k-\epsilon$ or a $k-\omega$ model. From this turbulent kinetic energy the turbulence intensities in the different directions can be derived with assumptions on the anisotropy.

- Differences in the modelling of the atmospheric boundary layer around the wind farm. The wind input is often described in a simple way, e.g. a constant wind speed in time and the rotor plane, or a hub height wind speed with wind shear. Also the wind direction is assumed to be constant. These simplified input conditions are related to the fact that many wind farm aerodynamic models are time averaged methods (e.g. RANS methods) i.e. they calculate the mean velocities in the wake and the statistical properties of 'small scale' velocity fluctuations around these mean values. This goes together with the assumption of 'straight' wakes, i.e. the wake follows the ambient wind direction throughout the entire wind farm. There is however also a large scale motion by which the real wake in a wind farm, which can have a length of several km's, fluctuates (i.e. meanders) around this mean wind direction. In principle this could be modelled with a Large Eddy Simulation (LES) model or with an engineering model as developed by [Larsen et al. \(2007\)](#).
- Differences in turbine aerodynamic modelling. Usually when talking on wake aerodynamics the attention is focussed on the aerodynamic process in the wake and less on the aerodynamics of the rotor. As a result many methods for wind farm aerodynamics model the turbines in a simplified way (e.g. with an actuator disc which considers axial momentum exchange only).

Examples are the above mentioned models from Ainslie, Lange and Farmflow/Wakefarm. Also the more advanced model from [El Kasmi and Masson \(2008\)](#) and the FlowNS-CFD and CFD-Wake models are still based on an actuator disc description of the rotor, although they do take into account a radial distribution of the loads.

Some CFD methods deal the rotor in a more detailed way. A full CFD description of the turbine in combination with a CFD modelling of the wakes in a large wind farm is obviously still beyond current computer capabilities. However, the group of Sørensen at DTU has modelled the blades as separate actuator lines (see [Troldborg et al. \(2007\)](#)) or even actuator surfaces (see [Shen et al. \(2009b\)](#)). [Shen \(2011\)](#) mentioned a

long calculational time (in the order of one week) for the modelling of the wakes in a 'tandem' configuration (two wind turbines behind each other) and rotor blades represented as lifting lines for one ambient condition.

- Some models, e.g. the models based on self similar velocity profiles and the models from Ainslie, Lange and Kasmi-Masson assume 2-dimensional (axi-symmetric) conditions. Other models, e.g. ECN's Farmflow/Wakefarm code and the more advanced CFD models cover the 3-dimensional wake flow.
- Many models are parabolized and they make a division between the near wake and far wake, see section 9.2. Usually the near wake is only modelled with a velocity profile at the end of the near wake at $x = x_{nw}$ which then serves as initial profile for the far wake. Different values for x_{nw} have been taken and also different representations for this velocity profile have been taken, see e.g. [Rados et al. \(2002\)](#). In principal full elliptic (CFD) models donot make the distinction between near and far wake. A special category is the hybrid Farmflow/Wakefarm model from ECN which is a parabolized method but it prescribes a pressure gradient from a free vortex wake method. However even these elliptic (or hybrid) methods still need some special treatment of the near wake in terms of turbulence modelling. This is in particular true when the rotor is modelled in a relatively crude way (e.g. through an actuator disc). Different solutions have been invented, see section 9.5.3.
- Differences in the way how the wake superposition (as needed for multiple situations) is modelled. For actuator disc models in multiple wake situations, there are also differences in the definition of the reference velocity which is needed to find the $C_{D,ax}$, see [Prospathopoulos et al. \(2010\)](#), and a further explanation on this problem in section 10.

9.5 Description of Farmflow/Wakefarm model

The wake model on which the present report mainly focuses is ECN's Wakefarm code.

Wakefarm is based on the UPMwake code as developed by the Universidad Polytechnica de Madrid (UPM), [Crespo et al. \(1985\)](#) and it can be characterized as a 3-dimensional parabolized RANS code with a $k-\epsilon$ turbulence model, largely based on the model from [Rodi \(1982\)](#). As such it is a more elaborate

model than the simplified two-dimensional eddy viscosity model as described in section 9.3 and it does not only calculate the velocity deficit but also, from the k -values, the turbulence intensities in the wake. The University of Madrid delivered the code to ECN in the 1990's after which several modifications were implemented and the code was renamed into Wakefarm. The main difference between UPMwake and Wakefarm lied in the near wake modelling where moreover Wakefarm could calculate multiple wakes in a line set-up. In 2007 the Wakefarm code has been integrated into ECN's wind farm design code Farmflow. This implies that multiple wake situation in lateral directions have been implemented. Moreover the parameters in the turbulence model have been refined together with different boundary conditions.

Figure 9.1 gives a schematic view of the wake modelling, where it should be known that the rotor is modelled as an actuator disc. Figure 9.1 still shows the division between the near and far wake as applied in the first versions of Wakefarm and in other parabolized methods. It requires an initial velocity profile applied at a distance $x=x_{\text{nw}}$ (note that x_{nw} was generally taken to be $2.25D$). The initial velocity profile was first calculated from the axial momentum theory (leading to the hat shaped velocity profile from figure 9.1) and later from an empirical Gaussian profile, see [Schepers \(2003\)](#). Starting from this initial velocity profile the turbulent processes in the far wake are modelled with a k - ϵ turbulence model. Farmflow/Wakefarm calculates a number of quantities in the far wake, among others the wake profile (i.e the mean wind speeds in 3 directions) and the turbulence intensities in the wake. These quantities are calculated at a discrete number of grid points in the wake. More details on the Farmflow/Wakefarm modelling are given in the sections 9.5.3 to 9.5.6. The improvements by which the near wake modelling is integrated with the far wake modelling is described in section 9.5.2.

9.5.1 Free stream modelling

In the Farmflow/Wakefarm program, the free stream wind is modelled according to [Panofsky and Dutton \(1984\)](#), which is a model for the surface layer in the lower part of the atmospheric boundary layer and which uses the friction velocity (u^*), the roughness height (z_0) and the Monin-Obukhov length scale (L).

The free stream wind speed as function of height (denoted as h or z) is cal-

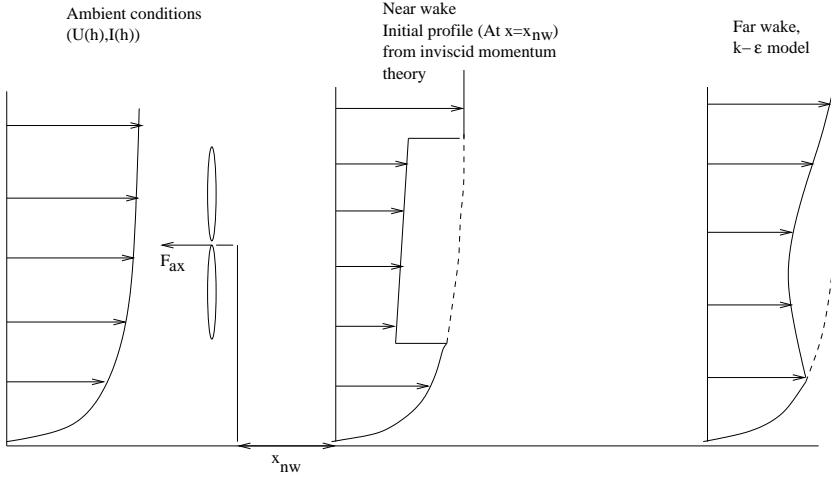


Figure 9.1: Wake modelling in the Wakefarm program (The figure only shows wind speed profiles)

culated from:

$$U_{\infty}(h) = 2.5u^* \left[\ln\left(\frac{h}{z_0}\right) - \Psi_m\left(\frac{h}{L}\right) \right] \quad (9.12)$$

The Monin-Obukhov length scale is a measure for the stability of the surface layer of the atmosphere. For $L > 0$ the surface layer is stable: The earth surface cools the air, which limits the vertical motion and the turbulent mixing. For $L < 0$ the surface layer is instable: The heating of the earth surface promotes the vertical motion and turbulent mixing in the atmospheric boundary layer. For $L = \infty$ the surface layer is neutral. The function Ψ_m is found from:

$$\Psi_m = \int_0^{\xi} [1 - \Phi_m(\xi)] \frac{d\xi}{\xi} \quad (9.13)$$

with $\xi = h/L$, i.e. the height above the ground non-dimensionalized with the Monin-Obukhov length scale.

With:

$$\Phi_m = (1 - 16\xi)^{-0.25} \quad (L < 0) \quad (9.14)$$

$$\Phi_m = 1 + 5\xi \quad (L > 0) \quad (9.15)$$

equation 9.13 reduces for stable conditions ($L > 0$) to:

$$\Psi_m = -5 \frac{h}{L} \quad (9.16)$$

For instable conditions ($L < 0$), equation 9.13 becomes more complicated:

$$\Psi_m = \ln\left[\frac{(1 + \gamma^2)(1 + \gamma)^2}{8}\right] - \text{atan}(\gamma) + \pi/2 \quad (9.17)$$

with $\gamma = 1/\Phi_m = (1 - 16\xi)^{+0.25}$

It should be noted that the above mentioned equations are only valid for $h \gg z_0$, which is usually the case for wind turbine applications.

Furthermore the ambient turbulence intensity is calculated via the turbulent kinetic energy (k_∞) in the free stream. Thereto the turbulent kinetic energy is assumed to follow the classical expression for the basic flow from the k - ϵ model, see e.g. [Hernandez and Crespo \(1990\)](#):

$$k_\infty(h) = \frac{u^{*2}}{\sqrt{C_\mu}} \left(1 - \frac{h}{L\Phi_m}\right)^{0.5} \quad (9.18)$$

C_μ is one of the closure parameters in the k - ϵ model. The common value for C_μ in k - ϵ models is set as 0.09 but a value of 0.033 is chosen to match experimental relations for k_∞ at neutral atmospheric conditions, as explained below.

The turbulence intensities (i.e. the standard deviation of the velocity fluctuations divided by the mean wind speed) at the different directions can be derived from this turbulent kinetic energy with:

$$k = 0.5\sigma_x^2 + 0.5\sigma_y^2 + 0.5\sigma_z^2 \quad (9.19)$$

in which σ denotes the standard deviation of the wind fluctuations in the different directions. Furthermore the anisotropy of turbulence in the free atmosphere is known from the following relations of [Panofsky and Dutton \(1984\)](#), who derived the coefficients in the equations from a set of experimental results:

$$\sigma_{x,\infty} = 2.4u^* \quad (9.20)$$

$$\sigma_{y,\infty} = 1.9u^* \quad (9.21)$$

$$\sigma_{z,\infty} = 1.25u^* \quad (9.22)$$

Substitution of 9.20, 9.21 and 9.22 into equation 9.19 yields for the free stream turbulent kinetic energy (k_∞):

$$k_\infty = 5.47u^{*2} \quad (9.23)$$

which matches equation 9.18 for neutral conditions if the value of C_μ is set to 0.033.

Then by combination of equation 9.20 and 9.23 the free stream turbulence intensity in x-direction is found to be

$$I_\infty(h) = \frac{\sigma_{x,\infty}}{U_\infty(h)} = 1.026 \frac{\sqrt{k_\infty(h)}}{U_\infty(h)} \quad (9.24)$$

9.5.2 Parabolization

As already mentioned before, the original Wakefarm code (and other parabolized codes) models the near wake with an empirical initial velocity profile (or the velocity deficit from the momentum theory). This profile then serves as a starting condition for the far wake. Several empirical velocity profiles and near wake distances have been applied where the near wake length for a single wake was often assumed to be shorter than the length in multiple wake, due to the fact that a rotor in a wake operates in an already developed shear flow.

The basic weakness of the approach was believed to lie in the fact that the approach relies on a data fit and/or on the complete neglect of turbulent mixing in the near wake.

Therefore an alternative approach was sought which retains the parabolization (and the resulting saving of computational effort) but which is based on a more physical sound method. This approach is described in [Schepers and van der Pijl \(2007\)](#). It is inspired by the procedure which is commonly followed to solve the boundary layer equations along a flat plate. Such boundary layers can be solved by prescribing a streamwise pressure gradient as a source term to the flow equations, where the streamwise pressure gradient is obtained separately from an inviscid calculation.

In the Farmflow/Wakefarm program a similar procedure is followed. Hence the streamwise pressure gradient is no longer neglected but it is prescribed in the form of a source term in the flow equations. The starting condition for

the wake model is formed by a velocity profile as calculated in the rotor plane based on the induced velocities which are known from the momentum theory (equation 2.10). The entire (near and far) wake is then calculated with a parabolized $k-\epsilon$ model where the prescribed pressure gradient term causes a further flow deceleration and wake expansion.

The pressure gradient is calculated from a free vortex wake method in which the following assumptions are made:

- The rotor is modelled as an actuator disc with a uniform loading across the disc.
- The conditions are assumed to be axisymmetric

In section 2.2 a free wake method is mentioned to be a relatively sophisticated aerodynamic model. Therefore, at first sight, one may think that such hybrid model, i.e. a combination of a free vortex wake method and a $k-\epsilon$ turbulence model is very time consuming. It is then important to realize that the above given assumptions make the resulting pressure gradient a function of the axial force coefficient (axial induction factor) only. This makes it possible to store the pressure gradient a-priori into a database for a large number of axial induction factors (i.e. axial force coefficients). This database is delivered along with the Farmflow/Wakefarm program and the program then finds the appropriate pressure gradient from interpolation between the two nearest axial induction factors in the database. This leads to an enormous saving of computational effort compared to the time needed to run a full free wake method.

9.5.3 Wake modelling

The turbulent mixing in the wake is modelled with a $k-\epsilon$ turbulence model. The model comprises a set of 7 equations:

- Continuity equation;
- 3 Momentum equation in x, y and z direction;
- Energy equation (for adiabatic temperature);
- Equation for turbulent kinetic energy;
- Equation for dissipation rate of turbulence

The equations solve the added values (i.e. the disturbances from the basic flow values) of the following 7 unknowns:

- Velocities in three directions (u, v, w);
- Pressure p_{add} ;
- Adiabatic temperature t_{add} ;
- Turbulent kinetic energy k_{add} ;
- Dissipation rate of turbulent kinetic energy ϵ_{add}

As explained in section 9.5.2 the model is parabolized by neglecting or prescribing the pressure gradient in streamwise direction. In this way all elliptic terms have disappeared.

The equations are described in more detail in [Rodi \(1982\)](#) and they include production terms due to buoyancy. The turbulent stresses are modelled using a turbulent kinematic viscosity for which closure relations are needed. The closure relations can be found in Rodi but a main modification is applied on the parameter C_μ which has become 0.033 in order to match the relations for the atmospheric free stream flow, see section 9.5.1. Moreover the parameters in the equation for the dissipation in the near wake have been modified by [Bot \(2011\)](#) using measurements from the ECN Wind Turbine Test Site Wieringermeer EWTW see section 11.2. This is a result of the observation that, after integrating the near wake modelling with the turbulence modelling according to the procedure from section 9.5.2, the velocity deficits in the near wake were often underpredicted. This is associated to the overshoot in turbulent kinetic energy from the standard k - ϵ model in regions of large shear. This large shear occurs at the edge of the wake behind an actuator disc leading to a (too) strong wake recovery. Similar observations were made by other researchers who apply a fully elliptic k - ϵ model behind an actuator disc, see e.g. [El Kasmi and Masson \(2008\)](#). In this reference it is suggested to suppress these overshoots and to delay the wake flow recovery by an additional term in the equation for the dissipation. In Farmflow, a similar effect has been achieved by making the parameters in the equation for the dissipation dependant on the generated turbulence (and hence the streamwise position). In addition Farmflow includes an intermediate wake region in which the increased production of turbulence due to the break down of tip vortices is included.

It is important to realize that the shear situation (and hence the turbulence production) at the edge of the wake for any actuator disc model is unrealistic. Hence the calibration of the turbulence modelling should be seen as a correction to these inconsistencies.

The wake turbulence intensities are found from k_w , i.e. the turbulent kinetic energy in the wake, under the assumption that the anisotropy in the wake is similar to the anisotropy in the free stream (and which is given by the equations 9.20 to 9.22). This assumption is in agreement with early observations from [Crespo and Hernandez \(1993\)](#).

Hence the wake turbulence intensity in x direction (I_w) is given by

$$I_w(z) = 1.026 \sqrt{k_w(z)} / U(z) \quad (9.25)$$

in which $k_w = k_\infty + k_{add}$. Note that care is needed on the definition of the wake turbulence intensities. They are sometimes normalized with the mean free stream velocity and sometimes with the mean wake velocity. The determinant parameter is obviously the standard deviation of the wind speed fluctuations in the nominator of the turbulence intensity.

9.5.4 Multiple wake modelling

In the original UPMWAKE model as delivered to ECN it was only possible to model single wake situations. The modelling of multiple wake conditions was added according to the following procedure (for the sake of simplicity only double wake is considered):

1. As a first step, a single wake calculation is performed. Hence the flow downstream of the first turbine is modelled. This yields the Wakefarm output properties i.e. the added velocity components in all three direction (u_1 , v_1 and w_1), the turbulent kinetic energy ($k_{add,1}$), the dissipation rate ($\epsilon_{add,1}$) and the temperature ($t_{add,1}$).
2. The single wake calculation behind the first turbine yields a rotor averaged wind speed at the location of the second turbine. This value is used as reference velocity to determine the axial force coefficient on the second turbine ($C_{D,ax,2}$) using the known $C_{D,ax}(U_{ref})$ curve.
3. The induced velocities in the rotor plane are calculated from equation 2.10 which acts as an additional velocity deficit ($u_{i,2}$) to the upstream wake flow, see also figure 9.2.
4. All other wake properties (i.e. v_1 , w_1 , and the turbulent kinetic energy, dissipation and temperature) which have been calculated just upstream of the second turbine are transferred into the rotor plane of the second

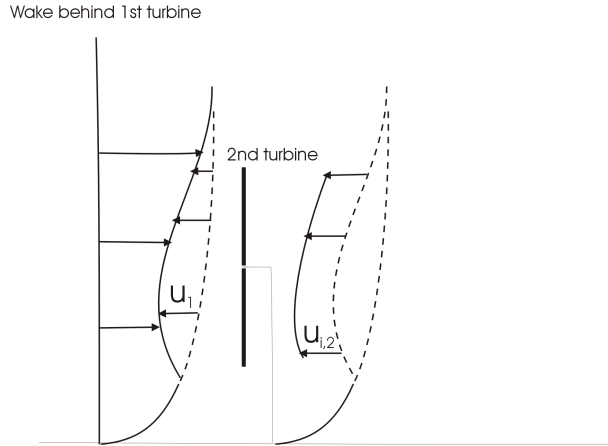


Figure 9.2: Double wake modelling

turbine. Together with the perturbation velocity in x direction ($u_1 + u_{i,2}$) they form the starting condition for the wake calculation behind this second turbine.

9.5.5 Wind direction fluctuations

Although Wakefarm assumed a constant wind direction throughout the farm, in the later Farmflow code a model is implemented which accounts for the horizontal wake meandering due to the fluctuating wind direction. Thereto the standard deviation of the wind direction changes is derived from the turbulence intensity. With this standard deviation a normal probability distribution is assumed from which the probability of a certain horizontal shift of the wake is calculated. Summation of these probabilities gives the averaged wake effect.

9.5.6 Grid size and boundary conditions

In the original Wakefarm model the computational domain was taken to be a rectangular box with 24x24 square cells in lateral and vertical direction of which 7x7 cells were located in the (expanded) rotor plane. The grid size in flow direction was 0.25D. In the Farmflow code 96x96 square cells are applied in lateral and vertical direction of which 15x15 cells are located in the

rotor plane. The step size in flow direction begins with $0.005D$ at the rotor area and increases exponentially.

These dimensions were chosen from a grid refinement study as a compromise between acceptable calculational effort and accuracy of results.

Boundary conditions are applied at all boundaries of the domain for all variables. As explained in section 9.5.2, the first versions of Wakefarm applied an initial velocity profile at the start of the far wake (at $x_{nw} = 2.25D$) but later a hat-shaped velocity deficit profile was prescribed in the rotor-plane, which corresponds to the actual induction from the momentum theory (equation 2.4). At the lateral boundaries of the domain boundary conditions are applied in the form of a Neumann condition. The Neumann boundary conditions dictates the normal derivatives of the wake disturbance to be zero but the boundary value itself may still be disturbed from the free stream value. In the original approach from Crespo et al. (1985) a Dirichlet boundary condition was applied which forced the disturbance velocity at the edge of the grid to be zero which led to an unrealistic high shear and production of turbulence, in particular for the relatively small grids as used in the past.

9.6 Summary on wind farm models

In this section several topics are described which are of relevance for wake modelling.

First it is shown that (under several simplifications) the velocity profile in the wake is self-similar. The velocity deficit decays with downstream distance x according to $x^{-2/3}$ and the wake radius increases with $x^{1/3}$.

Next a very rough classification of wake models is given. A large variety of models for wind farm aerodynamics is found. This is partly a result of the fact that a wind farm aerodynamic model should include both the rotor as well as the wake. Together with the large size of nowadays wind farms this can easily make the calculational time excessive. Basically wind farm models range between very simple empirical engineering methods to more advanced CFD methods. In almost all methods the wake generating wind turbine is modelled as an actuator disc. Some exceptions are found in which the rotor blades are modelled as actuator lines but a full modelling of the rotor and the wake is until now only feasible for single wake situations.

In the present section particular attention is paid to parabolized wake models which could be seen as an intermediate between the very simple engineering methods and the advanced CFD models. The developments on the field of wind farm aerodynamic modelling are then mainly described along ECN's Wakefarm model. In 2007 this model was implemented in the wind farm design code Farmflow. The Wakefarm model originates from the UPM-WAKE model as developed by the Universidad Polytechnica de Madrid [Crespo et al. \(1985\)](#). The original UPMWAKE model was only suitable to model single wakes but Farmflow is capable of modelling large wind farm arrays. Thereto several improvements have been implemented in terms of numerics as well as in terms of flow modelling. An important improvement lies in a more physical modelling of the near wake. Most parabolized methods model the near wake empirically but Farmflow prescribes the streamwise pressure gradients as a source terms into the equation, where the pressure gradient is calculated with a free vortex wake method. This went together with a modification of the dissipation parameters in the $k-\epsilon$ model as derived from EWTW measurements. The modifications were needed to correct the unrealistic high production of turbulence at the edge of the wake behind an actuator disc.

Chapter 10

Assumptions and uncertainties in wind farm aerodynamic models

As already mentioned in section 9.1 there is a large variety in wake aerodynamic models which all have their own assumptions and uncertainties. The present chapter mainly addresses the assumptions, simplifications and uncertainties in ECN's Farmflow/Wakefarm code from section 9.5. Although these uncertainties are described for the Farmflow/Wakefarm model they appear in other parabolized wake models too.

The main simplifications in the Farmflow/WakeFarm model are:

- The aerodynamics of the wind turbine rotor (i.e. the wake producing device) is modelled with an actuator disc see section 2.1.1, where the loading across the disc is assumed to be uniform. The real loading will generally be lower at the rotor centre and near the tip. Such non-uniform loading will lead to a velocity profile which deviates from the assumed hat shaped velocity profile in the near wake. This is confirmed by EWTW measurements which are described in [Schepers, Obdam and Prospathopoulos \(2012\)](#). It is noted that in principal a non-uniform disc-loading could be included in Farmflow/WakeFarm. The load distribution then needs to be determined from a separate rotor aerodynamic model (based on e.g. BEM). However, until now this has never been attempt-

ted.

Moreover the effects from wake rotation are neglected. In principal the wake rotation immediately behind the rotor could also be included by calculating it from the conservation of angular momentum, see section 2.1.4 (or from the root vortex see section 6.2) and added as a boundary condition on the v and w components in the rotor plane. However this could much more conveniently be done in a polar grid where the Wake-Farm grid is rectangular.

In [Wu and Porté-Agel \(2010\)](#) LES calculations of the wake behind an actuator disc are presented in which wake rotation and non-uniform loading are included according to the lines as described above. The results are compared with those from an actuator disc model with a uniform loading and without wake rotation (i.e. comparable to the Farmflow/Wakefarm approach). At 3D behind the turbine the effects from rotation and non-uniform loading are still clearly distinguishable but at 5D (the next station) the differences have become negligible. This is consistent with the analysis of EWTW measurements ([Schepers, Obdam and Prospathopoulos \(2012\)](#)) which show the effects from wake rotation to be visible until 3.5D behind the rotor.

However the assumption of an actuator disc also implies an infinite number of blades and a uniform flow within the rotor plane and the near wake. As such the flow non-uniformities due to the discrete number of blades are neglected. It also implies that the effect of the tip vortex and the viscous wake as released from every blade are not taken into account. These effects are anyhow present in the near wake as observed in the Mexico measurements. Since the near wake forms the starting condition for the far wake, some of these uncertainties will be 'transferred' to the far wake.

- The rotor is assumed to be aligned with the wind, i.e. yawed conditions cannot be modelled.
- Farmflow/Wakefarm assumes time averaged conditions throughout and around the wind farm, i.e. the 'response' of the farm is calculated on a time averaged wind speed. This response is not by definition the time averaged response to the fluctuating incoming wind speed. Even more important may be the assumption of a constant wind direction throughout and around the wind farm, since the wake conditions in the farm are

extremely sensitive to the precise value of the wind direction where it is also known that the wake within a farm will meander around the mean wind direction. This assumption is less relevant for the determination of the overall energy production of a farm. This is due to the meandering model from section 9.5.5 which has been included in Farmflow. Moreover the production is generally found by averaging over a large number of different wind direction bins. In this way the effects from wind direction fluctuations and meandering will, at least to some extent, be filtered out as is shown in the validation from section 11.3.2. This is not true however when the loads on a turbine in a wind farm are assessed.

Associated to this is the observation of a flow deflection for the downstream turbines which appears at closely spaced farms, see [Schepers, Obdam and Prospathopoulos \(2012\)](#). This flow deflection is not taken into account in Farmflow/Wakefarm.

- Farmflow/WakeFarm assumes flat terrain and a uniform flow around the entire wind farm. The huge size of current wind farms makes that the free stream flow over the area of the wind farm will, at least to some extent, be non-uniform. Associated to this is the interaction from the wind farm on the outer atmosphere, which then, in return affects the flow in the farm, see [Schepers et al. \(2002b\)](#). The mutual interaction between atmosphere and wind farms is generally not taken into account yet in wind farm models.
- The turbulent processes are modelled with a $k-\epsilon$ model. Like every other turbulence model this is a simplification of the real flow physics. However for wake aerodynamics the uncertainty in turbulence modelling is suspected to be even larger since several modifications had to be made to the standard $k-\epsilon$ model in order to make it suitable for atmospheric flows and for the near wake flow, see section 9.5.3. These modifications need to be related to the rotor aerodynamic modelling, since the details of the rotor aerodynamics determine the turbulence production in the near wake to a large extent.
- For load calculations on turbines located in the wake it is very important to know the turbulence intensities in all three directions. Farmflow/Wakefarm only calculates an overall turbulent kinetic energy from which, with assumptions on the anisotropy the turbulence intensities are derived. The anisotropy in the wake is assumed to be similar to the anisotropy in the wake in agreement with the observations made from

Crespo and Hernandez (1993). Measurements in the EWTW however indicate the flow in the wake to be more isotropic see Schepers, Obdam and Prospathopoulos (2012).

- Uncertainties exist in the modelling of the multiple wakes. As explained in section 9.5, the value of $C_{D,ax}$ on the second wind turbine is based on a reference velocity as calculated at the location of this second wind turbine using the $C_{D,ax} - U_{ref}$ curve (Note that for simplicity the second wind turbine is considered only. Similar remarks can be made for other downstream turbines in the farm).

However the $C_{D,ax} - U_{ref}$ curve is generally only valid for a turbine placed in an undisturbed free stream flow where the reference velocity at one or two diameters upstream of the turbine should be used. This undisturbed situation differs from the situation where the flow in front of the second turbine is still affected by the wake behind the first turbine. A physical more sound method to find the $C_{D,ax}$ is then proposed by Prospathopoulos et al. (2010). This procedure assures that the axial momentum theory relation (equation 2.10) between the axial induction factor and the axial force coefficient is fulfilled using the following definition of the axial induction factor:

$$a = \frac{U_{ref} - U_d}{U_{ref}} \quad (10.1)$$

In this equation U_d is the rotor averaged velocity at the location of the second turbine. The elliptic wake model as applied by Prospathopoulos makes U_d dependant on the value of $C_{D,ax}$ of the second turbine. An iterative procedure is then applied until a value of U_{ref} (and hence $C_{D,ax}$) is found with which the elliptic wake model calculates a value of U_d that fulfills equation 10.1 and the axial momentum relation.

In the current Farmflow approach the value of U_d does not depend on the $C_{D,ax}$ of the second turbine by which the procedure from Prospathopoulos cannot be applied. However a physical more sound approach for modelling multiple wakes would be to include the pressure gradient upstream of the turbine (see figure 2.2) in the flow equations, similarly to the inclusion of the pressure gradient in the downstream flow equations.

This pressure gradient obviously depends on the value of $C_{D,ax}$ of the second turbine and hence on the reference velocity. This also makes the U_d as calculated by the Wakefarm flow model dependant on $C_{D,ax}$ and

the reference velocity, by which the calculational procedure resembles an elliptic approach. In this way the reference velocity can be established with the procedure from Prospathopoulos.

Chapter 11

Progress on wind farm aerodynamic models at ECN using measurements from EU and national projects

11.1 Introduction on wind farm aerodynamic measurements and the ECN models used

In this chapter the progress is described which is made on the Farmflow model using measurements on wind farm effects.

As a matter of fact a first logical thought could be to use wind tunnel measurements for the validation and calibration of wind farm aerodynamic models, similar to the situation for rotor aerodynamics, where the NREL Phase VI and Mexico wind tunnel measurements play an important role.

However, the role of wind tunnel measurements for wind farm aerodynamics is generally more limited. Nevertheless the PIV flow field measurements from the Mexico project, though mainly intended for induction aerodynamics, also provided information which can be used for the near wake modelling in wind farm wake models. Wind tunnel measurements purely focussed on wind

farm aerodynamics were already carried out in the 1970's and 1980's by TNO in the Netherlands, see e.g. Vermeulen (1979). Later wind tunnel experiments were made by e.g. Hassan (1992) and Corten, Schaak and Hegberg (2004). These measurements were performed in atmospheric wind tunnels, where the mean wind speed and turbulence intensity profile to some extent resembles the atmospheric flow. The size of the model wind turbines in these studies was however much smaller than the size of the turbines in the above mentioned Mexico and NASA-Ames experiment. i.e. the diameter of the model turbines in Hassan (1992) was 27 cm and the diameter of the model turbines in Corten, Schaak and Hegberg (2004) was 25 cm. This makes the resulting data not representative for full scale farms in a quantitative sense. Nevertheless, similar to the situation for rotor aerodynamics, the advantage of wind tunnel measurements should be acknowledged. This advantage lies in the known and stationary conditions, which together with the very detailed flow field mapping facilitates the interpretation of results enormously. Thereto it should be realized that field measurements inevitably only cover a limited part of the flow field. They also suffer from severe scatter due to the stochastic atmosphere. This makes wind tunnel measurements very useful for providing qualitative information and insights in fundamental wake phenomena.

In this respect a very interesting intermediate between full scale and wind tunnel measurements should be mentioned. This intermediate is formed by the so-called scaled wind farm. The scaled farm is a worldwide unique research facility, owned and operated by ECN, which consists of ten wind turbines with a rotor diameter of 7.6 m and a rated power of 10 kW. The farm is heavily instrumented with a network of fourteen meteorological masts inside and outside the wind farm, which measure the wind velocity field from 3.6 m to 19 m height. This covers the rotor area and up to one rotor diameter above the rotor. The alignment of turbines and measurement masts within the wind farm permits to measure at the same time single, double, triple and quadruple wakes where the main wind farm lines are oriented along the dominant wind direction which ensures that a large amount of wake measurements can be collected to reduce the experimental scatter.

Most of the wind farm measurements have been done in full-scale atmospheric circumstances. Opposite to the situation for rotor aerodynamics there were no large joint measurement (and analysis) research projects on such experiments. Nevertheless wind farm measurements played a very important role in several EU research projects. This holds for example for the measurements on the Dutch Sexbierum wind farm and the Swedish Alsvik wind

farm which were used in the EU Dynamic Loads in Wind Farms projects, see [Tindal \(1993\)](#) and [Adams \(1995\)](#). The Alsvik wind farm consisted of 4 turbines with a rated power of 180 kW and the Sexbierum wind farm consisted of 18 turbines placed in a rectangular grid of 3x6 rows. These wind farms can be characterized as research farms, merely focussed on research by which much attention was given to an extensive instrumentation and measurement quality and where the turbine data (under certain restrictions) could be made available which enabled a good validation of various models. The turbines in these farms with a rated power of 180 kW and 300 kW were relatively small compared to nowadays wind turbines.

Later EU projects as the Endow project, see [Barthelmie et al. \(2003\)](#) and [Schepers \(2003\)](#) and the Upwind project, see e.g. [Barthelmie et al. \(2010\)](#), used measurements from commercial off-shore wind farms, e.g. the Vindeby farm as used in the Endow project and the Horns Rev and Nysted farm as used in the Upwind projects. These measurements were kindly made available by the farm owners (Dong Energy and Vattenfall AB) but the emphasis obviously lied on the commercial operation of the farm and not on research purposes by which the instrumentation was generally limited and the quality of the measurements was not always guaranteed.

In section 9.5 the development of the Farmflow model was described. This development was a continuous process which took place in the above mentioned projects using the associated measurements. The developments started with the basic UPMWAKE code which only modelled single wakes and which applied an initial velocity deficit from the momentum theory in the rotor plane. At a later stage the momentum theory deficit was applied at 2.25 D behind the rotor plane leading to an improved prediction of the Sexbierum and Alsvik (and Marchwood wind tunnel) results, see [Adams \(1995\)](#). The modelling of multiple wake conditions was added too. Thereafter the near wake was modelled with an empirical Gaussian velocity profile at 2.25 D behind the rotor, leading to a further improvement with measured results, see [Schepers \(2003\)](#). This was followed by the prescription of a pressure gradient from a free vortex wake method as described in [Schepers and van der Pijl \(2007\)](#).

The present section mainly describes the results obtained with the most recent version of Farmflow using measurements from the ECN Wind Turbine test site Wieringermeer EWTW. This research farm is owned and operated by ECN and consists of five 2.5 MW wind turbines placed in a line set-up with a mutual distance of 3.8 rotor diameter where this diameter is 80 meter.

Extensive machine and meteorological measurements have been collected over a period of more than 7 years, see chapter 11.2.

An analysis of EWTW measurements is summarized in section 11.2.4 based on [Schepers, Obdam and Prospathopoulos \(2012\)](#). In the sections 11.2.2 and 11.2.3 the comparison between Farmflow results and EWTW measurements is presented. Furthermore the comparison between Farmflow calculations and Horns Rev measurements is presented in section 11.3. It must be noted that many of these measurements have been used in the calibration of the dissipation parameters in the turbulence model, see section 9.5.2. As such the comparison can not be considered as a pure validation of Farmflow. On the other hand it should be realized that the adjustment of the dissipation parameters alone can never reach full agreement with all the measurements presented in this section.

A more extensive validation of Farmflow with measurements from the EWTW and commercial wind farms (as Horns rev, Nysted and the Offshore Wind Farm Egmond aan Zee) is reported in [Bot \(2011\)](#).

11.2 Wind farm measurements from the ECN Wind Turbine Test Site Wieringermeer, EWTW

11.2.1 Description of EWTW farm, turbines and instrumentation

The layout of the EWTW farm is given in figure 11.1. The figure shows two rows of wind turbines (i.e. a row denoted as 'Prototype turbines' and a row denoted as 'Research Turbines').

The southern row with prototype turbines is reserved for commercial testing of wind turbines. For the present study, the 5 research turbines at the northern part are of relevance. The research turbines are numbered from 5 to 9, with turbine 5 the most Westerly wind turbine. These turbines are variable speed, pitch controlled, and they have a diameter and a hub height of 80 m with a rated power of 2.5MW. Near the research farm, there is a 108 m high meteorological mast indicated with MM3.

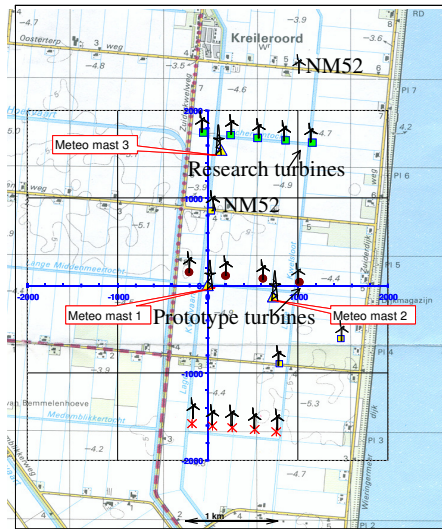


Figure 11.1: Lay-out of EWTW

The distance and angles between the turbines and the meteorological mast are given in figure 11.2. It can be noted that the wind farm line is directed 95-275 degrees with respect to the North where the distance between the turbines is $3.8D$. The meteorological mast is at a distance of $3.5D$ from turbine 5 at a wind direction of 315 degrees and a distance of $2.5D$ from turbine 6 at a wind direction of 31 degrees.

The farm is located in the Wieringermeer, a polder in the northeast of the province Noord-Holland, 35 km east of ECN Petten. The test site and its surroundings can generally be characterized by very flat polder land at an altitude of 5m below sea level, consisting of mainly agricultural area, with single farmhouses and a few rows of trees. The lake IJsselmeer is located at a distance of 2 km east of the EWTW.

Despite the flat character of the EWTW terrain some flow disturbances from obstacles (other than the 5 research turbines) are inevitable. One can think of crops on the fields, farmhouses, rows of trees, the IJsselmeer dike and the

small village of Kreileroord at 1 km north of the farm. Furthermore some turbines are located near to the research farm (i.e. the prototype turbines and a few scattered turbines as indicated on figure 11.1).

The most relevant obstacles are described in Eecen and Verhoef (2007). For the wind directions as considered in this study the disturbances are generally small.

Due to the presence of the IJsselmeer, the turbulence intensity at Eastern wind directions is lower than it is for Western wind directions. At Eastern direction the averaged turbulence level at hub height is in the order of 7.5% where it is 10% in the Western direction. The instrumentation of MM3 is

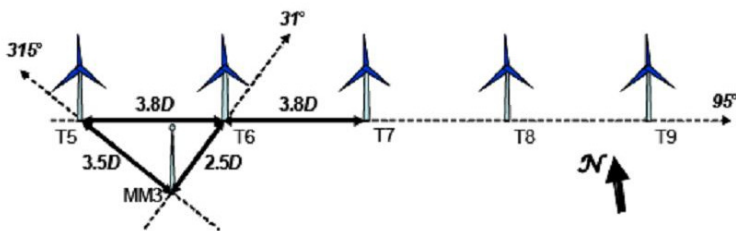


Figure 11.2: EWTW: Research farm and meteorological mast, distances and angles

shown in figure 11.3. It can be seen that wind speeds are measured at hub height ($h = 80\text{m}$), and hub height $\pm 70\%$ of the blade span (i.e. $h=52\text{ m}$ and $h = 108\text{ m}$) The wind speeds at the top of the mast are measured with a 3D sonic anemometer. At $h = 52\text{m}$ and $h = 80\text{m}$ the sensors are, dependent on the wind direction, disturbed by the mast wake which is the reason why they

are mounted on three booms. These booms are directed in the 0 degrees, the 120 degrees and the 240 degrees with respect to the North. In this way it is always possible to select data taken with an anemometer with limited flow disturbance from the mast. The boom in the Northern direction is equipped with a 3D sonic anemometer, the other two booms have cups and wind vanes.

Moreover turbine measurements are taken, e.g. the electrical power, the yaw angle and the pitch angles of the blades.

All data are stored into a database in the form of time series as well as 10 minute statistical data. Measurements have been collected over a period of several years.

The present chapter puts emphasis on the meteorological measurements in single wake at 2.5D and 3.5D behind the turbine and powers of turbines in the wake of several (up to 4) upstream turbines. Most of the presented results are averaged over a large number of samples, i.e. 10 minute statistical data, taken in the period from January 2005 until August 2009, where peculiar measurement points (points with large yaw errors, non-operating turbines etc) are eliminated.

In [Eecen and Verhoef \(2007\)](#) and [Schepers \(2009\)](#) some more information is given on the measurements, including an assessment of the quality of the data. In this respect it can be mentioned that ECN, on a regular basis, carries out extensive quality procedures to the data. One can think of a visual inspection of daily and monthly plots, and an automatic check on min-max values (spikes) and standard deviation ('frozen' sensors). Furthermore frequent calibration of sensors is carried out and where needed the sensors are replaced. In [Schepers \(2009\)](#) also some further study on the consistency and the reliability of signals relevant for the present investigation is reported. This study generally showed a good quality where the standard error of the averaged data was found to small as a result of the large number of data points.

11.2.2 Comparison between calculated and measured power losses

Figure 11.4 shows the power losses as function of the wind direction at a height of 80 m at Westerly winds. The results are averaged over a large num-

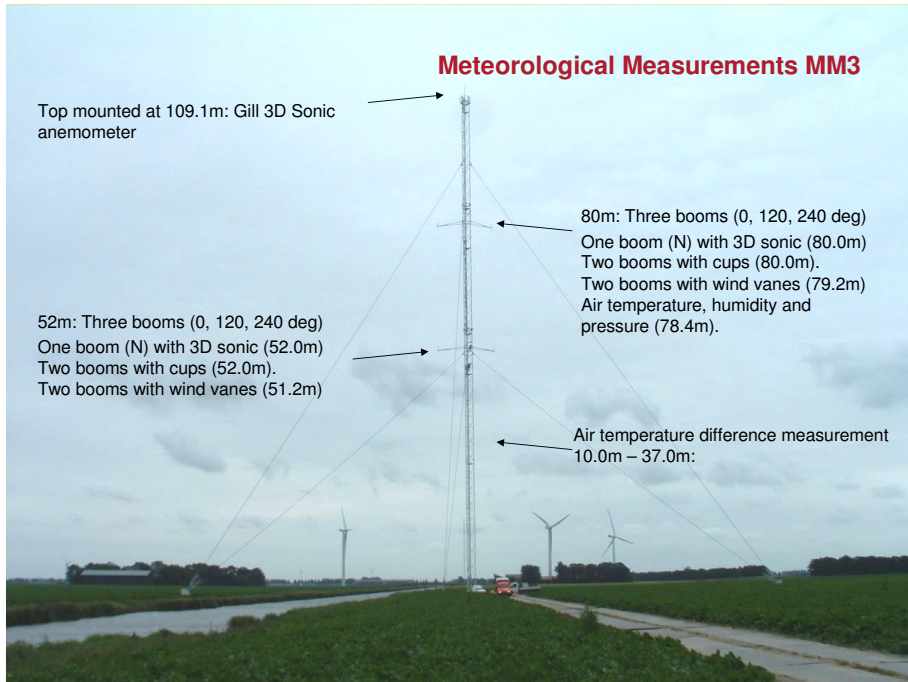


Figure 11.3: EWTW: Instrumentation on met-mast 3

ber of (10 minute averaged) data points for a wind speed bin between 6 and 8 m/s. The results are given as ratio of the power of the downstream turbine in the wake (indicated with P_x , in which x is the turbine number) relative to the power of the upstream turbine (P_5 or P_9). In both the measurements as well as the calculations, the maximum power loss is found for the second turbine in the farm, i.e turbine 6. The slight increase of power deeper into the farm can then be explained by the fact that the downstream turbines operate in a highly turbulent wake flow.

This is illustrated in figure 11.5 which shows the power losses of turbine 6 at Westerly winds at two turbulence intensity intervals:

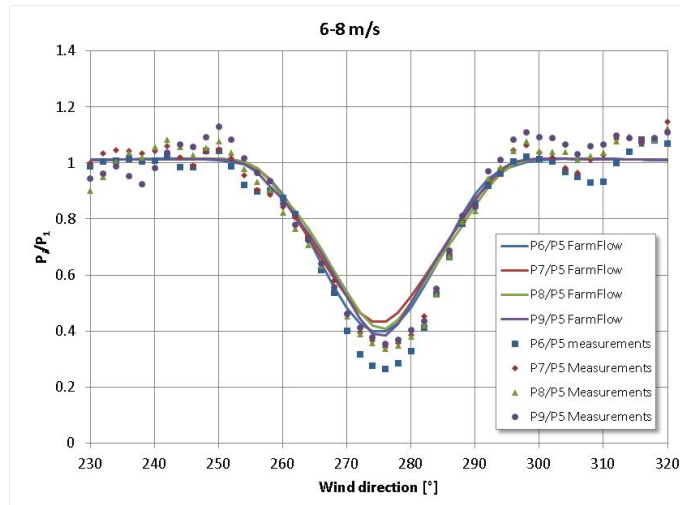


Figure 11.4: EWTW: Power losses at Westerly winds as function of wind direction for a wind speed bin between 6 and 8 m/s

- Turbulence intensity between 2 and 4% and
- Turbulence intensity between 10 and 14%.

It can be observed that the power losses are much larger at the lower turbulence level. It is noted that the difference in mean ambient wind speed for both cases is small (< 0.5 m/s) and is not expected to yield significantly different wake effects. Hence the differences in figure 11.5 can mainly be attributed to the difference in turbulence intensity.

Qualitatively speaking Farmflow predicts the correct trend with the power increasing for turbines deeper in the farm. This is confirmed further in the figures 11.6 to 11.8 which show the comparison between the Farmflow calculated and measured power deficits for three wind speed bins at a wind direction interval between 274 and 276 degrees (i.e. at the orientation of the wind farm line). A very good qualitative agreement can be noted in the sense that Farmflow calculates the minimum power for turbine 6 and a slightly higher

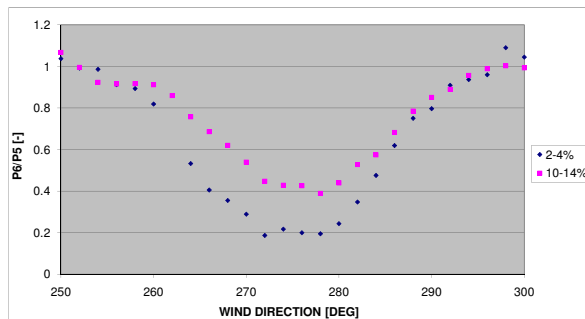


Figure 11.5: EWTW: Power losses at two turbulence intensity bins: 2-4% and 10-14%

power for the turbines 7 to 9. The quantitative agreement is very good for a wind speed bin between 4 and 6 m/s but for the other wind speed bins there is an overprediction of the power. As already indicated in section 10 there are very many uncertainties in wake aerodynamic models by which it is not easy to appoint the main cause for the discrepancies. It must anyhow be noted that a main uncertainty in the Farmflow model is expected to lie in the near wake modelling, due to the simplified rotor modelling which needs to be corrected with an adjustment of the dissipation parameters. The resulting uncertainties will be very prominent in the present farm since the mutual distance between turbines is only 3.8D.

11.2.3 Comparison between calculated and measured wake velocity and wake turbulence profiles

In Figure 11.9 the wind speeds as measured at hub height ($h = 80$ m) on the Meteorological Mast 3 are plotted as function of wind direction for the entire wind direction range from -180 to +180 degrees. They are compared with calculations from the Farmflow and the former Wakefarm model.

The results are given as ratio of the velocity measured at the mast and the free stream velocity. This free stream velocity is derived from the power of turbine 5, on basis of the measured power curve.

The results are averaged over all wind speeds. In the figure the wake effects from the different turbines are indicated, see also figure 11.2 for the orienta-

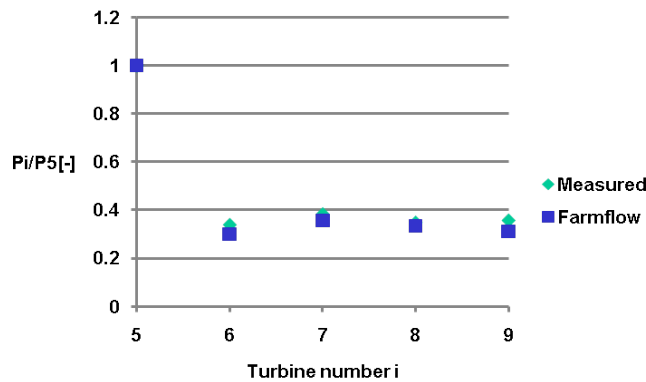


Figure 11.6: Farmflow calculated and measured power deficits in the EWTW wind farm at free stream wind speeds between 4 and 6 m/s for a wind direction sector from 274 to 276 degrees

tion of the masts with respect to the turbines. As an example T5 \rightarrow MM3 indicates the wind direction where MM3 is in the wake of Turbine 5. The figure also indicates that at a wind direction of 95 degrees, turbine 5 is in the wake of the other EWTW turbines by which the wind speed derived from the power is not representative for the free stream wind speed. The figure also shows the direction where turbine 5 is in the wake of turbine 14 which is the northern NM52 turbine as indicated on figure 11.1.

It must also be noted that both the wind speed as well as the wind direction have been measured on MM3 which is for many wind directions located in wake conditions. In principle this could make the wind direction slightly different from the free stream wind direction but the differences are not expected to be very significant on a time averaged basis. Generally speaking the velocity profiles behave as expected: The effect of the different turbine wakes can clearly be distinguished through a reduction in velocity, with the strongest reduction is at the shortest distance of $2.5D$ when the mast is in the wake of turbine 6. The Farmflow results underestimate the velocity deficit (i.e. they overestimate the absolute velocities in the wakes) but the results are anyhow in better agreement than the results from the former Wakefarm model.

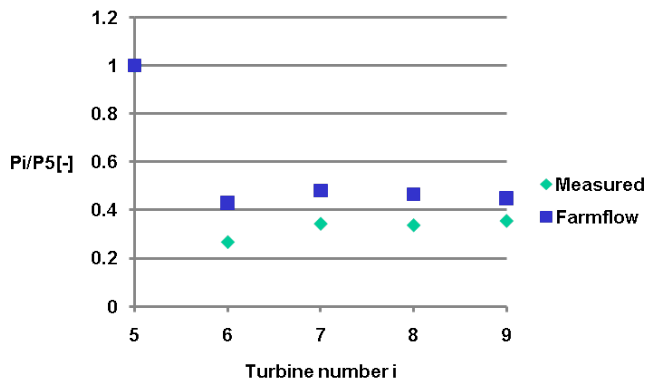


Figure 11.7: Farmflow calculated and measured power deficits in the EWTW wind farm at free stream wind speeds between 6 and 8 m/s for a wind direction sector from 274 to 276 degrees

Moreover it is interesting to investigate the measured turbulence intensities and compare them with the calculated values. Thereto figure 11.10 presents the turbulence intensity for the entire wind direction range from -180 to +180 degrees. A significant increase in turbulence intensity is found for those directions where the mast is in the wake of a turbine. The peaks at the edges of the wake are a result of turbulence production at that location. Again the results are predicted well on a qualitative basis. On a quantitative basis it is not easy to determine a general number for the differences in turbulence intensity but they are often less than 3%.

11.2.4 Some further analysis of EWTW measurements

The present subsection summarizes the observations on the EWTW measurements as described in [Schepers, Obdam and Prospathopoulos \(2012\)](#). They are included in the present thesis to illustrate the value of measurements in a research farm and to form inspiration for further model improvement. The main observations are:

- The effect of wake rotation is visible in the vertical velocities measured with the meteorological masts. This effect is visible until at least 3.5D behind the turbine. The vertical velocities from wake rotation are largest

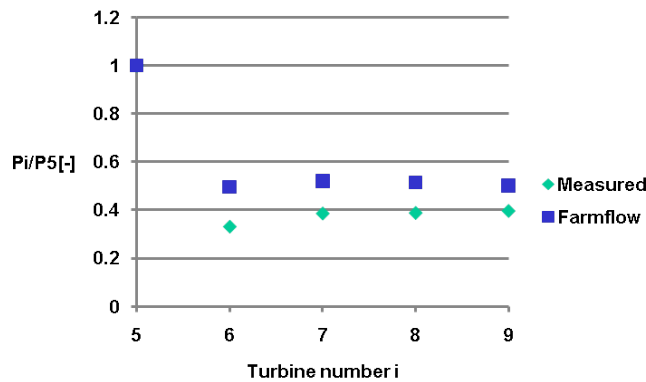


Figure 11.8: Farmflow calculated and measured power deficits in the EWTW wind farm at free stream wind speeds between 8 and 10 m/s for a wind direction sector from 274 to 276 degrees

at hub height but they are still noticeable at hub height $\pm 70\%$ span. This wake rotation in conjunction with the vertical wind shear makes the horizontal velocity profiles in the wake asymmetric, in agreement with results from CFD analysis made by RISØ, see [Zahle and Sorensen \(2008\)](#).

- The yaw angles of the turbines in the farm are found to be affected by wake operation due to a wake deflection. This leads to a yaw angles which can differ up to 4 degrees from the yaw angle of the wind turbine in the undisturbed flow. This effect could be reproduced by CRES with the CRES-flowNS solver, one of the CFD codes described in section 9.4. These calculations indicate the wake deflection to decrease for increasing distances between the turbines.
- A clear diurnal cycle appears on the vertical temperature gradient, wind shear and turbulence intensity, in particular at summer time and at below rated wind speeds. At night time a clear positive vertical temperature gradient is measured with a much lower turbulence level and higher wind shear. This leads to stronger wake effects in night time.
- It was possible to model the power deficit with a neural network approach in which hub height wind speed, turbulence intensity and wind

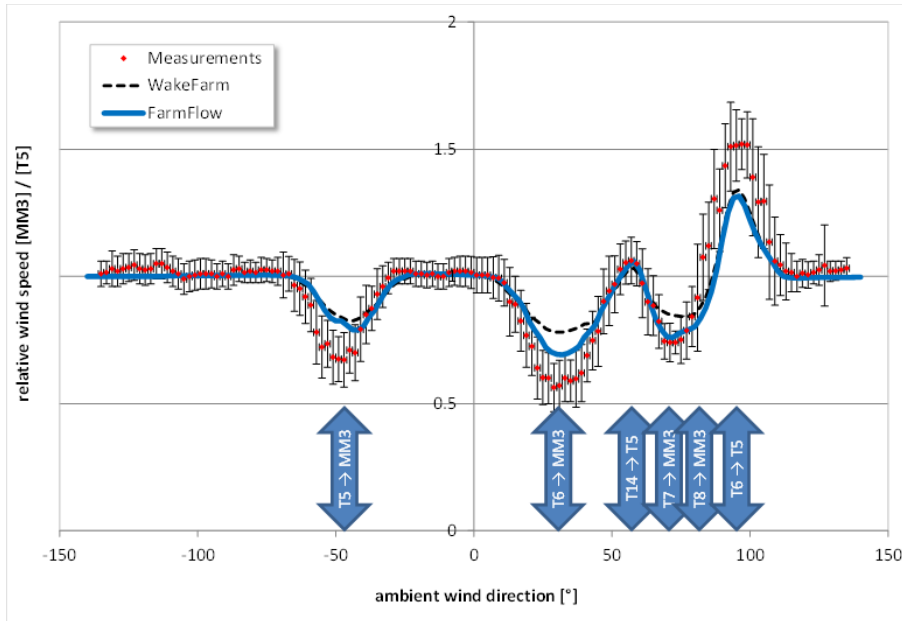


Figure 11.9: EWTW: Relative velocity at $h=80\text{m}$ as function of wind direction (averaged over all ambient wind speeds). Measurements and calculations from Farmflow and the former Wakefarm model

direction were the only independent variables. The addition of the Monin-Obukhov length scale did not lead to a further improvement. This indicates that the influence from atmospheric stability on the wake is already fully covered by its effect on the turbulence intensity.

- The turbulence in the wake appears to be more isotropic than the turbulence in the ambient flow. In the ambient flow the ratio between the standard deviation of the vertical velocity fluctuations and the standard deviation of the horizontal velocity fluctuations was found to be in the order of 0.52 as expected from section 9.5.1.
- The measured turbulent spectra fit very well to a Kaimal spectrum not only in the free stream but also in the wake. The resulting turbulence length scale in the wake is however much shorter. The wake length scale turns out to be in the order of 25% of the free stream length scale

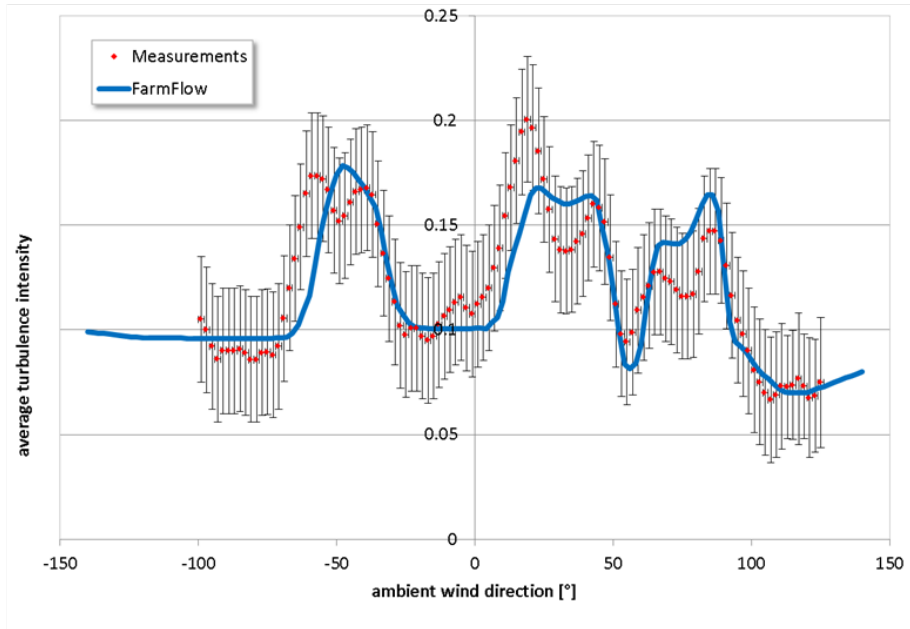


Figure 11.10: EWTW: Turbulence intensity at $h=80\text{m}$ as function of wind direction (averaged over all ambient wind speeds). Measurements and calculations from Farmflow

but the reduction is dependant on the height. In free stream, the turbulence length scale decreases with height. In the wake, the minimum length scale is found at hub height.

Some of these results will be used in a future validations/improvements of Farmflow. The observation of more isotropic turbulence in the wake is good news for the $k-\epsilon$ model as used in Farmflow since such model in principle is derived for isotropic turbulence. On the other hand it shows that the determination of the turbulence intensities from the overall turbulent kinetic energy k should not be based on the free stream anisotropy relations as is currently done in Farmflow, see section 9.5.3. Some of the other results/conclusions can be used for the improvement of more advanced wake models (e.g. the yaw angle deviation which occur at wake operation). The results for the reduction in turbulence length scales can be used to generate an empirical model

to be included in load calculations on turbines in a wind farm.

11.3 Wind farm effects in large off-shore wind farms

In this section the measurements from the large Horn's Rev off-shore wind farm are discussed and compared with Farmflow calculations.

11.3.1 Description of Horns Rev Wind farm

The Horns-Rev wind farm is located 14 to 20 km west from the coast of Jutland in Denmark. The lay-out of the farm is given in figure 11.11. In this figure the numbering of the turbines is according to a matrix notation consisting of 10 'columns' which are directed from (almost) north to south where each column consists of 8 rows that are directed from (almost) west to east. The turbine spacing is 7 D in both north-south and west-east directions. All 80 turbines are Vestas V80's, i.e. pitch regulated turbines, with a diameter of 80 m and a rated power of 2 MW.

The measurements are based on 10 minute averaged values of the generator powers from the SCADA system and the meteorological data from Mast 2 (as indicated in figure 11.11). These measurements were made available by the wind farm owners (Dong and Vattenfall, see also [Jensen \(2004\)](#)) where further processing and selection of data was carried out by the Technical University of Denmark within the Upwind project (for more information on the measurements and the processing of data, see e.g. [Barthelmie et al. \(2010\)](#)). The power curves and the axial force coefficients as needed for the Farmflow calculations were also supplied by the Technical University of Denmark.

11.3.2 Comparison between calculated and measured power losses

In figure 11.12 the comparison is shown between the calculated and measured power deficits for a wind direction interval between 255 to 285 degrees and a wind speed interval from 9 to 11 m/s. It shows the averaged power deficits P_i of the column i (i.e. P_2 gives the averaged power of turbines 21 to 28 relative to the averaged power of column 1).

A first observation lies in the continuous decrease of the power for turbines deeper into the farm. At first sight this result seems to oppose the observa-

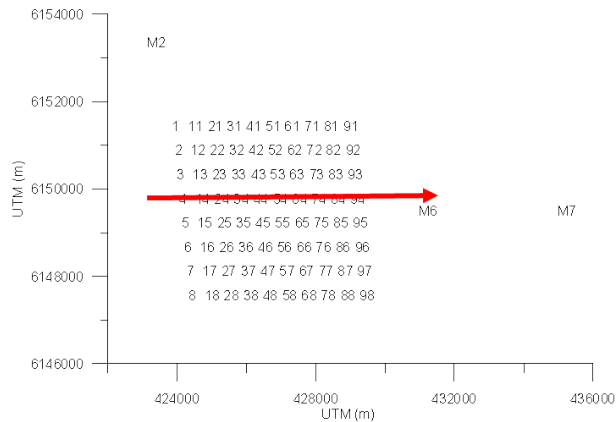


Figure 11.11: Lay-out of Danish Horns Rev off-shore wind farm. Also indicated are the meteorological masts around the farm and the wind direction around which data are selected

tion on the power deficits measured in the EWTW, see section 11.2.2 where the largest deficit was found for the second turbine in the row and where the power deficits deeper into the farm were 'stabilizing'.

These 'stabilizing' power deficits occur in relatively small wind farm lines like the EWTW, in which sufficient 'fresh' momentum from the outer atmosphere can be fed into the wake. However the size of the Horns Rev farm is much larger by which the surrounding atmosphere is 'depleted' and where 'lateral' wakes penetrate into adjacent wind farm lines. These lateral wake effects might even appear when the mean wind direction is along the wind farm line, due to the wind direction fluctuations around the mean value. Such lateral wake effects are obviously not present in the EWTW single line lay-out.

A second observation lies in the excellent agreement between Farmflow calculations and measurements. However, this good agreement is partly a result of the wide wind direction range from 255 to 285 degrees in which measurements are selected. This can be confirmed from figure 11.13 which shows a comparison between calculated and measured results for refined wind direction sectors of only 5 degrees. The deviations which are visible at such refined wind direction sectors, are filtered out when averaging over a large

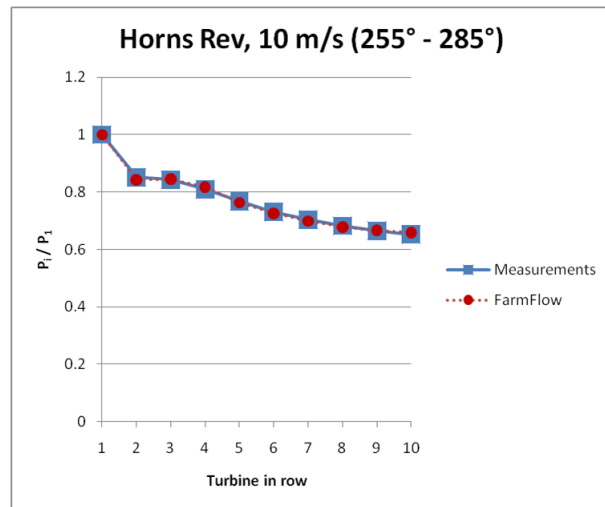
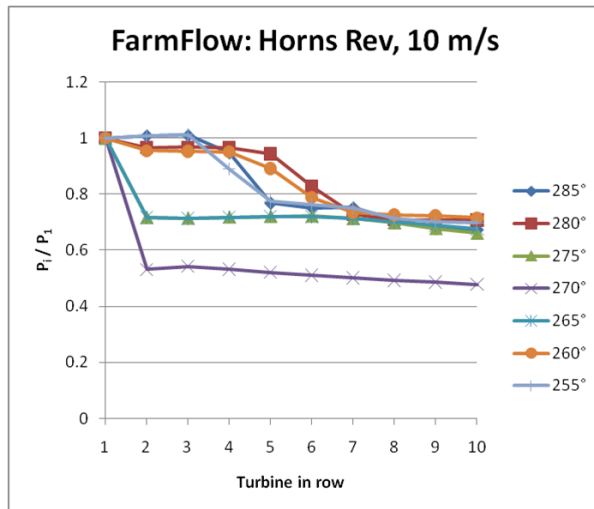


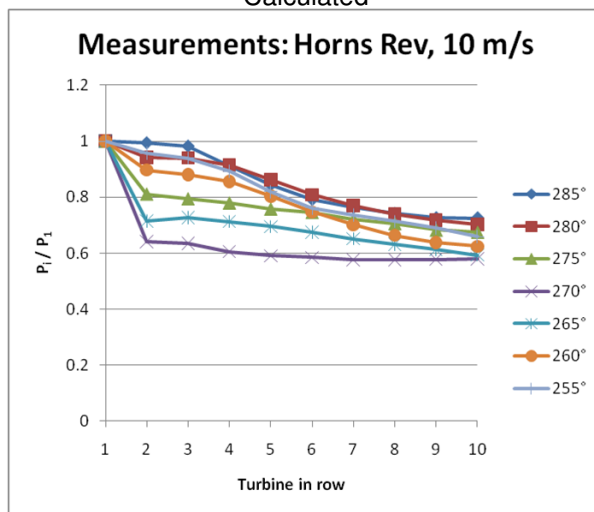
Figure 11.12: Calculated and measured power deficits in the Horns Rev wind farm at a free stream wind speed of 10 m/s for a wind direction sector from 255 to 285 degrees

number of wind direction bins. Hence the underpredictions at one wind direction sector are compensated by an overprediction at another sector.

The deviations which occur for the refined wind direction sectors are related to the assumption of 'straight' wakes in Farmflow, see section 9.1: Farmflow basically assumes the wake to follow the incident mean wind direction throughout the entire wind farm. There is however a large scale motion from the atmosphere around this mean wind direction associated to the meandering process of the wake by which the wind directions in the farm fluctuate around its mean value. This large scale motion can be very significant in the long period (≈ 10 minutes) which an air particle needs to cross the large Horns-Rev farm. Although Farmflow has included a meandering model (see section 9.5.5) this model is inevitably of an approximate nature.



Calculated



Measured

Figure 11.13: Calculated and measured power deficits in the Horns Rev wind farm at a free stream wind speed of 10 m/s (refined wind sectors)

Part IV

Conclusions and recommendations

Chapter 12

Conclusions and recommendations for further research

The overall goal of this research was to describe progress which has been made on the field of aerodynamic engineering methods (rotor and wind farm aerodynamics) in the last 2.5 decades using dedicated measurements. This section summarizes the most important conclusions and recommendations.

Before doing so a general recommendation is made to the wind energy society which states that there is an urgent need for consensus on common conventions, definitions, notations and reference systems. The background for this recommendation lies in the fact that the present thesis makes use of results from many research projects. However each project applied its own conventions and notations leading to an obvious risk of misunderstanding and mis-interpretation of data. These problems became even more prominent in projects where data were exchanged between different parties. The harmonization of results in such projects required a cumbersome and error-prone data processing.

12.1 Conclusions on rotor aerodynamics

- One of the most important conclusions on the field of rotor aerodynamics is that engineering methods have been improved significantly. This is proven by the fact that nowadays there isn't a single designer to find who would dare to design a wind turbine with the very basic aerodynamic modelling as applied in the codes from the Wind Turbine Benchmark Exercise on Mechanical Loads WTBE/ML [van Groenou et al. \(1991\)](#):
- The aerodynamic modelling as applied 25 years ago in the WTBE/ML was based on standard Blade Element Momentum Theory with corrections for the Prandtl tip loss and the turbulent wake, where yaw was modelled by means of the advancing and retreating blade effect only. Since then the following engineering (sub)models are added to state of the art design codes:
 - Models for unsteady airfoil aerodynamics.
 - * Dynamic stall models are developed which are often expressed in the form of an ordinary differential equation in time on the lift coefficient. Experimental evidence of dynamic stall has been found in field and wind tunnel measurements but a direct validation of dynamic stall models is not easy: In the field the stochastic excitation makes a validation virtually impossible. Wind tunnel measurements at yawed conditions are more suitable for validation purposes due to the well defined excitation. However these measurements suffer from the fact that dynamic stall effects interfere with yaw effects which complicate the analysis.
 - * Sometimes a correction for unsteady airfoil characteristics at attached flow is employed. This correction is, opposite to the dynamic stall correction, of an inviscid character. No clear experimental evidence for these effects have been found yet.
 - Models for Dynamic inflow. Dynamic Inflow models are developed which are usually cast in a first order differential equation on the induced velocity, i.e. as an unsteady form of the momentum relation. Experimental evidence of dynamic inflow has been found in the form of load overshoots after a step on the pitch angle or the rotor speed. These overshoots are generally predicted well with the dynamic inflow models. However the reduction of the time con-

stant towards the tip as implemented in most engineering methods seems exaggerated.

- Models for stall delay. Stall delay models have been developed which often add a fraction of the difference between the inviscid and actual 2D lift coefficient to the 2D lift coefficient. The main driving parameter is c/r . In this way the correction starts to work at high angles of attack which then resembles a stall delay effect mainly at the inner part of the blade. A large number of models have been developed for this effect. They sometimes perform well where they were found to perform poorer in other validation cases. In a limited number of cases the drag at rotation was considered. Pressure drag was found to be increased at high angles of attack.
- Models for tip effects on the airfoil characteristics. Measurements clearly indicated that the use of the Prandtl tip correction in combination with 2D airfoil characteristics still leads to an overprediction of tip loads. A limited number of models have been developed which take into account a reduction of the 2D airfoil data towards the tip.
- Models for the azimuthal variation of the induced velocity at yaw. Although several yaw models have been developed which account for the azimuthal variation of the induced velocity at yaw, they generally assume this variation to be sinusoidal, in correspondence with the variation from a skewed tip vortex wake. It is shown that such models are incorrect at the inner part of the blade due to the velocities induced by the root vortices. A model has been developed which takes into account these effects.
- Models for a root loss. The Prandtl tip correction is, despite its name tip correction, nowadays also applied at the root.
- It is difficult to translate the improvements in aerodynamic modelling from the last 25 years into an overall quantitative reduction of design uncertainties. This is partly due to the fact that historical validation material is lacking which could be used as reference. Moreover there are inherent uncertainties present in wind turbine validations, by which the establishment of conclusive numbers for design uncertainties is virtually impossible. These uncertainties amongst others originate from the stochastic atmosphere. Finally it should be realized that the design problem of nowadays wind turbines has become much more difficult by

which it is unfair to compare the present uncertainties with those from 25 years ago. A very rough estimate for the accuracy of current design calculations is 10-20% where the accuracy at off-design conditions can be much poorer.

- Detailed aerodynamic measurements, as carried out in IEA Tasks 14, 18, 20 and 29 played an important role in the improvement of aerodynamic engineering models. They made it possible to extract aerodynamic phenomena which are hidden in the very global information from overall measurement programs. As a matter of fact it can be concluded that only detailed aerodynamic measurements may be used for validation of aerodynamic design models: A validation on basis of global turbine(blade) loads does not give a decisive answer on the accuracy of aerodynamic models due to the fact that 'compensating errors' may occur.
- The development of engineering models also benefited from analysis with advanced aerodynamic models. In turn these advanced aerodynamic models could be improved and validated on basis of detailed aerodynamic measurements. Results from free vortex wake methods showed added value on several fields where the calculation of the induced velocities comes into play. This holds for dynamic inflow effects, tip losses and yawed conditions. CFD codes also proved to have added value on these fields. In addition they give good results for the aerodynamic blade loads in e.g. stall.
- Despite the significant progress achieved, several fundamental shortcomings remain in those methods. An important shortcoming lies in the assumption of independent annuli which is difficult to believe to be true for the inhomogeneous conditions which occur in the rotor plane. This (and other shortcomings) can only be overcome with the above mentioned advanced models.

12.2 Recommendations for further research on rotor aerodynamics

- As a first (general) recommendation it can be stated that a further improvement of engineering models for rotor aerodynamics is still needed. The higher accuracy from such models will enable a more accurate optimization towards a higher energy production and a more cost effective

design, where at the same time investment risks are reduced due to the prevention of design errors.

In order to do so, several aerodynamic (sub)models have been identified which are ready for further improvements. This holds for:

- Tip loss models. The non-uniformity of the flow between the blades is still modelled with the Prandtl tip loss factor. This factor has been derived in the pre-computer era from a simplified wake model. Improvements are possible by adjusting the dependency on the inflow angle with results from modern numerical free vortex wake methods.
- Stall delay models: A large number of models have been invented to correct airfoil data for rotational effects at the inner part of the blade (stall delay). CFD models have proven to give good predictions of the blade loads at the inner part of the blade at high angles of attack. As such it is recommended to use CFD as inspiration for further improvement of engineering methods of this type of engineering methods.
- Models to correct the 2D airfoil data at the tip. It is recommended to develop a physical model for the reduction of airfoil data at the tip. This can be based on thin airfoil theory applied on a semi-infinite long blade.
- Models for the drag on a wind turbine blade. The drag is an important quantity since it determines the power of a wind turbine to a large extent but it has got (too) little attention. This is partly due to the fact that the drag is largely determined by the boundary layer which is generally speaking difficult to measure on a wind turbine blade. An important uncertainty on the drag values is then introduced by the location of the boundary layer transition point which may be influenced by the turbulent environment in which a wind turbine operates. The transition point is relatively easy to measure (e.g. through a sublimation technique) and it is recommended to do so.
- Models for unsteady effects at attached flow conditions. Unsteady effects at attached flow conditions are generally modelled in a 2D way. Such model could be made more representative for wind energy situations by representing the wake with shed vorticity in a 3D

way.

- Models for the inflow induced by other blades. For three bladed rotors, the effect of the inflow at a blade as induced by the bound vortex of the other blades should be taken into account.
- Models for the annular averaged induced velocity at yawed conditions. The annular averaged induced velocity at yaw is calculated with a model from Glauert for which a physical basis is lacking. It is recommended to develop an empirical model for this velocity on basis of results from a free vortex wake method. Associated to this is the need for a more accurate calculation of power at yawed conditions which could also be based on results from free vortex wake methods.
- Models for Dynamic inflow. The time constant in the engineering methods for dynamic inflow is assumed to reduce very strongly towards the tip. Experiments showed the actual reduction to be less strong. This was predicted well with a free vortex wake method. As such it is recommended to perform an elaborate investigation of the radial dependency of the time constant with a free vortex wake method. On basis of this investigation a more accurate empirical model for the time constant can be developed.
- It is important to note that the improvements in rotor aerodynamic modelling have generally been achieved by independent consideration of the different submodels. It is recommended to employ a more integrated approach. As an example: stall effects are either considered as a 3D time averaged effects or as a 2D time dependant effect where they should be considered as a 3D time dependant effect.
- Despite the improvements which are still possible in BEM it should be acknowledged that some fundamental shortcomings cannot be 'repaired' by which eventually, the engineering methods will reach their limits. As a first logical next step it is then recommended to use a more time consuming, but still relatively efficient free vortex wake method. In order to avoid excessive calculational times, most load cases can still be calculated with BEM but the load cases where the induction plays an important role and where free vortex wake methods have shown added value are calculated with a free vortex wake code. One can think of yawed load cases, cases with fast pitching or rotor speed variations but also the calculation of tip loads. A code which is developed along this

philosophy is the ECN Aero-module, [Boorsma, Grasso and Holierhoek \(2008\)](#). This module can easily switch between the BEM engineering model and the free vortex wake method AWSM.

- The most important recommendation on the field of rotor aerodynamics lies in the need for much more experiments in order to gain further understanding on aerodynamics including those phenomena which are until now still largely concealed (e.g. boundary layer phenomena), or unclear (e.g. the non-predicted vortex shedding and the puzzling relation between loads and velocities from the Mexico experiment). As a matter of fact, the author sees an unbalance in the wind energy society: Much effort is spent on the development of aerodynamic models (of sometimes small mutual differences) where the amount of experimental validation material is very limited. Thereto it has to be realized that even the most advanced aerodynamic models require a more profound basis. As an example CFD models rely on turbulence closure relations which are derived for a fixed wing situation. Hence turbulence models with closure relations should be tuned for wind turbine conditions. The aerodynamic measurement programs are to be carried out in both the wind tunnel and the field in such a way that they act complementary.
 - The field experiments have to be performed on a state of the art modern wind turbine. Although difficult to achieve (perhaps even impossible to achieve due to the vast amount of data) a very long measurement period of several years is recommended. The long measurement period reduces the stochastic uncertainty, which enables sensitivity studies with sufficient statistical certainty. It also makes it more likely that very rare atmospheric conditions and their aerodynamic response (e.g. extreme shears, incoherent structures etc) can be caught.
 - Wind tunnel measurements have to be performed in the largest wind tunnel possible in order to achieve Reynolds numbers on the blade which are at least to some extent representative for Reynolds numbers on modern wind turbines. For (Western) Europe the largest tunnel is the DNW-LLF, but outside Europe one can think of larger alternatives e.g. the NASA-Ames wind tunnel. Apart from wind tunnel measurements on rotating wind turbine (models) it is recommended to perform wind tunnel measurements of basic 2D stationary airfoil characteristics at high Reynolds numbers in order to match the conditions on modern wind turbines.

The test programs should consider the most recent and advanced measurement techniques where as a minimum the following data need to be recorded (simultaneously!):

- Pressure distributions (and loads) along the blade to understand the blade aerodynamics.
- Boundary layer parameters (transition, shear stresses) to further understand the blade aerodynamics.
- Flow field data (inflow and near wake) to further understand the induction aerodynamics and to provide information on the external conditions which are needed to interpret the aerodynamic measurements. Note that the inflow in field tests is generally measured with a limited number of anemometers (either cup or sonic anemometers). These measurements have to be combined with LIDAR measurements and 5 hole pitot probes measurements ahead of the blade sections.
- Qualitative flow visualization of both the blade flow and the flow around the rotor in order to have a global overview of the main flow mechanisms.

12.3 Conclusions on wind farm aerodynamics

- On the field of wind farm aerodynamic modelling a large variety of models have been identified of very different degrees of complexity. Computational constraints play a very important role in the development of these models. As a consequence wind farm aerodynamic models range between simple semi-empirical models until CFD methods. However CFD modelling of wind farm aerodynamics often only refers to the modelling of the wake and not to the modelling of the rotor. An intermediate between the basic models and the CFD codes is formed by parabolized wake models. These models generally need an empirical treatment of the near wake which again goes together with a very simple modelling of the rotor.

As such the subject of wind farm aerodynamics is usually considered independently from the subject of rotor aerodynamics. An important step in the integration of rotor and wind farm aerodynamics is then made in ECN's Farmflow(Wakefarm) approach which combines a parabolized

k - ϵ method with results from a free vortex wake method.

- It can be concluded that progress on the field of wind farm aerodynamics is hampered by a shortage of high quality validation material. Nevertheless several experimental data have become available over the last decades with which wind farm aerodynamic models could be validated and improved. These measurements have been taken in both the wind tunnel on small model farms as well as in the full scale field environment:
 - An important drawback of wind tunnel measurements lies in the fact that scaling effects are inevitable. These scaling effects will at least be present in the aerodynamics of the near wake. Moreover the wind tunnel conditions are not fully representative for field conditions. This may even, although to a smaller extent, be true when measurements are done in an atmospheric wind tunnel.
 - An important drawback of field measurements lies in the very limited degree of detail:
 - * Usually it is only power which is measured on the turbines.
 - * In many cases meteorological data are only measured on 1 mast which, dependant on the wind direction, is placed either in the wake or in the free stream. As such the direct correlation between input and output of wake models (the free stream wind field and the wake wind field respectively) cannot be established.
 - * Furthermore field measurements are often taken on commercial wind farms, the owners of which (understandably) lay their first priority on the commercial exploitation of the farm. This makes that the quality of these measurements cannot always be assured. An exception is formed by the ECN Wind Turbine Test Site Wieringermeer (EWTW) which is one of the few research farms on which detailed measurements are performed on turbines in a line set-up. Both power of the turbines as well as meteorological data are collected. In the EWTW line set-up the largest power loss due to wake effects (and hence the lowest overall power) appears at the second turbine in the farm. The turbines deeper in the farm have a slightly higher power. This is opposite to the situation in large off-shore wind farms where the power keeps decreasing for turbines deeper into the

farm. This can be explained by lateral wake effects and the size of those large (array) wind farms. The EWTW measurements allowed a calibration of the Farmflow turbulence modeling parameters with which the behavior of the power and the meteorological data in the EWTW was predicted much better. Also the behavior of the power in large off-shore wind farms could be predicted well after calibration of the turbulence parameters.

- Despite the simplifications of wind farm aerodynamic models and the lack of validation possibilities, the most important conclusion is still that, similar to the situation for rotor aerodynamics, much progress has been achieved over the past decades. Again this is proven by the fact that there isn't a wind farm developer to find who would dare to design a nowadays large wind farm with a wake model from the early 1990's.

This can be illustrated with the developments from Wakefarm to Farmflow. In the beginning of the 1990's only single wakes were considered. These were modelled with a very simple approach: The wind turbine was represented by an actuator disc with a near wake model based on momentum theory (and later empiricism). The far wake was modelled with a turbulence model tuned for non wind energy applications. Since then the near wake model has been refined and multiple wake effects are taken into account in both axial and lateral direction. Furthermore the turbulence model has been calibrated for wind turbine wake situations. For the development of engineering models in general it is also important that some CFD models entered the (research) scene in which the rotor is modelled with more advanced methods than the actuator disc approach (e.g. by using actuator lines). Such advanced models can now be used for calibration of more simple models.

- It is difficult to establish a conclusive number on the discrepancies between calculated and measured power losses in wake operation. Nevertheless a very rough estimate for these discrepancies could be set as 10-20%. Although this is a seemingly small discrepancy, it represents a significant economical impact. Thereto it must be realized that nowadays almost all turbines are placed in wind farms where the increasing size of these farms makes that wake effects occur almost continuously.

12.4 Recommendations for further research on wind farm aerodynamics

- As a first (general) recommendation it is stated that wind farm aerodynamic (engineering) models need to be improved, not only for the prediction of wind farm power but also for the prediction of mechanical loads on turbines in a farm. Such better models represent a huge economic benefit since they enable a more accurate wind farm optimization (e.g. through farm control) leading to a higher energy production and lower loads.
- Some subjects have been found which until now have received relatively little attention. Therefore it is recommended to intensify research on these subjects:
 - The validation and improvement of multiple wake models (i.e. the modelling of wake overlapping mechanisms in lateral and axial direction). Associated to this is the subject of near wake modelling in combination with multiple wake modelling, i.e. the modelling of the wake just behind a turbine which is already in the wake of another turbine. Although some effort has been undertaken on these phenomena a better understanding could be gained from extensive meteorological measurements and/or detailed CFD methods of both the rotor and the wake.
 - The interaction of wind farms with the outer atmosphere. Nowadays wind farms are of a scale that they will affect the atmospheric boundary layer and vice versa. As such an interaction between wind farm models and mesoscale models should be established.
 - Refinement of turbulence models for wind farm aerodynamics. Although some effort has been undertaken on this field, the adjustment of turbulence parameters was often based on indirect information (e.g. turbine powers). It is recommended to refine the turbulence models on basis of direct turbulence measurements.
 - A main question to be answered is the importance of rotor aerodynamics for wake aerodynamics. More specifically it should be determined whether it is justified to model the rotor as an actuator disc. The answer to this question can be found by comparing results from CFD codes, which models both the rotor and the wake in

a detailed way, with results from a similar code in which the rotor is replaced by an actuator disc. It is anticipated that this shows the need to model the rotors in a closely spaced wind farms (say wind farms in which the spacing is less than $5D$) in a more refined way. For wind farms with larger distances between the turbines an actuator disc model might be sufficient.

- Some specific improvements have been identified for the Farmflow model which can relatively easy be implemented:
 - In case of multiple wake situations, the streamwise pressure gradient upstream of the rotor should be taken into account. The resultant reference velocity (and hence axial force coefficient) could be found in an iterative way such that the basic axial momentum theory relations are fulfilled.
 - The distribution of turbulent kinetic energy over the different directions should be based on empirical relations from e.g. the EWTW sonic anemometers. This is of importance for the calculation of mechanical loads on wind turbines in a farm.
 - The radial variation in loading over the actuator disc could be included based on a separate rotor aerodynamic calculation.
- The most important recommendation on the field of wind farm aerodynamics is a cry for much more good measurements. Only in this way the understanding of the dominant wind farm aerodynamic processes and dependencies can be enhanced. As a matter of fact a thorough understanding of the wind farm aerodynamic problem requires a detailed flow field mapping (at a high frequency resolution) in the entire farm in combination with detailed measurements of the aerodynamic behavior of all rotors.

In principle this could be done in a wind tunnel experiment. Despite the fact that these experiments are less representative for full scale field conditions they will help to gain fundamental understanding of wind farm aerodynamic processes.

It obviously remains essential to combine wind tunnel measurements with several field experiments on different wind farms. These field experiments should at least fulfill the following minimum requirements:

- Two meteorological measurement devices (either meteorological

masts with anemometers and/or LIDARS) are needed. This enables the simultaneous measurement of the wake wind speeds with the incoming free stream wind speeds by which a direct correlation can be established between the free stream input and the wake output.

- Power, blade loads and axial force need to be measured on all turbines in the farm. Thereto it should be noted that the axial force is rarely measured even though it is very determinant for wake aerodynamics.
- A very long measurement period (several years) is required in order to reduce the stochastic uncertainty and to enable sensitivity studies with sufficient statistical certainty.
- Seemingly trivial (but still necessary to mention) is the need for a good measurement quality.

An interesting compromise between the rather incomplete but representative full scale field measurements and the very complete but less representative wind tunnel measurements is formed by ECN scaled farm. This is a heavily instrumented research wind farm of relatively small scale.

As such a combination of wind tunnel, scaled farm and full scale measurements will form the most complete base to understand wind farm aerodynamic (models), even though it is acknowledged that each type of measurements has its own drawbacks.

Bibliography

- Adams B.M. (1995). "Dynamic loads in wind farms II". GH-Report 286/R/1, Garrad Hassan & Partners.
- Ainslie J. (1988). "Calculating the flow field in the wake of wind turbines". *Journal of Wind Engineering*, 27, 213–224.
- Anderson M.B., Milborrow D.J. and Ross J.N. (1982). "Performance and wake measurements on a 3m diameter horizontal axis wind turbine, Comparison of theory, wind tunnel and field test data". In *Proceedings Fourth International Symposium on Wind Energy Systems*, (pp. 113–136).
- Barlow J.B. and Rae W.H. and Pope A. (1999). *Low-speed wind tunnel testing* (Third ed.). John Wiley & Sons Inc.
- Barthelmie R. et al (2010). "Quantifying the Impact of Wind Turbine Wakes on Power Output at Offshore Wind farms". *Atmospheric and Oceanic Technology*, Vol. 27, pp1302.
- Barthelmie R.J. et al (2003). "Efficient Development of Off-Shore Wind Farms, Final Report of the ENDOW project". RISØ-R-1407(EN), RISØ.
- Barthelmie R.J. et al (2011). "Flow and wakes in large off-shore wind farms, Final report for Upwind WP8". RISØ-R-1765(EN), RISØ.
- Barthelmie R.J., Hansen K.S. and Pryor S.C. (2011). "Meteorological controls on wind turbine wakes". In *13th International conference on Wind Engineering, ICWE, held at Amsterdam*.
- Björck A. (1995). "Dynamic Stall and Three Dimensional Effect". FFA-TN–1995-31, The Aeronautical Research Institute of Sweden, FFA.
- Boorsma K., Grasso F., Holierhoek, J.G. (2011). "Enhanced approach for simulation of rotor aerodynamic loads". In *European Wind Energy Agency*

Off-shore Conference, Amsterdam, Netherlands.

Bot E.T.G. (2009). Personal communication.

Bot E.T.G. (2011). "Farmflow, Improved near wake modelling and validation against four full scale wind farms (Available in draft)". ECN-X-11-248, Energy Research Center of the Netherlands, ECN.

Bot E.T.G. (2001). "Aerodynamische Tabel Generator". ECN-C-01-077, Energy Research Centre of the Netherlands, ECN.

Bot E.T.G. and van Langen P. (2006). "Blade Optimisation Tool, User Manual". ECN-E-06-006, Energy Research Centre of the Netherlands, ECN.

Bramwell A.R.S. (1974). "Some remarks on the induced velocity field of a lifting rotor and Glauert's formula". ARC C.P. no 1301, Aeronautical Research Council.

Bruining A. (1993). "Pressure distributions from a rotating wind turbine blade measured on the Open Air Research Facility of Delft University of Technology". In *Proceedings of AWEA Conference, San Fransisco, 1993*

Burton T., Sharpe D., Jenkins N., Bossanye E. (2001). *Wind Energy Handbook*. John Wiley and Sons.

Cabezon D., Sanz J., Mart I., Crespo A (2008). "CFD modeling of the interaction between the Surface Boundary Layer and rotor wake". In *European Wind Energy Conference, Marseille, France*.

Chaviaropoulos P.K. and Douvikas D.I. (1998). "Mean-flow-field Simulations over Complex Terrain Using a 3D Reynolds Averaged Navier Stokes Solver". In *Proceedings of ECCOMAS 98, 1998, Vol. I, Part II*, (pp. 842–848).

Chaviaropoulos P.K. and Hansen M.O.L. (2000). "Investigating 3D and rotational effects on wind turbine blades by means of a quasi-3D Navier Stokes Solver". *Journal of Fluids Engineering*, 122(2), 330–336.

Chaviaropoulos P.K. et al (2001). "Viscous and Aeroelastic effects on Wind turbine blades. The Viscel project". In *Proceedings of European Wind Energy Conference, EWEC*, (pp. 347–351).

Corten G.P., Schaak P and Hegberg T.G. (2004). "Turbine Interaction in Large Offshore Wind Farms; Wind Tunnel Measurements". ECN-C-04-048, Energy Research Center of the Netherlands, ECN.

Crespo A. and Hernandez J. (1993). "Analytical correlations for turbu-

- lence characteristics in the wakes of windturbines". In *Proceedings of the ECWEC conference held at Travemunde 8 – 12 March 1993*.
- Crespo A. et. al. (1985). "Numerical Analysis of wind turbine wakes". In *Proceedings of Delphi Workshop on "Wind turbine applications"*.
- Dahlberg J.A. and Montgomerie B. (2005). "Research program of the Utgrunden Demonstration Offshore Wind Farm, Final report Part 2, Wake effects and other loads". FOI 2005-02-17, Swedish Defense Research Agency, FOI.
- Dahlberg J.A. et al. (1989). "Wind Tunnel Measurements of load variations for a yawed turbine with different hub configurations". In *Proceedings of EWEC Conference, Glasgow, 10-13 July 1989*, (pp. 95–100).
- de Vries O. (1979). "Fluid Dynamic Aspects of Wind Energy Conversion". *Agardograph*, 77(243).
- Dekker J.W.M. and Pierik J.T.G. (1997). "European Wind Turbine Standards, EWTS". ECN-C –99-073, ECN.
- Drela M. (1989). "XFOIL: An analysis and design system for low Reynolds number airfoils". In *Low Reynolds number aerodynamics, Lecture notes in Engineering 54*, (pp. 1–12).
- Du Z. and Selig M.S. (1999). "A 3D stall delay model for horizontal axis wind turbine performance prediction". In *ASME Wind Energy Symposium, Reno USA*.
- Eecen P.J. and Verhoef J.P. (2007). "EWTW meteorological database, description June 2003-May 2007". ECN-E-07-041, Energy Research Centre of the Netherlands, ECN.
- El Kasmi A. and Masson C. (2008). "An extended $k-\epsilon$ model for turbulent flow through horizontal axis wind turbines". *Journal of wind engineering and Industrial Aerodynamics*, (96), 103–122.
- Ewald, B. (1998). Wind tunnel wall correction. AGARDograph 336.
- Feigl L. (2003). "Analysis of aerodynamic field measurements on instrumented wind turbine rotors". EUREC-Agency Master Project, ECN.
- Glauert H. (1935). "Airplane propellers". In *Aerodynamics Theory*, 169-360. Durand W.F. (ed) Dover New York.
- Glauert H. (November 1926). "A general theory for the Autogyro". ARC R-M 1111.

- Graham J.M.R. and Brown C.J. (2000). "ROTOW-Investigation of the aerodynamic interaction between wind turbine rotor blades and the tower and its impact on wind turbine design". Final Publishable Report, Department of Aeronautics, Imperial College of Science and Medicine, London, UK.
- Grasso F. and van Garrel A. (2011). "Near Wake Simulation of Mexico Rotor in Axial and Yawed Flow Conditions with Lifting Line Free Wake Code". In *Proceedings of Wake Conference, Gotland University, Sweden*.
- Guntur S.K., Bak C. and Sørensen N.N. (2011). "Analysis of 3D stall models for wind turbine blades using data from the Mexico experiment". In *13th International conference on Wind Engineering, ICWE, held at Amsterdam*.
- Haans W. (2011). "Wind turbine aerodynamics in yaw, unravelling the measured rotorwake". PhD Thesis, Technical University of Delft.
- Hand M.M. et al (2001). "Unsteady Aerodynamics Experiment Phase VI Wind Tunnel Test Configurations and Available Data Campaigns". NREL/TP-500-29955, National Renewable Energy Laboratory, NREL.
- Hansen M.O.L. (2008). *Aerodynamics of wind turbines*. Earthscan. Second edition.
- Hansen M.O.L. and Johansen J. (2004). "Tip studies using CFD and computation with tip loss models". *Wind Energy*, (7), 343–356.
- Hansen M.O.L., Mikkelsen R. and Øye S. (2010). "Investigating the effect of extreme shear and yaw model using Actuator Line model". In *Proceedings of EAWE conference 'The Science of Making Torque from the Wind' held at Crete*.
- Hassan U. (1992). "A windtunnel investigation of the wake structure within small wind turbine farms". ETSU-WN-5113, ETSU.
- Hernandez J. and Crespo A. (1990). "Wind turbine wakes in the atmospheric surface layer". *The PHOENICS Journal of CFD and its applications*, 3(3).
- Himmelskamp, H. (1950). "Profiluntersuchungen an einem umlaufenden Propeller".
- Hur C. (2011). "Unsteady Two-dimensional Aerodynamic Forces and Aeroelastic Stability Based on Theodorsen Theory". Energy Research Center of the Netherlands, ECN.
- Jensen L. (2004). "Wake measurements from the Horns Rev wind farm". In *Proceedings EWEK conference, London, 22-25 November 2004*.

- Kamada Y. and Maeda T. (2011). "Experimental Study on Velocity Field around Wind Turbine Rotor". *Japan Society Mechanical Engineering Journal*, 71(701).
- Katz J. and Plotkin A. (2001). *Low Speed Aerodynamics*. Cambridge Aerospace series.
- Kuczaj A.K. (2009). "Virtual Blade Model Simulations of the Mexico experiment". NRG-21810/09.97106, Nuclear Research Consultancy, NRG.
- Lange B. et al (2003). "Modelling of off-shore wind turbine wakes with the wind farm program FlaP". *Wind Energy*, Vol. 6, pp87.
- Larsen G.C. et al (2007). "Dynamic wake meandering modelling". RISØ-R-1607(EN), RISØ.
- Leishman J.G. and Beddoes T.S. (1998). "A Generalised model for unsteady airfoil behaviour and dynamic stall using the indicial method ". In *42th Annual Forum of the American Helicopter Society Washington DC*.
- Lindenburg C. (2003). "Investigation into rotor blade aerodynamics, Analysis of the stationary measurements of the UEA Phase IV rotor in the NASA-Ames wind tunnel". ECN-C-03-025, Energy Research Centre of the Netherlands, ECN.
- Lindenburg C. and Hegberg T. (1999). "PHATAS – IV, User's manual". ECN-C- 99-093, ECN.
- Lissaman P.B.S. and Bate E.R. (1977). "Energy effectiveness of arrays of wind energy conversion systems". Report AV FR 7058, Aerovironment Inc, Pasadena.
- Machielse L.A.M. (2011). "Controlling Wind, Tunnel Theorie". ECN-E-11-065, Energy Research Center of the Netherlands, ECN.
- Madsen H.A. (1991a). "Aerodynamics of a Horizontal-Axis Wind Turbine in Natural Conditions". RISØ-M-2903, RISØ National Laboratory.
- Madsen H.A. (1991b). "Aerodynamics of a Horizontal-Axis Wind Turbine in Natural Conditions- Raw data overview". RISØ-M-2902, RISØ National Laboratory.
- Madsen H.A. (1991c). "Structural Dynamics of a 100 kW HAWT". RISØ-M-2887, RISØ National Laboratory.
- Madsen H.A. (1999). "Yaw simulation using a 3D actuator disc model". In *Proceedings, IEA aerodynamics Symposium Stockholm*.

- Maggio T. and Grasso F. (2011). "Numerical Investigation on Performance of Innovative Wind Turbine Blades for Loads Reduction ". In *Proceedings EWEA Annual conference 2011, Brussels*.
- Montgomerie B., Brand A.J., Bosschers J., van Rooij R. (1997). "Three-dimensional effects in stall". ECN-C –96-079, Energy Research Centre of the Netherlands, ECN.
- Obdam T. (2010). Personal communication.
- Øye S. (1991). "Tjæreborg wind turbine (Esbjerg) dynamic inflow measurements". AFM notat VK-197, Technical University of Denmark.
- Øye S. (1992). "Tjæreborg wind turbine (Esbjerg) yaw measurements". AFM notat VK-214, Technical University of Denmark.
- Panofsky H. and Dutton, J. (1984). *"Atmospheric Turbulence"*. John Wiley and Sons.
- Pascal L. (2009). "Analysis of Mexico measurements". ECN-Memo-09-010, Energy Research Center of the Netherlands, ECN.
- Prospathopoulos, J.M. (2010). Personal communication.
- Prospathopoulos J.M., Politis E.S., Rados K.F., and Chaviaropoulos P.K. (2010). "Evaluation of the effects of turbulence model enhancements on wind turbine wake predictions ". In *Wind Energy Journal, published online, DOI 10.1002/we.419*.
- Rados K. et al (2002). "Comparison of wake models with data for offshore windfarms". *Wind Engineering, Vol. 25, pp 271-280*.
- Rethoré P.E. (2009). "Wind Turbine Wake in Atmospheric Turbulence". RISØ-PhD-51(EN), RISØ.
- Rethoré P.E., Sørensen N.N., Zahle F., Bechmann A., Madsen H.A. (2011a). "MEXICO Wind Tunnel and Wind Turbine modelled in CFD". In *AIAA Conference*.
- Rethoré P.E., Sørensen N.N., Zahle F., Bechmann A., Madsen H.A. (2011b). "CFD model of the MEXICO wind tunnel". In *EWEA Annual Event held at Brussels*.
- Rodi W. (1982). *Turbulent buoyant jets and plumes*. Pergamon Press.
- Ronsten G. (1994). "Geometry and Installation in Wind Tunnels of a Stork 5.0 WPX Wind Turbine Blade Equipped with Pressure Taps". FFAP-A–1006,

- The Aeronautical Research Institute of Sweden, FFA.
- Rozendal D. (2003). "Flow field measurements on a small scale wind turbine model in the DNW PLST wind tunnel". NLR-CR-2003-484, National Aerospace Laboratory NLR.
- Sanderse, B (2009). "Aerodynamics of wind turbine wakes, a literature review". ECN-09-016, Energy Research Center of the Netherlands, ECN.
- Sant T. (2007). "Improving BEM based aerodynamic model in wind turbine design codes". PhD Thesis, Technical University of Delft.
- Sant T., van Kuik G. and van Bussel G.J.W. (2006). "Estimating the angle of attack from blade pressure measurements on the NREL phase VI rotor using a free wake vortex model: axial conditions". *Wind Energy*, (9), 549–577.
- Santos Pereira R., Schepers J.G. and Pavel M. (2011). "Validation of the Beddoes Leishman Dynamic Stall model for Horizontal Axis Wind Turbines using Mexico data". In *49th AIAA Aerospace Sciences meeting*.
- Schepers J.G. (1999). "An engineering model for yawed conditions developed on basis of wind tunnel measurements". In *Proceedings of ASME Wind Energy Symposium, held at Reno USA*.
- Schepers J.G. (2001). "EU project in German Dutch Wind Tunnel". ECN-RX-01-006, Energy Research Center of the Netherlands, ECN.
- Schepers J.G. (2003). 'ENDOW: Validation and improvement of ECN's wake model". ECN-C-03-034, Energy Research Center of the Netherlands, ECN.
- Schepers J.G. (2004a). "Annexlyse: Comparison between PHATAS calculations and IEA Annex XVIII measurements". Annexlyse, Task 3.4 report, Energy Research Center of the Netherlands, ECN.
- Schepers J.G. (2004b). "Annexlyse: Validation of yaw models on basis of detailed aerodynamic measurements on wind turbine blades". ECN-C -04-097, Energy Research Centre of the Netherlands, ECN.
- Schepers J.G. (2007a). "IEA Annex XX: Comparison between calculations and measurements on a wind turbine in the NASA-Ames wind tunnel". ECN-E-07-066, Energy Research Centre of the Netherlands, ECN.
- Schepers J.G. (2007b). "IEA Annex XX: Comparison between calculations and measurements on a wind turbine in yaw in the NASA-Ames wind tun-

- nel". ECN-E-07-072, Energy Research Center of the Netherlands, ECN.
- Schepers J.G. (2007c). "IEA Annex XX: Dynamic Inflow effects at fast pitching steps on a wind turbine placed in the NASA-Ames wind tunnel". ECN-E-07-085, Energy Research Center of the Netherlands.
- Schepers J.G. (2009). "Analysis of 4.5 years EWTW wake measurements". ECN-E-09-057, Energy Research Center of the Netherlands, ECN.
- Schepers J.G. (2012). "TUDelft lecture series Rotor Aerodynamics AE4-W12", Lecture notes.
- Schepers J.G., Barthelmie R., Politis E.P. (2010). "WP8 Flow: Wake reducing concepts". Deliverable D8.5, Upwind Project.
- Schepers, J.G., Boorsma, K. et al (2011). "Final report of IEA Task 29, Mexnext (Phase 1), Analysis of Mexico wind tunnel measurements". ECN-E-12-004, Energy Research Center of the Netherlands, ECN.
- Schepers J.G., Obdam, T., Prospathopoulos, J.M. (2012). "Analysis of wake measurements from the ECN Wind Turbine Test Site Wieringermeer, EWTW". *Wind Energy*, (15), Issue 4, 575-591.
- Schepers J.G., Pascal L. and Snel H. (2010). "First results from Mexnext: Analysis of detailed aerodynamic measurements on a 4.5 m diameter rotor placed in the large German Dutch Wind Tunnel DNW". In *Proceedings of European Wind Energy Conference, EWEC*.
- Schepers J.G. and Snel H. (1995). "JOULE2: Dynamic Inflow: Yawed Conditions and Partial Span Pitch". ECN-C-95-056, Energy Research Centre of the Netherlands, ECN.
- Schepers J.G. and Snel H. (2007). "Mexico, Model experiments in controlled conditions". ECN-E-07-042, Energy Research Center of the Netherlands.
- Schepers J.G., Snel H. and Boorsma K. (2010). "IEA Task 29 Mexnext: Analysis of wind tunnel measurements from the EU project Mexico". In *Proceedings of EAWC conference 'The Science of Making Torque from the Wind' held at Crete*.
- Schepers J.G. and van der Pijl S. (2007). "Improved modelling of wake aerodynamics and assessment of new farm control strategies". In *Proceedings of EAWC conference 'The Science of Making Torque from the Wind'*.
- Schepers J.G., van Rooij R. and Bruining A. (2003). "Detailed aerodynamic measurements: Analysis of results". In *Proceedings of European Wind*

Energy Conference, EWEC held at Madrid.

- Schepers J.G. and van Rooij R. (2005). "Final report of the Annexlyse project: Analysis of aerodynamic field measurements on wind turbines". ECN-C 05-064, Energy Research Centre of the Netherlands, ECN.
- Schepers J.G. et al. (1997). "Final report of IEA Annex XIV' Field Rotor Aerodynamics". ECN-C-97-027, Energy Research Centre of the Netherlands, ECN.
- Schepers J.G. et al. (2001). "Verification of European Wind Turbine Design Codes, VEWTD". In *Proceedings of European Wind Energy Conference, EWEC*.
- Schepers J.G. et al. (2002a). "Final report of IEA Annex XVIII Enhanced Field Rotor Aerodynamics Database". ECN-C-02-016, Energy Research Centre of the Netherlands, ECN.
- Schepers J.G. et al. (2002b). "Large Off-Shore Wind Farms: Linking Wake models with Atmospheric Boundary Layer Models". *Wind Engineering*, (Vol. 25, No.5), 307.
- Schepers J.G. et al. (2002c). "Verification of European Wind Turbine Design Codes". ECN-C-01-055, Energy Research Centre of the Netherlands, ECN.
- Schepers J.G. et al. (2004a). "Analysis of detailed aerodynamic measurements, using results from an aero-elastic code". *Wind Energy*(7) 357-371.
- Schepers J.G. et al. (2004b). "Validation of aero-elastic codes, using detailed aerodynamic measurements". In *Proceedings of EAWE, conference, 'The Science of Making Torque from the Wind' held at Delft*.
- Schepers J.G. et al. (2011). "Results from Mexnext: Analysis of detailed aerodynamic measurements on a 4.5 m diameter rotor placed in the large German Dutch Wind Tunnel DNW". In *Proceedings of European Wind Energy Conference, EWEC, held at Brussels*.
- Schlichting H. (2004). *Boundary layer Theory, 8th ed.* Springer Verlag.
- Schreck S. (2008). "IEA Wind Annex XX: HAWT Aerodynamics and Models from Wind Tunnel Measurements". NREL/TP-500-43508, The National Renewable Energy Laboratory, NREL.
- Shen W.Z. (2011). Personal communication, Danish University of Technology, DTU.

- Shen W.Z. et al. (2010). "Validation of the Actuator Line / Navier Stokes technique using Mexico measurements". In *Proceedings of EAWC conference 'The Science of Making Torque from the Wind' held at Crete*.
- Shen W.Z., Mikkelsen R., Sorensen J.N. and Bak C. (2005). "Tip loss corrections for wind turbine computations". *Wind Energy* (8) 457-475.
- Shen W.Z. et al (2009a). "Determination of the Angle of Attack on Rotor Blades". *Wind Energy*, (12), 91-98.
- Shen W.Z. et al (2009b). "The actuator surface model: A new Navier Stokes based method for rotor computations". *Journal of Solar engineering*, (Volume 131), 304-309.
- Shipley D.E. et al (1995). 'The baseline data sets for phase II of the combined experiment". NREL TP-442-6915, National Renewable Energy Laboratory, NREL.
- Simms D.A., Schreck S., Hand M.M., Fingersh L.J. (2001). "NREL Unsteady Aerodynamics Experiment in the NASA-Ames Wind Tunnel: A Comparison of Predictions to Measurements". NREL/TP-500-29494, The National Renewable Energy Laboratory, NREL.
- Smith D. (1990). "Wake measurements behind two interacting wind turbines with streamwise and crossflow separations". In *Proceedings of 12th BWEA Conference*.
- Snel H. (1997). "Heuristic modelling of dynamic stall characteristics". In *Proceedings of the EWEC 1997 Conference held at Dublin*, (pp. 429-433).
- Snel H. (2002). "1-Dimensional analysis of flow around turbine including collector effects". Discussion document for Mexico project group, Energy Research Center of the Netherlands, ECN.
- Snel H. (2004). "Application of a modified Theodorsen model to the estimation of aerodynamic forces and aero-elastic stability". In *Proceedings EWEC conference, held at London*.
- Snel H. and Schepers J.G. (1994). "JOULE1: Joint investigation of Dynamic Inflow Effects and Implementation of an Engineering Method". ECN-C-94-107, Energy Research Centre of the Netherlands, ECN.
- Snel H. et al. (1993). "Sectional prediction of lift coefficients on rotating wind turbine blades in stall". ECN-C -93-052, Energy Research Centre of the Netherlands, ECN.

- Snel H., Schepers J.G. and Siccama A. (2009). "Mexico, the database and results of data processing and analysis". In *47th AIAA Aerospace Sciences meeting*.
- Snel H., Schepers J.G., van Garrel A. and Barth S. (2008). "The Mexico experiment analysis of yaw measurements and comparison with existing models". In *Proceedings of European Wind Energy Conference, EWEC, held at Brussels*.
- Sørensen J.D., Frandsen S. and Tarp-Johansen N.J. (2007). *Fatigue Reliability in Wind Farms and effective turbulence models, in Applications of Statistics and Probability in Civil Engineering*. Taylor, Francis Group, London, ISBN 978-0-415-45211-3.
- Sørensen J.N. (2011). "Aerodynamics Aspects of Wind Energy Conversion". *Annual Review of Fluid Mechanics*, (43), 427–448.
- Sørensen J.N. and van Kuik G.A.M. (2011). "General momentum theory at low tip speed ratios". *Wind Energy*, (14), 821–839.
- Sørensen J.N., Mikkelsen R. (2001). "On the validity of the blade element momentum method". In *Proceedings of European Wind Energy Conference, EWEC*, (pp. 362–366).
- Spath M. and Stafanatos N. (1995). "Survey of frequency responses of pressure tubes installed in a 12.5 m rotor blade". ECN-I-92-028, ECN.
- Theodorsen T. (1935). "General Theory of Aerodynamic Instability and the Mechanism of flutter". NACA Report 496, National Advisory Committee for Aeronautics, NACA.
- Timmer N. (2010). Personal communication.
- Timmer W.A., van Rooij, R.P.J.O.M. (2001). "Some aspects of high-angle-of-attack flows on airfoils for Wind Turbine application". In *Proceedings of European Wind Energy Conference, Copenhagen*.
- Timmer W.A., van Rooij, R.P.J.O.M. (2003). "Summary of the Delft University Wind Turbine Dedicated airfoils". In *Journal of Solar Energy Engineering Volume 125, Issue 4*, (pp. 488–496).
- Tindal A.J. (1993). "Dynamic loads in wind farms I". GH-Report 205/R/12, Garrad Hassan & Partners.
- Troldborg N., Sørensen J.N. and Mikkelsen R. (2007). "Actuator line simulation of the wake of wind turbines operating in turbulent inflow". In *Proceed-*

- ings of EAWE conference 'The Science of Making Torque from the Wind, held at Lyngby'.*
- van Bussel G.J.W. (1995). "The aerodynamics of Horizontal Axis wind turbines explored with asymptotic expansion methods". *PhD thesis*.
- van Engelen T.G. and van der Hooft E.L. (2004). "Dynamic inflow compensation for pitch controlled windturbines". In *Proceedings EWEc conference, London, 22-25 November 2004*.
- van Garrel A. (2003). "Development of a wind turbine aerodynamics simulation module". ECN-C-03-079, Energy Research Centre of the Netherlands, ECN.
- van Groenewoud G.J.H., Boermans L.M.M. and van Ingen J.L. (1983). "Investigation of laminar-turbulent transition of the boundary layer on the 25 m HAT wind turbine. (in Dutch)". TUDelft Report LR-390, Faculty of Aerospace Engineering, Technical University of Delft.
- van Grol H.J., Snel H. and Schepers J.G. (1991). "Wind Turbine Benchmark Exercise on Mechanical loads. A state of the art report. Volume 1, part A & B". ECN-C-91-031, Energy Research Center of the Netherlands, ECN.
- van Ingen J.L. (1956). "A Suggested Semi-empirical Method for the Calculation of the Boundary Layer Transition Region". TUDelft Report VTH-74LR-390, Faculty of Aerospace Engineering, Technical University of Delft.
- van Rooij R. (1996). "Modification of boundary layer calculation for improved airfoil stall prediction". Report IW-96087R, Institute for Wind Energy, TUDelft.
- van Rooij R. (2005). "The effect of the test set-up on the steady state aerodynamic data (IEA-Annex XX)". In *Proceedings of the IEA Aerodynamics Symposium held at CENER, Pamplona*.
- van Rooij R., Bruining A. and Schepers J.G. (2003). "Validation of some rotor stall models by analysis of the IEA Annex XVIII field data". In *Proceedings of European Wind Energy Conference, EWEc*.
- Verhoef A. (2011). Personal communication.
- Vermeer N.J., Sørensen J.N., Crespo A. (2003). "Wind Turbine Wake Aerodynamics". *Progress in Aerospace Sciences, Elsevier Ltd*, (39), 467–510.
- Vermeulen P.E.J. (1979). "A wind tunnel study of the wake of a horizontal axis wind turbine". TNO-78-09674, Netherlands Organisation for Applied

- Scientific Research, TNO.
- Vermeulen P.E.J. (1980). "An experimental analysis of wind turbine wakes". In *3rd IEA International conference on Wind Turbine Systems, held at Lyngby Denmark*.
- Voutsinas S., Belessis M. & Huberson, S. (1993). "Dynamic inflow effects and vortex particle methods". In *Proceedings ECWEC conference, Travemunde, 8-12 March 1993*, (pp. 428).
- Voutsinas S. et al (2003). "Mexico WP2: Navier Stokes and Euler Simulations to determine the maximum rotor size". MEXICO-DOC- WP2-01-01, National Technical University of Athens.
- Wilson R.E. (1981). "Aerodynamic Pot Pourri". NACA CP 2185, Cleveland State University.
- Wilson R.E. (1986). "A wind turbine flow field model". *Trans. ASME*, (108), 344-345.
- Wu Y.T. and Poré-Agel F. (2010). "Large-Eddy Simulation of Wind-Turbine Wakes: Evaluation of Turbine Parametrisations". *Boundary-Layer Meteorology*, (138), 345-366.
- Yang H., Shen W.Z., Sørensen J.N. and Zhu W.J. (2011). "Extraction of airfoil data using PIV and pressure measurements". *Wind Energy*, (14), 539–556.
- Zahle G. and Sorensen N. (2008). "Overset Grid Flow Simulation on a Modern Wind Turbine". In *26th AIAA Applied Aerodynamics Conference, AIAA-2008-6727*

Part V

Appendices

Appendix A

IEA Task 14/18: Description of experimental facilities

In this Appendix the global characteristics of the IEA Task 14/18 facilities of TUDelft, ECN, IC/RAL, NREL, RISØ and Mie University are described.

A.1 Aerodynamic test facility of Delft University of Technology, TUDelft

The global characteristics of the TUDelft facility are:

- Blade, turbine and location: Prince Fiber Technics (Aerpac) blades mounted on an experimental turbine at the site of TUDelft, see figure A.1. The facility is located at the Delft University of Technology near Delft in the Netherlands. A roughness height of 0.25m can be assumed.
- Number of blades: 2
- Blade span (from flange to tip) = 4.4 m
- Rotor diameter = 10 m
- Blade profile: NLF(1)-0416
- Blade without twist and taper. The chord lengths is 0.5 meters.
- Pressure tap measurements around profiles at 4 different radial sta-

tions. These taps are positioned at 30%, 50%, 70% and 90% of the rotor radius. Note that the sections are not measured simultaneously.

There are 59 taps per station.

- The inflow angle is measured with a three hole probe mounted at 75% span. The length of this probe is $0.55c$ and the angle between the probe and the chord is 0° .



Figure A.1: TUDelft facility as used in IEA Task 14/18

A.2 Aerodynamic test facility of the Energy Research Center of the Netherlands, ECN

The global characteristics of the ECN facility are:

- Turbine, location and blade: A commercial Aerpac 25 WPX blade mounted on the HAT-25 experimental wind turbine see figure A.2. The HAT-25 wind turbine is located at ECN near Petten in the Netherlands. The prevailing wind direction is from South-West, at which most of the measurements are taken. In this direction, the terrain upstream of the turbine is obscured by dunes over around 600 m. As a result, the turbulence intensities at the site may depend strongly on the conditions. Generally, the values of the turbulence intensities are between 5% and 20%. A special feature of this turbine is the fact that a large range of pitch angles and the rotor speeds could easily be set by the control system.
- Number of blades: 2
- Blade span (from flange to tip) = 12.1 m
- Rotor diameter = 27.44 m
- Blade profile: NACA44xx
- Blade with twist and taper: Twist ≈ 12 degrees, root chord = 1.5 m, tip chord = 0.412 m.
- Pressure tap measurements around profiles at 3 different radial stations. These taps are positioned at 36%, 64% and 82% of the rotor radius with 47 taps per station. All 3 sections are measured simultaneously:
- Inflow angle and inflow velocity measured close at the inboard station with a 5 hole probe.

A.3 Aerodynamic test facility of Imperial College, IC and Rutherford Appleton Laboratory, RAL

The global characteristics of the IC/RAL facility are:

- Turbine, blade and location: A commercial LM - 8.5 blade mounted on a Windharvester wind turbine. The experimental facility is located at

the Rutherford Appleton Laboratory's wind site, about 80 km West of London: The Laboratory is set on a plateau to the north of a range of hills called The Ridgeway. The prevailing winds are from the Southwest with an annual mean of about 4.5m/s and typically 17% turbulence, a typical figure estimated for the roughness is 0.03m.

- Number of blades: 3
- Blade span (from flange to tip) = 8.2 m
- Rotor diameter = 17 m
- Blade profile: NACA632xxx
- Blade with twist and taper: Twist = 15 degrees, root chord = 1.09 m, tip chord = 0.445 m.
- Pressure tap measurements around profiles at 6 different radial stations. The stations are at 20%, 30%, 40%, 50%, 65% and 80% radius. There are 26 pressure taps per station with a greater concentration of holes near the leading edge where the larger pressure gradients are found.
- Inflow angle and inflow velocity is measured on 3 locations with 5 hole pitot probes.

A.4 Aerodynamic test facilities of National Renewable Energy Laboratory, NREL

The global characteristic of NREL facility are:

- Turbine, blade and location: NREL in house blade, mounted on an experimental turbine see figure A.3. All atmospheric testing was conducted at the National Renewable Energy Laboratory's (NREL) National Wind Technology Center (NWTC) located 10 miles north of Golden, Colorado, U.S.A. Although the local terrain is flat, with grassy vegetation extending over 0.8 km upwind, the site is situated approximately 5 km from the base of the Rocky Mountains which are located directly upwind.
- Number of blades: 3
- Blade span (from flange to tip) = 4.521 m

- Rotor diameter = 10 m
- Blade profile: NREL S809
- Two tests:
 - Phase II: Blade without twist and taper
 - Phase III and IV: Blade without taper but with twist: Twist = 45 degrees. The chord length = 0.46 m.
- Detailed pressure tap measurements around profiles at 4 (Phase II) or 5 (Phase III and IV) different radial stations. The Phase II experiment used 28 pressure taps at 30% span, 47% span, 63% span, and 80% span. During Phases III and IV, 22 taps were instrumented at 30% span, 47% span, 63% span, 80% span, and 95% span. Pairs of taps at 4% chord and 36% chord were installed at various other intermediate span locations (36%, 41%, 52%, 58%, 69%, 74%, 85%, 90%, 92%, and 98%).
- Inflow angle is measured slightly inboard of the 4 or 5 primary stations with wind vanes (Phase II and Phase III) or 5-hole probes (Phase IV).

A.5 Aerodynamic test facility of Mie University

The global characteristics of the facility at Mie University are:

- Turbine, blade and location: Mie in house blade, mounted on an experimental turbine. The Open Air Rotor Research Facility is located at the Experimental Farm in the Mie University at Tsu City in Japan.
- Number of blades: 3
- Blade span (from flange to tip) = 4.567 m
- Rotor diameter = 10 m
- Blade profile: DU91-W2-250 and DU93-W-210
- Blade with twist and taper. The root chord is 0.45 meter and the tip chord is 0.1 meters. The twist is 12.8 degrees.
- Pressure tap measurements around profiles at 4 different radial stations positioned at 4 rotor blade sections at 32.5% , 50% , 70% and 90% of the rotor radius. There are 60 taps per station with 0.4 mm diameter.

Note that the stations are not measured simultaneously.

- The inflow velocity and the inflow angle are measured with 2 five-hole spherical probes mounted at both sides of the measurement stations,
 - 20.5% and 38.5% span locations for the 32.5% measurement station;
 - 38.5% and 56% span locations for the 50% measurement station;
 - 56% and 76% span locations for the 70% the measurement station;
 - 76% and 96% span locations for the 90% the measurement station.

The probe length is 1 chord and the angle between the probe and the chord is 0 deg.

A.6 Aerodynamic test facility of RISØ

The RISØ measurements have been carried out on the 100 kW Tellus machine at the wind turbine test site at Riso. A detailed description of the facility and the experimental results can be found in the references [Madsen \(1991a\)](#), [Madsen \(1991b\)](#) and [Madsen \(1991c\)](#). It is a fixed pitch, stall controlled, three bladed turbine, with a rotor diameter of 19 meter see figure A.4. The turbine has a double wound generator which gives the following two synchronous rotational rotor speeds:

- 47.5 rpm, 47.9 rpm at rated power
- 35.6 rpm, 36.3 rpm at rated power

The tower is of the lattice type with three main tower poles and its height is 29.3 m. The blade type is the LM 8.2 m blade with a blade length of 8.2 meter. The blades have both twist and taper. The twist is 15 degrees, the root chord is 1.09 meter and the tip chord is 0.45 degrees. The airfoil along the blade is of the NACA 63n-2nn series. One of the blades has been modified so that the aerodynamic forces on three segments of the blades can be measured. Each blade segment is 0.5 m in spanwise length and is suspended on a 3 component balance. The radial positions of the mid of the blade segments are the following:

Segment 1:	Radius 3.56 m,	37 % radius
Segment 2:	Radius 6.48 m,	68 % radius
Segment 3:	Radius 9.26 m,	98 % radius

The inflow to the blade has been measured with a five hole pitot tube mounted on the blade about one chord length in front of the leading edge of the blade, just outboard the mid blade segment.



Figure A.2: ECN facility as used in IEA Task 14/18



Figure A.3: NREL facility as used in IEA Task 14/18



Figure A.4: RISØ facility as used in IEA Task 14/18

Appendix B

Model for induced velocities at yaw

In this Appendix a complete description is given for a model which predicts the induced velocity as function of azimuth angle under yawed conditions. For positive yaw this model reads as follows:

$$u_i = u_{i,0} [1 - A_1 \cdot \cos(\phi_r - \psi_1) - A_2 \cdot \cos(2\phi_r - \psi_2)] \quad (\text{B.1})$$

By mirroring, the induced velocity at negative yaw reads:

$$u_i = u_{i,0} [1 - A_1 \cdot \cos(360 - \phi_r - \psi_1) - A_2 \cdot \cos(360 - 2\phi_r - \psi_2)] \quad (\text{B.2})$$

The amplitudes A_1 en A_2 and the phases ψ_1 en ψ_2 are a function of the relative radius ($r_{\text{rel}} = r/R$) and the yaw angle (ϕ_y) (Note that the phases are expressed in degrees).

These amplitudes and phases can be found in the tables B.1, B.2, B.3 and B.4. (Note that the unit of the phases is degrees!). It requires the coefficients f_0 , f_1 etc. which follow from the tables B.5 until B.8. For clarification: $A_1(r_{\text{rel}}, 15)$ refers to the value of amplitude A_1 at r_{rel} and a yaw angle of 15 deg. The value of $\psi_1(0.29, \phi_y)$ refers to the value of ψ_1 at a yaw angle ϕ_y and $r_{\text{rel}} = 0.29$.

$ \phi_y \geq 15 \text{ deg}$	$f_{0,A1} + f_{1,A1} \cdot r_{\text{rel}} + f_{2,A1} \cdot r_{\text{rel}}^2 + f_{3,A1} \cdot \sin \phi_y + f_{4,A1} \cdot \sin^2\phi_y$
$ \phi_y < 15 \text{ deg}$	$(\phi_y /15) \cdot A_1(r_{\text{rel}}, 15)$

Table B.1: Expression for $A_1(r_{\text{rel}}, \phi_y)$

$ \phi_y \geq 15 \text{ deg}$	$f_{0,A2} + f_{1,A2} \cdot r_{\text{rel}} + f_{2,A2} \cdot r_{\text{rel}}^2 + f_{3,A2} \cdot \sin \phi_y + f_{4,A2} \cdot \sin^2\phi_y$
$ \phi_y < 15 \text{ deg}$	$(\phi_y /15) \cdot A_2(r_{\text{rel}}, 15)$

Table B.2: Expression for $A_2(r_{\text{rel}}, \phi_y)$

$r_{\text{rel}} \leq 0.15$	270
$0.15 < r_{\text{rel}} < 0.29$	$270 + [(r_{\text{rel}} - 0.15)/0.14] \cdot [\psi_1(0.29, \phi_y) - 270]$
$0.29 \leq r_{\text{rel}} \leq 0.71$	$f_{0,\psi1} + f_{1,\psi1} \cdot r_{\text{rel}} + f_{2,\psi1} \cdot r_{\text{rel}}^2 + f_{3,\psi1} \cdot \sin \phi_y + f_{4,\psi1} \cdot \sin^2\phi_y$
$0.71 < r_{\text{rel}} < 0.85$	$\psi_1(0.71, \phi_y) + [(r_{\text{rel}} - 0.71)/0.14] \cdot [90 - \psi_1(0.71, \phi_y)]$
$r_{\text{rel}} \geq 0.85$	90

Table B.3: Expression for $\psi_1(r_{\text{rel}}, \phi_y)$

$0 \leq r_{\text{rel}} \leq 1$ en $0 \leq \phi_y \leq 90$	$f_{0,\psi2} + f_{1,\psi2} \cdot r_{\text{rel}} + f_{2,\psi2} \cdot r_{\text{rel}}^2 + f_{3,\psi2} \cdot \sin \phi_y + f_{4,\psi2} \cdot \sin^2\phi_y$
--	---

Table B.4: Expression for $\psi_2(r_{\text{rel}}, \phi_y)$

coefficient	value	unit
$f_{0,A1}$	0.445	[-]
$f_{1,A1}$	-1.78	[-]
$f_{2,A1}$	1.63	[-]
$f_{3,A1}$	-0.0543	[-]
$f_{4,A1}$	0.367	[-]

Table B.5: Values of the coefficients in the function for A_1

coefficient	value	unit
$f_{0,A2}$	0.0523	[-]
$f_{1,A2}$	-0.284	[-]
$f_{2,A2}$	0.327	[-]
$f_{3,A2}$	-0.0134	[-]
$f_{4,A2}$	0.144	[-]

Table B.6: Values of the coefficients in the function for A_1

coefficient	value	unit
f_{0,ψ_1}	-51.2	[deg]
f_{1,ψ_1}	1009	[deg]
f_{2,ψ_1}	-1383	[deg]
f_{3,ψ_1}	387	[deg]
f_{4,ψ_1}	-260	[deg]

Table B.7: Values of the coefficients in the function for ψ_1

coefficient	value	unit
f_{0,ψ_2}	296	[deg]
f_{1,ψ_2}	60.9	[deg]
f_{2,ψ_2}	-71.3	[deg]
f_{3,ψ_2}	-335	[deg]
f_{4,ψ_2}	243	[deg]

Table B.8: Values of the coefficients in the function for ψ_2

Appendix C

Contribution of author to thesis

The research as described in this thesis is mainly devoted to engineering models in rotor and wind farm aerodynamics and the use of dedicated measurements in their development and validation. The research for rotor aerodynamic models is described in Part II and the research for wind farm aerodynamic models in Part III.

One of the main chapters in Part II is chapter 3 which describes the uncertainties in rotor aerodynamic models as seen by the author. The chapter also describes remedies (i.e. engineering add-on's) to overcome these uncertainties. The chapter is a summary of efforts which have been undertaken by the wind energy society as a whole. Thereafter the chapters 5 to 8 describe results from research to which the author has contributed significantly. Most of these results come from projects which were coordinated by the author. This was the case for the IEA Tasks 14, 18, 29 and for the EU Dynamic Inflow projects and the Mexico project (the latter two were jointly coordinated with Herman Snel from ECN, where IEA Task 29 is jointly coordinated with Koen Boorsma from ECN).

However the author also had a role in the assessment and processing of measurements and the analysis, validation, assessment and improvement of engineering add-on's for the ECN codes. More specifically he assessed the value of the ECN models for stall, flow non-uniformity in the rotor plane, dy-

dynamic inflow and yaw as described in sections 5.7.1, 5.7.2, 5.7.3 (and the supporting analyzes from sections 5.4 and 5.5), in section 6.3.4 (and the supporting analysis from section 6.3.3), and in sections 7 and 8. This led to the models from sections 5.7.4 and the model from Appendix B. He also identified the added value of more advanced models on the field of stall, dynamic inflow and yaw as a result of the analysis described in sections 5.7.3, 7.3, 8.4 and 8.5. This led to various recommendations to improve engineering models on these fields which will be implemented in future projects.

From a more fundamental point of view he assessed the behavior of the induced velocities from the momentum theory using the Mexico measurements in relation to the loading on the turbine, see the discussions in e.g. sections 6.3.1 and 6.3.2.

The structure of Part III on wind farm aerodynamics is very similar. In chapter 10 the uncertainties in wind farm aerodynamics models are described as seen by the author. In view of the large variety in models this is less straightforward to do than for the rotor aerodynamic models. Then chapter 11 describes results from research to which the author contributed. These contributions mainly lied on the assessment and improvements of the Wakefarm model for which he was responsible until 2006. This led to the first model improvements for multiple wake and near wake conditions as described in sections 9.5 and 11.1. Later his involvement on the Wakefarm and Farmflow code was more on the side line and the comparisons which are presented in section 11.2 were performed by his colleague Edwin Bot. The author remained responsible for the analysis of the EWTW measurements as described in section 11.2.4 and which were used in the improvement of Farmflow(Wakefarm) program.

Obviously the introductory and concluding chapters with the recommendations for model improvements also come from the author.

Most of these results have been reported in articles, conference papers and technical ECN reports. More specifically the following references formed an important source for this thesis:

- Chapter 5: [Schepers, van Rooij and Bruining, \(2003\)](#), [van Rooij et al. \(2003\)](#), [Schepers et al. \(2004a\)](#), [Schepers et al. \(2004b\)](#), [Schepers and van Rooij \(2005\)](#), [Schepers \(2007a\)](#), and [Schepers, Boorsma et al. \(2011\)](#);
- Chapter 6: [Schepers, Snel and Boorsma \(2010\)](#), [Schepers, Pascal and](#)

Snel (2010) and Schepers et al. (2011);

- Chapter 7: Snel and Schepers (1994), Schepers and Snel (1995) and Schepers (2007c);
- Chapter 8: Schepers (1999), Schepers (2007b), and Schepers, Pascal and Snel (2010);
- Chapter 11: Schepers (2003) Schepers and van der Pijl (2007) and Schepers, Obdam and Prospathopoulos (2012).

Curriculum-vitae

Gerard Schepers was born on December 3, 1959 in Winterswijk the Netherlands. After obtaining his High School (VWO) diploma from the Hameland College in that city he went to Delft for a Masters study in Aerospace Engineering. In 1986 he obtained his MSc on an investigation of shock wave boundary layer interaction in a transonic wind tunnel. Thereafter he joined the Unit Wind Energy of the Energy Research Center of the Netherlands, ECN. He worked as a researcher and coordinator of several large (inter)national research projects, mainly on the field of aerodynamics and aero-acoustics. He has also been active in various industrial consultancy projects.

With a special interest in educational activities he almost automatically got involved in various lecture series at Dutch and foreign universities. Since January 2012 he is also a HBO Professor at the University of Applied Sciences in Leeuwarden.

Working in early mornings, evenings, weekends and holidays he finished this PhD thesis. He lives in Alkmaar together with his wife Henrike and their two children: Erik and Sander.